

MATERIALS PHYSICS AND MECHANICS

Vol. 51, No. 4, 2023



MATERIALS PHYSICS AND MECHANICS

Principal Editors:

Alexander Belvaev

Andrei Rudskoi

Institute for Problems in Mechanical Engineering of the Russian Academy of Science (RAS), Russia

Peter the Great St. Petersburg Polytechnic University, Russia

Founder and Honorary Editor: Ilya Ovid'ko (1961-2017)

Institute for Problems in Mechanical Engineering of the Russian Academy of Sciences (RAS), Russia

Associate Editor:

Anna Kolesnikova

Artem Semenov

Institute for Problems in Mechanical Engineering of the Russian Academy of Sciences (RAS), Russia

Peter the Great St. Petersburg Polytechnic University, Russia

Editorial Board:

E.C. Aifantis

Aristotle University of Thessaloniki, Greece

K.E. Aifantis

University of Florida, USA

U. Balachandran

Argonne National Laboratory, USA

A. Bellosi

Research Institute for Ceramics Technology, Italy

S.V. Bobylev

Institute for Problems in Mechanical Engineering (RAS), Russia

A.I. Borovkov

Peter the Great St. Petersburg Polytechnic University, Russia

G.-M. Chow

National University of Singapore, Singapore

Yu. Estrin

Monash University, Australia

A.B. Freidin

Institute for Problems in Mechanical Engineering (RAS), Russia

Y. Gogotsi

Drexel University, USA

I.G. Goryacheva

Institute of Problems of Mechanics (RAS), Russia

D. Hui

University of New Orleans, USA

G. Kiriakidis

IESL/FORTH, Greece

D.M. Klimov

Institute of Problems of Mechanics (RAS), Russia

G.E. Kodzhaspirov

Peter the Great St.Petersburg Polytechnic University, Russia

S.A. Kukushkin

Institute for Problems in Mechanical Engineering (RAS), Russia

T.G. Langdon

University of Southampton, U.K.

V.P. Matveenko

Institute of Continuous Media Mechanics (RAS), Russia

A.I. Melker

Peter the Great St. Petersburg Polytechnic University, Russia

Yu.I. Meshcheryakov

Institute for Problems in Mechanical Engineering (RAS), Russia

N.F. Morozov

St.Petersburg State University, Russia

R.R. Mulyukov

Institute for Metals Superplasticity Problems (RAS), Russia

Yu.V. Petrov

St.Petersburg State University, Russia

N.M. Pugno

Politecnico di Torino, Italy

B.B. Rath

Naval Research Laboratory, USA

A.E. Romanov

Ioffe Institute (RAS), Russia

A.M. Sastry

University of Michigan, Ann Arbor, USA

B.A. Schrefler

University of Padua, Italy

N.V. Skiba

Institute for Problems in Mechanical Engineering (RAS), Russia

A.G. Sheinerman

Institute for Problems in Mechanical Engineering (RAS), Russia

R.Z. Valiev

Ufa State Aviation Technical University, Russia

K. Zhou

Nanyang Technological University, Singapore

"Materials Physics and Mechanics" Editorial Office:

Phone: +7(812)552 77 78, ext. 224 E-mail: mpmjournal@spbstu.ru Web-site: http://www.mpm.spbstu.ru

International scientific journal "Materials Physics and Mechanics" is published by Peter the Great St. Petersburg Polytechnic University in collaboration with Institute for Problems in Mechanical Engineering of the Russian Academy of Sciences in both hard copy and electronic versions.

The journal provides an international medium for the publication of reviews and original research papers written in English and focused on the following topics:

- Mechanics of composite and nanostructured materials.
- Physics of strength and plasticity of composite and nanostructured materials.
- Mechanics of deformation and fracture processes in conventional materials (solids).
- Physics of strength and plasticity of conventional materials (solids).
- Physics and mechanics of defects in composite, nanostructured, and conventional materials.
- Mechanics and physics of materials in coupled fields.

Owner organizations: Peter the Great St. Petersburg Polytechnic University; Institute of Problems of Mechanical Engineering RAS.

Materials Physics and Mechanics is indexed in Chemical Abstracts, Cambridge Scientific Abstracts, Web of Science Emerging Sources Citation Index (ESCI) and Elsevier Bibliographic Databases (in particular, SCOPUS).

© 2023, Peter the Great St. Petersburg Polytechnic University © 2023, Institute for Problems in Mechanical Engineering RAS



МЕХАНИКА И ФИЗИКА МАТЕРИАЛОВ

Materials Physics and Mechanics

Том 51, номер 4, 2023 год

Учредители:

Редакционная коллегия журнала Главные редакторы:

д.ф.-м.н., чл.-корр. РАН А.К. Беляев Институт проблем машиноведения Российской академии наук (РАН)

д.т.н., академик РАН А.И. Рудской Санкт-Петербургский политехнический университет Петра Великого

Основатель и почетный редактор: д.ф.-м.н. И.А. Овидько (1961-2017)

Институт проблем машиноведения Российской академии наук (РАН)

Ответственный редактор

д.ф.-м.н. А.Л. Колесникова

Институт проблем машиноведения Российской академии наук (РАН)

д.ф.-м.н. А.С. Семенов

Санкт-Петербургский политехнический университет Петра Великого

Международная редакционная коллегия:

д.ф.-м.н. С.В. Бобылев

Институт проблем машиноведения РАН, Россия

к.т.н., проф. А.И. Боровков

Санкт-Петербургский политехнический ун-т Петра Великого, Россия

д.ф.-м.н., проф. Р.З. Валиев

Уфимский государственный технический университет, Россия

д.ф.-м.н., академик РАН И.Г. Горячева Институт проблем механики РАН, Россия

д.ф.-м.н., академик РАН Д.М. Климов

Институт проблем механики РАН, Россия д.т.н., проф. Г.Е. Коджаспиров

Санкт-Петербургский политехнический ун-т Петра Великого, Россия

д.ф.-м.н., проф. С.А. Кукушкин

Институт проблем машиноведения РАН, Россия

д.ф.-м.н., академик РАН В.П. Матвеенко

Институт механики сплошных сред РАН, Россия д.ф.-м.н., проф. А.И. Мелькер

Санкт-Петербургский политехнический ун-т Петра Великого, Россия

д.ф.-м.н., проф. Ю.И. Мещеряков

Институт проблем машиноведения РАН, Россия

д.ф.-м.н., академик РАН Н.Ф. Морозов

Санкт-Петербургский государственный университет, Россия

д.ф.-м.н., чл.-корр. РАН **Р.Р. Мулюков**

Институт проблем сверхпластичности металлов РАН, Россия

д.ф.-м.н., чл.-корр. РАН Ю.В. Петров

Санкт-Петербургский государственный университет, Россия

д.ф.-м.н., проф. А.Е. Романов

Физико-технический институт им. А.Ф. Иоффе РАН, Россия

д.ф-м.н. Н.В. Скиба

Институт проблем машиноведения РАН, Россия

д.ф.-м.н., проф. А.Б. Фрейдин

Институт проблем машиноведения РАН, Россия

д.ф-м.н. А.Г. Шейнерман Институт проблем машиноведения РАН, Россия Prof., Dr. E.C. Aifantis

Aristotle University of Thessaloniki, Greece

Dr. K.E. Aifantis

University of Florida, USA

Dr. U. Balachandran

Argonne National Laboratory, USA

Dr. A. Bellosi

Research Institute for Ceramics Technology, Italy

Prof., Dr. G.-M. Chow

National University of Singapore, Singapore

Prof., Dr. Yu. Estrin

Monash University, Australia

Prof., Dr. Y. Gogotsi

Drexel University, USA

Prof., Dr. D. Hui

University of New Orleans, USA Prof., Dr. G. Kiriakidis

IESL/FORTH, Greece

Prof., Dr. T.G. Langdon

University of Southampton, UK

Prof., Dr. N.M. Pugno

Politecnico di Torino, Italy

Dr. B.B. Rath

Naval Research Laboratory, USA

Prof., Dr. A.M. Sastry

University of Michigan, Ann Arbor, USA

Prof., Dr. B.A. Schrefler

University of Padua, Italy Prof. Dr. K. Zhou

Nanyang Technological University, Singapore

Тел.: +7(812)552 77 78, доб. 224 E-mail: mpmjournal@spbstu.ru Web-site: http://www.mpm.spbstu.ru

Тематика журнала

Международный научный журнал "Materials Physics and Mechanics" издается Санкт-Петербургским политехническим университетом Петра Великого в сотрудничестве с Институтом проблем машиноведения Российской академии наук в печатном виде и электронной форме. Журнал публикует обзорные и оригинальные научные статьи на английском языке по следующим

- Механика композиционных и наноструктурированных материалов.
- Физика прочности и пластичности композиционных и наноструктурированных материалов.
- Механика процессов деформации и разрушения в традиционных материалах (твердых телах).
- Физика прочности и пластичности традиционных материалов (твердых тел).
- Физика и механика дефектов в композиционных, наноструктурированных и традиционных материалах.
- Механика и физика материалов в связанных полях.

Редколлегия принимает статьи, которые нигде ранее не опубликованы и не направлены для опубликования в другие научные издания. Все представляемые в редакцию журнала "Механика и физика материалов" статьи рецензируются. Статьи могут отправляться авторам на доработку. Не принятые к опубликованию статьи авторам не возвращаются.

Журнал "Механика и физика материалов" ("Materials Physics and Mechanics") включен в систему цитирования Web of Science Emerging Sources Citation Index (ESCI), SCOPUS и РИНЦ.

> © 2023, Санкт-Петербургский политехнический университет Петра Великого © 2023, Институт проблем машиноведения Российской академии наук

Contents

Study of the microstructure effect of SPD-treated titanium on microhardness and corrosion resistance in physiological environments for implantology purposes E.G. Zemtsova, A.A Petrov, S.O. Kirichenko, N.F. Morozov, V. K. Kudymov, A.Yu. Arbenin, B.N. Semenov, V.M. Smirnov	1-10
Tribological and tensile behaviour of Si ₃ N ₄ reinforced Cu-Sn matrix composites B. Adaveesh, G.V. Prabhushankar, M. Nagaral	11-22
Optimization of wear behaviour of hybrid Al (6061)-Al ₂ O ₃ -B ₄ C composites through hybrid optimization method P.K. Gupta, M.K. Gupta	23-37
The influence of friction stir processing on the microstructure and properties of the AD31T alloy A.E. Medvedev, V.V. Atroshchenko, A.S. Selivanov, A.R. Bogdanov, M.V. Gorbatkov, Y.V. Logachev, V.S. Lobachev, A.R. Sadrislamov	38-4 9
Study of burnishining effect on the thermal spray coatings A. Agnihotri, S.B.S Kalsi, H. Kansal	50-65
Peculiarities of the two-stage Zn diffusion profile formation from vapor phase into InGaAs/InP heterostructure for avalanche photodiode fabrication S.A. Blokhin, R.V. Levin, V.S. Epoletov, A.G. Kuzmenkov, A.A. Blokhin, M.A. Bobrov, Ya.N. Kovach, N.A. Maleev, E.V. Nikitina, V.V. Andryushkin, A.P. Vasiljev, K.O. Voropaev, V.M. Ustinov	66-75
The effect of ZnO cupping layer on the formation of sol-gel synthesized Ag nanoparticles L.A. Sokura, A.V. Kremleva, A.E. Romanov	76-84
Spin transistor effect in edge channels of silicon nanosandwiches L.E. Klyachkin, N.T. Bagraev, A.M. Malyarenko	85-95
Gas phase large-scale synthesis of Silicon carbide nanowires by industrial electron accelerator S.P. Bardakhanov, D.Y. Trufanov, I.K. Chakin, V.R. Gaponenko	96-106
Laser induced modification of nickel surface for non-enzymatic glucose detection A.S. Kondrateva, D.A. Strekalovskaya, B.V. Babuyk, A. Kuznetsov, L.A. Filatov, P.G. Gabdullin	07-11 7
Structural and mechanical relaxation on annealing in glass-metal layered composites M.A. Barbotko, O.N. Lyubimova, M.V. Ostanin	18-129

The influence of the altered structure zone characteristics after the material jet treatment on the samples stress state during tensility A.I. Verameichyk, M.V. Neroda, B.G. Holodar	130-141
The effect of mass collapse under hypervelocity impact of solid paraboloid into a thin screen A.F. Nechunaev, N.V. Naumova, N.P. Dorofeev	142-159
Simulation of the stress-deformed state of a rectangular bar using fast trigonometric interpolation in various statements of boundary value problems A.D. Chernyshov, V.V. Goryainov, E.N. Kovaleva	160-171
Ab initio study of Hydrogen and Lithium behaviors in Cu ₂ O A. Larabi, M. Mebarki, I. Abdellaoui, A. Mahmoudi, S. Merazga, N. Gabouze	172-185

Study of the microstructure effect of SPD-treated titanium on microhardness and corrosion resistance in physiological environments for implantology purposes

Submitted: October 30, 2022

Accepted: December 1, 2022

Approved: November 20, 2022

E.G. Zemtsova ¹ ¹ ², A.A. Petrov ¹, S.O. Kirichenko ¹, N.F. Morozov ¹, V.K. Kudymov ², A.Yu. Arbenin ¹, B.N. Semenov ¹ ¹, V.M. Smirnov ¹

¹ St. Petersburg State University, St. Petersburg, Russia
² St. Petersburg State University of Film and Television, St. Petersburg, Russia

⊠ ezimtsova@yandex.ru

Abstract. Increasing the duration and quality of human life requires solving a number of medical and materials science problems, in particular, the creation of materials designed for long-term work in contact with the biological environment. When creating such materials for medical devices, it is necessary to take into account that they must meet strict requirements, namely, be biologically compatible with tissues, have corrosion resistance to various biological fluids and have increased wear resistance. The study of the effect of Ti microstructure on microhardness and its corrosion resistance in physiological environments is necessary to create implants designed for long-term work in contact with the biological environment of the body. In accordance with this, the purpose of this work was to establish the nature of the relationship between the structural properties of ultrafine-grained Ti with different sizes of crystallites (grains) obtained using equal-channel angular pressing (ECAP) of different intensity, namely with a different number of processing cycles, on the microhardness and stability of Ti in a corrosive environment.

Keywords: ultrafine-grained titanium; corrosion resistance; microhardness; intense plastic deformation; implants

Acknowledgements. The research was conducted under the financial support the Russian Science Foundation grant (project No. 22-21-00573). The research was carried out using the equipment of the resource centers of the St. Petersburg State University Scientific Park "Nanotechnology" and "Innovative technologies of composite nanomaterials".

Citation: Zemtsova EG, Petrov AA, Kirichenko SO, Morozov NF, Kudymov VK, Arbenin AY, Semenov BN, Smirnov VM. Study of the microstructure effect of SPD-treated titanium on microhardness and corrosion resistance in physiological environments for implantology purposes. *Materials Physics and Mechanics*. 2023;51(4): 1-10. DOI: 10.18149/MPM.5142023_1.

Introduction

Currently, titanium is widely used as a material for dental implants. This is explained by a number of physical and mechanical properties of both pure Ti and its alloys, such as: high elasticity modulus, tensile strength, fatigue strength combined with low cytotoxicity. At the same time, Ti, due to the presence of a natural 2-6 nm thick oxide layer, is passive to most existing corrosive media under standard (e.g. physiological) conditions. A number of studies [1,2] have shown how the thickness and protective properties of the oxide film

© E.G. Zemtsova, A.A. Petrov, S.O. Kirichenko, N.F. Morozov, V.K. Kudymov, A.Yu. Arbenin, B.N. Semenov, V.M. Smirnov, 2023.

Publisher: Peter the Great St. Petersburg Polytechnic University

This is an open access article under the CC BY-NC 4.0 license (https://creativecommons.org/li-censes/by-nc/4.0/)

on the Ti surface depend on the external conditions of the physiological environment. Our research was aimed at identifying the relationship between the nano- and microstructure of Ti and its corrosion resistance in the physiological environments. Mechanical processing of metals makes it possible to obtain nanostructured Ti with a reduced crystallite size in order to enhance its physical and mechanical characteristics. In particular, severe plastic deformation (SPD) of Ti and its alloys is used for the production of ultrafine-grained titanium (UFG-Ti) with a tensile strength above 1000 MPa [3–6], which is significantly higher than the usual values of the tensile strength of coarse-grained (CG) Ti.

The main studies devoted to the corrosion stability of Ti with a reduced crystallite size were aimed at identifying the relationship between corrosion resistance in acidic media (HCl, H₂SO₄) and the microstructure of samples [7–9]. A number of studies are devoted to Ti corrosion in artificial physiological media (simulated body fluid) [10–12]. The conducted studies show that the corrosion resistance of UFG-Ti is explained by a combination of the effects of grain size reduction and the basic surface texture [11,13,14].

It is known that electrochemical corrosion of Ti in saliva-type physiological media can trigger allergic reactions [15], in addition, the presence of Ti ions can have a negative effect on the survivability and differentiation of osteoblasts [16], which certainly affects the feasibility and prospects of using dental implants. It is also known that prophylactic agents often contain fluorides in their composition, which lead to the destruction of the passivation film on the Ti surface and its further dissolution [17]. A comprehensive analysis of the mechanical and corrosion properties of UFG-Ti will expand the scope of application of this type of materials in implantology [18,19]. In accordance with this, the purpose of this work was to establish the nature of the relationship between the mechanical and structural properties of UFG-Ti with different sizes of crystallites (grains) obtained using Equal channel angular pressing (ECAP) of different intensity (with different number of processing cycles), and its resistance in a corrosive environment. As a corrosive medium, an environment was chosen that, in terms of salt composition and temperature regime, is close to physiological body fluids and at the same time enriched with fluoride ions. The results will contribute to the development of methods for synthesizing materials for implantology with specified mechanical and corrosion properties.

Experimental

Microhardness measurements. Square-shaped Ti samples were made from rods of commercially available Ti ASTM Grade 4 alloy of nominal composition (wt. %) Fe 0.10 %, Si 0.12 %, O 0.04 %, N 0.01 % H and 0.3 % other elements. The samples were subjected to severe plastic deformation (SPD) on an ECAP unit with a channel intersection angle of 105° at 400 °C. Depending on the number of repeated passage cycles in the ECAP channel, the samples are designated UFG 2, UFG 4, UFG 6, UFG 8, UFG 10, UFG 12, respectively. The sample designated "(CG) coarse grained" was used without deformation treatment as a reference.

Thick (3 mm) samples were cut transversely from the rods of the material on an electric erosion machine, filled with epoxy resin into the slice, and then their surface was mechanically polished on carbide-silicon sandpapers of grades 320, 600, 800, 1000 and 1200, and then sequentially polished on a Buehler Automet 250 grinding and polishing machine using polishing suspensions based on corundum and silicon oxide (5, 1 μ m, 200 and 50 nm), respectively. At the end of the mechanical processing, the samples were extracted from the fillings, washed in an ultrasonic bath in isopropanol and deionized water and dried.

Transmission electron microscopy. TEM studies of the structures were performed on transmission electron microscopes JEM 2000EX and JMX200CX at accelerating voltages of

200 and 120 kV, respectively. Foils for electron microscopic studies were prepared by standard methods on a jet electropolishing device.

Measurement of microhardness. Microhardness was measured on a HMV-2T microhardometer manufactured by Shimadzu Corporation, which allows stepwise application of loads from 250 mN to 20 N. The Vickers method of the recovered print was used. The indenter was a regular four-sided diamond pyramid with an angle of 136° between opposite faces. The correctness of the microhardness determination was checked by reference samples with hardness 278 HV, 467 HV and 768 HV. Hereafter, the hardness is given in conventional HV units in accordance with the standards; the implied physical dimension is [kgs/mm²]. For each material, 10 hardness determinations were carried out on 2 separate samples, the values were averaged, indentation was carried out near the geometric center of the grinds with the application of a load for 15 seconds.

Electrochemical measurements. All electrochemical measurements were carried out using a Solartron 1287 potentiostat/galvanostat with a Solartron 1260 impedance meter (Solartron Analytical) with native software. An original electrochemical cell was made according to the classical three-electrode scheme with a sponge Pt counter electrode, a AgCl electrode with a saturated KCl solution connected to the cell via a salt bridge (Luggin capillary) served as a reference electrode, a Ti sample was the working electrode. The potentiodynamic measurements were carried out with a standard sweep speed of 0.1667 mV/s. During measurements in the cell, the solution was maintained at 35 \pm 0.5 °C using an external thermostat. 15 minutes before and during the measurement, the solution was stirred with a mechanical stirrer and bubbled with nitrogen (purity 99.999, 100 mL/min). A working solution of 0.15 M NaCl and 0.05 M NH₄F was prepared from chemically pure reagents using deionized water (25 MOhm·cm, Millipore Simplicity UV). 500 mL of the solution was used for each measurement. The pH was maintained at 7.2 with a pH electrode control on the Hanna Instruments meter.

Results and Discussion

Microstructure of samples. To determine the microstructure of samples subjected to SPD, their high-resolution EBSD maps were obtained, fragments of which are shown in Fig. 1. These maps show a complex grain structure, grain size and grain boundaries in Ti samples: small-angle (SA), large-angle (LA), as well as double grain misorientation.

Already after the first two ECAP cycles (sample UFG 2), the transformation of the initial titanium grains led to a microstructure complication (Fig. 1(b)). In Russian publications, it is also known as fragmentation [9]. During the further increase of accumulated deformation, intensive formation of equiaxed grains of submicrocrystalline size took place in the structure of UFG 4 and UFG 6 samples (Fig. 1(b,c)). Note also the almost complete disappearance of the twin boundaries from the microstructure (Fig. 1(c)) as the deformation increases.

A further increase in deformation in UFG 8 - UFG 12 samples did not lead to significant changes in the microstructure morphology, but only contributed to a gradual increase in the small grains fraction (Fig. 1(g)).

Figure 2 shows the dependences of the density of small-angle and large-angle grain boundaries, as well as the total density of the boundaries on the number of ECAP cycles. It is possible to note an increase in the proportion of large-angle grain boundaries as a result of SPD after 1-12 cycles of ECAP and a decrease in the proportion of small-angle grain boundaries after 8 cycles of ECAP.

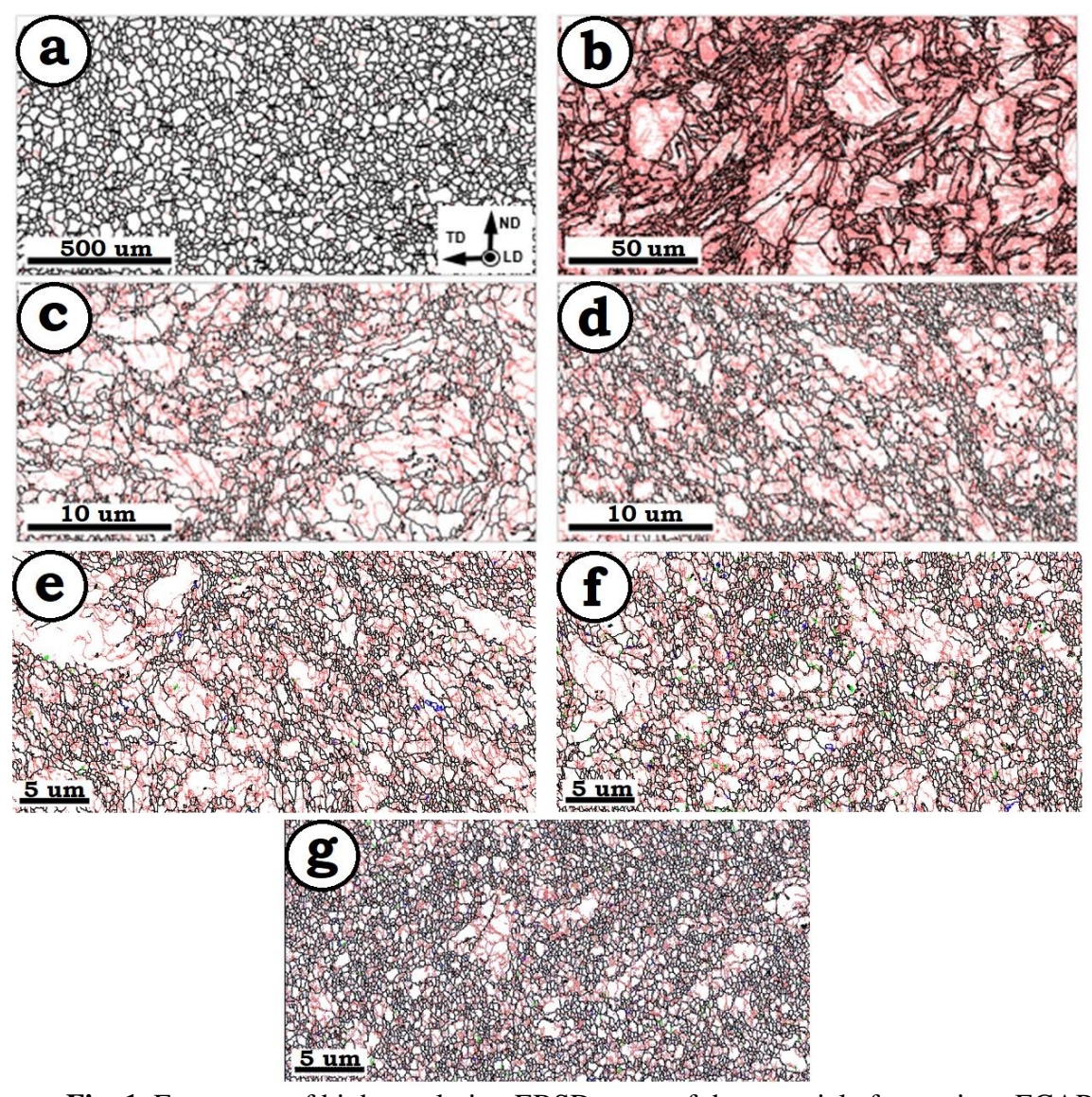


Fig. 1. Fragments of high-resolution EBSD maps of the material after various ECAP stages: coarse grained (CG) (a), 2 cycles (b), 4 cycles (c), 6 cycles (d), 8 cycles (e), 10 cycles (f), 12 cycles (g). On the SD cards SA, LA, and disorientation 85° <2110> and 74° <2110> are indicated by red, black, blue and green lines, respectively

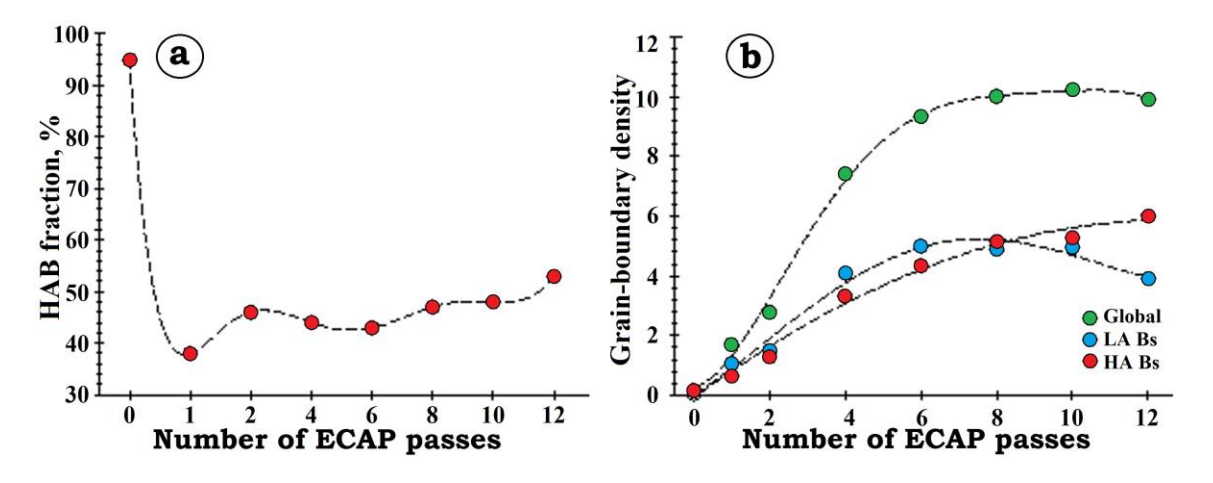


Fig. 2. Dependences of grain boundary density (a) and the proportion of large-angle boundaries (b) on the number of ECAP cycles

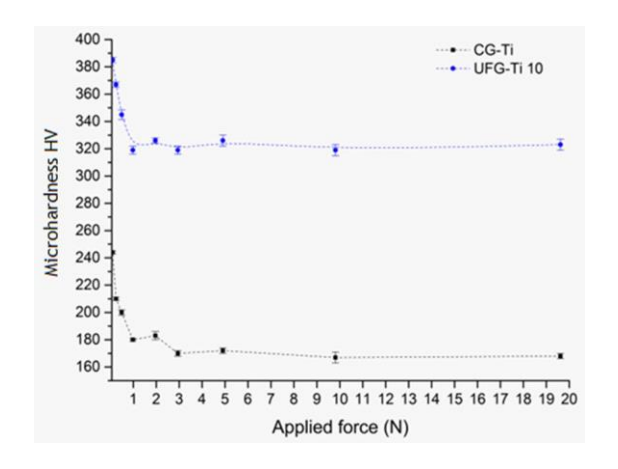
The crystallite sizes in the samples measured using the scattered electrons diffraction are shown in Table 1. These values indicate that SPD of Ti samples led to a significant decrease in the grain size.

Table 1. Average	size of CG-Ti	crystallites and	SPD-sub	iected Ti samples

Sample	Size of crystallites, μm
CG-Ti	30-60
UFG-Ti 2	5.0-10.0
UFG-Ti 4	1.0
UFG-Ti 6	0.5-1.0
UFG-Ti 8	0.4-0.6
UFG-Ti 10	0.2-0.3
UFG-Ti 12	0.2

Microhardness measurements. When measuring hardness using the Vickers method, a well-known difficulty is the dimensional effect – the dependence of the measured hardness on the magnitude of the applied load or the depth of indenter insertion (indentation size effect). Therefore, to determine the load boundary at which this effect influences the results, microhardness was measured on the samples of CG and UFG-Ti 10 at loads 0.01, 0.025, 0.05, 0.1, 0.2, 0.3, 0.5, 1 and 2 HV (98.07, 245.20, 490.30, 980.70 mN, 1.960, 2.942, 4.903, 9.807 and 19.614 N, respectively), see Fig. 3.

The resulting hardness values become almost constant at loads above 0.3 HV (Fig. 3). As a result, we selected a load of 0.3 HV as the operating value. The obtained microhardness data of the samples are shown in Fig. 4.



300 - 289 310 319 326 300 - 289 250 - 200

Fig. 3. Dependence of microhardness (at 15-second exposure) on the applied load for the CG-Ti comparison sample and for UFG-Ti 10 sample subjected to 10 cycles of ECAP

Fig. 4. Change in the microhardness measured at a load of 0.3 N for 15 seconds for Ti, depending on the ECAP cycles number

It can be seen that, in general, UFG-Ti samples exceed CG-Ti samples in microhardness by more than 1.5 times, while the microhardness dependence on the number of SPD treatments is much weaker.

Apparently, the increased hardness of UFG-Ti is mainly a consequence of a grain size decrease. The grain size decrease, in turn, is associated with high shear deformations that occurred in the material during processing. According to ECAP along the BC route, Ti samples were subjected to SPD when passing through the matrix from 2 to 12 times. Estimating the Vickers microhardness values, we can conclude that the main increase in the mechanical properties of Ti is achieved already at the first 2–4 passes. Compared with Ti of

the initial grain size, the microhardness increases by more than 1.5 times. During further processing, no significant changes in microhardness are observed: 12 passes increased the hardness by only 6.5 % relative to the sample subjected to 4 passes.

Corrosion measurements. The difference in the corrosion behavior with a decrease in the size of Ti crystallites is demonstrated by measurements of the linear polarization resistance (Fig. 5).

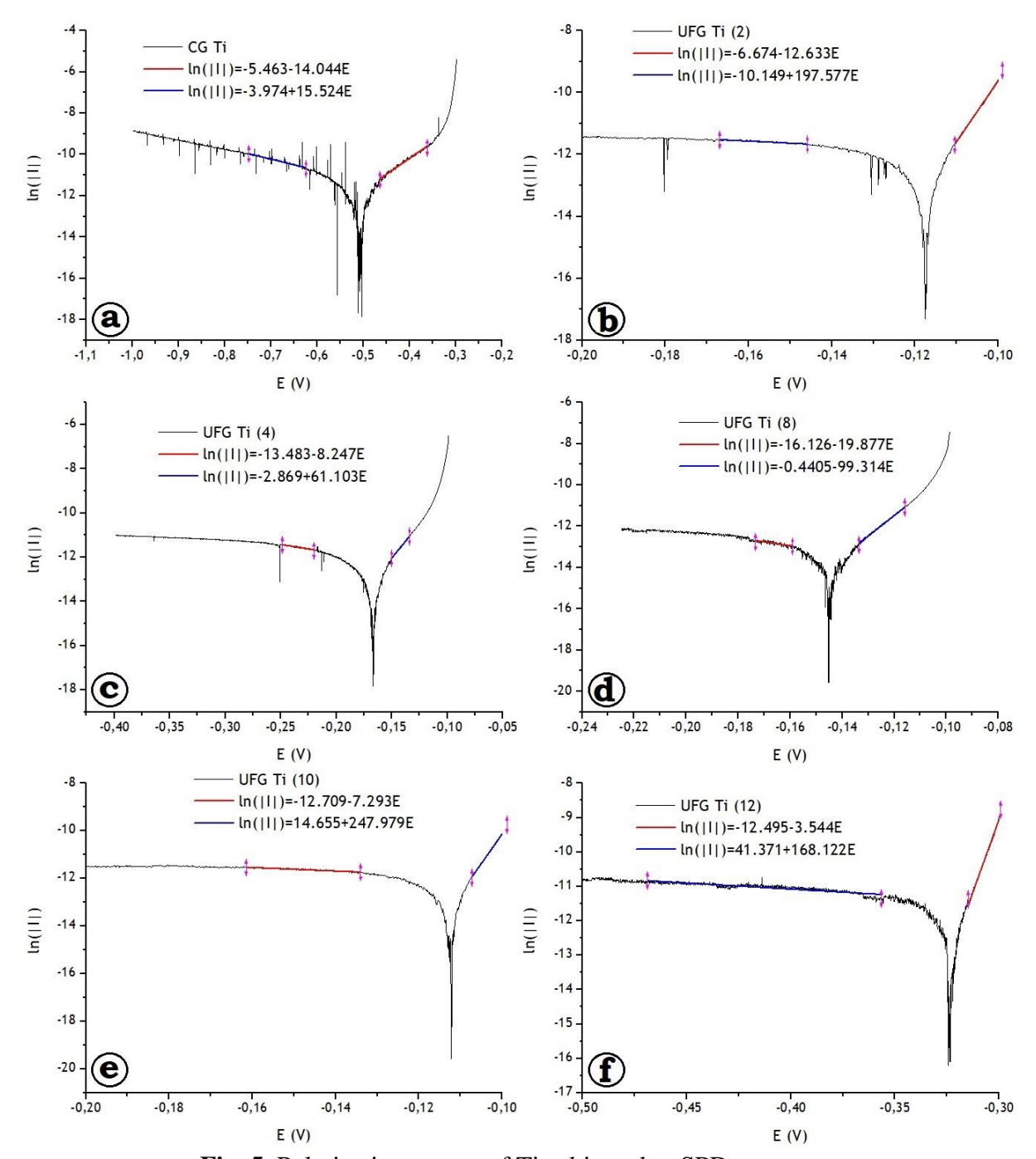


Fig. 5. Polarization curves of Ti subjected to SPD treatment

By approximating the linear sections of the polarization curves of Ti samples, the values of current and corrosion potential were obtained. The data are presented as dependencies on the number of passes through the ECAP device in Fig. 6.

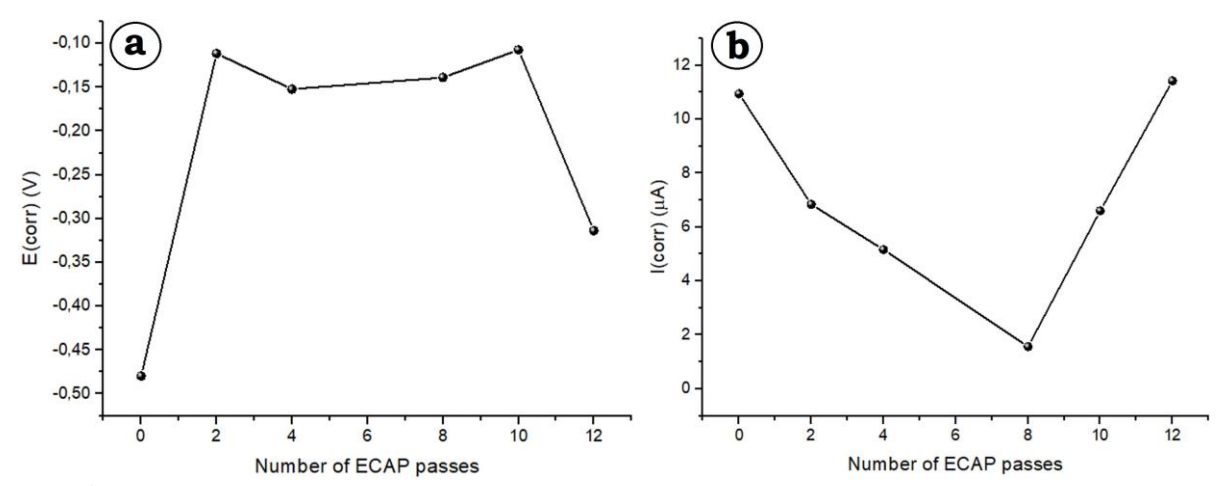


Fig. 6. Dependences of the potential (on the left) and the corrosion current of Ti on the number of ECAP cycles

Note the non-monotonic nature of the dependencies, which manifests itself in an increase in the corrosion resistance of titanium samples in the range from 0 to 8 cycles, followed by its decrease. This is expressed in the potential increase and the current decrease at the start of the dependence, followed by a potential decrease and the corrosion current increase. At the same time, if the dependence of the Ti corrosion current on the number of ECAP cycles has a pronounced minimum at 8 cycles, then the corrosion potential dependence has a plateau area between from 2 and 10.

Taking into account the extremely high values of Tafel slopes at the anode site and anode exchange currents (Fig. 5), it can be assumed that the corrosion current is most limited by the depolarization process speed (reduction of components of the corrosive medium on the corroding metal surface). This can be verified by comparing the dependence in Figure 6 with the dependences of the Tafel slope of the cathode section and the cathode exchange current on the number of ECAP cycles (Fig. 7).

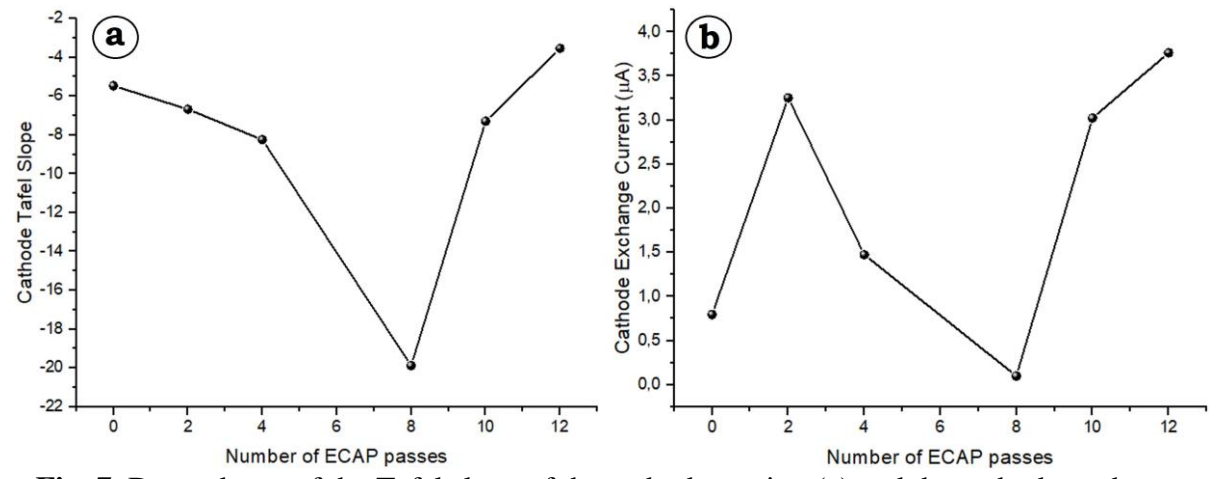


Fig. 7. Dependence of the Tafel slope of the cathode section (a) and the cathode exchange current (b) on the number of ECAP cycles

Despite the fact that the dependence of the absolute value of the Tafel slope of the cathode section has a maximum in the same region in which the minimum dependence of the corrosion current is detected, the presence of a minimum exchange current leads to the formation of a minimum corrosion current in this region.

Thus, it can be confidently assumed that the factor largely determining the corrosion rate of ECAP-subjected Ti is the cathodic exchange current. This means, that the process speed is limited by the depolarization. This may be due to the depassivation of the TiO₂ film when interacting with a medium containing fluoride ions, in relation to the semi-reaction of Ti oxidation. At the same time, the preservation of the oxide film leads to difficulties in the process of electron transfer through the electrode-electrolyte surface, as a result of which the depolarization reaction becomes limiting.

At the same time, the depolarization rate can be limited not only by the oxide film thickness, but also by the degree of saturation of the Ti (electrode) surface with hydrogen, including also the areas of grain boundaries reaching the surface. This statement is true for all samples, regardless of the number of ECAP cycles.

Based on these statements, the following explanation of the observed dependencies can be put forward. As follows from the EBSD data (Fig. 2), the use of 2 to 8 ECAP cycles leads to an increase in the density of large-angle grain boundaries in the Ti bulk. The increase in corrosion resistance may occur due to the disordering of the surface of the sample slice in the area of the existence of the LA, in particular, as a result of hydrogen saturation of the grain interface. With an increase in the proportion of areas of the LA output to the electrode (Ti) surface, the degree of hydrogen saturation of the metal surface increases due to the increased rate of hydrogen diffusion in disordered regions. In addition, the influence of the preferential orientation of crystallites is possible, but the discussion of this effect requires more experiments. With further (> 8 cycles) ECAP of Ti, the factor of reducing the grain size and the proportion of grain boundaries begins to play an important role. The subsequent changes in the texture of the slice and an increase in the reaction surface area of the grains, as well as the disordering of the oxide film, lead to an increase in the corrosion current, which leads to a sharp drop in the corrosion resistance of Ti.

Conclusion

Thus, this paper demonstrates the relationship between the microstructure, mechanical properties and corrosion resistance of Ti samples subjected to equal-channel angular pressing (ECAP).

The microhardness data of the samples demonstrate an increase in the hardness of fine-grained titanium due to a decrease in the grain size in the Ti bulk. Analysing the Vickers microhardness values, we can conclude that the main increase in the mechanical properties of Ti (more than 90 %) is achieved already after the first 2-4 cycles of ECAP processing. Compared with the initial Ti, the microhardness of SPD-treated Ti samples increases by more than 1.5 times.

It was shown that the electrochemically determined corrosion resistance of Ti subjected to ECAP, varies non-linearly depending on the structure of Ti. The non-monotonic nature of the dependencies, which manifests itself in an increase in the corrosion resistance of titanium samples in the interval from 2 to 8 cycles, followed by its decrease, may occur due to the disordering of the surface of the sample section in the region of the existence of the proportion of large-angle grain boundaries in the volume of titanium, in particular, as a result of the With further Ti ECAP, more than 8 cycles, a significant role in the corrosion resistance of titanium begins to be played by the factor of reducing the grain size in the bulk sample and, as a consequence, an increase in the reaction surface area of the grains, which leads to a sharp drop in the Ti corrosion resistance. Therefore, to create Ti implants with improved strength characteristics and at the same time resistant to corrosion in physiological body fluids, it is necessary to use Ti blanks subjected to 4 to 8 ECAP cycles.

References

- 1. Mathew MT, Abbey S, Hallab NJ, Hall DJ, Sukotjo C, Wimmer MA. Influence of pH on the tribocorrosion behavior of CpTi in the oral environment: synergistic interactions of wear and corrosion. *J. Biomed. Mater. Res. Part B.* 2012;100B(6): 1662–1671.
- 2. Li J, Li SJ, Hao YL, Huang HH, Bai Y, Hao YQ, Guo Z, Xue JQ, Yang R. Electrochemical and surface analyses of nanostructured Ti–24Nb–4Zr–8Sn alloys in simulated body solution. *Acta Biomater*. 2014;10(6): 2866–2875.
- 3. Stolyarov VV, Zhu YT, Lowe TC, Islamgaliev RK, Valiev RZ. A two-step SPD processing of ultrafine-grained titanium. *Nanostruct. Mater.* 1999;11(7): 947–954.
- 4. Stolyarov VV, Zeipper L, Mingler B, Zehetbauer M. Influence of post-deformation on CP-Ti processed by equal channel angular pressing. *Mater. Sci. Eng. A.* 2008;476(1-2): 98–105.
- 5. Sabirov I, Perez-Prado MT, Molina-Aldareguia JM, Semenova IP, Salimgareeva GK, Valiev RZ. Anisotropy of mechanical properties in high-strength ultra-fine grained pure Ti processed via a complex severe plastic deformation route. *Scripta Mater*. 2011;64(1): 69–72.
- 6. Zhao X, Fu W, Yang X, Langdon TG. Microstructure and properties of pure titanium processed by equal-channel angular pressing at room temperature. *Scripta Mater*. 2008;59(5): 542–545.
- 7. Wang ZB, Hu HX, Zheng YG. Determination and explanation of the pH-related critical fluoride concentration of pure titanium in acidic solutions using electrochemical methods. *Electrochim. Acta.* 2015;170: 300–310.
- 8. Balyanov A, Kutnyakova J, Amirkhanova NA, Stolyarov VV, Valiev RZ, Liao XZ, Zhao YH, Jiang YB, Xu HF, Lowe TC, Zhu YT. Corrosion resistance of ultra fine-grained Ti. *Scripta Mater*. 2004;51(3): 225–229.
- 9. Wanga ZB, Hua HX, Zhenga YG, Kea W, Qiaob YX. Comparison of the corrosion behavior of pure titanium and its alloysin fluoride-containing sulfuric acid. *Corrosion Science*. 2016;103: 50–65.
- 10. Balakrishnan A, Lee BC, Kim TN, Panigrah BB. Corrosion Behaviour of Ultra Fine Grained Titanium in Simulated Body Fluid for Implant Application. *Trends Biomater*. *Artif. Organs*. 2008;21(1): 58–64.
- 11. Gurao NP, Manivasagam G, Govindaraj P, Asokamani R, Suwas S. Effect of texture and grain size on bio-corrosion response of ultrafine-grained titanium. *Met. Mater. Trans.* 2013;44A: 5604–5610.
- 12. Rosalbino F, Delsante S, Borzone G, Scavino G. Influence of noble metalsalloying additions on the corrosion behaviour of titanium in a fluoride-containing environment. *J. Mater. Sci.-Mater. Med.* 2012;23: 1129–1137.
- 13. Hoseini M, Shahryari A, Omanovic S, Szpunar JA. Comparative effect of grain size and texture on the corrosion behaviour of commercially pure titanium processed by equal channel angular pressing. *Corros. Sci.* 2009;51(12): 3064–3067.
- 14. Wang ZB, Hu HX, Liu CB, Zheng YG. The effect of fluoride ions on the corrosion behavior of pure titanium in 0.05 M sulfuric acid. *Electrochim. Acta.* 2014;135: 526–535.
- 15. Sicilia A, Cuesta S, Coma G, Arregui I, Guisasola C, Ruiz E, Maestro A. Titanium allergy in dental implant patients: a clinical study on 1500 consecutive patients. *Clin. Oral. Implants. Res.* 2008;19(8): 823–835.
- 16. Mine Y, Makihira S, Nikawa H, Murata H, Hosokawa R, Hiyama A, Mimura S. Impact of titanium ions on osteoblast-, osteoclast- and gingival epithelial-like cells. *J. Prosthodont. Res.* 2010;54(1): 1–6.
- 17. Mabilleau G, Bourdon S, Joly-Guillou ML, Filmon R, Baslé MF, Chappard D. Influence of fluoride, hydrogen peroxide and lactic acid on the corrosion resistance of commercially pure titanium. *Acta Biomater*. 2006;2(1): 121–129.

- 10 E.G. Zemtsova, A.A. Petrov, S.O. Kirichenko, N.F. Morozov, V.K. Kudymov, A.Yu. Arbenin, B.N. Semenov, V.M. Smirnov
- 18. Nazarov DV, Zemtsova EG, Solokhin A, Valiev RZ, Smirnov VM. Enhanced Osseointegrative Properties of Ultra-Fine-Grained Titanium Implants Modified by Chemical Etching and Atomic Layer Deposition. *ACS Biomaterials Science and Engineering*. 2018;4(9): 3268–3281.
- 19. Zemtsova EG, Morozov NF, Semenov BN, Valiev RZ, Smirnov VM. Mechanical properties of nanostructured titanium with bioactive titanium-organic nanocoating. *Materials Physics and Mechanics*. 2017;32(3); 253–257.

THE AUTHORS

Zemtsova E.G. (D)

e-mail: ezimtsova@yandex.ru

Kirichenko S.O.

e-mail: sergkirichenko@gmail.com

Kudymov V. K.

e-mail: v.k.kudymov@gmail.com

Semenov B.N.

e-mail: b.semenov@spbu.ru

Petrov A.A

e-mail: st068921@student.spbu.ru

Morozov N.F.

e-mail: n.morozov@spbu.ru

Arbenin A.Yu.

e-mail: aua47@yandex.ru

Smirnov V.M.

e-mail: vms11@yandex.ru

Tribological and tensile behaviour of Si₃N₄ reinforced Cu-Sn matrix composites

Submitted: November 3, 2022

Approved: November 14, 2022

Accepted: March 22, 2023

B. Adaveesh ¹, G.V. Prabhushankar ¹, M. Nagaral ¹ ² ²

¹ Department of Industrial Engineering and Management, Siddaganga Institute of Technology, Tumkur, Karnataka, India

² Aircraft Research and Design centre, Hindustan Aeronautics Limited, Bangalore, Karnataka, India

☐ madev.nagaral@gmail.com

Abstract. In the present research, Cu-Sn alloy with 7.5 wt. % of Si₃N₄ particles reinforced composites were fabricated by using conventional stir casting method. As-cast Cu-8 %Sn alloy and Cu-8 %Sn alloy with 7.5 wt. % of Si₃N₄ reinforced composites were evaluated for microstructural studies using SEM and EDS, density, tensile properties and wear behaviour as per ASTM method. Cu-Sn alloy with 7.5 wt. % of silicon nitride particles reinforced composites shown lesser densities as compared to the base Cu-Sn alloy. Further, these composites were exhibited superior tensile strength with slight reduction in the ductility. Pin on disc wear apparatus was used to conduct the wear tests at varying loads and speeds. The wear resistance of Cu-Sn alloy increased with the incorporation of Si₃N₄ particles. Further, applied load and speeds were impacted in the wear behaviour of Cu-Sn alloy composites. As load and speed increased, there was more material loss in as-cast alloy and its composites. Tensile fractured surfaces indicated various fracture modes in Cu-Sn alloy and composites.

Keywords: Cu-Sn alloy; Si₃N₄; tensile behaviour; wear; fractography

Citation: Adaveesh B, Prabhushankar GV, Nagaral M. Tribological and tensile behaviour of Si₃N₄ reinforced Cu-Sn matrix composites. *Materials Physics and Mechanics*. 2023;51(4): 11-22. DOI: 10.18149/MPM.5142023_2.

Introduction

The requirement for lightweight composites with certain features over conventional materials increased as advanced science and technology. This opened the door for additional study into metal matrix composites (MMCs). To enhance the properties of the base metal, materials are reinforced with carbides or organic compounds. MMCs are primarily used in the automotive, aeronautical, and aviation industries [1]. Excellent electrical and thermal, corrosion resistance, and ease of alloying are some highly valuable characteristics of copper. Because of these properties, it is a promising option for most electrical and thermal applications [2]. On the other hand, its subpar mechanical performance prevents its use in many applications. However, this problem can be overcome by incorporating hard ceramic particles like carbides, borides, oxides, and nitrides. These elements increase strength and hardness at the cost of a negligible reduction in electrical conductivity [3].

Many studies illustrate the addition of reinforcements like carbon nanotube, graphite, fly-ash, rice-husk ash, Al₂O₃, Cr₂O₃, TiO₂, TiC, B₄C, SiC, etc., can increase the mechanical properties of copper matrix [4–6]. With high thermal conductivity and less thermal expansion coefficient, Si₃N₄ (silicon nitride) has drawn significant attention because of its superior wear, corrosion thermal shock resistance, and good mechanical properties. Si₃N₄ is an interesting

and potential option due to its chemical and mechanical stability at high temperatures for high-temperature applications. Less work is carried out on the effect of Si₃N₄ on copper matrix [7,8].

Several fabrication techniques can produce MMCs, including friction stir, compocasting; squeeze casting, ultrasonic-assisted casting, spray deposition, powder metallurgy, and diffusion bonding. Stir casting is the most practical and effective for mass production [9,10]. The size, shape, characteristics, proportion, dispersion of the reinforcements, matrix and reinforcement bonding, heat treatment process, and manufacturing method are factors to determine the characteristics of MMC. Decreasing the dislocation motion in the crystal lattice by adding nanoscale reinforcements to the matrix helps to avoid wear [11,12]. It was observed that adding MoS₂ reinforcements to the Al-Si10Mg successfully reduced wear by approximately 65 % [13]. Graphite particles were added as reinforcement to the aluminum alloy to improve its tribological characteristics. These MMCs are capable of self-healing and self-lubrication [14,15]. When sliding distance and velocity increased, the wear rate and specific wear of epoxy/cenosphere syntactic foams dropped, according to a study [16]. According to a study, 5 %, Al₂O₃ added as one of the reinforcements that can improve the composite's wear properties [17]. The composite's hardness and tensile strength are enhanced by enhancing the weight percentage of reinforcement [18].

Machine parts with copper alloy are used where the part experiences significant friction, for example, bearings. Cu-Sn alloys employed in bearings need grease as lubricants, which is more eco-friendly than copper-lead alloys, which constantly use at high temperatures and cause damaging gas releases [19]. Bearings are desired for their higher thermal conductivity, which dissipates heat through friction, excellent wear resistance, compressive strength, fatigue, tensile, shear, and corrosion resistance, and their capacity to handle shocks and vibrations. Higher compressive and tensile strengths boost the bearing material's capacity to withstand the development of cracks and spreading under higher contact pressures and to stop extrusion or other long-term deformation of the bearing [20].

Therefore, this work makes an effort to develop Cu-Sn alloy with 7.5 wt. % of Si₃N₄ particles reinforced composites using stir cast method. Thus prepared composites were evaluated for density, tensile and wear behaviour as per ASTM standards.

Experimental Details

Materials used and composites preparation. In the market today, copper-tin, copper-zinc, and copper-aluminum alloys are the most common bearing materials available. Wear performance is crucial in some applications, especially when exposed to higher loads. Cu-Sn alloys are used in various mechanical and electronic industrial applications because they have outstanding characteristics. Alloys rich in Sn are lead-free solder materials, whereas alloys with rich Cu are used as structural materials. Due to safety and environmental concerns, researchers have become interested in the later application because it eliminates lead toxicity [21].

For the preparation of the composite, a commercially available Cu-Sn alloy was considered. Table 1 shows the elemental composition of Cu-Sn alloy.

Table 1. Chemical composition of Cu-Sn alloy.
--

Element	Weight, %
Sn	7.85
Al	0.47
Si	0.06
Others	0.20
Cu	Balance

In the current investigation, Si_3N_4 particles with a diameter of 25-30 μm were used as reinforcement material to improve the mechanical behaviour of the Cu-Sn alloy. Cu-Sn/Si₃N₄ composites were fabricated using the liquid stir casting process. Figure 1 shows the Si_3N_4 particles used in the present study.

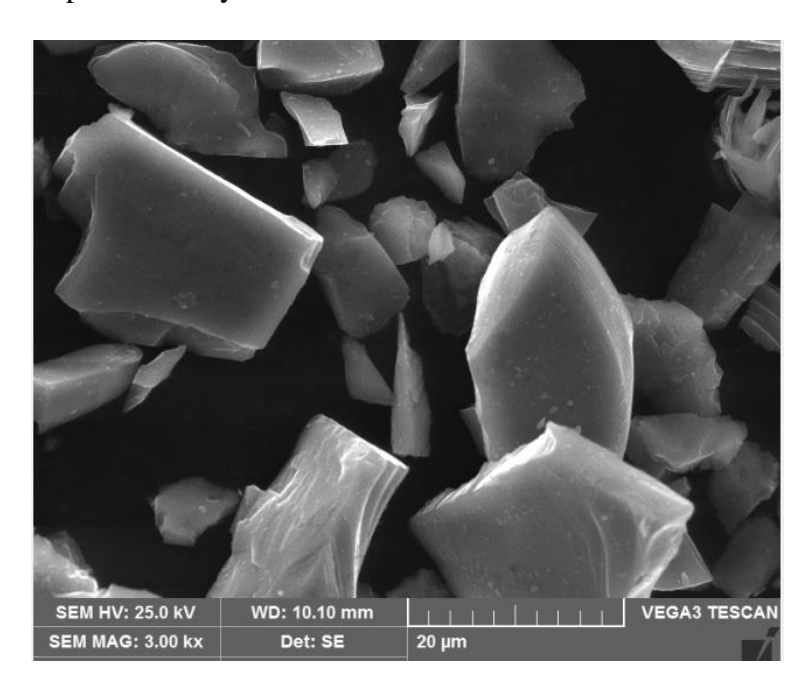


Fig. 1. SEM micrograph of Si₃N₄ particles

The Cu-Sn alloy with micro Si₃N₄ composites was made using a stir process based on the liquid metallurgy method. Metal ingots of a specific amount of Cu 8 % Sn alloy are loaded into an electric furnace and heated until they melt. In this case, the molten metal is heated to a superheated temperature of 1150 °C, whereas the typical melting point of copper tin alloy is 1070 °C. The melting point and the superheated temperature are measured and recorded using thermocouples selected for their accuracy over the relevant temperature range. For about three minutes, solid hexachloroethane (C₂Cl₆) [22] is used to degas the superheated molten metal in the crucible. The molten metal is stirred by a rotor with steel blades, mounted on a shaft and coated with zirconium ceramic. The stirrer is submerged to a depth of about 60 % within the crucible, and the molten metal is agitated to the point of vortex creation by rotating the stirrer at a speed of about 300 rpm. While the molten metal is being stirred, a separate heater is used to heat micro silicon nitride particulates to temperatures of up to 500 °C; these are then slowly poured into the molten metal vortex in stages, amounting to 7.5 % by weight of charged copper tin alloy. Interfacial shear strength is established by continuing to stir until the CuSn alloy matrix and Si₃N₄ reinforcement particulates are completely wet. In order to create Cu-Sn and 7.5 wt. % of Si₃N₄ composites, the molten metal mixture of CuSn alloy matrix and Si₃N₄ composites were poured into the cast iron moulds. Figure 2 shows the Cu-Sn alloy with 7.5 wt. % of Si₃N₄ composites after casting.



Fig. 2. Cu-Sn alloy and Si₃N₄ composite

Testing of prepared composites. Cu-Sn base alloy and Cu-Sn 7.5 wt. % Si_3N_4 composites were used for the microstructural study. Using a 200-320 grit size abrasive paper, the specimen's surface was initially made flat, and then finer lines were added by using 600-1200 grit size. Using Keller's reagent for an etching process, the last layer is removed chemically, and an SEM is employed to inspect it.

The displacement method and density measurements per ASTM D792-66 were used to determine measured density values, and the rule of mixture was utilized to calculate theoretical density. The specimen is initially submerged in a known volume of distilled water. Physical, digital balance equipment calculates the specimen's mass after it has been immersed in water. After the sample is submerged, the volume is determined by the amount of displaced water. The mass and volume data were collected for both copper-tin alloy and copper-tin alloy with 7.5 wt. % of Si₃N₄ composites. Then theoretical and experimental densities were compared.

Tensile tests were conducted on the composites to look into their mechanical properties. Round test specimens made of Cu-Sn base alloy and Cu-Sn with 7.5 wt. % of Si₃N₄ composites are employed for tensile testing based on standard ASTM-E8 at room temperature using a computerized UTM with a 400 kN capacity. Three samples were used to compute yield strength, UTS (ultimate tensile strength), and elongation %, three samples were taken and calculated average value for results. Figure 3 shows the schematic diagram of tensile test specimen and machined tensile test specimen as per standard respectively.

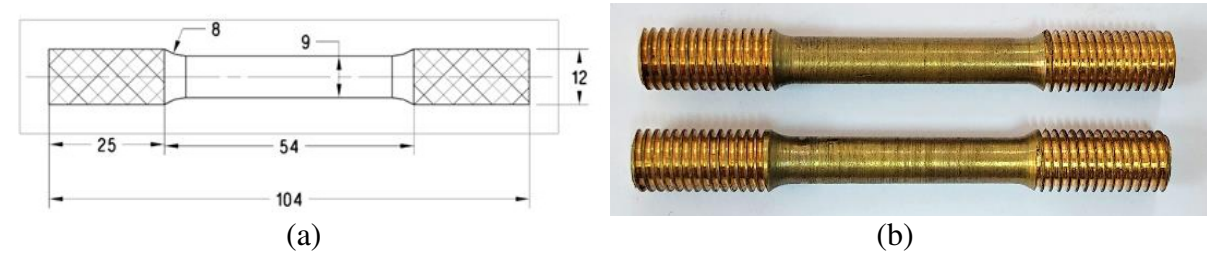


Fig. 3. Schematic diagram of tensile test specimen (a) and machined tensile test specimen (b)

Wear is removing material from one or more solid surfaces that are in friction. The standard wear test estimates the amount of material removed under specific circumstances. A wear test was performed on numerous specimens using pin-on-disc equipment. The samples hold the counter head of a revolving circular disc firmly with a 120 mm circumference wear track by a pin holder. Dead weights were put to the pin on the other side of the circular disc to calculate the wear.



Fig. 4. Wear test specimen

The specimens are fabricated based on standard ASTM-G99, and the disc is cleaned using acetone. Samples prepared for the wear test collect information about wear from electronic sensors. The pin's surface was initially flawed. The rotating disc is meticulously cleaned to provide precise readings. The next step is to fix the samples to the chuck. The track

has a diameter of 120 mm. Figure 4 shows the samples that were used in the wear test, having 8 mm in diameter and 30 mm length. Wear test were carried out at varying loads and speeds. Varying loads of 1 to 3 Kg at 300 rpm and varying speeds of 100 to 300 rpm at 3 Kg load at 2500 m sliding distance were used.

Results and Discussion

Microstructural study. The microstructural characterizations of specimens are examined by SEM with EDS attachment. Figure 5 demonstrates the SEM micrographs of Cu-Sn alloy and micro Si_3N_4 reinforced composites. Figure 5(a) shows the SEM of CuSn alloy. Figure 5(b) shows the SEM images of Cu-Sn alloy with 7.5 wt.% of Si_3N_4 reinforced composites. It confirms that most of micro Si_3N_4 particles are mixed uniformly in Cu-Sn alloy. Further, these figures disclose the uniformity of the prepared composites.

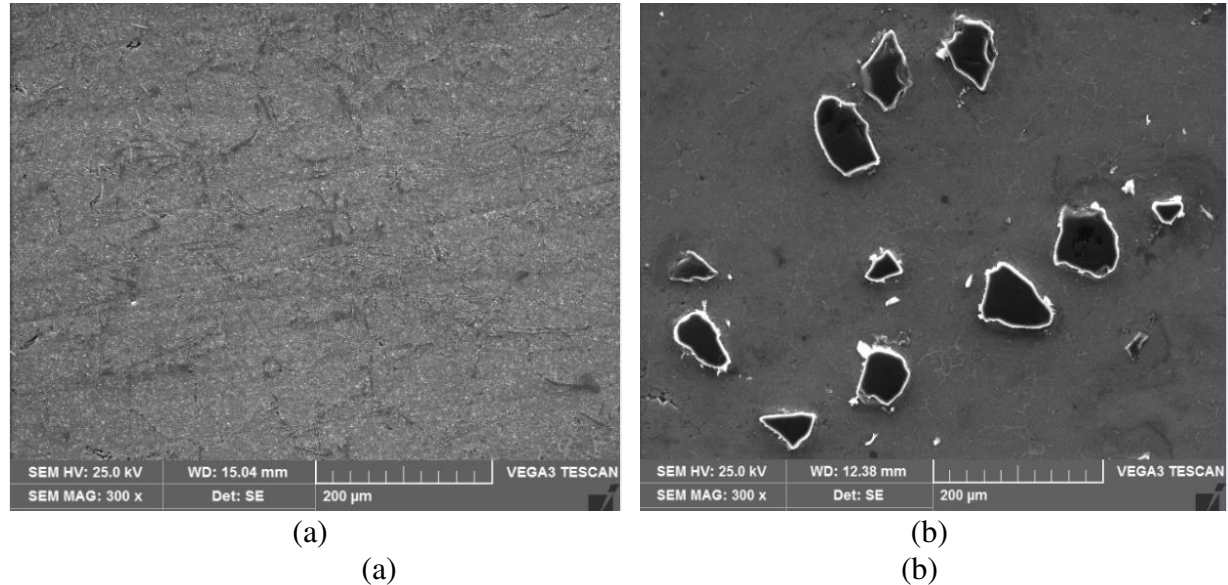


Fig. 5. SEM micrographs of (a) As-cast Cu-Sn alloy (b) Cu-Sn alloy with 7.5 wt. % of Si₃N₄ composites

As can be seen in Fig. 5(b), micro Si₃N₄ reinforcement particles are evenly dispersed throughout the CuSn matrix, as revealed by scanning electron micrographs. This also shows that there are no cracks, holes, or pores present. Micro Si₃N₄ reinforcement particles and the 'CuSn alloy matrix are observed to form strong interfacial bonds. From the above SEM images, it is clear that the CuSn with micro Si₃N₄ particulate composite is extremely strong and has a significant impact on both mechanical and tribological properties due to the uniform distribution of reinforcement particles, the lack of defects in the casting process, and the good interfacial bonding between the different materials.

Element detection by spectroscopy (EDS) is a powerful and useful technique for identifying elements and their relative abundance. While chemical analysis can identify which elements are present in a given sample, a more precise measure of their relative abundance requires EDS. Compositions of the aforementioned composites are shown in Fig. 6, and EDS is used for elemental analysis of both Cu-Sn alloy and Cu-Sn with Si₃N₄ reinforcement (Fig. 6(a,b)).

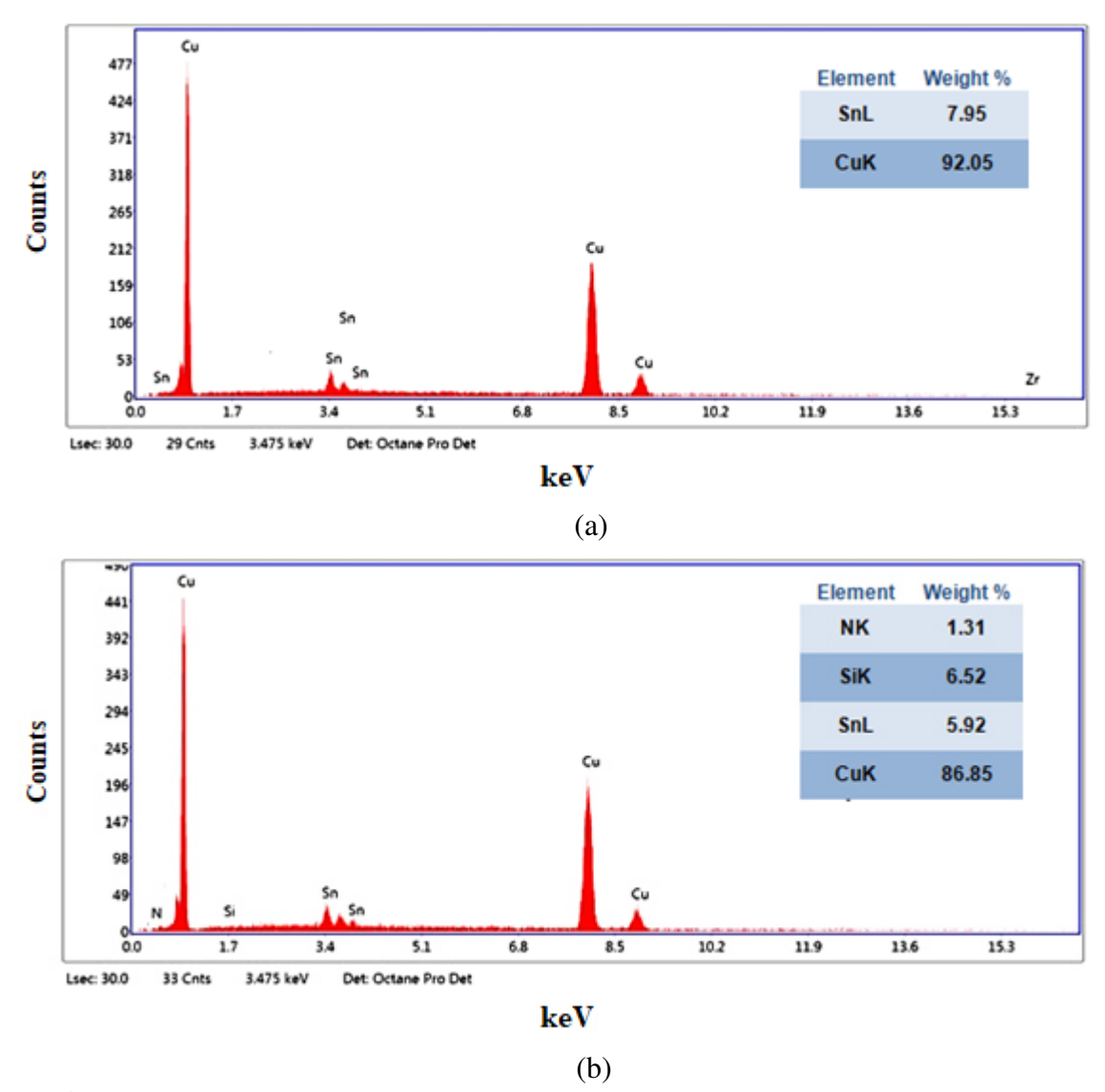


Fig. 6. EDS spectrums of (a) As-cast Cu-Sn alloy (b) Cu-Sn alloy with 7.5 wt.% of Si₃N₄ composites

As can be seen from the preceding graphs, the Y axis represents the number of occurrences and the X axis represents the intensity of those occurrences. The EDS spectrograph of as cast Cu-Sn alloy is shown in Fig. 6(a). Copper is the most abundant element in the sample, with tin as an alloying element also confirmed by the spectrum. The presence of silicon nitride is confirmed with Si and N peaks in the EDS spectrum of Cu-Sn alloy with 7.5 wt.% of Si_3N_4 particles composites, shown in Fig. 6(b).

Density measurements. Explanations of the theoretical and experimental values obtained for various samples are provided in Fig. 7. In this study, it is expected that experimental values will be similar to the calculated theoretical values. Since theoretical values are calculated using standardised formulas, it is extremely unlikely that the experimental values will match exactly.

Figure 7 displays a comparison between the theoretical and experimental densities of an as cast Cu-Sn alloy and a Cu-Sn alloy reinforced with 7.5 wt. % of Si_3N_4 composites. The density of Si_3N_4 is only 3.17 g/cm³, while the density of Cu-Sn alloy is 8.80 g/cm³. Since Si_3N_4 has a lower density than CuSn alloy, adding 7.5 wt. % of Si_3N_4 to the alloy results in a lower composite density of 7.765 g/cm₃. Furthermore, the difference between the theoretical and experimental densities can be seen to be smaller than expected. When Si_3N_4 is added,

density drops, which is consistent with the findings of other researchers [23]. The closeness of the experimental densities to the theoretical densities, as shown in Fig. 7, is further evidence of the high quality of the specimens prepared.

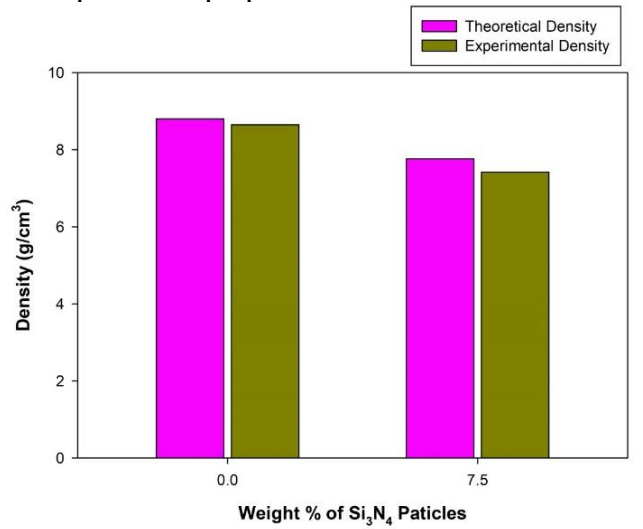


Fig. 7. Theoretical and experimental densities of Cu-Sn alloy and its Si₃N₄ reinforced composites

Tensile behaviour. The analysis of the tensile behaviour of base metal Cu-Sn and Cu-Sn 7.5 wt. % Si₃N₄ composites are shown in Figs. 8–10. These properties include UTS, yield strength, and percentage of elongation.

Figures 8 and 9 represent the ultimate and yield tensile strength of Cu-Sn alloy and Cu-Sn alloy with 7.5 wt. % of Si₃N₄ composites. Cu-Sn 7.5 wt. % Si₃N₄ composites demonstrated a 32.941 % increase in UTS, a 28.865 % rise in YS, and a 23.002 % decrease in elongation percentage when compared to Cu-Sn base metal. It is clear from Figs. 8 and 9 that Si₃N₄ particles significantly increase the tensile strength of the Cu-Sn matrix. Dislocations occur through the matrix due to the application of a uniaxial tensile load. Plastic zones are created when they aggregate close to the reinforcement particle boundary. The difference in the thermal expansion coefficient between the matrix and the reinforcement phase determines the size of this plastic zone. The copper matrix-reinforcement interface acts as an effective barrier against the spread of dislocations across the interface. Si₃N₄ hard particles give the matrix strength, and as a result of this process of strengthening, the composite gives greater resistance to tensile force.

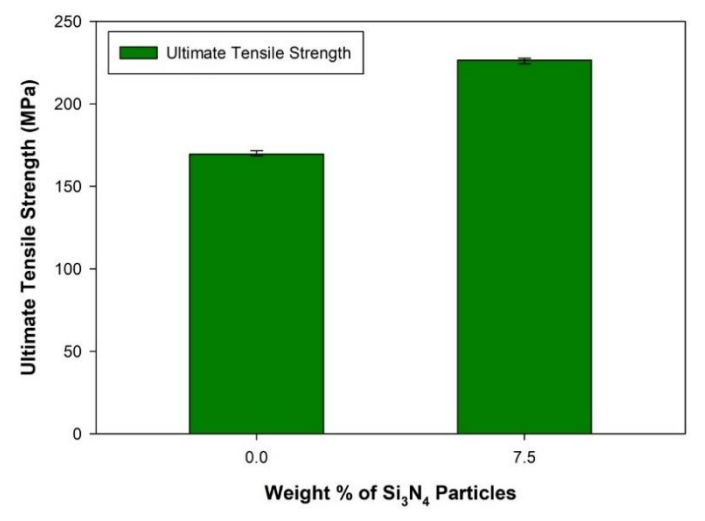


Fig. 8. Ultimate strength of Cu-Sn alloy with Si₃N₄ composites

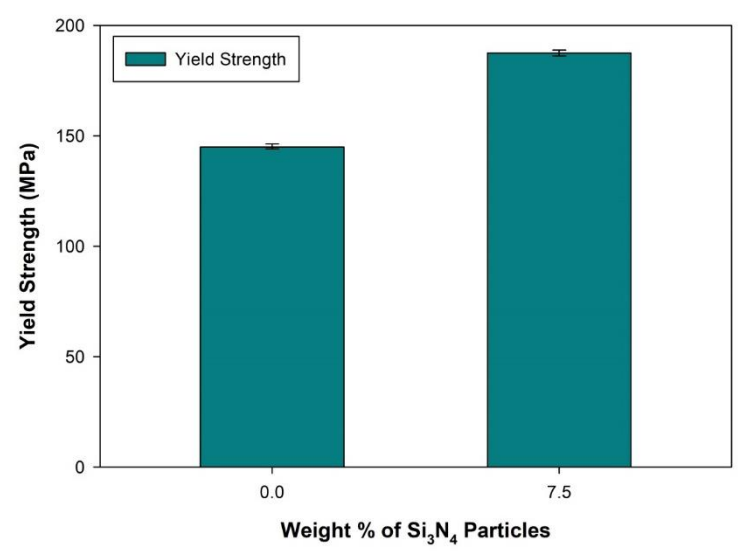


Fig. 9. Yield strength of Cu-Sn alloy with Si₃N₄ composites

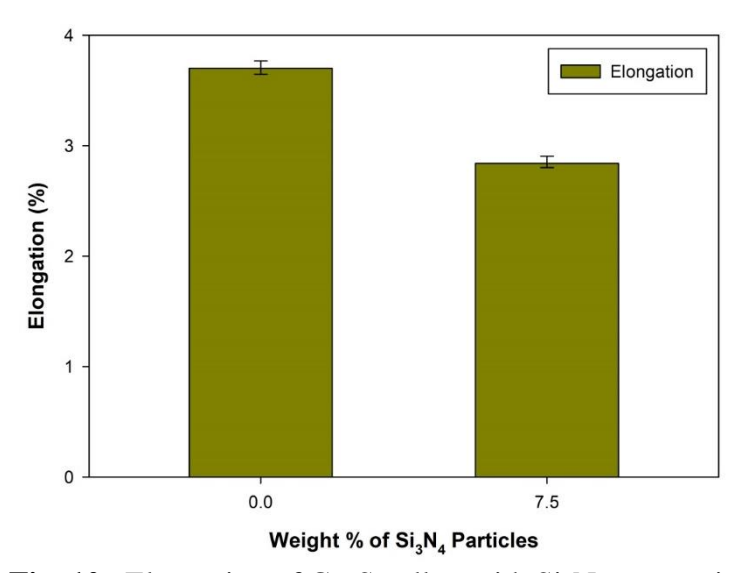


Fig. 10. Elongation of Cu-Sn alloy with Si₃N₄ composites

According to the results of the present study, the hard Si_3N_4 particles are directly responsible for the improvement in yield quality of the composite by delectating the Cu-Sn amalgam system and bringing greater quality obstruction of the composite against the associated pliability load. Miniaturized scale molecule reinforced composites have a redesigned quality because of the uniformly sized, hard fired particles in the lattice that act as an impediment to the plastic flow.

Micro Si_3N_4 particles' influence on Cu-Sn alloy and composites' ductility is depicted in Fig. 10. When an axial load is applied to a specimen, the material stretches to accommodate the stress. The elongation of a tensile test specimen is calculated by dividing the gauge length it has at failure by the original gauge length. When describing the ductility of a material, the elongation of a specimen is typically expressed as a percentage and is greater the more the material can be stretched. Tensile testing results for as cast Cu-Sn alloy and Cu-Sn alloy reinforced with 7.5 wt. % Si₃N₄ particulates are shown in Fig. 10. When Si₃N₄ particles are added to as-cast Cu-Sn alloy, the elongation percentage drops.

Fractography. This study analyses the materials fractured surface. Figure 11 depicts the SEM of the tensile fractured samples of base metal Cu-Sn and Cu-Sn 7.5 wt. % Si₃N₄ composites. Figure 11(a) shows the ductile fracture of the Cu-Sn base metal. In SEM image, wrinkles are observed on the surface. Initially voids are observed, and these are developed because of plasticity, and at last cracks are observed that cause the material to ductile fracture. Figure 11(b) shows the cracked surface images of Cu-Sn 7.5 wt. % Si₃N₄ composites in comparison to its matrix, with more minor wrinkles visible. This demonstrates that the Cu-Sn 7.5 wt. % Si₃N₄ composites have brittle fracture behaviour. The SEM images reveal large voids and crack propagation. The strong reinforcing particles trapped in the matrix material are essential in slowing the spread of cracks in the materials. Therefore, compared to the matrix material, these materials have greater tensile strength.

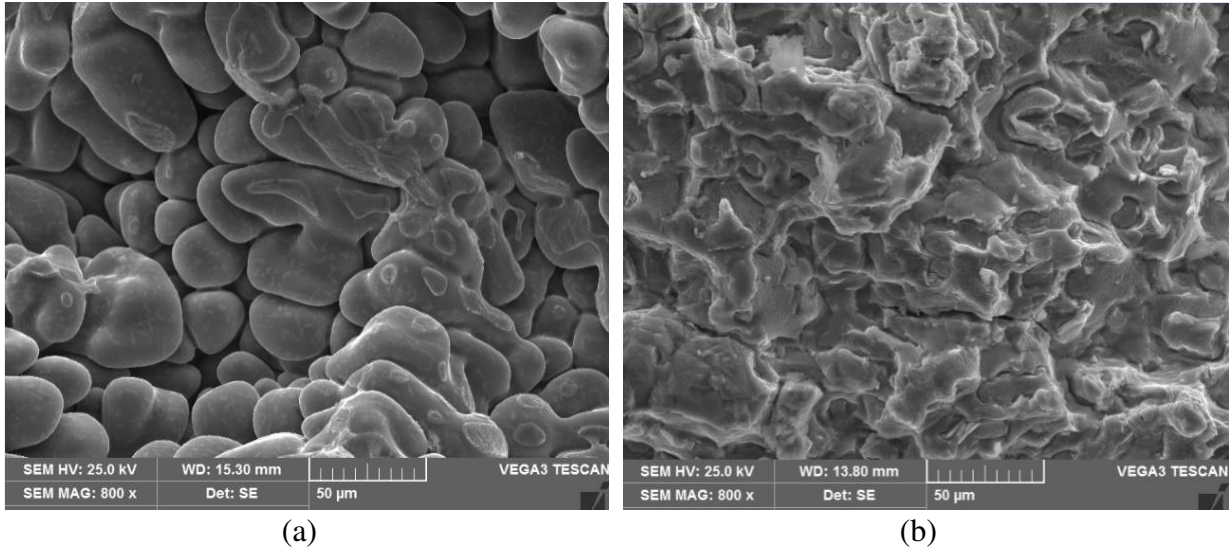


Fig. 11. Tensile fractured surfaces SEM images (a) as-cast Cu-Sn alloy and (b) Cu-Sn alloy - 7.5 wt. % of Si₃N₄ composites

Wear Properties. Wear tests were performed on the composites that were reinforced with Si_3N_4 . Initially, castings are machined according to ASTM-G99 for wear testing. Six specimens were tested with various loads and constant speeds for each composition test, while another six samples were tested with different speeds and constant loads. The results of using pin-on-disc technology under different conditions. Based on this finding, the wear behaviour is examined. Here it is analysed how the loaded speed affects the wear loss.

Influence of Load. The load is a key factor in the wear and tear that occurs. The effect of normal load in wear experiments has been the subject of extensive research in order to better understand the wear rate of copper alloys. Moreover, graphs for wear loss against different loads of 1, 2, and 3 kg at a constant distance of 2500 metres and speed of 300 rpm have been plotted to investigate the impact of load on wear. Load's influence on the wear behaviour of Cu-Sn alloy and Si_3N_4 reinforced composites is depicted in Fig. 12.

When moving the load up from 1 to 3 kg, the graph 12 shows that wear increases for both the composites and the base Cu-Sn alloy. The temperature of the sliding surface and the pin rises above the critical value at a maximum load of 3 kg. Accordingly, wear loss of the matrix Cu-Sn alloy and Cu-Sn alloy with 7.5 wt. % of Si₃N₄ composites increases with the increase in pin load. As shown in Fig. 12, as cast Cu-Sn alloy experiences the greatest wear loss under all loading conditions. We can see that by incorporating reinforcement into the Cu-Sn alloy, the composites' wear loss is reduced. Some research suggests that the high hardness of Si₃N₄ particulates, which acts as a barrier for the wear loss, is responsible for the

improved wear resistance of the Cu-Sn alloy with 7.5 wt. % of Si_3N_4 composites. The increased wear misfortune as the load is increased from 1 to 3 kg is mainly due to the increased contact area between the pin and the steel plate. As the area of contact increases during a wear test, more heat is generated, eventually leading to the delamination of the compound or composite.

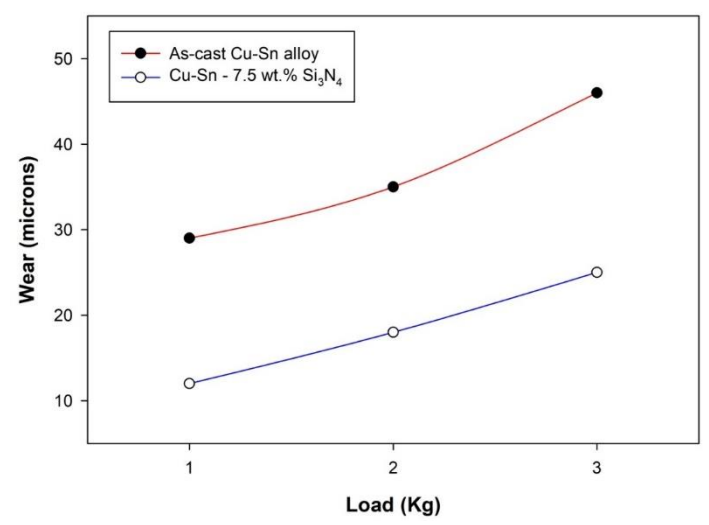


Fig. 12. Effect of load on the wear behaviour of Cu-Sn alloy and its Si₃N₄ composites

Influence of Speed. It is absorbed, that wear loss varies depending on speed. Experiment is conducted with a fixed weight of 3 kg and a variable speed disc revolving at 100, 200, and 300 rpm. It is observed that the sliding speed increases with increase in wear rate, as shown in Fig. 13. Wear loss is more pronounced in base alloys than in composites reinforced with Si₃N₄. All wear loss in Cu-Sn matrix alloy and Si₃N₄ composites is determined by sliding speed. The Cu-Sn matrix alloy and generated composites experience significant wear as the speed is raised from 100 to 300 rpm. Composites degrade at high temperatures; therefore, wear happens as the sliding speed rises.

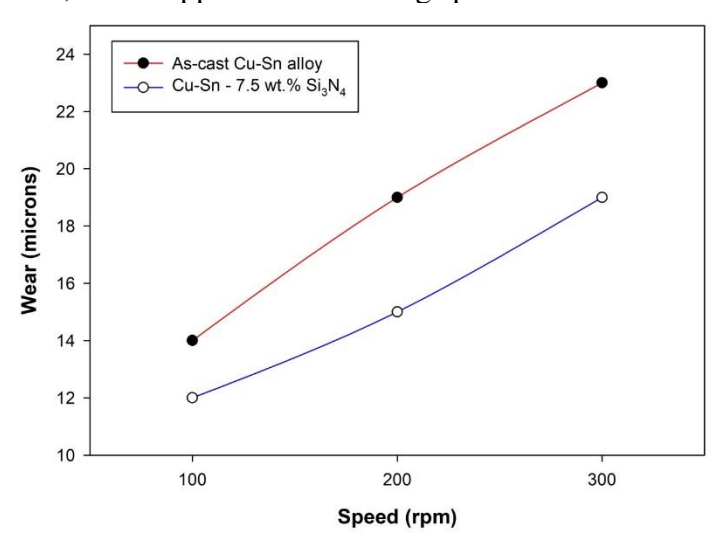


Fig. 13. Effect of speed on the wear behaviour of Cu-Sn alloy and its Si₃N₄ composites

It can be inferred from Fig. 13 that wear misfortune volume increases with velocity. When comparing Si₃N₄-enhanced composites to their base Cu-Sn counterparts, the effect of sliding rate is greater for the latter. The wear loss of the composites is much less than that of the Cu-Sn matrix alloy at all sliding speeds, and it is especially low in the case of the Cu-Sn

alloy with 7.5 wt.% of Si_3N_4 composites. Wear losses in the composite are reduced when Si_3N_4 powder is added to the mix. The wear loss of the composites is less than that of the Cu-Sn alloy and the Cu-Sn compound with Si_3N_4 composites at all sliding velocities. Wear problems in the composite are fundamentally alleviated by the addition of Si_3N_4 particles. Additionally, wear loss increases as sliding rate increases due to the expansion of the composite at elevated temperatures caused by scouring activity. Temperature increases brought on by greater sliding rates also lead to plastic deformation of the test specimen. Therefore, increased wear problems are a direct result of widespread delamination.

Conclusions

A stir casting process was used to make Cu-Sn alloy with 7.5 wt. % of Si₃N₄ composites. The prepared composites were studied for microstructural characterization by using SEM and EDS. Scanning electron micrographs were shown the dispersion of Si₃N₄ particles in the Cu-Sn alloy matrix. Further, Si₃N₄ particles in the Cu-Sn alloy matrix were confirmed by the EDS spectrums containing the Si and N elements. With the incorporation of micro sized Si₃N₄ particles, various mechanical properties like, ultimate and yield strengths were improved. Ultimate tensile strength of as-cast Cu-Sn alloy was 170 MPa, with 7.5 wt. % of Si₃N₄ particles it was found 225.96 MPa. Addition of hard nitride particles decreased ductility of Cu-Sn alloy, the lowest ductility was observed in the case of Cu-Sn alloy with 7.5 wt. % of Si₃N₄ particles. Tensile fractured surfaces of as-cast `Cu-Sn alloy indicated the ductile mode of fracture, whereas composites shown brittle fracture. Wear resistance of Cu-Sn alloy improved with the addition of silicon nitride particles. Further, as load and speed increased, wear loss increased in the base Cu-Sn alloy and its composites.

References

- 1. Sallahauddin A, Nagaral M, Reddappa HN, Auradi V. Effect of B₄C particulates addition on wear properties of Al7025 alloy composites. *American Journal of Materials Science*. 2015;5(3C): 53-57.
- 2. Matti S, Shivakumar BP, Shashidhar S, Nagaral M. Dry sliding wear behavior of mica, fly ash and red mud particles reinforced Al7075 alloy hybrid metal matrix composites. *Indian Journal of Science and Technology*. 2021;14(4): 310-318.
- 3. Davis JR. Copper and Copper Alloys. In: *ASM Specialty Handbook*. ASM International; 2001. p.446–448.
- 4. Rathod S, Modi OP, Prasad BK, Chrysanthou A, Vallauri D, Deshmukh VP. Cast in situ Cu-TiC composites: synthesis by SHS route and characterization. *Materials Science and Engineering A*. 2009;502(1–2): 91–98.
- 5. Dash K, Chaira D, Ray BC. Microstructural evolution and sliding wear studies of copper-alumina micro and nanocomposites fabricated by spark plasma sintering. *Journal of Mechanical Behaviour of Materials*. 2015;24(1-2): 25–34.
- 6. Shojaeepour F, Abachi P, Purazrang K, Moghanian AH. Production and properties of Cu/Cr₂O₃ nanocomposites. *Powder Technology*. 2012;222: 80–94.
- 7. Saravanakumar S, Gopalakrishnan S, Kalaiselvan K. Development of empirical relationships for prediction of mechanical and wear behavior of copper matrix surface composite by friction stir processing technique. *Archives of Metallurgy and Materials*. 2021;66(2): 617–626.
- 8. Ying DY, Zhang DL. Processing of Cu-Al₂O₃ metal matrix nanocomposite materials by using high energy ball milling. *Materials Science and Engineering A.* 2000;286(1): 152–156.
- 9. Zhao Y, Fan H. Effect of pulse parameters on the microstructural evolution and properties of jet electrodeposited Cu–Al₂O₃ nanocomposite coating. *Materials Transactions*. 2021;62(6): 726–730.

- 10. Wang F, Li Y, Wang X, Koizumi Y, Kenta Y, Chiba A. In-situ fabrication and characterization of ultrafine structured Cu-TiC composites with high strength and high conductivity by mechanical milling. *Journal of Alloys and Compounds*. 2016;657: 122–132.
- 11. Sathiskumar R, Murugan N, Dinaharan I, Vijay SJ. Characterization of boron carbide particulate reinforced in situ copper surface composites synthesized using friction stir processing. *Materials Characterization*. 2013;84: 16–27.
- 12. Zhao N, Li J, Yang X. Influence of the P/M process on the microstructure and properties of WC reinforced copper matrix composite. *Journal of Materials Science*. 2004;39(15): 4829–4834.
- 13. Vinoth KS, Subramanian R, Dharmalingam S, Anandavel B. Mechanical and tribological characteristics of stir-cast Al-Si10Mg and self-lubricating Al-Si10Mg/MoS₂ composites. *Materials Technology*. 2012;46(5): 497–501.
- 14. Venkat Prasat S, Subramanian R, Radhika N, Anandavel B. Dry sliding wear and friction studies on AlSi10Mg–fly ash–graphite hybrid metal matrix composites using Taguchi method. *Tribology and Materials Surface Interfaces*. 2011;5(2): 72–81.
- 15. Rajesh S, Gopala Krishna A, Rama Murty Raju P, Duraiselvam M. Statistical analysis of dry sliding wear behavior of graphite reinforced aluminum MMCs. *Procedia Materials Science*. 2014;6: 1110–1120.
- 16. Vyasaraj M, Gururaj P, Mrityunjay D, Gaitonde VN, Siddhalingeshwar IG, Kishore VasanthCS, Nikhil. Dry sliding wear of epoxy/cenosphere syntactic foams. *Tribology International*. 2015;92: 425–438.
- 17. Kanthavel K, Sumesh KR, Saravana Kumar. Study of tribological properties on Al/Al₂O₃/MoS₂ hybrid composite processed by powder metallurgy. *Alexandria Engineering Journal*. 2016;55(1): 13–17.
- 18. Radhika N, Subramanian R. Effect of reinforcement on wear behavior of aluminum hybrid composites. *Tribology and Materials Surface Interfaces*. 2013;7: 36–41.
- 19. Kestursatya M, Kim JK, Rohatgi PK. Wear performance of copper–graphite composite and a leaded copper alloy. *Materials Science and Engineering A.* 2003;339(1-2): 150–158.
- 20. Balakrishnan S, Baker CE, Rahnejat H. Fundamental of hydrodynamic journal bearings: an analytical approach. In: *Tribology and dynamics of engine and powertrain: fundamentals, applications and future trends*. Woodhead Publishing; 2010. p.591–594.
- 21. Zhai W, Wang WL, Geng DL, Wei B. A DSC analysis of thermodynamic properties and solidification characteristics for binary Cu-Sn alloys. *Acta Materials*. 2012;60(19): 6518–6527.
- 22. El-Daly AA, Hammad AE, Fawzy A, Nasrallh DA. Microstructure, mechanical properties, and deformation behaviour of Sn–1.0Ag–0.5Cu solder after Ni and Sb additions. *Materials Design*. 2013;43: 40–49.
- 23. Nagaral M, Deshapande RG, Auradi V, Satish BP, Samuel Dd, Anilkumar MR. Mechanical and wear characterization of ceramic boron carbide-reinforced Al2024 alloy metal composites. *Journal of Bio-and Tribo-Corrosion*. 2021;7(1): 1–12.

THE AUTHORS

B. Adaveesh

G.V. Prabhushankar

e-mail: badaveesh@yahoo.co.in

e-mail: gvpshankar@sit.ac.in

Madeva Nagaral 🗓

e-mail: madev.nagaral@gmail.com

Optimization of wear behaviour of hybrid Al(6061)-Al₂O₃-B₄C composites through hybrid optimization method

Submitted: September 22, 2022

Approved: October 31, 2022

Accepted: April 26, 2023

P.K. Gupta, M.K. Gupta [™]

Motilal Nehru National Institute of Technology Allahabad, India

☑ mnnit.manoj@gmail.com

Abstract. Al-based hybrid metal matrix composites were prepared through stir casting method by reinforcing aluminium oxide or alumina (Al₂O₃) and boron carbide (B₄C) particles into Al matrix with their varying proportions. The wear analysis of prepared hybrid MMCs was performed using the Pin-on-disc method and wear parameters were also optimized with objectives of minimizing the weight loss (WL) and coefficient of friction (COF) through integrated Grey-Taguchi techniques. Morphological analysis was also performed to explain the wear mechanism through a Scanning electron microscope (SEM). The maximum improvement in the weight loss of 71.33 % and in coefficients of friction of 35.35 % was found for the hybrid composites as compared to that of Al-alloy matrix. Further, the ANOVA results suggested that compositions has the maximum contribution of 94.47 %, sliding speed has 1.06 %, sliding distance has 1.04 %, and load has 3.16 % on the wear performance of the present hybrid composites.

Keywords: metal matrix composites; hybrid composites; aluminium; wear analysis; optimization; scanning electron microscope

Acknowledgement. Authors would like to thank the Mechanical Engineering Department, Motilal Nehru National Institute of Technology Allahabad, Prayagraj, India. The Author would also like to thank the Indian Institute of Technology Kanpur and MANIT Bhopal for providing the facilities.

Citation: Gupta PK, Gupta MK. Optimization of wear behaviour of hybrid Al(6061)-Al₂O₃-B₄C composites through hybrid optimization method. *Materials Physics and Mechanics*. 2023;51(4): 23-37. DOI: 10.18149/MPM.5142023_3.

Introduction

In recent decades, the demand for metal matrix composites (MMCs) has been increasingly increased in different sectors of automobile, aerospace, sporting goods, and other industries on account of their excellent properties of specific stiffness and strength, desirable coefficient of thermal expansion, and superior wear and corrosion resistance [1]. Among the available MMCs, Al is more preferred matrix material because of its low density, ease of fabrication ability and good engineering properties [2]. Aluminium-based MMCs have been utilized as newer materials in the field of high-performance tribological applications because of their improved mechanical properties, good wear resistance, higher thermal conductivity, and low coefficient of thermal expansion [3]. The aluminium based MMCs have been found to be utilized in the following parts: brake drums, pistons, connecting rods, drive shafts, cylinder liners, cylinder blocks, gears, valves, and suspension components etc. [4]. These composites can be fabricated by the following methods such as powder metallurgy, stir casting techniques, chemical vapour deposition, physical vapour deposition, and spray deposition. In © P.K. Gupta, M.K. Gupta, 2023.

Publisher: Peter the Great St. Petersburg Polytechnic University

stir casting, the particles are mechanically well distributed with the help of a stirrer in the liquid – particles mixture before the solidification [5].

Wear is one of the important material interface phenomenons that occur at an interface MMCs with hard particle reinforcement that offers superior wear resistance [6,7]. Zhang et al. [8] reported that wear resistance of MMCs varies linearly with an increase in concentrations of reinforcement. Yu et al. [9] worked on Al6061-SiC composites and found that wear rate decreased with increasing applied load. A. Martin et al. [10] suggested that a characteristics physical mechanism involved in the wear process for 6061- Al₂O₃ composites. Kumar et al. [11] prepared Al6063-10 % Si₃N₄ MMCs by the stir casting and found that the MMCs had a higher wear resistance in comparison to the base alloy. A similar type of observations was reported by Anand et al. [12] for the composite (Al6061-5SiC-4.5Porcelain). Zheng et al. [13] worked on TiB +TiC/ Ti6Al4V composites and suggested that if the reinforcement content of composites is increased the main wear mechanism is changed. Cygan et al. [14] observed a considerable change in wear rate of the composites due to changes in applied loads. A similar observation was also reported by Xiao et al. [15].

Abbas et al. [16] worked on CNTs/AZ31 composites fabricated by the stir casting process and found that the wear rate decreased substantially with rising CNT weight fraction as in both cast and aged materials because of their interfacial peeling effect of a magnesium alloy of AZ31. Ambigai and Prabhu [17] investigated the tribological behaviour of Al-Gr-Si₃N₄ hybrid composite under dry sliding conditions and they concluded that the sliding distance was significant parameters followed by the applied load. In another research work, it was suggested that the sliding velocity was found to be the most significant parameter followed by the reinforcement percentage, sliding distance, and contact stress [18]. Muthu [19] worked on LM25-SiC-Cu hybrid MMCs and observed that the sliding velocity was more dominating parameter than the load and sliding distance. It was also reported that significantly affected by types could be and concentrations reinforcements [20,21].

From the above discussion, it is clear that a good number of works are reported on wear analysis of MMCs, and wear resistance was found to be significantly affected by concentrations and types of reinforcements, wear parameters, temperatures and fabrication process of composites. It was also observed that hybrid MMCs exhibited better wear resistance than single reinforced MMCs. However, study on the effect of variations in proportions of reinforcements on wear resistance of hybrid MMCs is not attempted so far. Therefore, wear analysis and optimization of process parameters using hybrid GRA-Taguchi method for hybrid Al-based MMCs reinforced B₄C and Al₂O₃ particles are presented in this work.

Experimental details

Materials. For the development of Al alloy (6061) based hybrid MMCs, two types of reinforcement were as such: Al_2O_3 (purity 99 % and 100-325 mesh size) and B_4C (purity 99 % and 400 mesh size). All the consumable materials were purchased from UMA Scientific traders, Prayagraj, India.

Fabrication of composites. The present hybrid MMCs containing a constant wt.% of reinforcement of 6 with varying proportions of Al₂O₃ and B₄C particles were prepared by two stages of stir casting process. The small pieces of Al alloy were placed into a graphite crucible for melting inside an electric coil furnace heated to 750 °C. Then, Al₂O₃ and B₄C particles along with empty crucible were preheated to 400 °C. Thereafter, preheated powders were mixed into molten Al alloy using a stirrer (600 rpm) in two consecutive steps of 3 wt. % each for half of 10 min. For the duration of the mixing process, there was a temperature crash of

around 15–20 °C. Eventually, the mixture of reinforcements and molten Al alloy was poured into the cast iron finger die in order to prepare the specimens for wear analysis. Nomenclature given for prepared hybrid composites is provided in Table 1. Figure 1 represents the casted samples.



Fig. 1. Casted samples

Table 1 Nomenclature used for hybrid metal matrix composites

Composites	Types of composites	Boron carbide, %	Alumina, %	Total reinforcement, wt. %
B0A0	Cast Al alloy (6061)	0	0	0
B100A0	Single B4C reinforced	100	0	6
B75A25	Hybrid	75	25	6
B50A50	Hybrid	50	50	6
B25A75	Hybrid	25	75	6
B0A100	Single Al ₂ O ₃ reinforced	0	100	6

Wear test. The pin on disc test was employed for the analysis of dry sliding wear behaviour of prepared hybrid Al (6061)-Al₂O₃-B₄C composites in order to determine the weight loss and coefficient of friction (COF). The specification of wear test set up is given in the Table 2. Tests were conducted using L18 orthogonal array under dry sliding condition as per ASTM G99-95 at a temperature of 28 °C. The samples for wear test shown in the Fig. 2.

Table 2. The specifications of wear test setup for hybrid metal matrix composites

Specifications	Values		
Specimen, Pin, mm	Dia-3, 4, 6, 8, 10, 12 and length- 25 to 32		
Sliding speed, m/s	0.5 to 10		
Normal load, N	Min–5 and Max-200		
Wear disc material	EN-31 Hardened,60 HRC		



(a)



(b)

Fig. 2. Samples for wear test: (a) aluminium alloy and (b) hybrid composite

Table 3. The input factors for a wear test of hybrid metal matrix composites

Input parameters				Level		
input parameters	1	2	3	4	5	6
Sample code	M1 (A0B0)	M2 (B100A0)	M3 (A100B0)	M4 (B25A75)	M5 (B75A25)	M6 (B50A50)
Rotation, rpm	150	200	250	-	-	-
Sliding distance, m	1500	2000	2500	-	-	-
Load, N	15	25	35	-	-	-

Table 4. Experimental results of wear rate and coefficient of friction for hybrid metal matrix composites

composit	Co	1					
S. No	Samples	Rotation,	Sliding	Load, N	Weight	Wear rate,	COF
5. 110	code	rpm	distance, m	Load, N	Loss, g	mg/m	COI
1	1	1	1	1	0.1756	0.117	0.595
2	1	2	2	2	0.2141	0.107	0.586
3	1	3	3	3	0.2333	0.093	0.584
4	2	1	1	2	0.0612	0.041	0.399
5	2	2	2	3	0.0772	0.039	0.396
6	2	3	3	1	0.0403	0.016	0.4
7	3	1	2	1	0.1215	0.061	0.521
8	3	2	3	2	0.1231	0.049	0.509
9	3	3	1	3	0.1323	0.088	0.506
10	4	1	3	3	0.1627	0.065	0.406
11	4	2	1	1	0.1296	0.086	0.44
12	4	3	2	2	0.1473	0.074	0.415
13	5	1	2	3	0.1054	0.053	0.372
14	5	2	3	1	0.0559	0.022	0.392
15	5	3	1	2	0.0782	0.052	0.377
16	6	1	3	2	0.0416	0.017	0.343
17	6	2	1	3	0.0749	0.05	0.337
18	6	3	2	1	0.0311	0.015	0.348

Initially, the test specimens are polished metallographically to make sample in the form of flat. The preliminary weight of specimen was measured by an electronic balance (Shimadzu Corporation, D307032807) with a precision of $0.0001\,\mathrm{g}$. After the test, the specimens were removed, cleaned with acetone, dried and again specimen was weighted to find its final weight. The W_L was calculated by using the equation (1).

$$Weight\ loss = Initial\ weight\ of\ sample - Final\ weight\ of\ sample.$$
 (1)

The COF was calculated by getting a ratio of frictional force (F) and normal force (F_N) of equation (2):

$$\mu = \frac{F}{F_N} \,. \tag{2}$$

The experiments are conducted on the prepared composites with various input parameters sample's composition, rotation (rpm), sliding distance (m) and load (N) with an objective to minimize W_L and COF. The following input parameters were used for wear test as shown in Table 3. The experiments were designed by Taguchi method and L_{18} array are used for conducting the experiments. The experimental results are shown in Table 4.

Grey Relational Analysis (GRA). It is a multi response optimization process to find the optimum combination of process parameters and the influence of each input parameters on the responses. The outputs/responses such as WL and COF are minimized so that the following the criteria "smaller the better characteristics", for signal to noise ratio can be found by the given equation (3):

$$\frac{S}{N} = -10\log_{10}\left[\frac{1}{n}\sum_{i=1}^{n}y_{ij}\right]$$
 (3)

where n = no of observations, $y_{ij} = \text{observed response/outputs}$, I = 1,2,3, ..., n, and j = 1, 2, 3, ..., k, performance characteristics/ outputs responses.

It is required to normalize the output responses prior to analyzing them with the grey relation theory. The normalization for every experimental result is performed by using equation (4):

$$Z_{ij} = \frac{\max(y_{ij}, i = 1, 2, 3, ..., n) - y_{ij}}{\max(y_{ij}, i = 1, 2, 3, ..., n) - \min(y_{ij}, i = 1, 2, 3, ..., n)},$$
(4)

where y_{ij} is the j^{th} performance characteristics and min y_{ij} and max y_{ij} values of j^{th} performance characteristics for the i^{th} experiments respectively.

The grey relational coefficients for the individual output can be found from the normalised values by using equation (5) and coefficient constant is assumed to be $\xi = 0.5$:

$$(y_0(k), y_i(k)) = \frac{\Delta \min + \xi \Delta \max}{\Delta_{0i}(k) + \xi \Delta \max},$$
(5)

where

- a) i = 1, 2, 3, ..., n, k = 1, 2, ..., m, n is the number of experimental data items and m is the number of responses;
- b) $y_0(k)$ is the reference sequence $(y_0(k) = 1, k = 1, 2, ..., m)$, $y_j(k)$ is the specific comparison sequence;
- c) $\Delta_{0j} = ||y_0(k) y_j(k)||$, the absolute value of the difference between $y_0(k)$ and $y_j(k)$.
- d) $\Delta_{\min} = ||y_0(k) y_j(k)||$, the smallest value of $y_j(k)$.
- e) $\Delta_{\text{max}} = ||y_0(k) y_j(k)||$, the largest value of $y_j(k)$.
- f) ξ is the coefficient constant, which is defined in the range $0 \le \xi \le 1$.

The grey relational grade (GRG) for combined multi-objective can be obtained from grey relational coefficient of the responses. The grade which decides the rank or performance characteristics was obtained by using the equation (6).

$$\delta j = \frac{1}{k} \sum_{i=1}^{m} y_{ij} \quad , \tag{6}$$

where δ_j is the values of GRG for the j^{th} experiment and k is the number of performance characteristics.

Results and Discussion

Multi-objective-GRA. The experimental results are normalised using equation (4) and the normalised results are converted into grey relational coefficient to represents the correlation between desired and actual data. At last, the grey relational grades are calculated by the equation (6). The S-N ratio and its normalised values for W_L and COF are tabulated in the Table 5.

Table 5. The signal to noise ratio and the normalized value of weight loss and coefficient of

friction for hybrid metal matrix composites

incuon for ny	oria metai matrix c	omposites		
S. No	S/N ratio (Wl)	S/N ratio (COF)	Normalised value (W_L)	Normalised value (COF)
1	15.1095	4.50966	0.285361	0
2	13.3877	4.64205	0.094955	0.034884
3	12.6417	4.67174	0	0.042636
4	24.2650	7.98054	0.851137	0.75969
5	22.2477	8.04610	0.772008	0.771318
6	27.8939	7.95880	0.9545	0.755814
7	18.3085	5.66325	0.552918	0.286822
8	18.1948	5.86564	0.545005	0.333333
9	17.5688	5.91699	0.499505	0.344961
10	15.7722	7.82948	0.349159	0.732558
11	17.7479	7.13095	0.512859	0.600775
12	16.6359	7.63904	0.425321	0.697674
13	19.5432	8.58914	0.632542	0.864341
14	25.0518	8.13428	0.877349	0.786822
15	22.1359	8.47317	0.767062	0.844961
16	27.6181	9.29412	0.948071	0.976744
17	22.5104	9.44740	0.783383	1
18	30.1448	9.16842	1	0.957364

Table 6. The grey relational coefficient and grey relational grade value for hybrid metal matrix composites

1110001171	composites		1			1
S.No	Deviation sequence (W _L)	Deviation sequence (COF)	GRC (W _L)	GRC (COF)	GRG	RANKS
1	0.714639	1	0.411645	0.333333	0.372489	16
2	0.905045	0.965116	0.355861	0.34127	0.348565	17
3	1	0.957364	0.333333	0.343085	0.338209	18
4	0.148863	0.24031	0.770579	0.675393	0.722986	6
5	0.227992	0.228682	0.686821	0.68617	0.686495	8
6	0.0455	0.244186	0.916591	0.671875	0.794233	4
7	0.447082	0.713178	0.527937	0.412141	0.470039	14
8	0.454995	0.666667	0.523563	0.428571	0.476067	13
9	0.500495	0.655039	0.499753	0.432886	0.466319	15
10	0.650841	0.267442	0.434465	0.651515	0.54299	11
11	0.487141	0.399225	0.506513	0.556034	0.531274	12
12	0.574679	0.302326	0.465255	0.623188	0.544222	10
13	0.367458	0.135659	0.576397	0.786585	0.681491	9
14	0.122651	0.213178	0.803018	0.701087	0.752053	5
15	0.232938	0.155039	0.682186	0.763314	0.72275	7
16	0.051929	0.023256	0.905914	0.955556	0.930735	2
17	0.216617	0	0.697723	1	0.848861	3
18	0	0.042636	1	0.921429	0.960714	1

In the next section, the grey relational coefficient is calculated by equation (5) to present association between the ideal (best) and specific normalised experimental results. Finally the grey relational grades are calculated by equation (6) to represent the level of correlation between the reference sequence and the comparability sequence. The higher value of GRG indicates that the comparability sequence has a stronger correlation to reference sequence. In other words, the higher the value of GRG corresponds to better performance. Here, the reference sequence was selected as "smaller the better" characteristics and the comparability sequence with larger value of GRG gives smaller W_L and COF. The GRC, GRG values and their ranks are shown in the Table 6.

Taguchi Method. It is an integrated approach to discover the best range of designs for quality, computational cost and performance. The traditional experimental design procedure focuses on the average process performance characteristics but this method concentrated on the effect of variation of the process quality characteristics rather than on its averages. It used a statistical measure of performance called signal to noise ratio (S/N) which is logarithmic function of outputs/ responses. The S-N ratio considers both mean and variability and is defined as the ratio of the mean (signal) to the standard deviation (noise). The ratio (S/N) depends on the quality characteristic of the product/ process to be optimized. Here, the Taguchi optimization technique is employed on the basis of GRG values. The outcome of this optimization is presented in the Table 7. Generally, a higher GRG value offers better output/ response. The multi-objective (minimum weight loss and coefficient of friction) optimum condition could be found from the response table: sample code of level 6, rotation of level 3, sliding distance of level 3 and load of level 1.

Table 7. Response Table of wear test for hybrid metal matrix composites (Means)

Level	Samples code	Rotation, RPM	Sliding distance, m	Load, N
1	0.3531	0.6201	0.6108	0.6468
2	0.7346	0.6072	0.6153	0.6242
3	0.4708	0.6377	0.6390	0.5941
4	0.5395			
5	0.7188			
6	0.9134			
Delta	0.5603	0.0305	0.0283	0.0527
Rank	1	3	4	2

Analysis of Variance (ANOVA). ANOVA is performed using a Minitab version 17 to find which parameters significantly affect the quality/ multi-objective/responses. The mean data of overall grey relational grade is used to analyse the effect of sample code, rotational speed sliding distance and load on the total variance of the results. The result of the ANOVA is tabulated in the Table 8. The ANOVA table shows the percentage contribution of each and every parameter. The percentage contributions of parameters were found 94.47 % for sample code, 1.06 % for rotation, 1.04 %, for sliding distance, and 3.16 %, for the load. The main effect plot for grey relational grade values for means are given in the Fig. 3. The optimal combination of factors and their levels is abbreviated as SC6R3SD3L1 based on the mean effect plot. Sahoo and Pal [22] performed similar work on the tribological performance on the electroless Ni-P coatings and found that the three test parameters, load, speed and time have a significant influence on the friction and wear behaviour at the confidence level of 95 % within the specific test range. Paranthaman et al. found that the applied load is significant parameter and wt % of reinforcement and sliding distance are insignificant for studying tribological behaviour Al metal matrix composites [23].

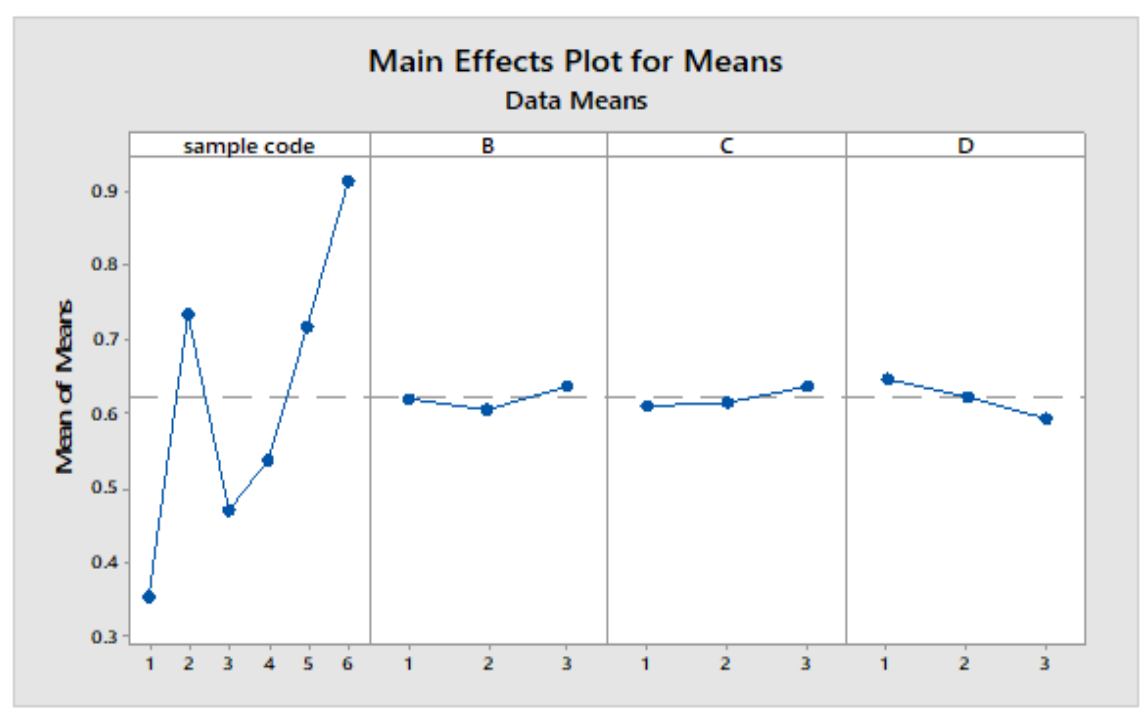


Fig. 3. Main effect plot for means- wear rate of hybrid metal matrix composites (higher is better)

Table 8 . ANOVA results for h	ybrid metal matrix composites
--------------------------------------	-------------------------------

Tuble 0: 111 10 111 legales for hybrid metal matrix composites									
Source	Degree of freedom	Sum of square	Mean square	Percentage Contribution	P Value				
Sample code	5	0.626851	0.125370	94.47	0.0				
Rotation (RPM)	2	0.002817	0.001409	1.06	0.968				
Sliding distance, m	2	0.002770	0.001385	1.04	0.968				
Load, N	2	0.008402	0.004201	3.16	0.906				
Residual Error	6	0.002002	0.000334	0.25					
Total	17			100					

Confirmation Tests. After the optimum level of wear behaviour parameters is identified, a confirmation test was performed for checking the accuracy of the analysis. The predicted grey relational grade γ_{pre} value may be found by the following equation:

$$\gamma_{\text{Pr}e} = \gamma_m + \sum_{i=1}^n (\bar{\gamma} - \gamma_m) \quad , \tag{7}$$

where, γ_m is the total mean of the grey relational grade, $\bar{\gamma}$ is the mean of grey relational grade values at the optimum level and n is the number of main parameters that significantly affect the overall quality characteristics.

Table 9 shows the comparison between predicted value of grey relational grade and experimental value of grey relational grade obtained by combination of optimal parameters. The confirmation test was performed and it was found that the experimental GRG value for response characteristics increased by 0.063656. The W_L and COF were decreased by 0.0061 g and 0.021 respectively from the initial to optimal parameters. Hence, the integrated Grey Taguchi approach improved the multiple performance characteristics in terms of W_L and COF by 8.05 % and 6.18 %, respectively.

TOOLS ALLES OF THE CO	t was to a title of the ordinary was tot in a title in the title in the title in the title of the ordinary of					
Courage	Initial testing	Optimum testing parameters				
Sources	parameters	Prediction	Experimental			
Combination of testing parameters	SC6R2SD1L3	SC6R3SD3L1	SC6R3SD3L1			
Weight loss	0.0749		0.0688			
COF	0.337		0.316			
GRG	0.84886	0.970814	0.912516			

Table 9. Results of the confirmation test for hybrid metal matrix composites

Parametric effect on the outputs/ responses (weight loss and coefficient of friction).

Figure 4 represents the weight loss at different wear parameters, whereas variations of coefficient of friction and wear rate with load at different rotations and sliding distances for hybrid composites in presented in Figs. 5 and 6 respectively. It can be observed that the Al-alloy A0B0 has the highest weight loss in comparison to all the hybrid composites samples of B100A0, A100B0, A75B25, B75A25 and B50A50 for all the variable wear parameters. The phenomenon is happened due to lower asperities to asperities contact between two counter surfaces or particles of reinforcements (i.e. Al₂O₃ & B₄C) are harder, and unreinforced al alloy (6061) is softer than the reinforced composites which causes heavy plastic deformation on the surface also. Bardeswaran et al. [24] found that COF decreases on increases the B₄C particles content and wear resistance of the composites increased on increasing the contents of B₄C particles in the matrix materials.

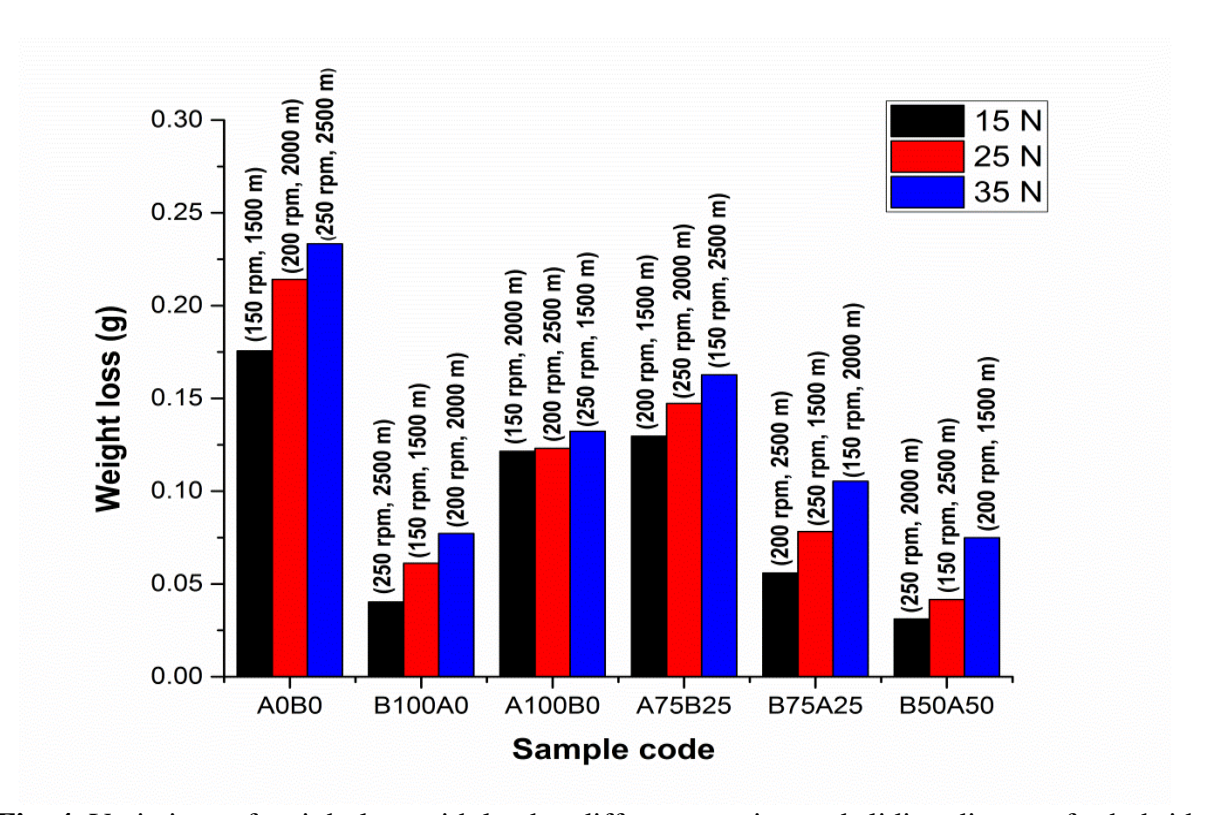


Fig. 4. Variations of weight loss with load at different rotation and sliding distance for hybrid composites

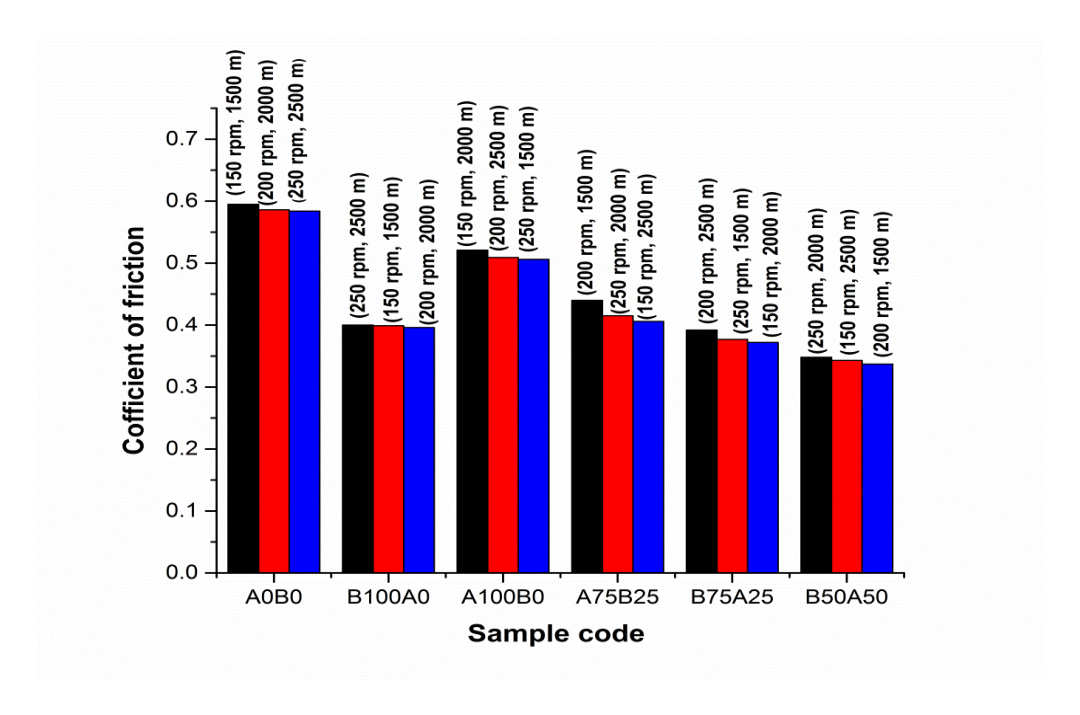


Fig. 5. Variations of coefficient of friction with load at different rotation and sliding distance for hybrid composites

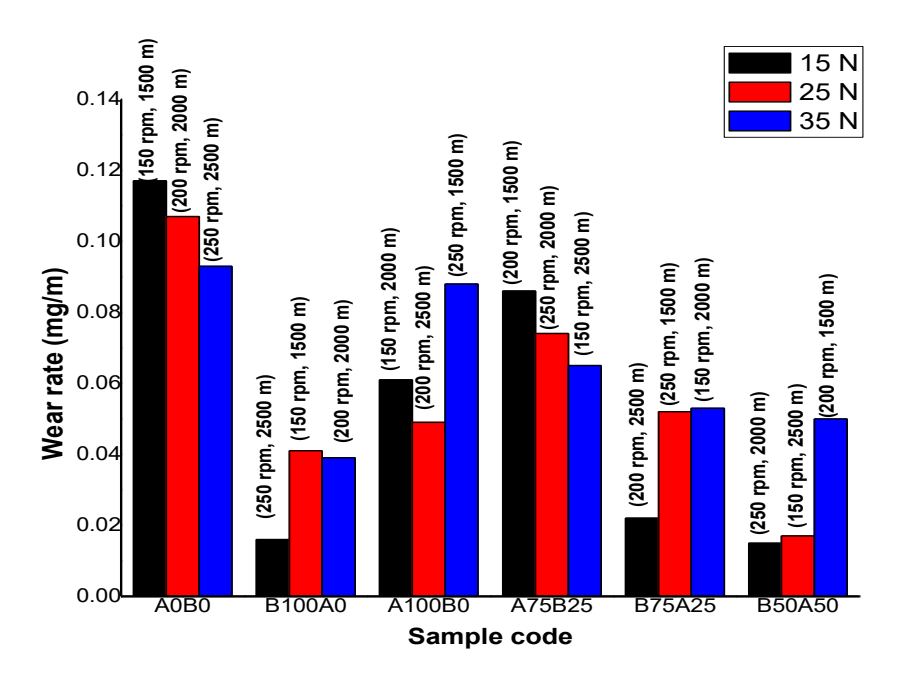


Fig. 6. Variations of wear rate with load at different rotation and sliding distance for hybrid composites

The weight losses were found to be increased with increase in loads for all the composites due to increased plastic deformation of asperities to asperities contact between the contacting surfaces at wear parameters. Also the similar trend was followed by weight loss with rotation of disc or sliding distance for all the composites at different wear parameters. For B50A50 sample, the weight loss was the lowest among all the composites due to contribution of hard ceramic particles as reinforcements and its better interfacial bonding between the matrix of al alloy 6061 with dispersed particles of alumina and boron carbide.

For the samples A0B0 and A100B0, the weight loss was increased with increasing rotation of disc or sliding distance due to softening of materials. The composites B100A0 and B50A50 showed lower weight loss at higher rotation of disc or sliding distance due to formation of tribo-layer between the sample and counter surface body. Also, for the composites A75B25 and B75A25, the weight loss was higher at lower speed than the other speed due to delimitation of particles taking place for all particular wear parameters. On comparing with Al alloy A0B0, all the composites offer a higher coefficient of friction at all the conditions. This happened due to addition of dispersed particles of alumina and boron carbide in the matrix material. For all the composites including alloy, initially the coefficient of friction was high because of sharp asperities on the counter face that deformed the material then decreased with increasing load (15N-35N) due to deformation of asperities, which also causes work hardening of matrix material.

The wear rate of Al alloy A0B0 is highest in comparison to all the composites B100A0, A100B0, A75B25, B75A25 and B50A50 due to softer nature of matrix materials of Al alloy or higher asperities to asperities contact between counter surfaces or presence of harder Al₂O₃ and B₄C powder particles in the composites for all wear parameters.

For Al alloy A0B0 (at all the wear conditions), B100A0 (200 rpm, 2500 m) and A100B0 (200 rpm, 2500 m), there is formation of oxides which spreads and form a layer on the pin surfaces. Once, the oxide later are formed there were spalling, distortion and fractures of that layer may be happened between mating surfaces during sliding but all the oxides are not dislodge from the mating surfaces. Hence, it may prevent metal to metal or particles to metal contacts leads to reduction in wear rate.

For A75B25 composites, the wear rate is decreased with increasing load from 15-35 N because of better interfacial bonding between reinforcing and matrix materials for all wear conditions. The wear rate of composites B75A25 and B50A50 are increased with increasing applied load from 15 to 35 N due to increasing temperature leads to no longer formation of mechanically mixed layer. A larger load produces large uncertainties in the formation of mechanically mixed layer. Similar trends followed by the composites B100A0 and A100B0.

Morphological study of wear surfaces. Figure 7 shows the micrographs of worn surfaces for hybrid metal matrix composites at different loads: A0B0 at 15 N, A50B50 at 35 N, B100A0 at 25 N, and A100B0 at 25 N. It was seen that longitudinal grooves and some pits are present in each of the specimens. The grooves refer to the occurrence of plastic deformation. The fine scratches were visible along with the sliding direction for hybrid composites A50B50, B100A0, and A100B0. However, the grooves and scratches have been reduced to a relatively finer form for hybrid composite A50B50. The presence of grooves indicates the micro-cutting and micro-ploughing effect. It is the indication of abrasive wear. From the SEM images, the pits and heavy flow of material along the sliding direction could also be observed, so there is adhesive wear. Severe abrasive wear along with adhesive wear was observed for the hybrid composites. The present result was found in line with the reported result by Zhu et al. [25].

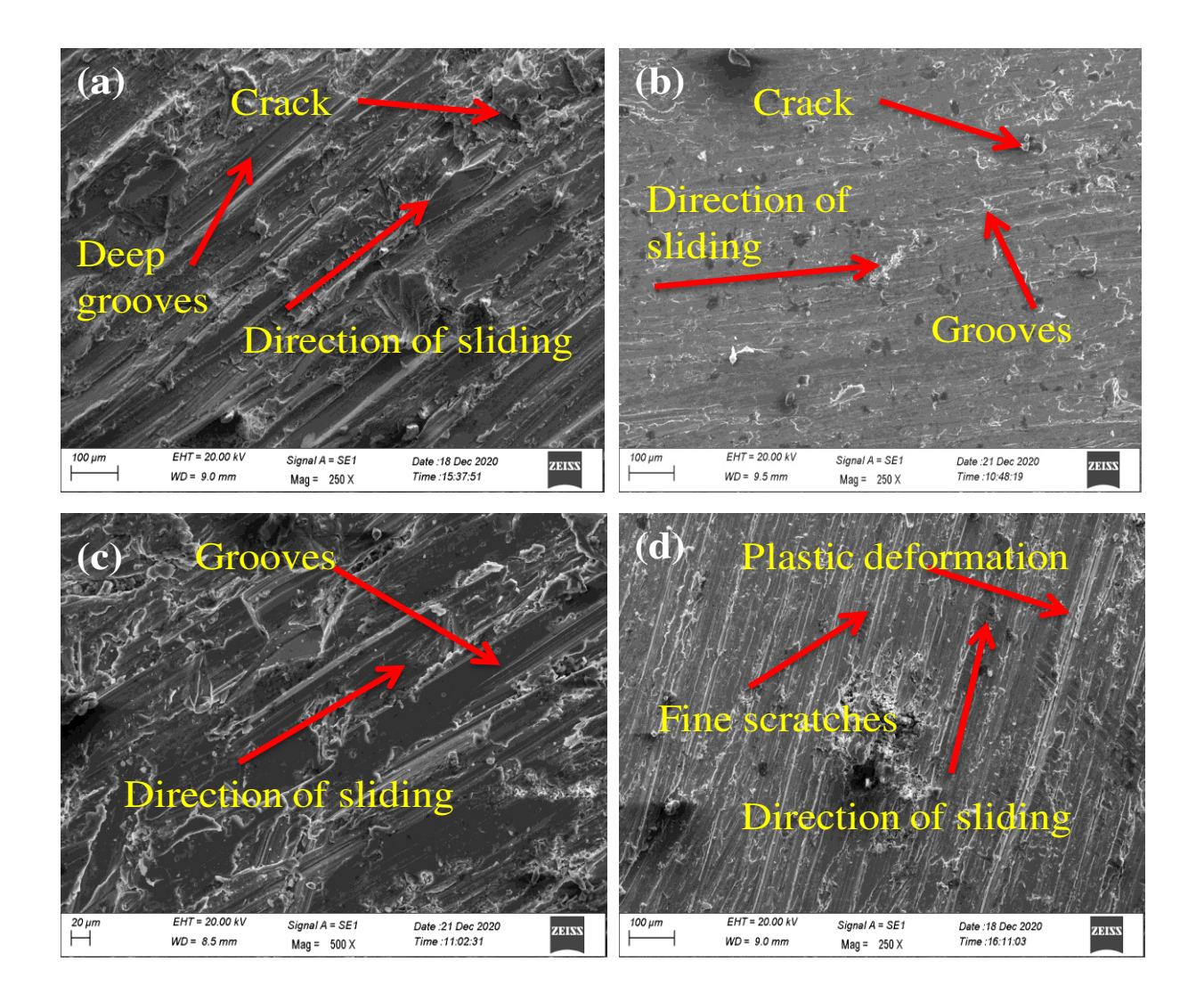


Fig. 7. Micrographs of worn surfaces for hybrid metal matrix composites: (a) A0B0 at 15 N, (b) B100A0, (c) B0A100 at 25 N, and (d) B50A50 at 35 N for different rotation of the disc and sliding distance

The degree of the grooves formed for a specimen (A0B0) at a load of 15 N was higher than the specimens A50B50 at a load of 35 N, B100A0 and A100B0 at a load of 25 N. The grooves formed in composites were reduced with the addition of hard alumina and boron carbide particles, indicating lower material loss for hybrid composite. At the beginning of the wear test, the material may be subjected to abrasive wear. Later, when the sliding distance increases, the adhered reinforcements may come out from the composites material and act as abrasive between pin and disc material (EN-31, hardened), leading to three-body abrasion behaviour. The EDS analysis of worn surfaces of Al-Al₂O₃/B₄C composites is shown in Figure 8. The presence of Si, Mn, Cu, Cr, Fe, B, C, O and Mg particulates can be seen by EDS analysis. The EDS images of fabricated Al6061-Al₂O₃/B₄C composites show the presence of B, C, O along with monolithic Al alloy constituents (Al-Mg-Si). Thus, it can be confirmed about reinforcements in the samples by the EDS analysis.

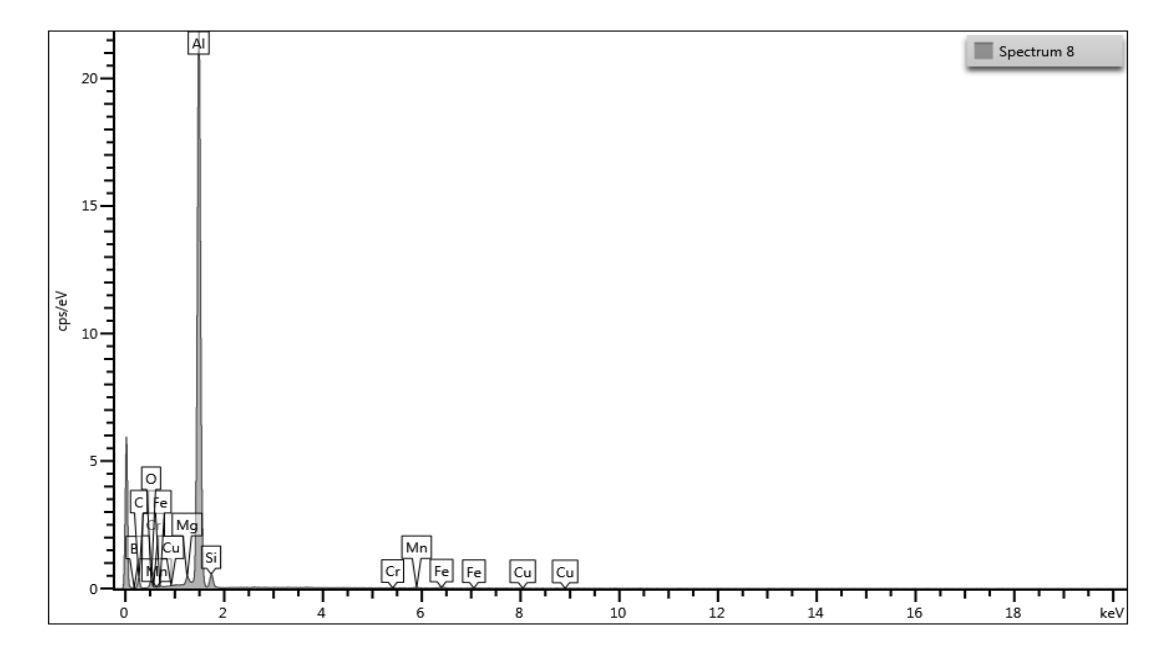


Fig. 8. EDS spectrum of Al-Al₂O₃/B₄C metal matrix composites

Conclusions

The wear analysis of the prepared hybrid MMCs was performed using the pin-on-disc method and wear parameters were also optimized with objectives of minimizing the weight loss and coefficient of friction through integrated Grey-Taguchi techniques. The main findings are as follows:

- 1. In comparison with Al alloy matrix and single reinforced MMCs, the minimum values of weight loss and coefficient of friction were seen for the hybrid composite with equal percentages of reinforcements.
- 2. The optimum values of weight loss and coefficient of friction through an integrated GRA-Taguchi analysis were reported as such: sample composition of $B_4C=50\,\%$ and $Al_2O_3=50\,\%$, rotation (sliding speed) of 250 RPM, the sliding distance of 2500 m and the load of 15 N.
- 3. The results of the ANOVA indicated the percentage contribution of each input factor as such: compositions of 94.47 %, rotation (sliding speed) of 1.06 %, sliding distance of 1.04 %, and load of 3.16 %.
- 4. The abrasive along with adhesive wear mechanism was found in the composites through SEM analysis.
- 5. Based on experimental outcomes from wear analysis of hybrid metal matrix composites, it can be concluded that better wear resistance was offered by hybrid composites than Al matrix and single reinforced composites which makes the hybrid composites more suitable for applications where economical and high wear resistance materials are required.

References

- 1. Gupta PK, Gupta MK. Mechanical and microstructural analysis of Al-Al₂O₃/B4C hybrid composites. *Proc. IMechE Part L: J Materials: Design and Applications*. 2020;234(12): 1503-1514.
- 2. Abdizadeh H, Baghchesara MA. Investigation into the Mechanical Properties and Fracture Behavior of A356 Aluminum Alloy-Based ZrO₂-Particle-Reinforced Metal-Matrix Composites. *Mechanic. Compos. Mater.* 2013;49: 571-576.

- 3. Gupta PK, Gupta MK. Hybrid Optimization Approach on Electrical Discharge Machining Process for Hybrid Al-Al₂O₃/B4C Composites. *Mater. Phys. Mech.* 2022;50(2): 200-215.
- 4. Rao RN, Das S. Effect of SiC content and sliding speed on the wear behaviour of aluminium matrix composites. *Mater. Des.* 2011;32(2): 1066-1071.
- 5. Sharma AK, Bhandari R, Aherwar A and Pinca-Bretotean C. A study of fabrication methods of aluminum based composites focused on stir casting process. *Mater. Today: Proc.* 2020;27: 1608-1612.
- 6. Yılmaz O, Buytoz S. Abrasive wear of Al₂O₃-reinforced aluminium-based MMCs. *Compos. Sci. Technol.* 2001;61(16): 2381-2392.
- 7. Thakur SK, Dhindaw BK. The influence of interfacial characteristics between SiCp and Mg/Al metal matrix on wear, coefficient of friction and microhardness. *Wear*. 2001;247(2): 191-201.
- 8. Zhang Z, Chen Y, Zhang Y, Gao K, Zuo L, Qi Y and Wei Y. Tribology characteristics of ex-situ and in-situ tungsten carbide particles reinforced iron matrix composites produced by spark plasma sintering. *J. Alloy. Compd.* 2017;704: 260-268.
- 9. Yu SY, Ishii H, Tohgo K, Cho YT, Diao D. Temperature dependence of sliding wear behavior in SiC whisker or SiC particulate reinforced 6061 aluminum alloy composite. *Wear*. 1997; 213(1-2): 21-28.
- 10. Martin A, Rodríguez J, Llorca J. Temperature effects on the wear behavior of particulate reinforced Al-based composites. *Wear*. 1999;225: 615-620.
- 11. Kumar GV, Panigrahy PP, Nithika SR, Rao CS. Assessment of mechanical and tribological characteristics of Silicon Nitride reinforced aluminum metal matrix composites. *Compos. Part B: Eng.* 2019;175: 1-29.
- 12. Anand VK, Aherwar A, Mia M, Elfakir O, Wang L. Influence of silicon carbide and porcelain on tribological performance of Al6061 based hybrid composites. *Tribol. Int.* 2020;151: 106514.
- 13. Zheng B, Dong F, Yuan X, Huang H, Zhang Y, Zuo X, Luo L, Wang L, Su Y, Li W, Liaw PK. Microstructure and tribological behavior of in situ synthesized (TiB+TiC)/Ti6Al4V (TiB/TiC=1/1) composites. *Tribol. Int.* 2020;145: 106177.
- 14. Cygan T, Petrus M, Wozniak J, Cygan S, Teklińska D, Kostecki M, Jaworska L, Olszyna A. Mechanical properties and tribological performance of alumina matrix composites reinforced with graphene-family materials. *Ceram. I.* 2020;46(6): 7170-7177.
- 15. Xiao P, Gao Y, Xu F, Yang C, Li Y, Liu Z, Zheng Q. Tribological behavior of in-situ nanosized TiB2 particles reinforced AZ91 matrix composite. *Tribol. Int.* 2018;128: 130-139.
- 16. Abbas A, Huang SJ, Ballokova B, Sülleiová K. Tribological effects of carbon nanotubes on magnesium alloy AZ31 and analyzing aging effects on CNTs/AZ31 composites fabricated by stir casting process. *Tribol. Int.* 2020;142: 105982.
- 17. Ambigai R, Prabhu S. Optimization of friction and wear behaviour of Al–Si3N4 nano composite and Al–Gr–Si3N4 hybrid composite under dry sliding conditions. *Transac. Nonfer. Met. Soc. China.* 2017;27(5): 986-997.
- 18. Siriyala R, Alluru GK, Penmetsa RM, Duraiselvam M. Application of grey-taguchi method for optimization of dry sliding wear properties of aluminum MMCs. *Front. Mech. Eng.* 2012;7: 279-287.
- 19. Muthu P. Multi objective optimization of wear behaviour of Aluminum MMCs using Grey-Taguchi method. *Manuf. Rev.* 2020;7: 16.
- 20. How HC, Baker TN. Dry sliding wear behaviour of Saffil-reinforced AA6061 composites. *Wear*. 1997;210(1-2): 263-272.

- 21. Straffelini G, Bonollo F, Molinari A, Tiziani A. Influence of matrix hardness on the dry sliding behaviour of 20 vol.% Al₂O₃-particulate-reinforced 6061 Al metal matrix composite. *Wear.* 1997;211(2): 192-197.
- 22. Sahoo P, Pal SK. Tribological performance optimization of electroless Ni–P coatings using the Taguchi method and grey relational analysis. *Tribol. Lett.* 2007;28: 191-201.
- 23. Paranthaman P, Ramesh Babu R, Mahesh R. The multi-objective optimization on tribological behaviour of hybrid Al MMC by grey relation analysis. *J. Crit. Rev.* 2020;7(9): 200-202.
- 24. Baradeswaran AE, Perumal AE. Influence of B4C on the tribological and mechanical properties of Al 7075–B₄C composites. *Composites Part B: Engineering*. 2013;54: 146-152.
- 25. Zhu J, Qi J, Guan D, Ma L, Dwyer-Joyce R. Tribological behaviour of self-lubricating Mg matrix composites reinforced with silicon carbide and tungsten disulfide. *Tribol. Int.* 2020;146: 106253.

THE AUTHORS

Pankaj K. Gupta

e-mail: guptammmecpankaj@gmail.com

Manoj K. Gupta 🗓

e-mail: mkgupta@mnnit.ac.in

The influence of friction stir processing on the microstructure and properties of the AD31T alloy

Submitted: March 29, 2023

Approved: May 5, 2023

Accepted: June 13, 2023

A.E. Medvedev ¹ ^{1 ™}, V.V. Atroshchenko ², A.S. Selivanov ², A.R. Bogdanov ¹,

M.V. Gorbatkov ³, Y.V. Logachev ², V.S. Lobachev ², A.R. Sadrislamov ²

Abstract. The effect of friction stir processing treatment (FSP) on the microstructure and physical and mechanical properties of an aluminum alloy of the Al-Fe-Mg-Si system (AD31T alloy) has been studied. In particular, the influence of various processing modes on the formation of structural and bulk defects in the stir zone (SZ) was studied. The optimal technological parameters that ensure the formation of a tool with a relatively homogeneous defect-free structure for a given tool geometry is a tool rotation speed of 1120 rpm at a tool linear speed of 200 mm/min. It is shown that an increase in the linear speed of the tool in the range of 50–200 mm/min leads to a decrease of the heat-affected zone (HAZ), a smaller size of volume defects in the SZ, and more uniform deformation. The microstructure analysis data is confirmed by the microhardness and electrical conductivity measurement values. It is shown that the decrease in the electrical conductivity in the SZ does not exceed 2 % of the electrical conductivity of the base material.

Keywords: FSP; Al-Mg-Fe-Si; aluminium alloy; fine-grained structure: microhardness; electrical conductivity

Citation: Medvedev AE, Atroshchenko VV, Selivanov AS, Bogdanov AR, Gorbatkov MV, Logachev YV, Lobachev VS, Sadrislamov AR. The influence of friction stir processing on the microstructure and properties of the AD31T alloy. *Materials Physics and Mechanics*. 2023;51(4): 38-49. DOI: 10.18149/MPM.5142023_4.

Introduction

The aluminum in the modern industry plays a key role; aluminum production is one of the strategic directions in non-ferrous metallurgy [1]. Due to low density, high thermal conductivity, low electrical resistance, high ductility, corrosion resistance, good manufacturability, assimilation in metallurgical production, and a set of performance characteristics, aluminum alloys are the basic structural materials in the aerospace industry, construction, railway transport, automotive industry, and shipbuilding [2]. The application sphere of aluminum alloys is constantly expanding. The technologies of its production and processing are being improved - both new methods for obtaining aluminum and alloys based on it [3,4], as well as methods for obtaining products and prepacks from them do appear [5]. At the same time, tasks related to the development of new and the development of existing technologies are relevant for modern mechanical engineering [4]. Recently, the creation of

© A.E. Medvedev, V.V. Atroshchenko, A.S. Selivanov, A.R. Bogdanov, M.V. Gorbatkov, Y.V. Logachev, V.S. Lobachev, A.R. Sadrislamov, 2023.

Publisher: Peter the Great St. Petersburg Polytechnic University

39

gradient structures in materials, including those based on aluminum, has been actively developed. The structure of such materials is characterized by a designed inhomogeneity, providing different properties in the material's volume [6]. The most common method for obtaining gradient structures is surface treatment, due to the relative availability of the process, many ways of providing the treatment and the readiness of the product at the output. One approach to surface treatment to obtain a gradient structure is friction processing. Friction processing includes several methods, such as friction stir welding, friction stir processing, radial friction welding, friction soldering, etc. [7]. The most common of the methods listed above is friction stir processing (FSP). Processing by FSP [5] is a technology aimed at modifying the structure and properties of the surface of materials in the solid phase. Its difference from traditional methods is the absence of melting, which can lead to oxidation and overburning of the metal [8], and a decrease in its strength properties [9]. Studies on FSP have shown that this method, in addition to creating permanent joints, is able to modify the surface layer of the processed material, providing a different level of properties. It has been shown that FSP with superposition of tracks on aluminum surface makes it possible to achieve a reduction in the average grain size to 100-200 nm on a relatively large area, reaching an ultrafine-grained (UFG) state [10–12]. The authors propose a similar approach as one that makes it possible to obtain large-sized products with an UFG structure of the near-surface layer. The authors of [13] claim a more than 20-fold decrease in the average grain size because of one pass of FSP, which led to an increase in the yield strength of the material by 2.4 times. FSP has also found its way to modify surface chemistry and create aluminum-based composites. For example, application of FSP makes it possible to introduce reinforcing particles into the near-surface layer of a material without the formation of a liquid phase [14]. At the same time, the FSP itself contributes to the strengthening of the treated area. Thus, a combined effect on the product surface is achieved, which is unattainable by other approaches [15–17]. However, the published scientific results often lack precise data regarding tool configuration or processing mode details. Only approximate ranges of values for the speeds of movement and rotation of the tool, and the general configuration of the tool are given [18–20]. For further work, the exact values of these parameters are necessary, because their non-observance is fraught with the appearance of volumetric defects in the weld material [17,21,22]. The objective of this study is to analyze the microstructure and properties of AD31T aluminum alloy processed by FSP for four modes and to provide the recommendations on the exact geometry of the welding tool and processing conditions. The modes are tested on a model aluminum alloy, and the optimal mode will subsequently be applied to other aluminum alloys of the Al-Fe-Si system.

Materials and Experimental Methods

As a research material, hot-rolled aluminum alloy plates of 10 mm thick and 200x200 mm in size were used. The plates were obtained in the "T" state which means quenching and natural aging of the plate. This resulted in the inhomogeneity of the structure – there are coarse grains near the surfaces of the samples and finer grains closer to the middle of the sample. The chemical composition of the commercially produced AD31T alloy is given in Table 1.

Table 1. Chemical composition of the AD31T alloy

	Concen	tration of the	element, wt.	%		
Al Si Fe Mg Mn Cu Zn						
Base material	0.410	0.390	0.390	≤0.035	≤0.035	≤0.035

The processing of the material was carried out on a vertical console milling machine FSS-400, adapted for FSP, in 4 different processing modes (Table 2). During FSP the shoulder penetration was 0.635 mm at a tool inclination angle of 3°. The tool dwelling time after

immersion is 10 sec. Each mode provides 1 tool pass. During the FSP, the temperature in the treatment area was monitored using a TESTO 868 thermal imager.

		1	^	TOD	1
•	าก	Ω	,	$H \setminus P$	modes
_	av	ı	4.	101	moucs

Sample marking for the X-Ray	Tool rotation speed,	Tool linear speed,	Max. temperature of
control	rpm	mm/min	the tool, °C
205		50	600
204	1120	100	560
206	1120	160	470
207		200	440

A sketch of the tool is shown in Fig. 1. The tool is made of steel grade 20X13 (the closest analogue is AISI 420). Before use, the tool is hardened, after which its hardness is 580 HB. Most authors do not disclose the details of the geometry of the stirring tool, however, the general recommendations for aluminum alloys are that the tool pin should be a tapered cone or a threaded one [16,22]. However, the production of the threaded tool is more expensive and complex, than the production of the tapered cone tool [23]. Further it will be demonstrated that the simple tapered cone shape of the tool can provide the defectless structure, without having a need for the threaded tool.

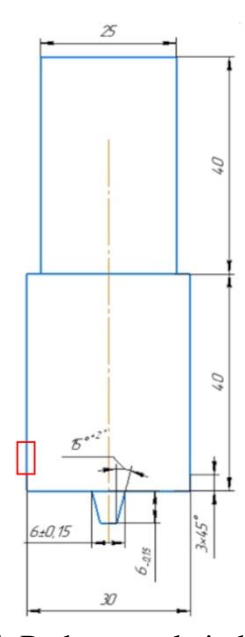


Fig. 1. Schematic of the stirring tool. Red rectangle indicates the location within the stirring tool, in which temperature measurements were conducted

X-ray control was carried out on the hardware-software complex of digital radiography "Tsifrakon". Microstructure studies were performed on an Olympus Q15OR optical microscope. For metallographic analysis, microsections were made, cut in the middle of the length of the treated zone in the direction perpendicular to the processing direction. Surface finishing was carried out in a 3 % hydrofluoric acid solution to reveal the macrostructure. Microhardness (HV) was evaluated by the Vickers method on a Buehler MicroMet 5101 instrument at a load of 1 N and a holding time under load of 10 s. The HV value was calculated using the Omnimet Imaging System software. Microhardness was measured on transverse sections of specimens along lines parallel to the surface of the original slab. The measurements were taken at the middle of the sample thickness, and ½ of the height from the bottom and top surfaces of the slab. When measuring the microhardness of the stir zone, the line of

measurements passed through all sections of the cross section of the FSP sample at a measurement step of 0.5 mm (about 60 measurements per line). The specific electrical conductivity (ω) of the alloy samples was determined with a relative error of 2 % using a VE-27NTs/4-5 eddy current electrical conductivity meter according to ASTM E1004-09. The electrical conductivity value of the samples relative to annealed copper (International Annealed Copper Standard) was calculated using formula (1):

$$IACS = \omega_{Al}/\omega_{Cu} \times 100 \, [\%], \tag{1}$$

where ω_{Al} is the experimentally determined value of the electrical conductivity of the aluminum alloy sample, ω_{Cu} is the electrical conductivity of annealed copper, equal to 58 MSm/m. The electrical conductivity was measured at 10 points on a line located in the middle of the sample thickness.

Results and discussion

Stir zone (**SZ**) **assessment.** The overview of the treated samples and their X-ray control images are presented in Fig. 2.

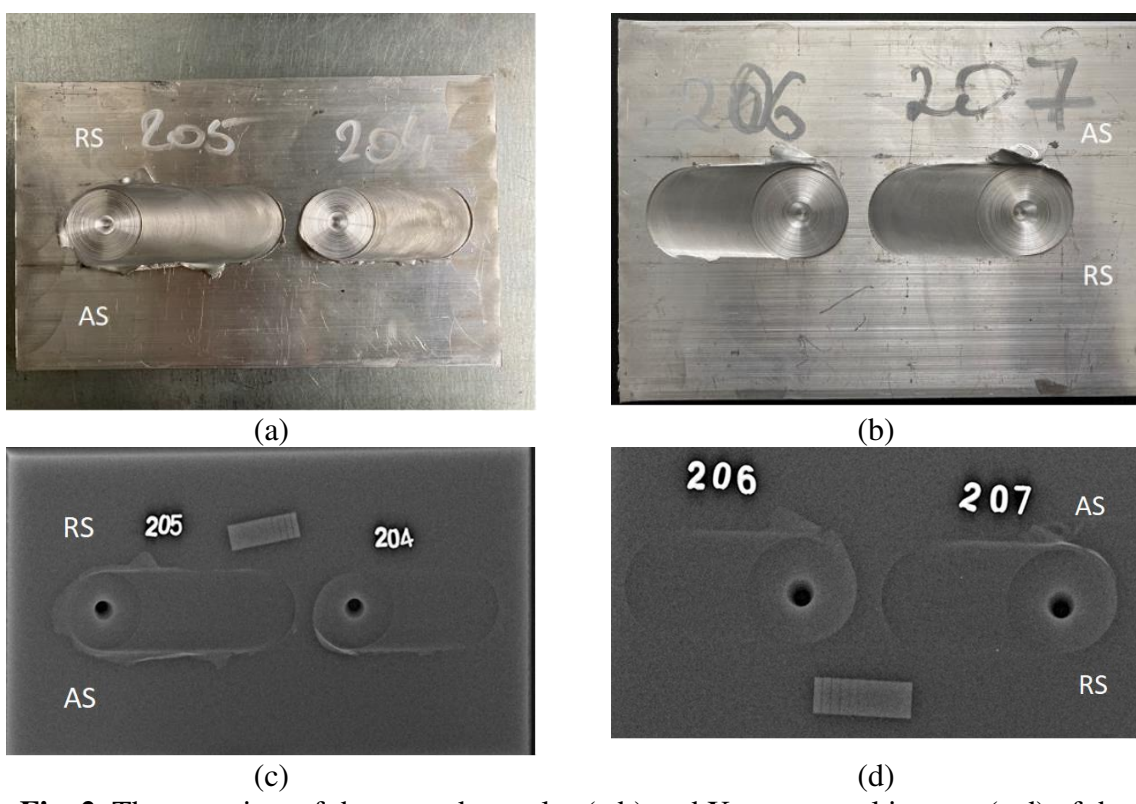


Fig. 2. The overview of the treated samples (a,b) and X-ray control images (c,d) of the samples 205, 204, 206 and 207. Advancing side (AS) and retreating side (RS) are indicated for each sample

X-ray quality control of the processed zone (PZ) showed that there are no macroscopic defects and discontinuities in the PZ in all four modes. The temperature in the PZ decreases with increasing linear speed of the tool (Table 2). With a decrease in the process temperature, both a decrease in the plasticity of the metal and an increase in the probability of the occurrence of bulk defects take place, as well as a decrease in the risks of melting, oxidation and the occurrence of recovery and recrystallization processes. Thus, the balance of the temperature should be maintained to prevent the abovementioned negative effects.

Macrostructure assessment. A stir zone (SZ), a thermomechanically affected zone (TMAZ), a heat-affected zone (HAZ) and a base material (BM) can be distinguished in the PZ. It should be noted that the width of the HAZ is small in all the samples, and only the SZ, HAZ, and BM are distinguished clearly. The width and geometry of the PZ (Fig. 3) directly depends on the parameters of energy input due to friction and is determined by two main parameters the tool rotation speed and the linear speed of the tool movement. It should be noted that the TMAZ and HAZ decrease with an increase in the linear velocity of the tool (Table 2) and turned out to be the smallest for samples 206 and 207.

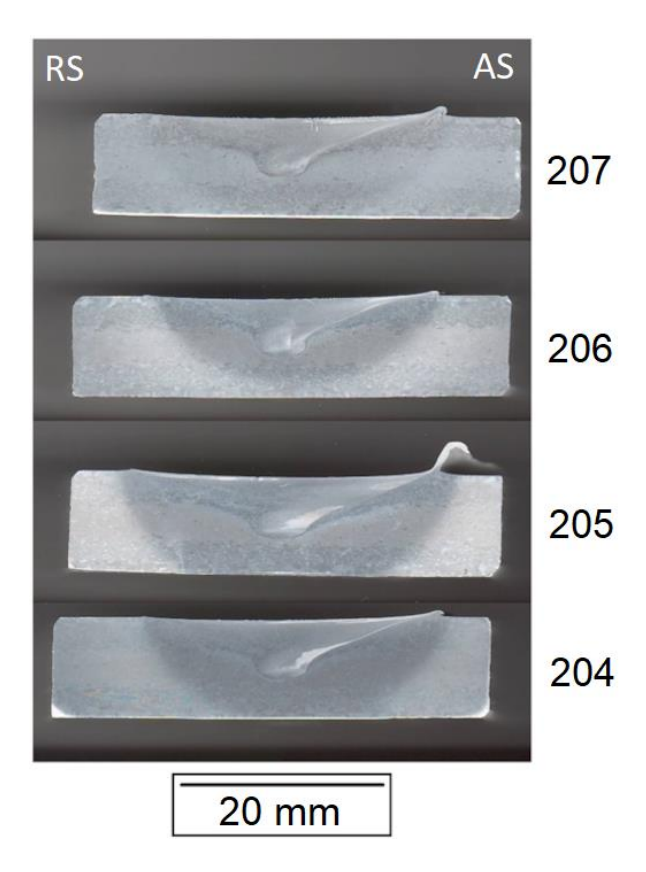


Fig. 3. The results of optical metallography of transverse sections of the studied samples

Figures 4 and 5 present the results of optical metallography of the structural features of the samples. Figure 4 shows the central part of the PZ of samples 204-207. The most uniform state of the material volume is observed in sample 207. Samples 205, 204 and 206 are characterized by the presence of volume defects in the central part of the SZ.

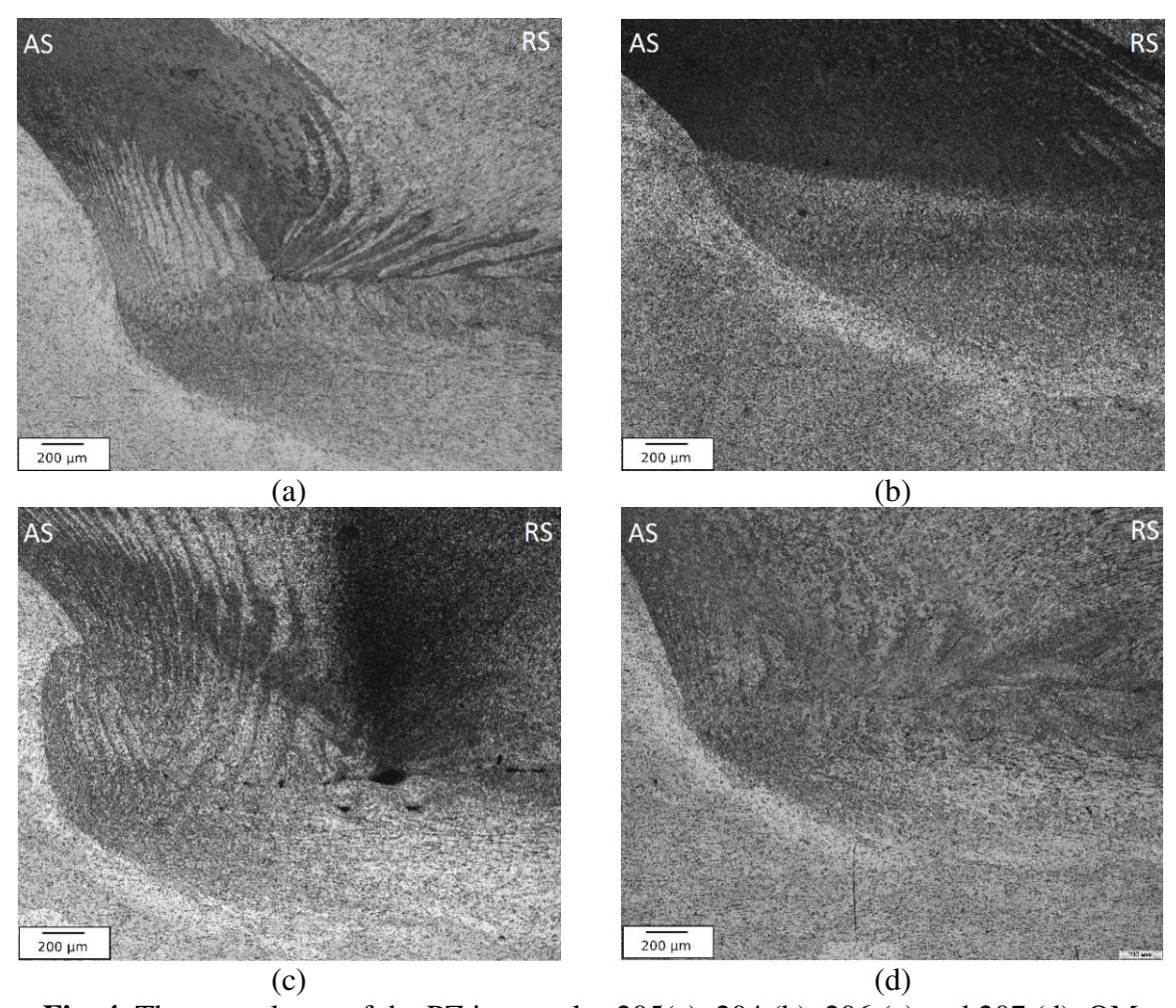


Fig. 4. The central part of the PZ in samples 205(a), 204 (b), 206 (c) and 207 (d), OM

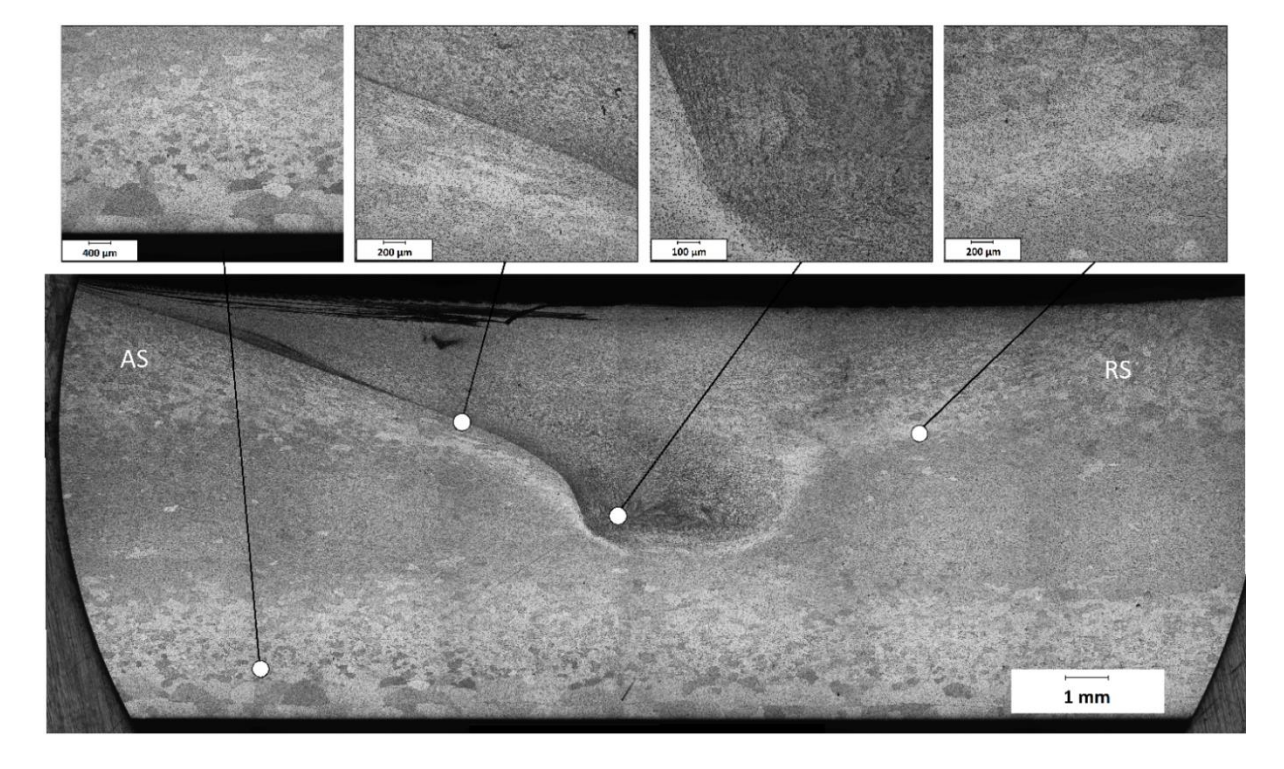


Fig. 5. Panoramic image of the microstructure of sample 207 after polishing and etching, OM

Figure 5 illustrates a panoramic image of the microstructure of sample 207. There is practically no transition layer between the SZ and the HAZ. The edge of the SZ is clearly visible. The slab of the base material is characterized by a heterogeneity of the structure over the cross section - at the surfaces (upper and lower) the grain size is large (522 \pm 56µm), gradually decreasing towards the middle of the sample (from 324 to 53 µm with average size of $131\pm8~\mu m$); in the middle layer - fine, not detectable by etching. The similar microstructure could be observed in samples 205 and 206 as well. The difference in grain size throughout the sample, observed in the initial metallic plate, is the results of the quenching and natural aging.

Microstructure assessment. The sample 207 was previously characterized as the preferable from the absence of defects point of view. The microstructure of the sample 207 is presented on Fig. 6.

Intermetallic particles, presented in the material, don't have a significant impact on the structure and properties of the sample. According to Fig. 6(a-d) there is no notable difference in the size and morphology of the intermetallic particles before and after the FSP. The treatment, however, results in the decrease of the average grain/subgrain size within the PZ – from 274 ± 22 nm to 173 ± 10 nm (Fig. 6(e,f))

The presented experimental results show that in the FSP there is a significant refinement of the average grain size in the central region of the PZ, with the formation of a fine-grained equiaxed structure. The average grain size in the SZ decreases by a factor of 4–5 compared to the initial structure of the alloy (decreasing is more notable in the edges of the sample, where the initial grains are the largest).

The exact processes that occur during the FSP within the material structure are numerous and may happen simultaneously. Due to the combination of the high temperature and high deformation value within the SZ the dynamic recrystallization (both continuous and discontinuous), recovery, dislocation emission and annihilation, grain refinement take place. Usually, the structure of the material after FSP consists of the grain with the different degree of recrystallization and/or recovery place [13,24]. The exact combination of abovementioned mechanisms depends on the material and the FSP conditions, and to pinpoint each of them, the thorough structure analysis is required. However, in case of friction stir processing the processes on a microscale are not of an importance, since the presence/absence of macro defects has bigger value [8,25]. Since the recovery and recrystallization are inherent to the FSP, their presence might be used to an advantage – it is suggested that UFG materials could be subjected to FSP without loss of the UFG structure [9].

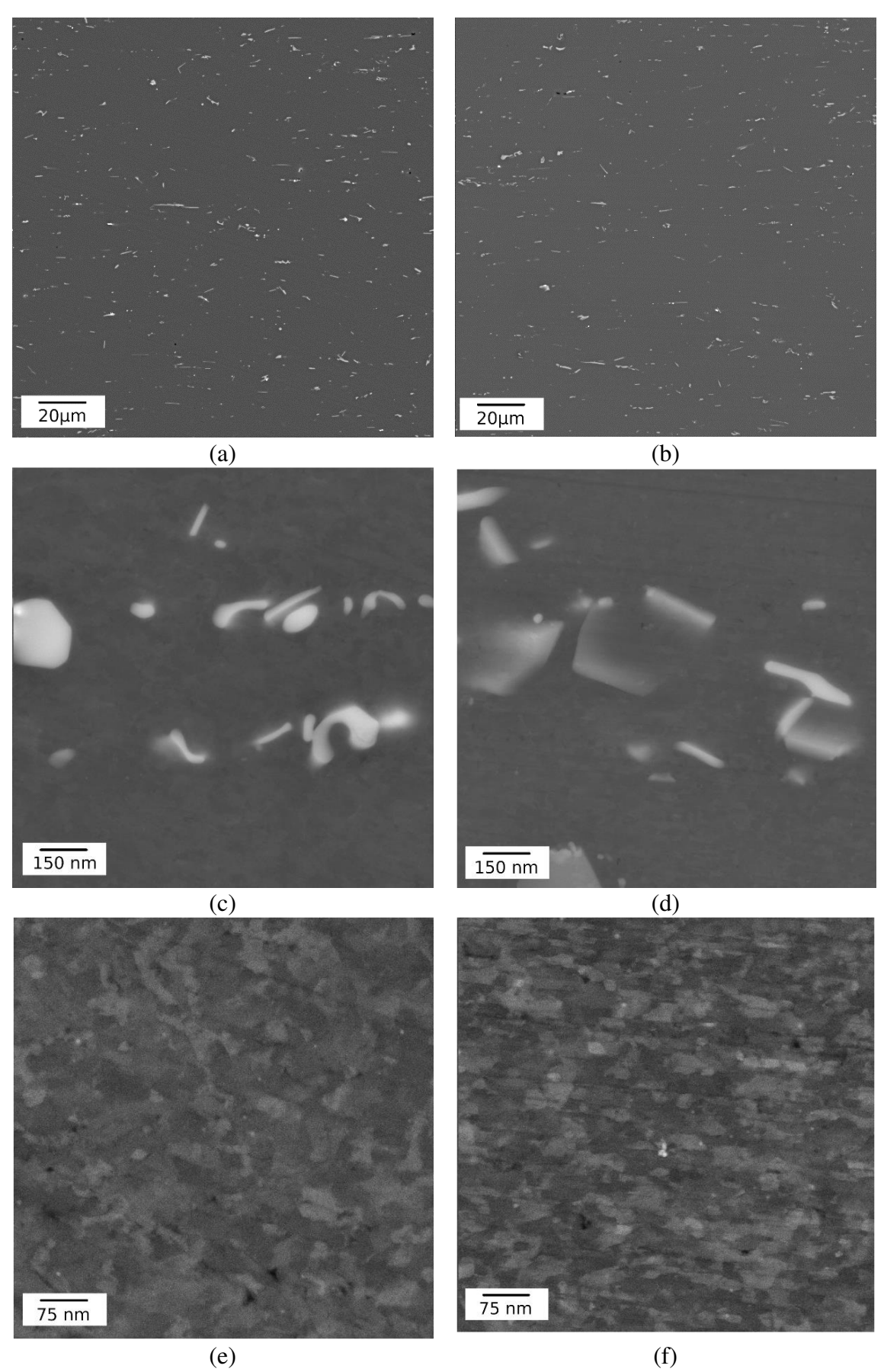


Fig. 6. Microstructure of the 207 sample: (a,c,e) - BM, (b,d,f) - SZ, SEM. Images a-d illustrate particles, e-f – grains/subgrains

Microhardness and electrical conductivity results. Figure 7 shows the obtained data on the distribution of microhardness over the cross section of the sample. For each sample three microhardness profiles were measured: at the bottom of the sample, in the middle and at the top.

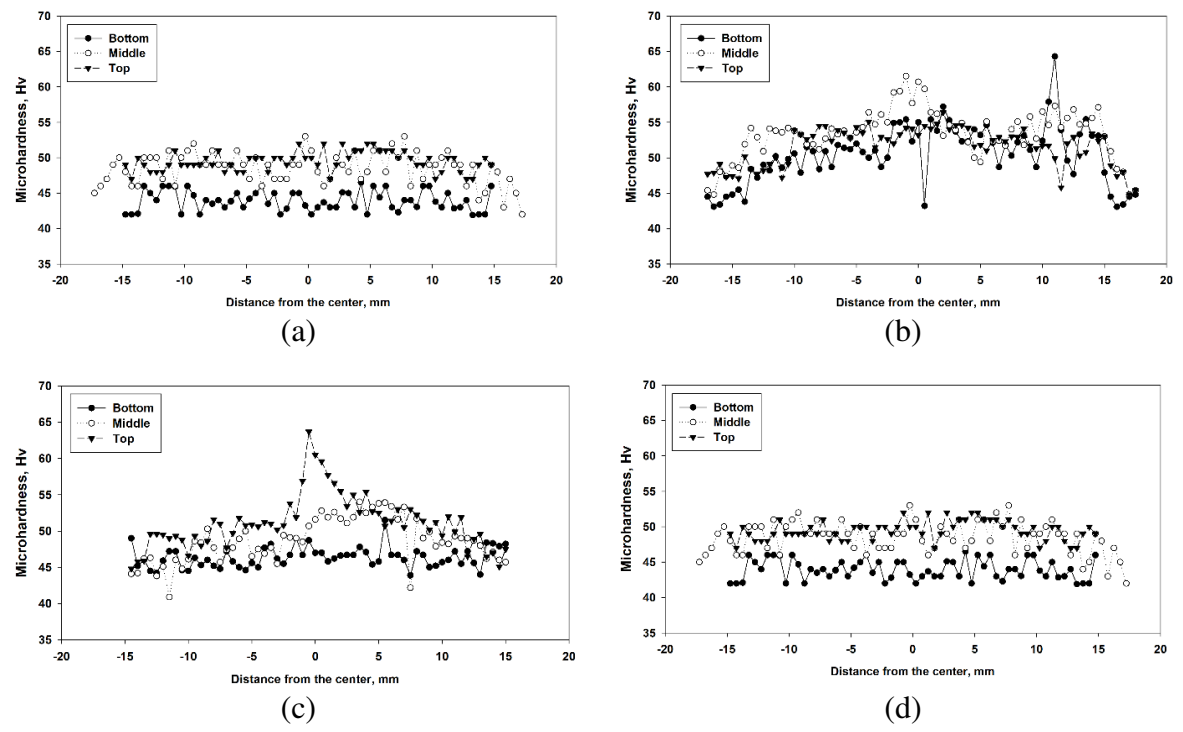


Fig. 7. Distribution of microhardness over the cross section of the samples 204 (a), 205 (b), 206 (c) and 207 (d). On all images the AS is on the right

The measurements showed that the microhardness values HV for all the samples under study are in the range of 40-65 HV. The middle profile is slightly higher for each of the samples due to the lower average grain size. Due to the uneven structure of the initial plate, there is no data for the microhardness of the BM, since it is different in different regions of the samples. At the same time, the microhardness profiles have tendency to rise (and even have a peak in sample 206) in the region of the PZ. The increase in microhardness is the result of grain boundary strengthening, which, in turn, is caused by a decrease in the average grain size in the SZ because of the thermomechanical treatment. It is noteworthy that the highest peak values of microhardness are observed in the sample obtained according to mode 206. Highest average microhardness values are demonstrated by the 205 sample.

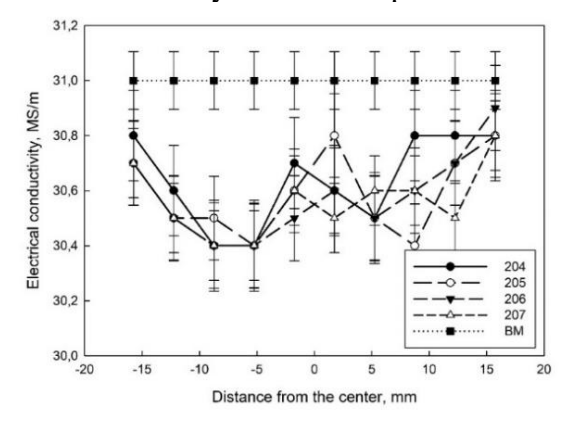


Fig. 8. Distribution of electrical conductivity over the cross section of the SZ in the samples 204-207. AS is on the right

Figure 8 shows the graphs of the distribution of the electrical conductivity of the investigated alloy after FSP. Since the electrical conductivity parameter is sensitive to structural defects, its change can be used to judge the homogeneity of the deformation.

Although all samples are characterized by a decrease in electrical conductivity in SZ relative to BM, associated with an increased density of structural defects, the difference in electrical conductivity values is relatively small and lies within the error value. Still, electrical conductivity measurements present the trend of electrical conductivity changes. The scatter of electrical conductivity values in samples 205 and 204 is higher than in samples 206 and 207, indicating a greater structural inhomogeneity in samples 205 and 204. All four samples are characterized by a local decrease in electrical conductivity in the first third of the sample, exactly where the transition zone between the BM and the HAZ is. From the point of view of the formation of a homogeneous structure within the PZ, mode 207 is optimal, which makes it possible to recommend it for further research.

The conducted studies of the relationship between the processing conditions of the FSP and the microstructure and properties of the obtained samples showed that with a decrease in the linear speed of the tool movement, the thermomechanical effect on the microstructure of the PZ increases noticeably. In the region of the PZ root, volumetric defects begin to be detected with a decrease in the linear speed of the tool. However, the size of these defects is relatively small, and continues to decrease with increasing linear speed of the tool. The importance of the macro defects within the stir zone cannot be overestimated – the presence of the crack or left by the FSP can led to a premature failure of the material, nullifying all the attempts to increase the material's strength [8,17,25]. Thus, only after obtaining defectless structure, any further strength/performance attempts can be made.

The revealed patterns of structure formation during FSP and the tests carried out made it possible to select the technological parameters of the FSP, which provide both a decrease in the number and size of bulk defects and local hardening in the core. The proposed FSP mode can be transferred to other aluminum alloys.

The results obtained can be used for further work aimed at obtaining aluminum-based materials with modified structure and surface properties. Since the FSP conditions for the studied alloy were established, the different schemes of the FSP could be safely applied to this alloy. The further research is focused on providing the overlapping tracks [10–12], processing the material plate from both sides, doubling the processing routes [7].

Conclusions

- 1. The optimal technological parameters that ensure the formation of PZ with a relatively homogeneous defect-free structure with a small grain size at a given instrument geometry is a tool rotation frequency of 1120 rpm with a processing speed of 200 mm/min for the AD31T alloy.
- 2. An increase in the linear velocity of the stirring tool leads to a decrease in the heating temperature of the tool and the surrounding material and leads to a decrease of the HAZ. Since it is important not to overheat the material (to avoid recovery, oxidation, formation of a liquid phase and other undesirable processes) the increase in linear velocity of the tool not only decreases the treatment time, but also provides absence of the aforementioned defects.
- 3. Suggested FSP conditions provide the decrease of the electrical conductivity within the SZ by 2 % of the BM conductivity level without the loss of the microhardness, making this technique applicable to the installation of electric conductors.

References

- 1. Polmear I, StJohn D, Nie JF, Qian M. *Light Alloys: Metallurgy of the Light Metals*. 5th ed. Butterworth-Heinemann; 2017.
- 2. Verma RP, Kumar Lila M. A short review on aluminium alloys and welding in structural applications. *Mater. Today Proc.* 2021;46: 10687–10691.
- 3. Valiev RZ, Murashkin M, Sabirov I. A nanostructural design to produce high-strength Al alloys with enhanced electrical conductivity. *Scr. Mater.* 2014;76: 13–16.
- 4. Sabirov I, Murashkin MY, Valiev RZ. Nanostructured aluminium alloys produced by severe plastic deformation: New horizons in development. *Materials Science and Engineering A.* 2013;560: 1–24.
- 5. Christy JV, Mourad AHI, Sherif MM, Shivamurthy B. Review of recent trends in friction stir welding process of aluminum alloys and aluminum metal matrix composites. *Transactions of Nonferrous Metals Society of China (English Edition)*. 2021;31: 3281–3309.
- 6. Rambabu K, Gandhi P, Susmitha M, Sravanthi K. A review on different techniques to produce gradient structured material. *Mater. Today Proc.* 2022;60: 2262–2265.
- 7. Nicholas ED. Friction Processing Technologies. Welding in the World. 2003;47: 2–9.
- 8. Manjhi SK, Das A, Prasad SB. Review on joining of aluminum alloy by solid-state welding technique. *Mater. Today Proc.* 2020;26: 1255–1261.
- 9. Vysotskii I, Malopheyev S, Mironov S, Kaibyshev R. Deformation behavior of friction-stir welded Al-Mg-Mn alloy with ultrafine-grained structure. *Mater. Charact.* 2022;185: 111758.
- 10. Su JQ, Nelson TW, Sterling CJ. Friction stir processing of large-area bulk UFG aluminum alloys. *Scr. Mater.* 2005;52: 135–140.
- 11. Su JQ, Nelson TW, Sterling CJ. Microstructure evolution during FSW/FSP of high strength aluminum alloys. *Materials Science and Engineering A*. 2005;405: 277–286.
- 12. Su JQ, Nelson TW, Sterling CJ. A new route to bulk nanocrystalline materials. *Journal of Materials Research*. 2003;18: 1757–1760.
- 13. Yadav D, Bauri R. Effect of friction stir processing on microstructure and mechanical properties of aluminium. *Materials Science and Engineering A*. 2012;539: 85–92.
- 14. Mimmi A, Merzoug M, Ghazi A, Dellal N. Mechanical behavior of structures welded with friction stir lap welding process. *Materials Physics and Mechanics*. 2023;51: 151–163.
- 15. Liyakat NA, Veeman D. Improvement of mechanical and microstructural properties of AA 5052-H32 TIG weldment using friction stir processing approach. *Journal of Materials Research and Technology*. 2022;19: 332–344.
- 16. Sarmadi H, Kokabi AH, Seyed Reihani SM. Friction and wear performance of copper-graphite surface composites fabricated by friction stir processing (FSP). *Wear.* 2013;304: 1–12.
- 17. Sharma V, Gupta Y, Kumar BVM, Prakash U. Friction Stir Processing Strategies for Uniform Distribution of Reinforcement in a Surface Composite. *Materials and Manufacturing Processes*. 2016;31: 1384–1392.
- 18. Sharma A, Khan ZA, Siddiquee AN. A short review of the effect of plunge depth on friction stir welding of aluminium pipes. *Mater. Today Proc.* 2022;64: 1504-1506.
- 19. Isa MSM, Moghadasi K, Ariffin MA, Raja S, bin Muhamad MR, Yusof F, Jamaludin MF, Yusoff N, Ab Karim MS. Recent research progress in friction stir welding of aluminium and copper dissimilar joint: a review. *Journal of Materials Research and Technology*. 2021;15: 2735–2780.
- 20. Singh VP, Patel SK, Ranjan A, Kuriachen B. Recent research progress in solid state friction-stir welding of aluminium–magnesium alloys: a critical review. *Journal of Materials Research and Technology*. 2020;9: 6217–6256.
- 21. Mishra RS, De PS, Kumar N. Friction Stir Processing. *Friction Stir Welding and Processing*. Springer; 2014. p.259–96.

- 49 A.E. Medvedev, V.V. Atroshchenko, A.S. Selivanov, A.R. Bogdanov, M.V. Gorbatkov, Y.V. Logachev, V.S. Lobachev, A.R. Sadrislamov
- 22. Memon S, Paidar M, Ojo OO, Cooke K, Babaei B, Masoumnezhad M. The role of stirring time on the metallurgical and mechanical properties during modified friction stir clinching of AA6061-T6 and AA7075-T6 sheets. *Results Phys.* 2020;19: 103364.
- 23. Wakchaure K, Thakur A. Mechanical and microstructural characteristics of underwater friction stir welded AA 6061-T6 joints using a hybrid GRA-artificial neural network approach. *Materials Physics and Mechanics*. 2023;51: 119–141.
- 24. Bauri R, Yadav D, Suhas G. Effect of friction stir processing (FSP) on microstructure and properties of Al-TiC in situ composite. *Materials Science and Engineering A.* 2011;528: 4732–4739.
- 25. Kumar N, Das A. Ecofriendly energy efficient welding of aluminium matrix composites for aerospace applications: A state of art review. *Mater. Today Proc.* 2020;26: 1666–1675.

THE AUTHORS

Medvedev A.E.

e-mail: medvedevandreyrf@gmail.com

Selivanov A.S.

e-mail: selivanov@naks-rb.ru

Gorbatkov M.V.

e-mail: m.gorbatkov@krus-zapad.ru

Lobachev V.S.

e-mail: vladik1997okt@mail.ru

Atroshchenko V.V.

e-mail: 91250@mail.ru

Bogdanov A.R.

e-mail: bogdanov-alb02@mail.ru

Logachev Y.V.

e-mail: logachev.sts@mail.ru

Sadrislamov A.R.

e-mail: artem22sad@gmail.com

Study of burnishining effect on the thermal spray coatings

Submitted: November 30, 2022

Approved: May 1, 2023

Accepted: June 13, 2023

A. Agnihotri ^{1 ™}, S.B.S Kalsi ², H. Kansal ³

¹ Khalsa College of Engineering and Technology Amritsar, Punjab, India

² I. K. Gujral Punjab Technical University Kapurthala, Punjab, India

³ University Institute of Engineering and Technology, Panjab, India

⊠ er.atul84@gmail.com

Abstract. The present study is focused on the protection of alloys against hot corrosion by burnishing the thermal spray coatings. The research study aims to appraise the hot corrosion behavior of WC-Co coatings deposited on boiler steel SA213-T11 using a High-Velocity Oxy-Fuel process (HVOF) followed by a burnishing process. This study also aims to develop a suitable protective burnished-coated material system to enhance the life of metals and alloys operating under a hot corrosion environment. Therefore, the performance of the thermal spray coating followed by the burnishing process is required to be studied for the primary modes of degradation against oxidation and hot corrosion modes of material failure. Various microstructural and mechanical characterizations techniques such as X-Ray Diffractometry (XRD), Scanning Electron Microscopy (SEM), Optical Microscopy, and Microhardness tester were employed to evaluate coating properties. The performance of the thermal spray coating followed by the burnishing process is studied for the primary modes of degradation against oxidation and hot corrosion modes of material failure.

Keywords: HVOF; burnishing; WC-Co; thermal spray coatings

Citation: Agnihotri A, Kalsi SBS, Kansal H. Study of burnishining effect on the thermal spray coatings. *Materials Physics and Mechanics*. 2023;51(4): 50-65. DOI: 10.18149/MPM.5142023_5.

Introduction

Hot corrosion. Presently, alloys are put forth to enhance the utility life span of steam generators, superheaters, etc primarily in the superheated zones of recently brewed ultrasupercritical boilers. Combustion gases create an intemperate atmosphere, and hot corrosion is inevitable when metals are heated for long periods.. Deterioration of the properties of alloys while working under extreme temperature conditions and critical pressure leads to an untimely and premature degradation of metallic components with the cognate endangerment of plant shutdown resulting in the loss in economy, rise in environmental pollution and anticipating the human lives risk. The materials exercised for high-temperature purposes are subjected to hightemperature wear and hot corrosion [1]. Hot corrosion results in the deterioration and subsequent catastrophe of mechanical components and their systems operating in both manufacturing and processing industries thereby affecting their service life expectancy [2]. Hot corrosion has become a very serious problem nowadays in the Power plant equipment industry, which cannot be neglected. Generally, it is observed in hot sections of boilers, gas turbines, coal gasification plants, diesel engines, and incinerators [3]. Many Ferritic sheets of steel are reported to endure high depletion rates under fluidized-bed conditions due to erosioncorrosion [4]. Engineers and researchers have given more intension to this phenomenon when very severe corrosion was observed in the gas turbine engines of military aircraft during the Vietnam conflict [5].

Preventive measures. In many technical applications, alloy material components must withstand high temperatures, harsh chemicals, erosion, corrosion, and oxidation [6]. It is difficult to arrest corrosion entirely but it can be scaled down significantly using convenient and well-suited anticipatory protective measures. Surface modification and upgrades are needed to protect these components from various deprivations [7]. Protective coatings are the most effective, reliable, and economically possible way to avoid superheater and re-heater hot corrosion [8]. The enhancement in manufacturing technology alone is not enough to reduce the cost issue [9]. Koch et al. [10] reported that corrosion disbursements can be retained approximately by 25-30 % yearly with appropriate preventive measures by controlling hot corrosion. Efforts to reduce the maintenance costs of components employed under high-temperature conditions have raised the awareness of shielding them with protective coatings among researchers [8]. The employment of protective outings are the utmost effective, trustworthy, and economically feasible mode to curb or prevent the hot corrosion problems of superheater and re-heater boilers.

High-velocity oxy-fuel process. Thermal spray coatings augment the lifespan of components that operate at extreme temperature conditions. The application of thermal sprayed coatings is found to be a unique, practical, reliable, and economically feasible way to control or avoid hot corrosion [11–13]. The high-velocity oxy-fuel (HVOF) process of coatings is regarded as the "most popular thermal spraying technology" [9]. HVOF spraying is a fastgrowing method for treating high-temperature corrosion, challenging the costly vacuum plasma spraying technique (VPS). The HVOF method of spraying has been adopted by several thermal spray industries because of its "cost-effectiveness", flexibility, and exceptional coating quality. The coatings generated by this process exhibit higher bond strength and hardness value along with low porosity as compared to other thermal spraying processes such as plasma spraying, flame spraying, and arc spraying [14]. The HVOF thermal spray method of coatings is widely employed in several applications including gas turbines, paper and pulp, petroleum, chemical, automotive industries, and energy-conversion [1,9]. These are also applied in manufacturing industries, boilers, superheaters, reheaters, pipe systems, and valve bodies [15,16]. HVOF thermal spraying deposits a coating with smaller porosity, better bond strength, greater hardness, and less decarburization [17]. HVOF is used in aviation, automobile, marine, and petrochemical process components. Sidhu et al. [9] reported that HVOF coating had lower roughness, porosity, and oxide content than conventional thermal coating methods.

Burnishing process on the applied coating. The protection provided by the coating against hot corrosion depends upon many factors. But one very important factor is the porosity of thermal sprayed coating because corrosion species travel through these pores to the substrate. Still, even with the advancement in thermal spray technologies, it is impossible to attain poresfree thermal spray coatings. Some voids are always formed at the splat boundaries during the thermal spray coating process and corrosion species penetrate through the voids [18]. Various researchers had employed the post-treatment process to deposit coatings to reduce their porosity value. A mechanical process known as 'burnishing' is used as a super finishing treatment for metallic components. In this process, a super-finished and hardened material in the form of a roller or ball is allowed to move over the surface of the component with the application of some pressure. This results in the elastic-plastic deformation of the component surface. The rolled surface gets finished and its porosity reduces to a greater extent. Luca et al. [19] opined that in addition to constructing a good surface finish, the burnishing process also improved the other properties of the material such as hardness, corrosion resistance, and fatigue life. The Burnishing process is used to achieve a high surface finish on metals resulting in a smooth hardened surface with some improved mechanical properties [20].

Burnishing as a novel approach can be employed in this research study to reduce the porosity of thermal spray coating. The research study aims to determine the effect of burnishing on thermal spray coatings against high-temperature aggressive environmental applications of boilers, gas turbines, waste-to-energy plants, etc. This study also aims to develop a suitable protective burnished-coated material system to enhance the life of metals and alloys operating under a hot corrosion environment.

Materials and Methods

Substrate Metal Alloys. The substrate base metal alloys selected for the present study are "ASTM-SA213-T-11" (T11). This alloy is utilized as a boiler tube material in the "Power Plants situated in North India". The substrate alloy was provided by "Cheema Boilers Private Limited" (India) in the rolled sheet form for research purposes to examine their protective behavior against high temperature corrosive environmental conditions. Nominal and actual chemical compositions of these alloys along with their applications are provided in Table 1.

Table 1. Nominal and actual composition along with an industrial application of T11 alloy

A 11 ov	Commonition	Chemical composition, wt. %							
Alloy	Composition	C	Mn	Si	S	P	Cr	Mo	Fe
SA213-	Nominal	0.15	0.3-0.6	0.5-1	0.03	0.03	1-1.5	0.44-0.65	Bal.
T11	Actual	0.1369	0.4292	0.3038	0.0065	0.0124	0.9114	0.5125	Bal.

Feedstock Powders for Coating. The commercially available WC-Co feedstock material in a powdered form have been utilized as the coating powder to be deposited on base metal substrate alloys for appraising their hot-corrosion performance at high-temperature conditions. The chemical composition and size of particles of these feedstock materials are given in Table 2.

Table 2. Composition of feedstock powders

Feedstock alloy	Chemical composition, wt. %	Shape	Nominal composition	Weight percentage, %
			Tungsten carbide	Base
WC-Co powder	80WC- 20Co	Spherical	Total Carbon	5.3-5.4
			Cobalt	11-13

Table 3. Spray parameters employed for HVOF coating

Parameters	Gun DJH 2600 & Nozzle DJH 2603		
Oxygen flow rate, SLPM*	14-16		
Fuel (LPG) flow rate, SLPM	26-31		
Air flow rate, SLPM	33		
Spraying distance, inch	9		
Fuel pressure, kg/cm ²	8-10		
Oxygen pressure, kg/cm ²	12		
Air pressure, kg/cm ²	9		
Feed rate, gm/min	50-60		

^{*} SLPM =Standard Liters Per Minute

Development of Coatings. The boiler steel alloys were sectioned and specimens were cut to the dimensions of $20 \times 15 \times 5$ mm The dimensioned specimens were abraded down with silicon carbide papers to 180 grit. Then, these specimens underwent sandblasting by alumina (Grit 45) preceding the application of coatings. This task is performed to obtain healthier adhesion between coating and substrate. The utmost attention was considered to evade any sort of structural changes in all physically formulated. The coatings were thermally sprayed at Spraymet Surface Technologies Private Limited, Bengaluru (India) utilizing High-velocity

oxy-fuel (HVOF) thermal spray systems. The spraying parameters engaged while thermal spraying are given in Table 3.

Post-treatment of coating by burnishing process. In this study, the coated specimens underwent a burnishing process by high strength roller as the burnished tool was affixed to the Shaper machine. Burnishing is done with a force of 60 N at a constant speed of 200 rpm for 50–60 passes at a feed rate of 0.05 mm/rev. Figure 1 depicts the specimens' burnishing.

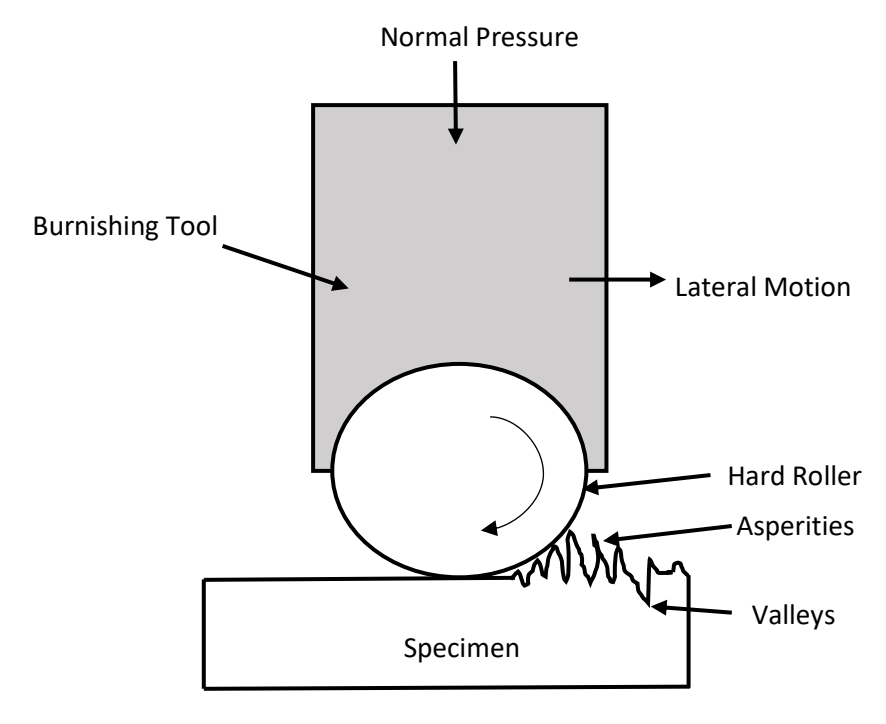


Fig. 1. Burnishing technique

Experimentation. As-sprayed specimens and burnished-coated specimens were cold mounted in the cold-setting epoxy compound along their surface. Then the specimens were polished with 220, 400, and 600 grate silicon carbide emery papers having 1/0, 2/0, 3/0 and 4/0 grades and subsequently polished on the wheel polishing machine with 1 µm alumina powder suspension. As-sprayed and burnished-coated specimens were then cross-sectioned through a low-speed diamond cutter (Buehler's Precision Diamond Saw, Model: ISOMET 1000, Make: USA) for their cross-sectional analysis. The cross-sectioned specimens were cold-mounted using an epoxy cold-setting compound along their cross-section. Subsequently, these specimens were polished according to a similar procedure as explicated for surface preparation. These specimens were then cross-sectioned through a low-speed diamond cutter (Buehler's Precision Diamond Saw, Model: ISOMET 1000, Make: USA) for their cross-sectional analysis. The cross-sectioned specimens were cold-mounted using an epoxy cold-setting compound along their cross-section. Subsequently, these specimens were polished according to a similar procedure as explicated for surface preparation. The formulated specimens were polished to expose their coating microstructure and their porosity is analyzed by an Image Analyser System using PMP3 Inverted Metallurgical Microscope (Make: Japan) incorporated with Material Plus software based on ASTM standards. The surface morphologies and cross-sectional microstructures of these specimens were obtained by an Inverted Optical Microscope (Model: Axiovert-200 MAT, Make: Carl Zeiss, Germany) conjugated with the Imaging software (Zeiss Axio Vision, Germany). The microhardness values of all specimens across their cross-section were assessed by a Microhardness Tester (Miniload 2, Make: Germany) equipped with Vickers Pyramidal Diamond Indenter.

Results

Scanning electron microscopy (SEM) and X-ray diffractometry (XRD) analysis. SEM morphology of WC-Co feedstock powders shows its spherical morphology as shown in Fig. 2. The diffraction patterns for the WC-Co powder is shown in Fig. 3 on the moderated scale. In the W-Co-C system, WC and W_2C double carbides, are the most stable phases. The principal phase comprising Co-based fcc for WC-Co powder specifies the formation of a solid solution. Reduction in the amount of carbon in WC-Co alloys causes the WC carbide to convert into W_2C carbides.

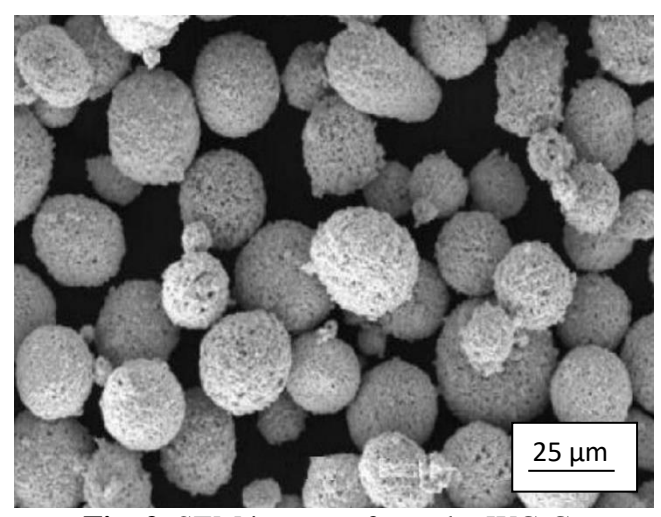


Fig. 2. SEM images of powder WC-Co

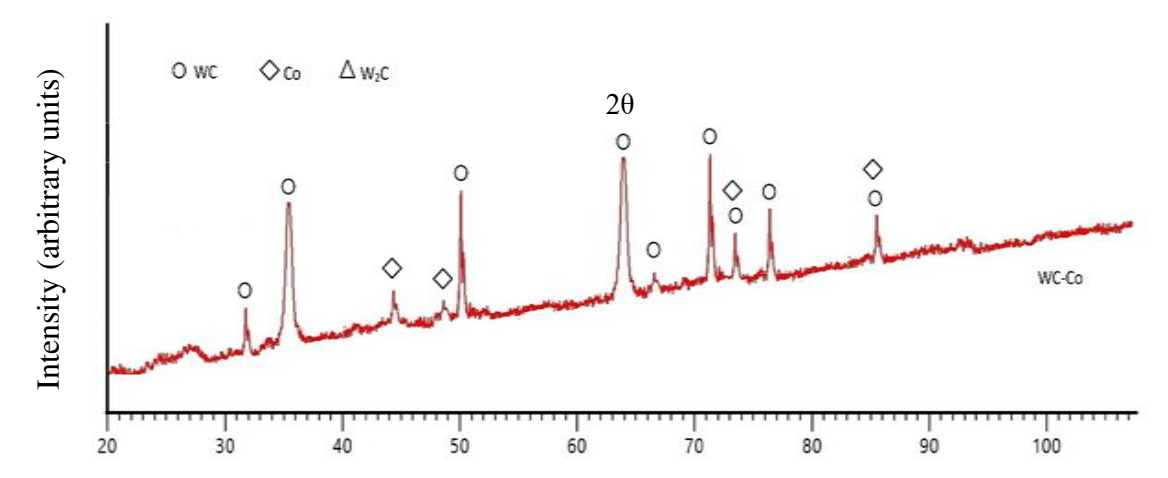


Fig. 3. XRD patterns for the HVOF feedstock WC-Co coating powder

Substrate alloys. The optical microstructures of substrate materials under the present research study are shown in Fig. 4. The microstructures of selected substrates have been characterized by assessing them with comparable international standard superalloys as presented in ASM and Metals Handbooks. These substrates steel are generally signified as 'ferritic' low alloy steels which exhibit a bainite microstructure [21]. This microstructure ensures the finest creep resistance, while its extensive period usage and assessing strength is governed by fine precipitates present inside that microstructure. Chromium presence in these substrates not only enhances the property of the resistance against oxidation but also retards the transformation on cooling from austenite i.e. martensite becomes the predominant microstructure. While tempering, Mo₂C which is the most stable carbide gets formed having low nucleation energy. Mo₂C configuration has needle-shaped fine particles which develop

gradually at normal servicing temperature as a result of a great coherency among the lattice configurations of carbide particles and enclosing 'ferrite' matrix [22].

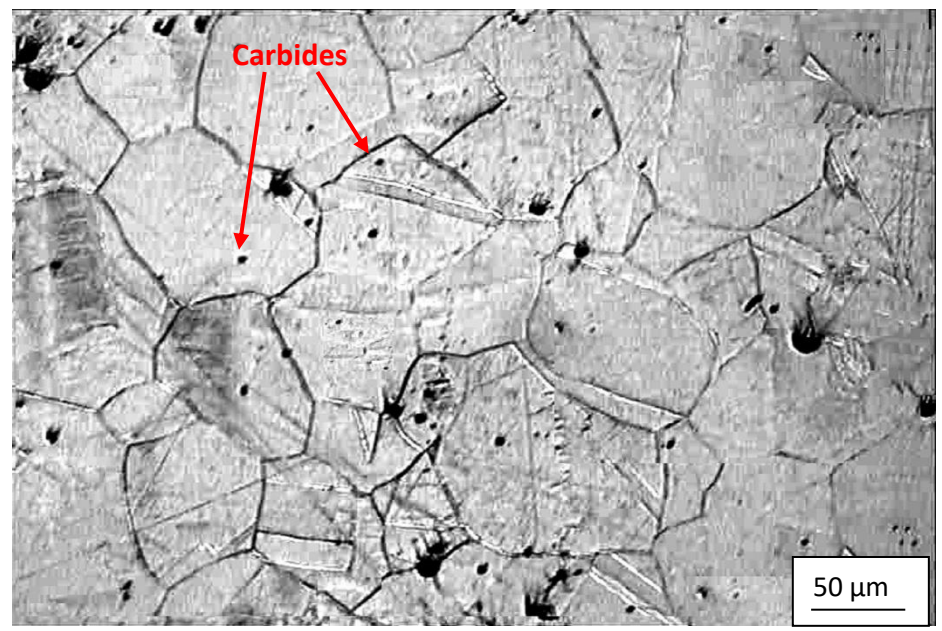


Fig 4. Optical micrographs of SA213-T11 substrate

Coated alloys. Visual Examinations. Optical micrographs of the as-sprayed specimens are shown in Fig. 5. It can be noticed that as-sprayed WC-Co coatings exhibit a shining silver-grey color. After burnishing, the same specimens indicate a dull deep grey appearance. Visual observations also show that as-sprayed coating has smooth surfaces, whereas after burnishing the coated specimen has a rough surface. Further, no surface cracks were found on any coatings surface. A surface recorder of resolution 0.008 μ m "SE-1200, Kosaka Laboratory Ltd., Tokyo, Japan" were used to measure surface roughness values which came in the range of 4-6 μ m.

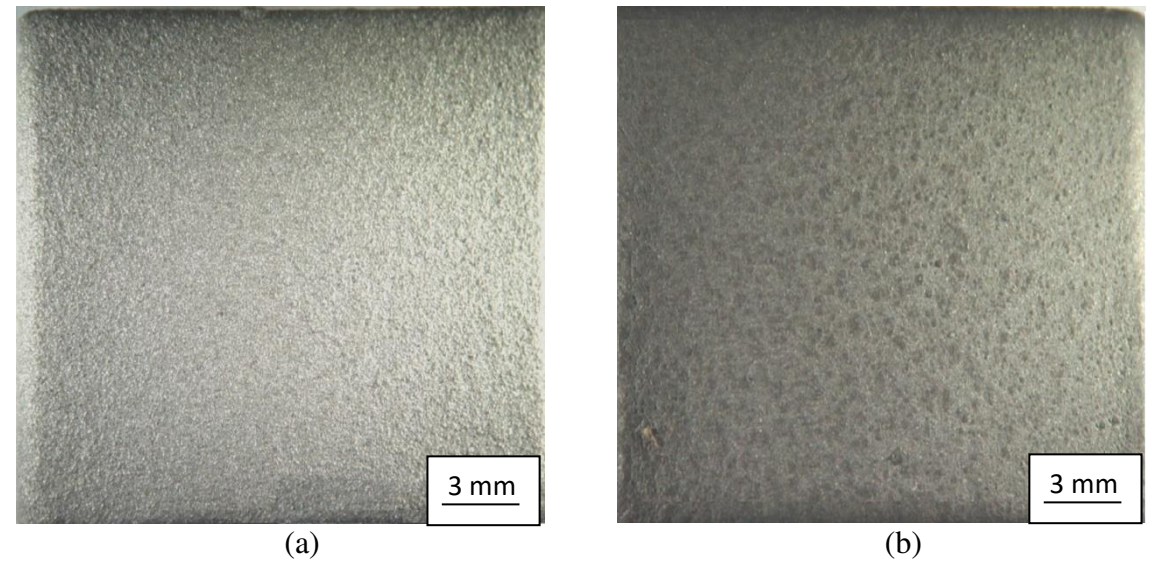


Fig. 5. Optical micrographs of as-sprayed coatings on substrate T11 with (a) WC-Co coating; (b) burnished WC-Co coating

Measurements of Coating Thicknesses. The coating thickness was determined from Back scattered electron images (BSEI) obtained along the cross-section of coated specimens. The average thickness of the burnished coated specimen is 280 μm and WC-Co coated specimen is 290 μm off. The BSE image for burnished WC-Co-coated specimen for representation is shown in Fig. 6.

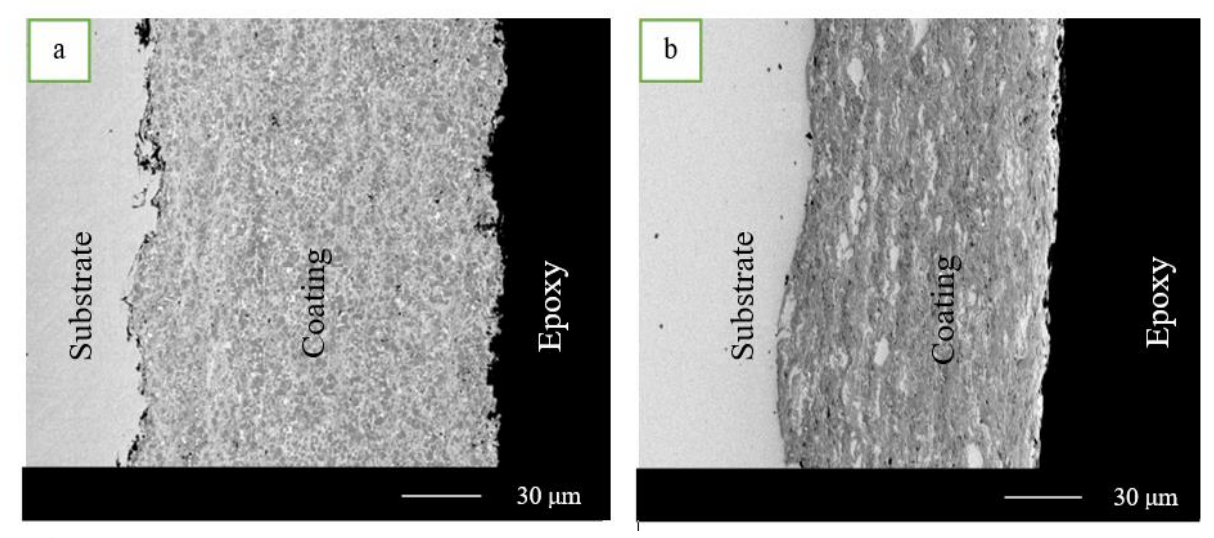


Fig. 6. BSEI micrographs showing cross-section morphologies of different HVOF coatings on: (a) burnished WC-Co coating on T11; (b) WC-Co coating on T11

Porosity Analysis. The area of pores in a view field was analyzed with an analyzing software in which the grey area of pores transform into a red background while the rest microstructure persists in its primary color. The area of one feature is statistically interrelated to the overall area of the image, as the software reckons the number of pixels of one color type (red) and establishes that as a proportion of the over-all number of pixels in an image (entire area). Five readings of porosity values have been assessed for each specimen. The average porosity of burnished coatings and as-sprayed coatings of specimens are observed to be less than 1.2 and 2 % respectively.

Microhardness measurements. Microhardness profiles along the cross-section of coatings as a function of distance from the interface of coating-substrate are shown in Fig. 7. The hardness value of substrate T11 is observed in the range of 310 to 400 HV. The hardness of the burnished WC-Co coated specimen is 919-999 HV, while the hardness of the WC-Co coated specimen is on the order of 630 HV.

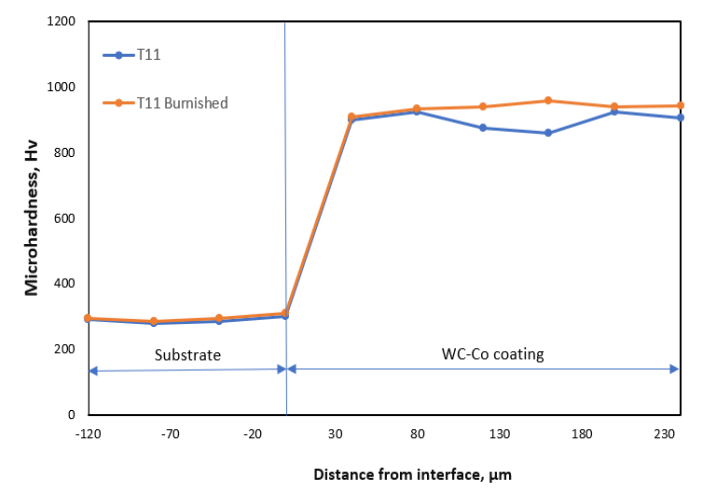


Fig. 7. Microhardness profiles for T11 substrate with WC-Co coating

Metallographic studies of WC-Co the coatings. Surface microstructure of coating.

The optical micrographs of WC-Co coating and burnished coatings on T11 substrates selected for the present study are shown in Fig. 8. The irregularly shaped flat splats appear to be uniformly dispersed in the coating. The white globules distributed throughout the structure appear as melted regions. Some unmelted particles and limited voids are also observable in the coating structure. The un-melted particles in the coating structures are identified by their surface morphology including shape and size.

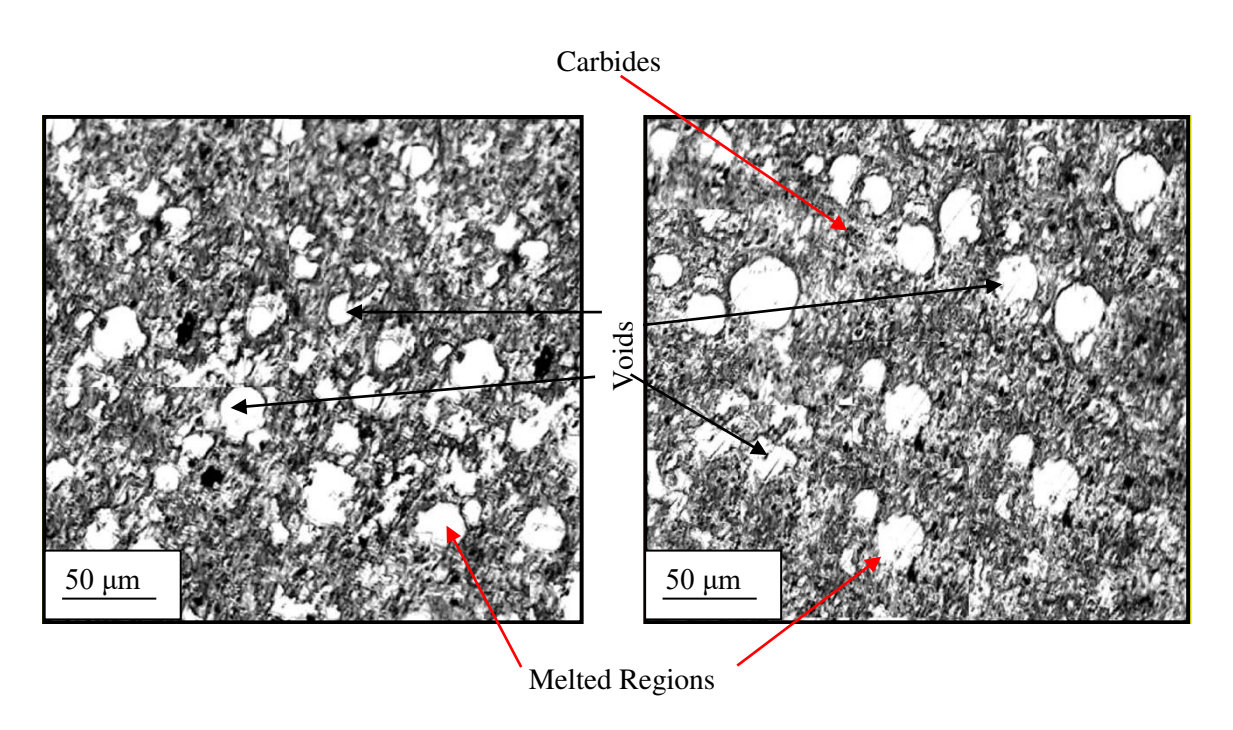


Fig. 8. Optical micrographs displaying surface morphology of WC-Co coating on substrate: (a) T11 and (b) T11 burnished

Cross-Section Microstructures. Optical micrographs displaying WC-Co coatings having cross-sectional microstructure are shown in Fig. 9. WC-Co coating has a relatively fine grain microstructure including white globules disbursed all over the structure.

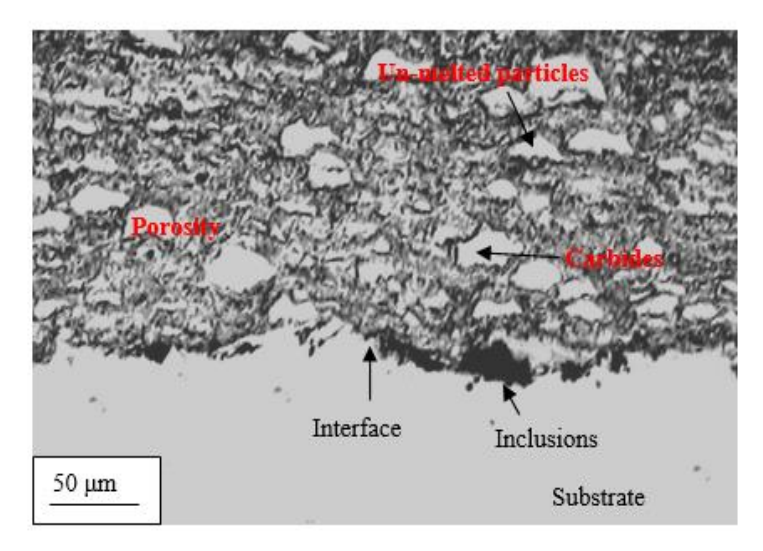


Fig. 9. Optical micrographs displaying cross-sectional microstructures of WC-Co coating

X-ray diffractometer study. XRD pattern on a reduced scale for the as-sprayed WC-Co coating is shown in Fig. 10. The presence of WC-based fcc as the principal phase for the selected as-sprayed coatings signifies the establishment of a solid solution matrix.

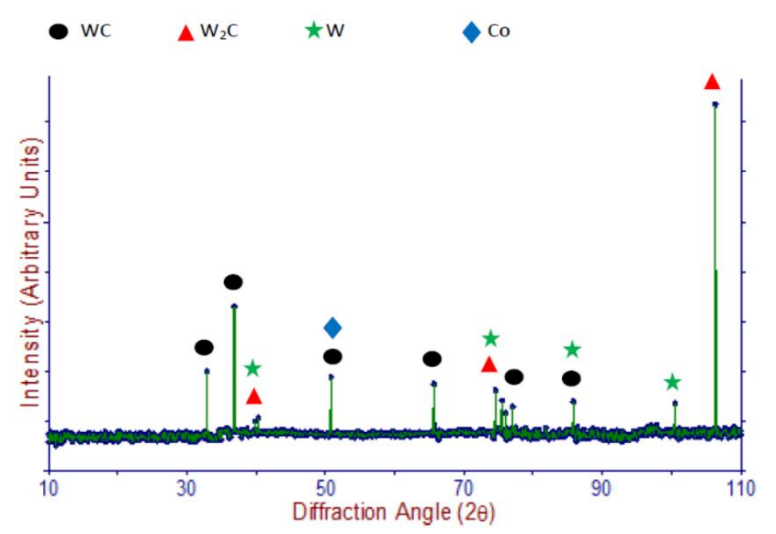


Fig. 10. Diffraction patterns for "WC-Co coatings" on T11

SEM analysis. SEM morphologies for WC-Co and burnished WC-Co coatings deposited over the T11 substrates are shown in Fig. 11(a) and 11(b) respectively. As evident from the micrographic features, the coatings are homogeneous and substantial as well as free from cracks.

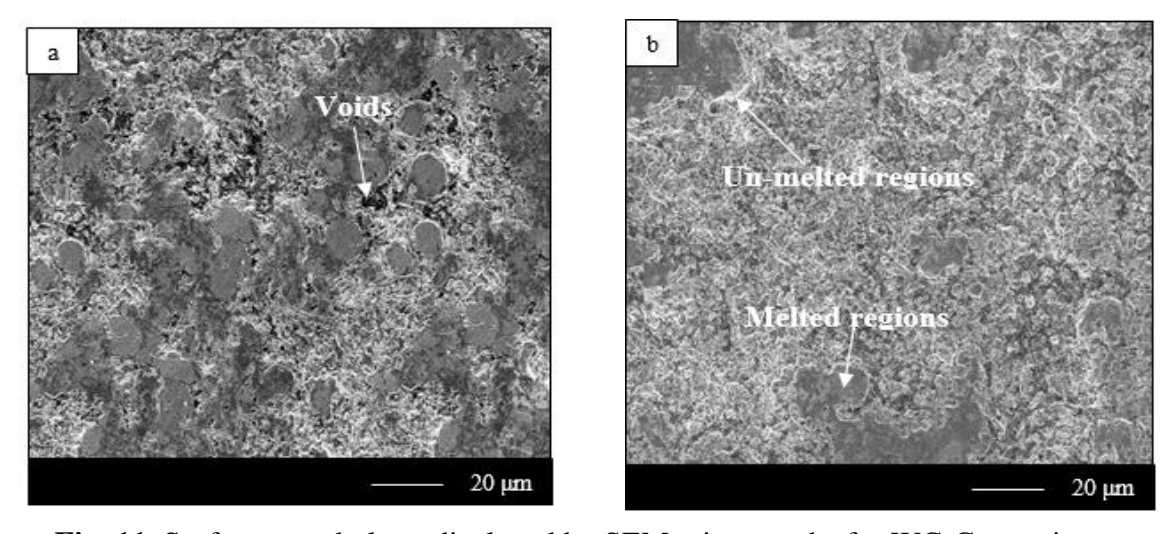


Fig. 11. Surface morphology displayed by SEM micrographs for WC-Co coating on substrates: (a) T11; (b) T11 burnished

A minimal number of unmelted particles are spotted in the structure of the coating. These unmelted particles may adhere to the substrate surface due to high impact while HVOF spraying. The coatings exhibit the presence of certain oxide inclusions and very limited open pores. Further, some localized areas which have greater densities of open pores are also observed in some micrographs. However, the burnishing technique covers the open pores to a larger extent. Surface morphologies disclosed the crystalline structures of all coatings deposited on the substrates. The burnished coated specimen has small size splats, whereas medium-sized splats are noticed in the case of the applied coating.

Energy-dispersive X-ray analysis. Energy-dispersive X-ray (EDAX) analysis of the WC-Co coated specimen was done at selected spots, as shown in SEM micrographs shown in Fig. 12. The melted and partly melted regions as well as black areas are clearly distinguished in WC-Co coating. Partially molten state regions contain 87 % tungsten carbide and 11 % cobalt, which is nearby to the composition of WC-Co coating powder. The black regions visible in this coating seem to WC dominant.

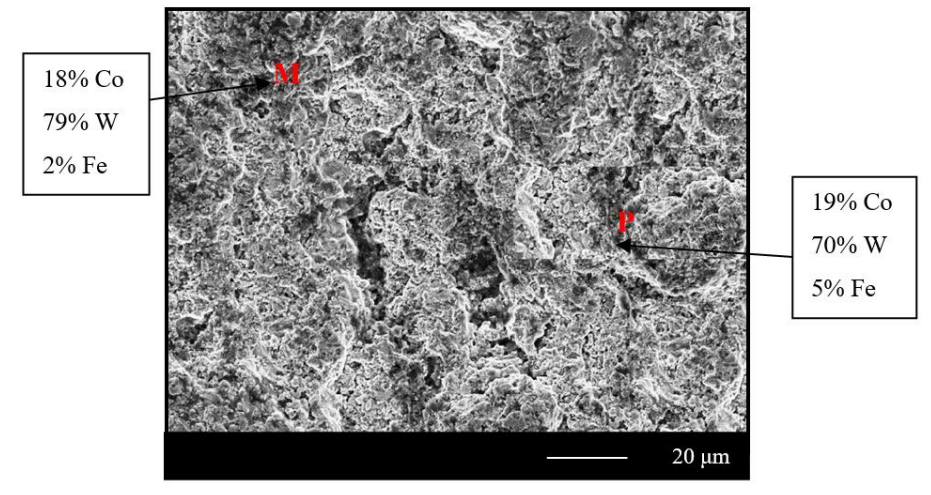


Fig. 12. Elemental composition (wt. %) at selected points analyzed by EDAX for WC-Co coating indicating elemental composition (wt. %) at selected points

Cross-section analysis. Back scattered electron (BSE) images shown in Fig. 13 were taken across the cross-section of coated as well as a burnished-coated specimen for their cross-sectional investigation. In WC-Co coated specimen, the weight percentage of iron shows a slight drop i.e. from 43.9 to 41.49 % while the chromium weight percentage increases from 32 to 35.6 % which is slightly greater than the nominal composition of the substrate. BSE Images and EDAX study at point 2 and point 4 indicate that the distinguish matrix phase has a similar composition as the coating powder. At location 3, the white phase of chromium-rich splat is observed.

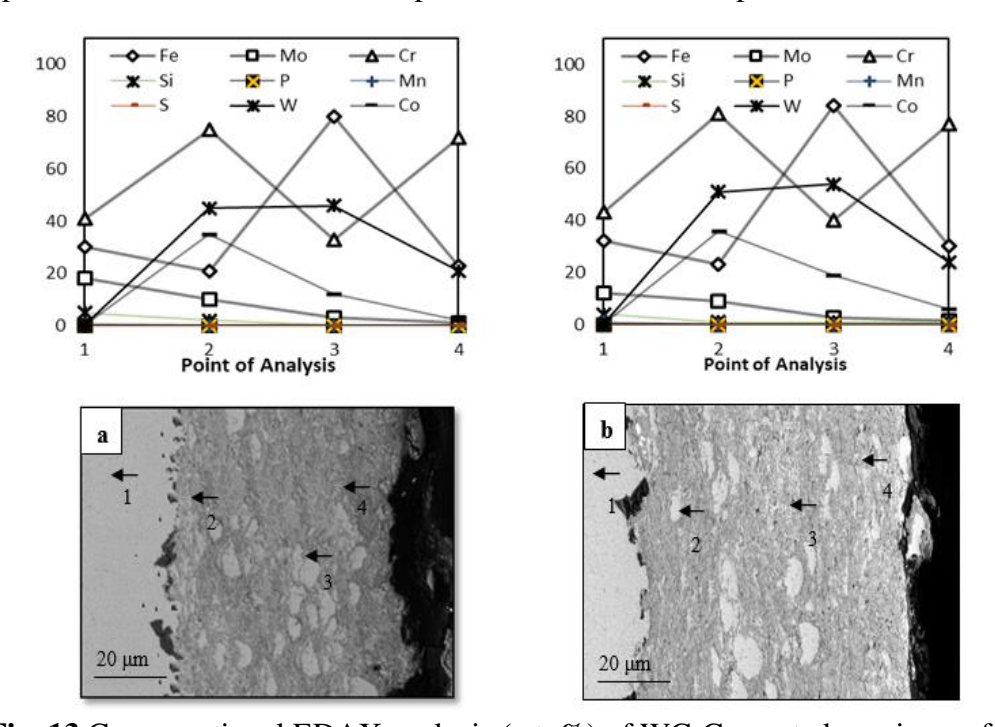


Fig. 13 Cross-sectional EDAX analysis (wt. %) of WC-Co coated specimens for: (a) T11 and (b) burnished-coated T11

Discussion

Both the specimens i.e. under analysis have a solid suspension matrix. The consistent presence of carbides was noticed in all the selected specimens. The strength of these chromium-based specimens depends upon the mechanism of precipitation hardening, in addition to the solid solution hardening. The burnishing technique on the specimen also increases the surface hardness of the specimen comprehensively. Different types of carbides formed due to precipitation with the assistance of various elements present in the superalloy. WC has the greatest possibility of formation in all specimens since it is primarily promoted by the tungsten [23]. Further, W₂C carbide tends to precipitate at the grain boundaries [24]. Some large globules observed in Fig. 4 signify the presence of the WC phase. Thicker coatings show better resistance against corrosion [25]. However, the self-disintegration of thicker coatings limits the thickness of the coatings [26]. Therefore, the deposition of 280-298 µm thick HVOF coating on substrates was selected in the present research study to certify the integrity of the coating [27]. The thickness of coating evaluated along the cross-section of specimens has been attained to the required extent of 280-298 µm as mentioned earlier in the study. HVOF coatings have a comparatively smooth as-sprayed surface finishing with surface roughness ranging between 4-6, as observed in Fig. 5. In HVOF coatings, high-impact energy is imposed upon the impinging particles. This cause a better mechanical bonding of sprayed particles for developing a homogenous structure thereby requiring less finishing compared to the other thermal spraying techniques.

Porosity is regarded as the most significant property of the coatings tested under high-temperature applications of hot-corrosion environments. Materials with larger porosity have lower mechanical strength because the connection between the particles and the matrix weakens as porosity rises. The corrosive species can penetrate through the porosities (preferred corrosion paths) to approach the surface of the substrate thereby resulting in a prompt attack of corrosion. Dense coatings have a very low value of porosity and therefore, impart better resistance against corrosion [28]. The as-sprayed HVOF coatings have lesser porosity because of the greater momentum of feedstock material powder particles. The uniformly flat disc powder particles tremendously adhere to the substrate surface producing a very dense coating structure. The appraised porosity values of the applied coatings are similar to the results of [29–34].

Hardness has been regarded as the most common mechanical property of the coating. The erosion-corrosion degradation conduct of coatings is generally affected by their hardness value [35]. Noteworthy observations have been made after examining the microhardness profiles in detail. As noticed in Fig. 7, the substrate region adjacent to the coating-substrate boundary indicated a higher hardness value than their core region. The augmented hardness value adjoining the coating-substrate interface is attributed to the "strain-hardening effect" due to the execution of abrasive blasting over the substrate surface before the deposition of [36]. The higher hardness value of coating is also contributed by the "high impact speed" of coating droplets while HVOF spraying results in superior density as well as better cohesive strength of distinct splats [34–37].

The microhardness of the applied coatings in a present research study is ascertained to be much better than the substrate alloy. The hardness value further gets improved after burnishing the coated specimens [38]. Certain variations in the hardness value of each coating along their cross-section of substrates have been also observed. These differences in the hardness values are due to the presence of permeability, melted, un-melted, and partly melted particles as well as oxide inclusions as shown in the cross-sectional micrographs of coatings in Fig. 9. The microhardness values of HVOF coatings assessed in the present research study are compatible with the outcomes of [39–45]. The insignificant diffusion of substrate elements to the coating also contributes towards the different microhardness values as specified by EDAX analysis.

The coatings micrographs on substrates along their cross-section are shown in Figs. 6 and 9 respectively. Inference can be drawn from the observations that the applied coatings possess uniform dense structures. The coatings also exhibit the layered morphologies of distinctive splats as a result of re-solidification and accumulation of melted or semi-melted precipitations. The long axis of an "impacted splat is orientated parallel to the surface" of the substrate. As observed from the micrographs, the un-melted particles in microstructures are very less in number since the major proportion of the feedstock powders got melted completely or partly before their impact with the substrate. The microstructures have not shown any significant difference between individually applied coating on selected substrate. Microstructures examined in the current investigation are almost comparable to the results of HVOF-applied coatings [46–48].

SEM/EDAX analysis presented in Fig. 12 specifies that HVOF coatings employed under the research study meet the requisite composition. In Fig. 12, the region marked "M" which appears to be featureless, is established by the collision of completely melted feedstock material droplets. Consequently, these droplets got hardened at a high rate of cooling i.e. 10^7 K/s [49]. The microcrystalline structure developed due to a high cooling rate as also reported by [50]. These micro-crystalline grains undergo solidification precisely from the molten state by heterogeneous nucleation on already prevailing oxide granules [51].

As shown in EDAX analysis in Fig. 13, point 4 exhibits the presence of little content of oxygen leading to the oxide phase which specifies that some inadequate oxidation has happened on the surface of the coating or onboard particles before the buildup of the subsequent layer. Similar outcomes regarding oxide growths in HVOF-sprayed coatings have been informed by [52,53]. Certain inclusions of oxides are also spotted in "SEM/EDAX analysis" (Fig. 11) where some inclusions were present consistently among all coatings at the interface of substrate and coating. EDAX analysis in Fig. 13, has indicated the existence of chromium oxide inclusions due to the presence of chromium and oxygen at these points [54].

EDAX results for the HVOF sprayed coatings under research study (as shown in Fig. 12) indicate that there exists an "inter-diffusion of various elements between the substrate and coatings" as evident from Fig. 13. This inter-diffusion mechanism can affect the hot corrosion behavior of any particular coating on different substrates. Chromium and tungsten are observed as the most vulnerable elements to the phenomenon of diffusion. Mo, Fe, Co, and Mn are some of the elements which are susceptible to minor diffusion. The diffusion of elements between the coating and substrate can influence the performance of coating under high-temperature applications [55–56].

Conclusions

The burnishing force increases the wear resistance of the selected specimens. The continuous rolling of the burnishing tool over the surface of specimens leads to their plastic deformation. This results in the work-hardening effect on the surface and it becomes harder than the remaining surface of the specimen. The surface hardness of the material is directly proportionate to the applied strength i.e. an increment in the burnishing force surges the surface hardness of the material. The increment in hardness of the material is attributed to the increase of penetration depth and flow of metal which enhances the extent of deformation of voids present in the metal. The hardness of the disturbed layer of the surface improves significantly when the burnishing process is continuously applied for a longer period on the metal surface. Hence, the burnishing process decreases surface roughness by improving the smoothness of the surface.

References

- 1. Hao E, Wang Y, Zhao X, Gao M, Chen J, An Y, Yan F. Influence of molten salt with or without V2O5 on hot corrosion and high-temperature tribological performance of HVOF-sprayed Ni-based self-lubricating composite coating. *Surface and Coatings Technology*. 2021;417: 127210.
- 2. Yu Z, Chen M, Wang J, Li F, Zhu S, Wang F. Enamel coating for protection of the 316 stainless steel against tribo-corrosion in molten zinc alloy at 460° C. *Journal of Materials Science & Technology*. 2021;65: 126–136.
- 3. Abu-Warda N, López AJ, López MD, Utrilla MV. High temperature corrosion and wear behavior of HVOF-sprayed coating of Al2O3-NiAl on AISI 304 stainless steel. *Surface and Coatings Technology*. 2019;359: 35–46.
- 4. Faes W, Lecompte S, Ahmed ZY, Van Bael J, Salenbien R, Verbeken K, De Paepe M. Corrosion and corrosion prevention in heat exchangers. *Corrosion Reviews*. 2019;37(2): 131–155.
- 5. Rapp RA. Hot corrosion of materials. *Pure and Applied Chemistry*. 1990;62(1): 113–122.
- 6. Binal G. Isothermal oxidation and hot corrosion behavior of HVOF sprayed 80Ni-20Cr coatings at 750° C. *Surface and Coatings Technology*. 2023;454: 129141.
- 7. Singh S, Goyal K, Bhatia R. A review on protection of boiler tube steels with thermal spray coatings from hot corrosion. *Materials Today: Proceedings*. 2022;56: 379–383.
- 8. Wang Q, Zhou D, Yu M, Shi L, Li X, Sun Q. Oxidation and hot corrosion behaviors of Modoped NiMoAlY alloys at 750° C. *Corrosion Science*. 2022;201: 110262.
- 9. Sidhu TS, Agrawal RD, Prakash S. Hot corrosion of some superalloys and role of high-velocity oxy-fuel spray coatings—a review. *Surface and Coatings Technology*. 2005;198(1–3): 441–446.
- 10. Koch GH, Brongers MP, Thompson NG, Virmani YP, Payer JH. *Corrosion cost and preventive strategies in the United States*. United States: Federal Highway Administration; 2002.
- 11. Zhou W, Zhou K, Li Y, Deng C, Zeng K. High temperature wear performance of HVOF-sprayed Cr3C2-WC-NiCoCrMo and Cr3C2-NiCr hardmetal coatings. *Applied Surface Science*. 2017;416: 33–44.
- 12. Dzhurinskiy D, Babu A, Pathak P, Elkin A, Dautov S, Shornikov P. Microstructure and wear properties of atmospheric plasma-sprayed Cr3C2-NiCr composite coatings. *Surface and Coatings Technology*. 2021;428: 127904.
- 13. Singh V, Singh I, Bansal A, Omer A, Singla AK, Goyal DK. Cavitation erosion behavior of high velocity oxy fuel (HVOF) sprayed (VC+ CuNi-Cr) based novel coatings on SS316 steel. *Surface and Coatings Technology*. 2022;432: 128052.
- 14. Parker DW, Kutner GL. HVOF-spray technology: poised for growth. *Advanced Materials & Processes*. 1991;139(4): 68–74.
- 15. Wu Q, Zheng H, Zhang Z, Hu P, Fan C, Zhong N, Liu Y. High-temperature wear and cyclic oxidation behavior of (Ti, W) C reinforced stainless steel coating deposited by PTA on a plain carbon steel. *Surface and Coatings Technology*. 2021;425: 127736.
- 16. Luo K, Li S, Xu G, Hosseini SR, Lu J. Hot corrosion behaviors of directed energy deposited Inconel 718/Haynes 25 functionally graded material at 700° C and 900° C. *Corrosion Science*. 2022;197: 110040.
- 17. Kaushal G, Singh H, Prakash S. High-temperature erosion-corrosion performance of high-velocity oxy-fuel sprayed Ni-20 Cr coating in actual boiler environment. *Metallurgical and Materials Transactions A*. 2011;42: 1836–1846.
- 18. Kumar S, Kumar R, Singh S, Singh H, Handa A. The role of thermal spray coating to combat hot corrosion of boiler tubes: a study. *Journal of Xidian University*. 2020;14(5): 229–239.
- 19. Luca L, Neagu-Ventzel S, Marinescu I. Burnishing of Hardened Steel Components-An Alternative Method of Finishing. *Proceedings of Annual Meeting for American Society for Precision Engineering*. 2001;27: 110–114.
- 20. Vinitha M, Rao AN, Mallik MK. Optimization of speed parameters in burnishing of samples fabricated by fused deposition modeling. *Int. J. Mech. Ind. Eng.* 2012;2(2): 10–12.

- 21. Shibli A. Boiler steels, damage mechanisms, inspection and life assessment. In: *Power plant life management and performance improvement*. Woodhead Publishing; 2011. p.272–303.
- 22. Yamasaki S, Bhadeshia HK. Modelling and characterisation of Mo2C precipitation and cementite dissolution during tempering of Fe–C–Mo martensitic steel. *Materials Science and Technology*. 2003;19(6): 723–731.
- 23. Davis JR. (Ed.) ASM specialty handbook: tool materials. ASM International; 1995.
- 24. Alhaji A, Shamanian M, Salehi M, Nahvi SM, Erfanmanesh M. Electroless nickel–phosphorus plating on WC–Co powders using HVOF feedstock. *Surface Engineering*. 2019;35(2): 120–127.
- 25. Heath GR, Heimgartner P, Irons G, Miller RD, Gustafsson S. An assessment of thermal spray coating technologies for high temperature corrosion protection. *Materials Science Forum*. 1997:251: 809–816.
- 26. Sadeghi E, Markocsan N, Joshi S. Advances in corrosion-resistant thermal spray coatings for renewable energy power plants. Part I: Effect of composition and microstructure. *Journal of Thermal Spray Technology*. 2019;28: 1749–1788.
- 27. Singh G, Bala N, Chawla V. Microstructural analysis and hot corrosion behavior of HVOF-sprayed Ni-22Cr-10Al-1Y and Ni-22Cr-10Al-1Y-SiC (N) coatings on ASTM-SA213-T22 steel. *International Journal of Minerals, Metallurgy and Materials.* 2020;27: 401–416.
- 28. Zhao S, Xie X, Smith GD, Patel SJ. The corrosion of INCONEL alloy 740 in simulated environments for pulverized coal-fired boiler. *Materials Chemistry and Physics*. 2005;90(2–3): 275–281.
- 29. Gil L, Staia MH. Microstructure and properties of HVOF thermal sprayed NiWCrBSi coatings. *Surface and Coatings Technology*. 1999;120: 423–429.
- 30. Guilemany JM, Fernandez J, Delgado J, Benedetti AV, Climent F. Effects of thickness coating on the electrochemical behaviour of thermal spray Cr3C2–NiCr coatings. *Surface and Coatings Technology*. 2002;153(2–3): 107–113.
- 31. Faes W, Lecompte S, Ahmed ZY, Van Bael J, Salenbien R, Verbeken K, De Paepe M. Corrosion and corrosion prevention in heat exchangers. *Corrosion Reviews*. 2019;37(2):131–155.
- 32. Palomino LM, Suegama PH, Aoki IV, Montemor MF, De Melo HG. Electrochemical study of modified non-functional bis-silane layers on Al alloy 2024-T3. *Corrosion Science*. 2008;50(5): 1258–1266.
- 33. Guilemany JM, Dosta S, Miguel JR. The enhancement of the properties of WC-Co HVOF coatings through the use of nanostructured and microstructured feedstock powders. *Surface and Coatings Technology*. 2006;201(3–4): 1180–1190.
- 34. Sidhu TS, Prakash S, Agrawal RD. Characterisation of NiCr wire coatings on Ni-and Fe-based superalloys by the HVOF process. *Surface and Coatings Technology*. 2006;200(18–19): 5542–5549.
- 35. Meghwal A, Matthews S, Howse H, Berndt CC, Ang AS. Steam and air oxidation behaviour of thermal spray chromium carbide-based composite coatings. *International Journal of Refractory Metals and Hard Materials*. 2023;111: 106088.
- 36. Khan MA, Sundarrajan S, Natarajan S, Parameswaran P, Mohandas E. Oxidation and hot corrosion behavior of nickel-based superalloy for gas turbine applications. *Materials and Manufacturing Processes*. 2014;29(7): 832–839.
- 37. Sidhu HS, Sidhu BS, Prakash S. Mechanical and microstructural properties of HVOF sprayed WC–Co and Cr3C2–NiCr coatings on the boiler tube steels using LPG as the fuel gas. *Journal of Materials Processing Technology*. 2006;171(1): 77–82.
- 38. Singh V, Singla AK, Bansal A. Influence of TiC Content on Slurry Erosion Behaviour of HVOF Sprayed Titanium Carbide and Cupronickel-Chromium Based Coatings. *Journal of Thermal Spray Technology*. 2023;6: 1–9.
- 39. Uusitalo MA, Vuoristo PM, Mäntylä TA. High temperature corrosion of coatings and boiler steels below chlorine-containing salt deposits. *Corrosion Science*. 2004;46(6): 1311–1331.
- 40. Agnihotr A, Kalsi SS, Kansal HK, Singh V, Singh H, Handa A. Critical Appraisal of Burnished HVOF Sprayed WCCrC-Ni Coatings against Hot Corrosion in Actual Environmental

- Conditions of Coal Fired Boiler. *International Journal of Advanced Science and Technology*. 2020;29(2): 4420–4432.
- 41. Kim HJ, Lee CH, Hwang SY. Superhard nano WC–12% Co coating by cold spray deposition. *Materials Science and Engineering: A.* 2005;391(1-2): 243–248.
- 42. Chen L, Wang SQ, Zhou SZ, Li J, Zhang YZ. Microstructure and mechanical properties of Ti (C, N) and TiN/Ti (C, N) multilayer PVD coatings. *International Journal of Refractory Metals and Hard Materials*. 2008;26(5): 456–460.
- 43. Zhao S, Xie X, Smith GD, Patel SJ. Research and improvement on structure stability and corrosion resistance of nickel-base superalloy INCONEL alloy 740. *Materials & Design*. 2006;27(10): 1120–1127.
- 44. Planche MP, Normand B, Liao H, Rannou G, Coddet C. Influence of HVOF spraying parameters on in-flight characteristics of Inconel 718 particles and correlation with the electrochemical behaviour of the coating. *Surface and Coatings Technology*. 2002;157(2–3): 247–256.
- 45. Guo X, Planche MP, Chen J, Liao H. Relationships between in-flight particle characteristics and properties of HVOF sprayed WC-CoCr coatings. *Journal of Materials Processing Technology*. 2014;214(2): 456–461.
- 46. Kong G, Zhang D, Brown PD, McCartney DG, Harris SJ. Microstructural characterisation of high velocity oxyfuel thermally sprayed Stellite 6. *Materials Science and Technology*. 2003;19(8): 1003–1011.
- 47. Sundararajan T, Kuroda S, Itagaki T, Abe F. Steam oxidation resistance of Ni-Cr thermal spray coatings on 9Cr-1Mo steel. Part 1: 80Ni-20Cr. *ISIJ International*. 2003;43(1): 95–103.
- 48. Ma N, Zhang K, Yin D, Zhao D, Zhu Z, Ye F. Synthesis and Characterization of Nanostructured WC-Co/Al Powder Prepared by Mechanical Alloying. *Journal of Nanomaterials*. 2016;2016: 9080684.
- 49. Sidhu TS, Prakash S, Agrawal RD. Studies of the metallurgical and mechanical properties of high velocity oxy-fuel sprayed stellite-6 coatings on Ni-and Fe-based superalloys. *Surface and Coatings Technology*. 2006;201(1-2): 273–281.
- 50. Kalsi SS, Sidhu TS, Singh H, Karthikeyan J. Behavior of cold spray coating in real incineration environment. *Materials and Manufacturing Processes*. 2016;31(11): 1468–1475.
- 51. Kalsi SS, Sidhu TS, Singh H, Karthikeyan J. Analysis of material degradation for uncoated and NiCoCrAlY cold spray coated Superfer 800H in the secondary chamber of medical waste incinerator. *Engineering Failure Analysis*. 2014;(46): 238–246.
- 52. Dent AH, Horlock AJ, McCartney DG, Harris SJ. Microstructural characterisation of a Ni-Cr-BC based alloy coating produced by high velocity oxy-fuel thermal spraying. *Surface and Coatings Technology*. 2001;139(2–3): 244–250.
- 53. Singh H, Sidhu TS, Kalsi SB. Behaviour of cold sprayed superalloy in incinerator at 900°C. *Surface Engineering*. 2015;31(11): 846–852.
- 54. Singh H, Sidhu TS, Karthikeyan J, Kalsi SB. Evaluation of characteristics and behavior of cold sprayed Ni–20Cr coating at elevated temperature in waste incinerator plant. *Surface and Coatings Technology*. 2015;261: 375–384.
- 55. Somasundaram B, Kadoli R, Ramesh MR. Evaluation of Thermocyclic Oxidation Behavior of HVOF Sprayed WC-CrC-Ni Coatings. *Bonfring International Journal of Industrial Engineering and Management Science*. 2015;5(2): 83–89.
- 56. Selvam Kevin P, Tiwari A, Seman S, Beer Mohamed SA, Jayaganthan R. Erosion-corrosion protection due to Cr3C2-NiCr cermet coating on stainless steel. *Coatings*. 2020;10(11): 1042.

THE AUTHORS

Atul Agnihotri (b) e-mail: er.atul84@gmail.com

Kalsi S.B.S.

e-mail: kalsi_asr@yahoo.com

Harmesh Kansal

e-mail: harmeshkansal@gmail.com

Peculiarities of the two-stage Zn diffusion profile formation from vapor phase into InGaAs/InP heterostructure for avalanche photodiode fabrication

Submitted: May 11, 2023

Approved: June 9, 2023

Accepted: July 6, 2023

¹ Ioffe Institute, St. Petersburg, Russia

St. Petersburg, Russia

⁵ JSC OKB-Planeta, Veliky Novgorod, Russia

⊠ blokh@mail.ioffe.ru

Abstract. In this paper was presented the research results of the dependence of the InGaAs surface layer thickness on the process of Zn diffusion into InGaAs/InP heterostructures from a diethylzink source. One-dimensional distribution profiles of electrically active dopants were obtained by electrochemical volt-capacitive profiling. The influence of technological parameters (process time, temperature, and pressure in the reactor) on the hole concentration and the depth of the p-type dopant was studied. The principal possibility of simultaneously forming a highly doped InGaAs:Zn layer has been experimentally shown due to the higher Zn solubility limit in InGaAs compared to InP and to implement a two-stage p-type dopant profile in one Zn diffusion process by controlling the thickness of the InGaAs surface layer.

Keywords: zinc diffusion; diethylzinc; indium phosphide

Acknowledgements. Authors thank RZD for financial support of the fabrication of InGaAs/InP heterostructures for comprehensive studies of the Zn diffusion process.

Citation: Blokhin SA, Levin RV, Epoletov VS, Kuzmenkov AG, Blokhin AA, Bobrov MA, Kovach YN, Maleev NA, Nikitina EV, Andryushkin VV, Vasiljev AP, Voropaev KO, Ustinov VM. Peculiarities of the two-stage Zn diffusion profile formation from vapor phase into InGaAs/InP heterostructure for avalanche photodiode fabrication. *Materials Physics and Mechanics*. 2023;51(4): 66-75. DOI: 10.18149/MPM.5142023_6.

² Alferov University, St. Petersburg, Russia

³ Connector Optics LLC, St. Petersburg, Russia

⁴ Submicron Heterostructures for Microelectronics, Research & Engineering Center, RAS,

Introduction

The most promising approach for the creation of compact telecommunication range single photon detectors is the usage of avalanche photodiodes (APDs) with a planar design based on InP-InGaAs heterostructures, where the photon absorption region in the InGaAs layer and multiplication of the photogenerated charge carrier region in the InP layer are separated [1,2]. The key point in the manufacturing of this type of APD is the formation of a two-stage p-type doping profile in the InP layer. For these purposes, a local Zn diffusion process into the InP layer through a dielectric mask [3,4] is used based on one of several technological approaches: Zn diffusion from a coated Zn₃P₂ or Zn₃P₂/Zn layer [5,6], diffusion in a sealed ampoule using a planar source based on Zn₃P₂ [7,8], Zn diffusion through a narrow gap using a planar source based on Zn₃P₂ [9,10], diffusion from the vapor phase in an open tube [4,11].

One of the main problems of the mentioned above approaches is the low level of p-type dopant concentration in the InP layer, which makes it difficult to form high-quality ohmic contacts to the p-InP layers. The simplest solution is the use of Zn-containing metal contacts [4,10]. However, the usage of Zn-containing metal contacts is associated with several new problems, such as low reliability, complex surface morphology and deep penetration of contact metallization materials into the p-InP layer during contact annealing, which significantly affects the final characteristics of the device.

Another problem in the creation of effective single photon APDs is related to the formation of a two-stage p-type dopant profile with local diffusion of Zn, which is necessary to suppress the local edge electric breakdown in the single photon APD [12,13]. There are two main approaches. The first one is based on double Zn diffusion processes through two different dielectric masks [11,14] and requires high reproducibility of the process and uniformity of the Zn diffusion over the sample area. The implementation of this approach is potentially possible from the vapor phase using metal-organic chemical vapor deposition (MOCVD) reactors [15,16]. The second approach is based on the formation of the InP layer surface relief followed by a single Zn diffusion process through dielectric mask [4,5,10] and requires the formation of a flat bottom of the etching well with smooth walls to suppress undesirable local electrical breakdown on the roughness of the Zn diffusion front. It is difficult to ensure a flat bottom of the well using non-selective chemical etching, and the use of stop layers for the implementation of a selective chemical etching is associated with a lateral anisotropic etching under the mask [17]. A plasma chemical etching of the InP layer potentially allows to provide the necessary parameters of the well [10], however, a few studies have noted its negative effect on the dark counts of the single photon APD [18].

A potential solution to these problems is the use of the InGaAs surface layer, which makes it possible to achieve a p-type doping level above 1×10^{19} cm⁻³ due to a higher Zn solubility limit in InGaAs compared to InP layers [19] and to apply the selective chemical etching through InAlAs/InGaAsP stop layers to form the required surface relief. A few studies have shown the possibility of Zn diffusion into InP layers from the vapor phase through the InGaAs layer [20-23] and demonstrated the usage of such technology for creating high-speed photodiodes in waveguide geometry [23]. The technological parameters of the Zn diffusion process from the vapor phase and type of Zn atom source set the concentration and the depth of the Zn diffusion into the InP layer [4,11,15,16,19,25,26]. However, the difference between the Zn solubility limits in the InP and InGaAs layers leads to some features of the Zn diffusion process into InP through the InGaAs layer [20-22].

This paper presents a study of the InGaAs surface layer thickness influence on the Zn diffusion process into the InP layer through the InGaAs layer from the diethylzinc (DEZn) metal organic source. The dependences of the obtained distribution profile of the electrically active p-type dopant on the process time, temperature, and pressure in the reactor during the technological process are considered.

Experiment

The investigated InGaAs/InP heterostructures were grown on the InP substrates and consisted of an undoped InP $3.5~\mu m$ thick layer, an undoped InGaAs 50~nm thick layer, an undoped InAlAs 10~nm thick stop layer and an undoped InGaAs 250~nm thick surface layer. The InGaAs surface layer thickness was varied by dry etching.

The process of Zn diffusion from the vapor phase into InGaAs/InP heterostructures was produced at the MOCVD Aixtron AIX-200 system. DEZn was used as a source of Zn atoms and hydrogen (H₂) was used as a carrier gas. The maximum flow of DEZn was ~2.55·10⁻⁵ mol/min at a thermostat temperature of 17°C. A stabilizing flow of arsine (AsH₃) was fed into the reactor to prevent surface degradation of the InGaAs layer at temperatures above 400 °C. The temperature range of the Zn diffusion process below 460 °C is limited by the precipitation of Zn compounds in the solid phase, and at temperatures above 550 °C the temperature range is limited by the deterioration of the surface morphology of the InGaAs layer. The amount of electrically active p-type dopant in the InP layer also depends on the parameters of the thermal activation dopant process [21,26,27]. After the Zn diffusion process, InGaAs/InP heterostructure samples were subjected to ex-situ rapid thermal annealing (RTA) in a nitrogen flow at 450 °C for 5 min.

The unidimensional distribution profiles of electrically active dopants in the studied InGaAs/InP heterostructures after Zn diffusion and RTA processes were determined by electrochemical capacitance-voltage profiling (ECV).

To carry out local diffusion into InP through a thin InGaAs layer a SiN_x dielectric mask with window topology was formed on the surface of InGaAs/InP heterostructures [28]. To obtain a two-stage profile of a p-type dopant in a single Zn diffusion process recesses with a defined shape and depth were etched within the dielectric mask windows (which defined the photosensitive region) formed on the surface of InGaAs/InP heterostructures. The recesses were made by selective chemical etching of the InGaAs layer to the InAlAs stop layer, followed by selective removal of the InAlAs stop layer.

Two-dimensional distribution profiles of electrically active p-type dopants in the studied samples were controlled by contrast on cross-sectional images obtained by scanning electron microscopy (SEM). SEM images were obtained in the secondary electron mode at low (<5 keV) accelerating voltages.

Results and discussion

Figure 1 shows the distribution profiles of electrically active p-type dopants in InGaAs/InP heterostructures depending on the thickness of the InGaAs surface layer, which demonstrates the effect of the InGaAs surface layer thickness on the Zn diffusion process. The process temperature was 500 °C, the reactor pressure was 50 mbar, and the process time was 60 minutes. In the direction from the surface of the structure the concentration of holes in the InGaAs layer monotonically decreases and its maximum value in the InGaAs layer reaches (3–4)·10¹⁹ cm⁻³, which is sufficient for the formation of ohmic contacts [19,24]. In this case, the near-surface region (~ 10-30 nm) is excluded from consideration because it is affected by the depletion of the surface and/or the effect of reverse diffusion near the surface. The local decrease in the hole concentration to 6.10^{18} cm⁻³ coincides with the position of the InAlAs stop layer. The first sharp decrease in the hole concentration to (1-3)·10¹⁸ cm⁻³ coincides with the position of the InGaAs-InP interface [21]. The second sharp drop below 1·10¹⁷ cm⁻³ is related to the Zn diffusion front [29]. There is a sharp increase in the depth of the p-type dopants (at the level of $1 \cdot 10^{17}$ cm⁻³) and an increase in the maximum concentration of holes in the InP layer to 3.10^{18} cm⁻³ as the thickness of the InGaAs surface layer decreases. This is due to the existence of an initial transitional stage of Zn diffusion in the InGaAs/InP heterostructure when Zn diffusion first occurs only in the InGaAs layer. The demonstration of the hole segregation

effect in the InGaAs layer near the InGaAs-InP heterointerface is due to the higher limit of solubility of the Zn dopant in the InGaAs layer.

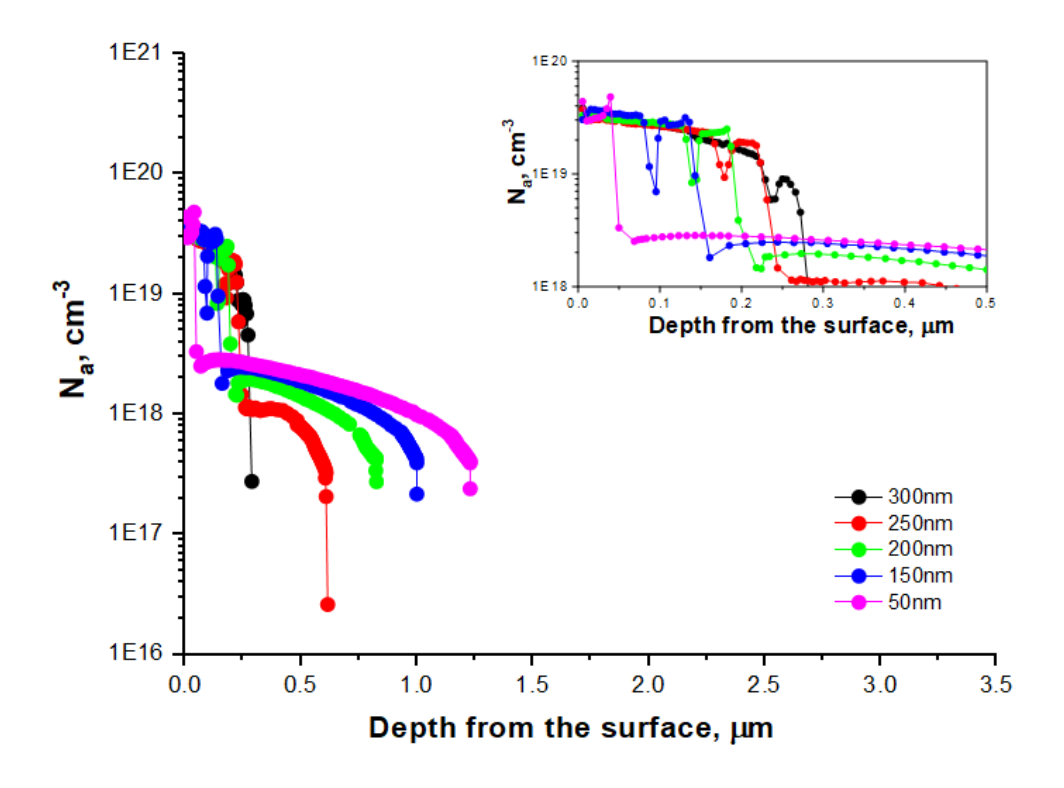


Fig. 1. Distribution profiles of electrically active p-dopants in the InGaAs/InP heterostructure for different thicknesses of InGaAs surface layer measured by ECV profiling. Temperature: 500 °C, pressure: 50 mbar, process time: 60 min

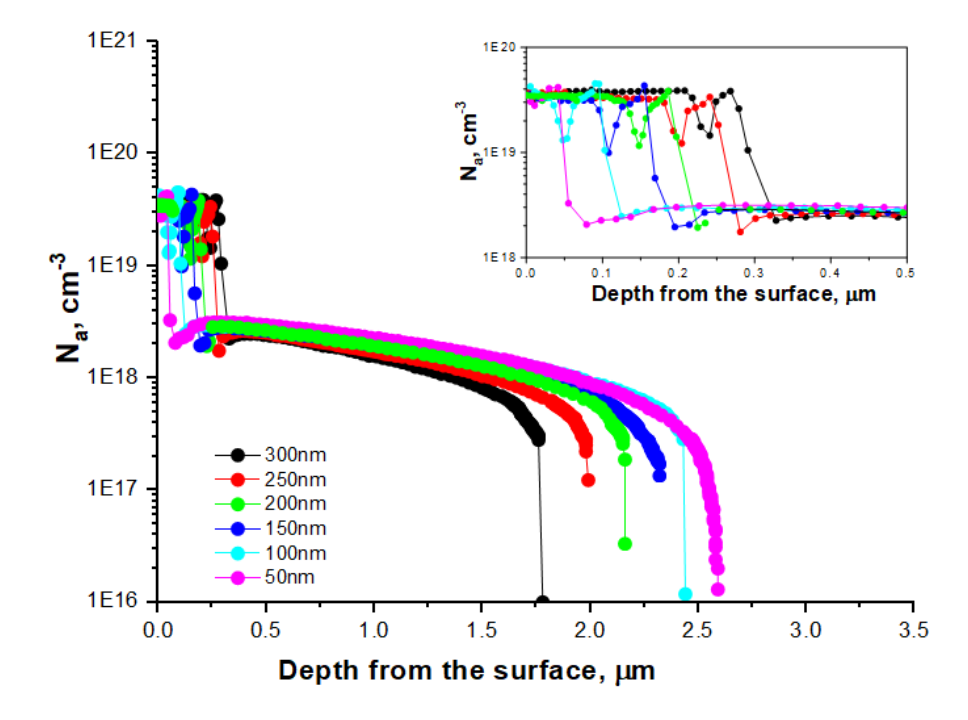


Fig. 2. Distribution profiles of electrically active p-dopants in the InGaAs/InP heterostructure for different thicknesses of InGaAs surface layer measured by ECV profiling. Temperature: 500 °C, pressure: 50 mbar, process time: 180 min

Figure 2 shows the distribution profiles of electrically active p-type dopants in InGaAs/InP heterostructures with different thicknesses of the InGaAs surface layer for a process time of 180 min with other fixed technological parameters. An increase in the Zn diffusion process time made it possible to achieve saturation of the hole concentration at the level of (3–4)·10¹⁹ cm⁻³ over the entire thickness of the InGaAs layer (with the exception of the InAlAs stop layer) and minimize the difference in the maximum hole concentration in the InP layer. Thus, Zn diffusion from an infinite solid-state source mode was realized (the concentration of the diffusant was constant). More detailed studies of the effect of the process time on the Zn diffusion in the InGaAs/InP have shown that in the case of saturation of the hole concentration in InGaAs, the difference in the depth of the Zn diffusion front in InP between samples with different thickness of the InGaAs surface layer remains constant.

An important issue is the influence of the Zn diffusion process temperature with the other fixed technological parameters. According to Fig. 3 a decrease in temperature from 500 to 475 °C leads to an increase in the maximum hole concentration in the InGaAs layer to 5.5·10¹⁹ cm⁻³ and to an increase in the maximum hole concentration in the InP layer to 5.5·10¹⁸ cm⁻³ and in the depth of the p-type dopant occurrence. This behavior is apparently due to an increase in the amount of diffusant due to a decrease in the desorption of Zn from the near-surface region with a decrease in the process temperature (similarly with the Zn diffusion into the InP layer [4,26] and into the InGaAs layer [19]). In addition, there is an increase in the effect of hole segregation in the InGaAs layer near the InGaAs-InP heterointerface and a sharp decrease in the difference of the Zn diffusion front depth in InP layer between samples with different thicknesses of the InGaAs surface layer, especially at thicknesses less than 200 nm. It should be noted that an increase in temperature during the Zn diffusion process leads to a drop of the near-surface diffusant concentration due to increased desorption and, as a result, to decreased hole concentration and depth of the Zn diffusion into the InP layer.

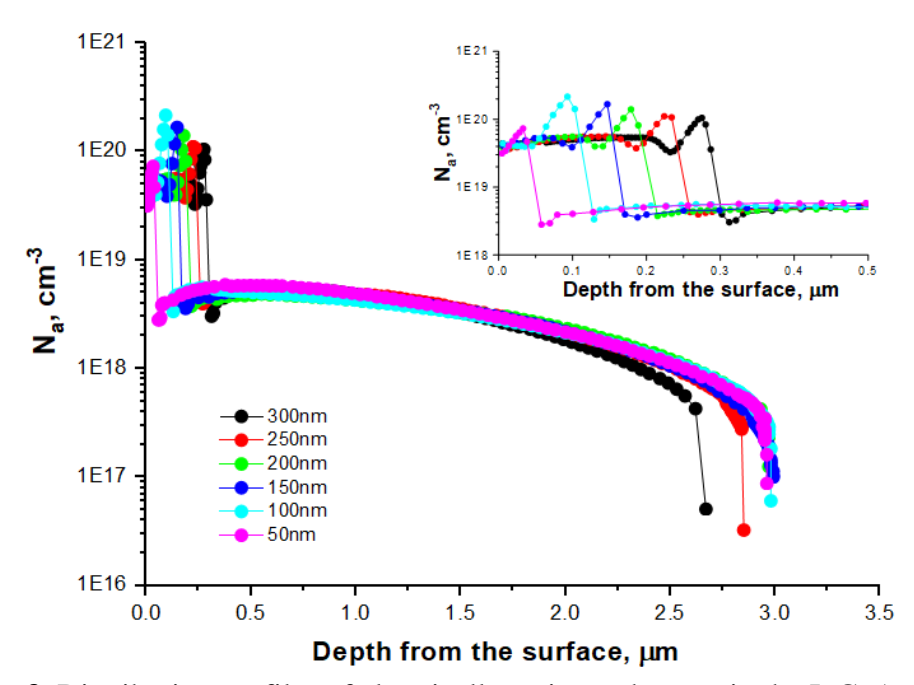


Fig. 3. Distribution profiles of electrically active p-dopants in the InGaAs/InP heterostructure for different thicknesses of InGaAs surface layer measured by ECV profiling. Temperature: 475 °C, pressure: 50 mbar, process time: 180 min

The effect of reactor pressure on Zn diffusion in InGaAs/InP was analyzed depending on the thickness of the InGaAs surface layer. The process temperature was 500 °C and the process time was 60 minutes. According to Figure 4 an increase in pressure in the reactor from 50 to 200 mbar leads to a sharp increase in the maximum hole concentration in the InGaAs layer to 8·10¹⁹ cm⁻³. Moreover, it leads to the disappearance of a local decrease of the hole concentration in the InAlAs stop layer and an increase in the effect of hole segregation near the InGaAs-InP heterointerface. The observed decrease of the hole concentration in the InGaAs layer near the surface is due to the process of reverse diffusion near the surface, for example, during sample cooling or thermal activation of a p-type dopant [4,21]. The high diffusant concentration in the InGaAs layer made it possible to reduce the depth spread and to obtain the Zn diffusion depth in the InP layer of more than 2.5 µm in a significantly shorter process time. At the same time, there is a sharp increase (compared with the results in Figs. 1 and 2) in the maximum hole concentration in the InP layer to $7 \cdot 10^{18}$ cm⁻³ which is comparable to the results of Zn diffusion from dimethylzinc into the InP layer [4,11,26]. This behavior is similar to the effect of the temperature decreasing and shows an increase in the diffusant concentration due to the suppression of Zn desorption from the near-surface region with an increase in pressure. At higher pressures in the reactor the solubility of the Zn dopants in the InGaAs layer is possibly limited, so the permeability of the InGaAs:Zn layer deteriorates, which negatively affects the Zn diffusion depth into the InP layer.

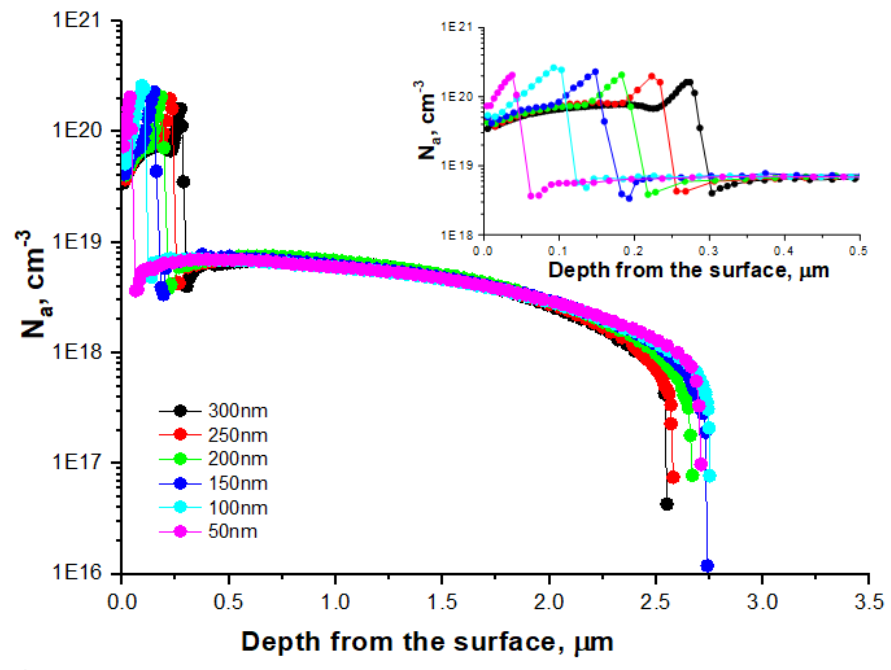


Fig. 4. Distribution profiles of electrically active p-dopants in the InGaAs/InP heterostructure for different thicknesses of InGaAs surface layer measured by ECV profiling. Temperature: 500 °C, pressure: 200 mbar, process time: 60 min

Thus, it can be concluded that during the Zn diffusion process from the vapor phase into the InP layer through the InGaAs layer the thickness variation of the InGaAs surface layer makes it possible to effectively control the Zn diffusion depth in the InP layer.

Figure 5 shows a typical scanning electron microscope (SEM) cross-section image of a sample with local Zn diffusion through a SiN_x dielectric mask. The Zn diffusion process temperature was 500 °C, the reactor pressure was 50 mbar, and the process time was 180 minutes. The position of the Zn diffusion front in the InP layer was determined by the image contrast boundary between regions with different types of conductivity. It should be noted that

it is difficult to determine the absolute value of the diffused Zn depth by the contrast since the observed contrast is complexly related to the distribution of the electric field on the studied sample cross-section. Nevertheless, the relative distance Δd_{Zn} between the first and second local Zn diffusion fronts can be estimated with relatively high accuracy (the measurement error does not exceed 10 %). At the etching depth Δd_{etch} of the InGaAs surface layer of about 0.2 μ m the difference in the depth of the p-type dopant was 0.45 μ m which is less than the target difference $\Delta d_{Zn} \sim 0.8 \ \mu$ m, which was estimated from test processes of Zn diffusion into InGaAs/InP heterostructures without a dielectric mask. This effect can be caused both by an effective increase of the diffusant concentration in the near-surface region using a dielectric mask and by an inaccuracy of determining the depth of the p-type dopant in test processes by ECV profiling due to the curvature of the recesses bottom at large etching depths.

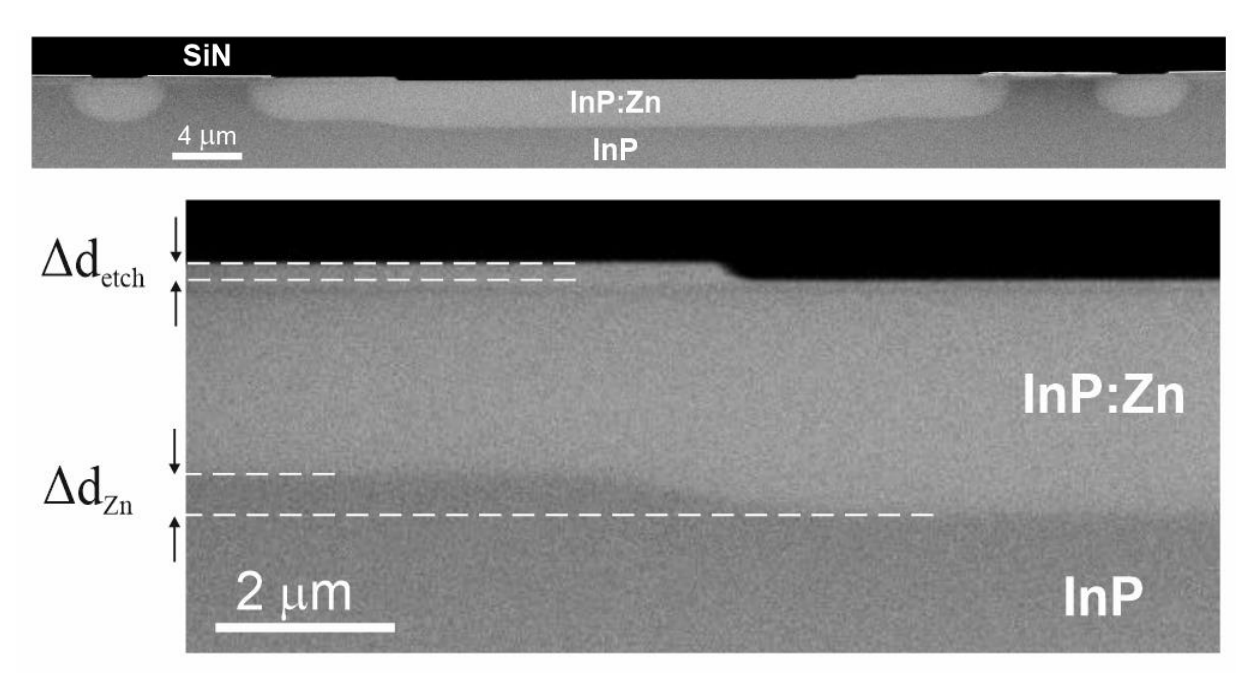


Fig. 5. SEM cross-section image of a sample with local diffusion of Zn into InGaAs/InP through a SiNx dielectric mask with a variation in the thickness of the InGaAs surface layer within the central window. Temperature 500 °C, pressure 50 mbar, process time 180 min

Conclusion

The results of the Zn diffusion from the vapor phase into the InP layer through the InGaAs surface layer with various thicknesses are presented. The Zn diffusion process was carried out according to the open tube scheme in the MOCVD reactor, where DEZn was used as a Zn source.

It was shown that a decrease of the InGaAs surface layer thickness leads to a sharp increase in the depth of the electrically active p-type dopant (Zn diffusion front at the level of $1\cdot10^{17}$ cm⁻³). Additionally, an increase in the process temperature from 475 to 500 °C with other fixed technological parameters leads not only to a decrease of the hole concentration in the InGaAs surface layer and the depth of the p-type dopant but also to the increased difference in the depth of the Zn diffusion front with variations in the thickness of the InGaAs surface layer. An increase of the pressure in the reactor from 50 to 200 mbar with other fixed technological parameters leads to a sharp decrease in the difference of the Zn diffusion depth with variations in the thickness of the InGaAs surface layer.

The revealed behavior is due to the existence of an initial transitional stage of Zn diffusion into the InGaAs/InP heterostructure when Zn diffusion first occurs only in the InGaAs surface layer until the full saturation of the hole concentration is reached in it. At the same time, an

increase of the effective hole concentration in the InGaAs layer due to a weakening of the Zn desorption from the near-surface region (with a decrease in temperature and/or an increase in pressure in the reactor) leads to a faster implementation of the Zn diffusion process from an infinite solid-state source.

The studies have shown the principal possibility of controlled formation of a two-stage diffusion profile of a p-type dopant in a single Zn diffusion process from the vapor phase through the dielectric mask SiN_x into the InP layers by controlling the thickness of the InGaAs surface layer. This approach makes it possible to simultaneously provide a high level of p-type doping in the InGaAs surface layer, which is important for the formation of an ohmic p-contact. The results are important for the creation of single-photon APDs for quantum communication systems.

References

- 1. Zhang J, Itzler MA, Zbinden H, Pan JW. Advances in InGaAs/InP single-photon detector systems for quantum communication. *Light: Science & Applications*. 2015;4(5): e286–e286.
- 2. Ceccarelli F, Acconcia G, Gulinatti A, Ghioni M, Rech I, Osellame R. Recent Advances and Future Perspectives of Single-Photon Avalanche Diodes for Quantum Photonics Applications. *Advanced Quantum Technologies*. 2021;4(2): 2000102.
- 3. Tosi A, Calandri N, Sanzaro M, Acerbi F. Low-Noise, Low-Jitter, High Detection Efficiency InGaAs/InP Single-Photon Avalanche Diode. *IEEE Journal of selected topics in quantum electronics*. 2014;20(6): 192–197.
- 4. Jun DH, Jeong HY, Kim Y, Shin C-S, Park KH, Park W-K, Kim M-S, Kim S, Han SW Moon S. Single-step metal-organic vapor-phase diffusion for low-dark-current planar-type avalanche photodiodes. *Journal of the Korean Physical Society*. 2016;69(8): 1341–1346.
- 5. Kim MD, Baek JM, Kim TG, Kim SG, Chung KS. Characterization of double floating guard ring type InP-InGaAs avalanche photodiodes with Au/Zn low resistance ohmic contacts. *Thin Solid Films*. 2006;514(1–2): 250–253.
- 6. Chen Y, Zhang Z, Miao G, Jiang H, Song H. Optimized Selective-Area p-Type Diffusion for the Back-Illuminated Planar InGaAs/InP Avalanche Photodiodes by a Single Diffusion Process. *Physica Status Solidi* (A). 2022;219(2): 2100577.
- 7. Lee K, Yang K. Analysis of InGaAs/InP Single-Photon Avalanche Diodes With the Multiplication Width Variation. *IEEE Photonics Technology Letters*. 2014;26(10): 999–1002.
- 8. Yun I, Hyun K-S. Zinc diffusion process investigation of InP-based test structures for high-speed avalanche photodiode fabrication. *Microelectronics Journal*. 2000;31(8): 635–639.
- 9. Preobrazhenskii VV, Chistokhin IB, Putyato MA, Valisheva NA, Emelyanov EA, Petrushkov MO, Pleshkov AS, Neizvestny IG, Ryabtsev II. Single Photon Detectors Based on InP/InGaAs/InP Avalanche Photodiodes. *Optoelectronics, Instrumentation and Data Processing*. 2021;57(5): 485–493.
- 10. Petrushkov MO, Putyato MA, Chistokhin IB, Semyagin BR, Emel'yanov EA, Esin MYu, Gavrilova TA, Vasev AV, Preobrazhenskii VV. Zinc Diffusion into InP via a Narrow Gap from a Planar Zn3P2-Based Source. *Technical Physics Letters*. 2018;44: 612–614.
- 11. Acerbi F, Tosi A, Zappa F. Growths and diffusions for InGaAs/InP single-photon avalanche diodes. *Sensors and Actuators A: Physical*. 2013;201: 207–213.
- 12. Jiang X, Itzler MA, Ben-Michael R, Slomkowski K. InGaAsP–InP Avalanche Photodiodes for Single Photon Detection. *IEEE Journal of Selected Topics in Quantum Electronics*. 2007;13(4): 895–905.
- 13. Signorelli F, Telesca F, Conca E, Della Frera A, Ruggeri A, Giudice A, Tosi A. Low-Noise InGaAs/InP Single-Photon Avalanche Diodes for Fiber-Based and Free-Space Applications. *IEEE Journal of Selected Topics in Quantum Electronics*. 2022;28(2): 1–10.

- 14. He T, Yang X, Tang Y, Wang R, Liu Y. High photon detection efficiency InGaAs/InP single photon avalanche diode at 250 K. *Journal of Semiconductors*. 2022;43(10): 102301.
- 15. Wada M, Seko M, Sakakibara K, Sekiguchi Y. Zn Diffusion into InP Using Dimethylzinc as a Zn Source. *Japanese Journal of Applied Physics*. 1989;28(10A): L1700.
- 16. Wisser J, Glade M, Schmidt HJ, Heime K. Zinc diffusion in InP using diethylzinc and phosphine. *Journal of Applied Physics*. 1992;71(7): 3234–3237.
- 17. Lee K, Lee B, Yoon S, Hong JH, Yang K. A Low Noise Planar-Type Avalanche Photodiode using a Single-Diffusion Process in Geiger-Mode Operation. *Japanese Journal of Applied Physics*. 2013;52(7R): 072201.
- 18. Lee K, Yang K. Performance comparison of wet-etched and dry-etched Geiger-mode avalanche photodiodes using a single diffusion process. *Physica Status Solidi* (*C*). 2013;10(11): 1445–1447.
- 19. Franke D, Reier FW, Grote N. Post-growth Zn diffusion into InGaAs/InP in a LP-MOVPE reactor. *Journal of Crystal Growth*. 1998;195(1–4): 112–116.
- 20. Andryushkin VV, Gladyshev AG, Babichev AV, Kolodeznyi ES, Novikov II, Karachinsky LYa, Rochas SS, Maleev NA, Khvostikov VP, Ber BYa, Kuzmenkov AG, Kizhaev SS, Bougrov VE. Investigation of the zinc diffusion process into epitaxial layers of indium phosphide and indium-gallium arsenide grown by molecular beam epitaxy. *Journal of Optical Technology*. 2021;88(12): 87–92.
- 21. Van Geelen A, De Smet TMF, Van Dongen T, Van Gils WMEM. Zinc doping of InP by metal organic vapour phase diffusion (MOVPD). *Journal of Crystal Growth*. 1998;195(1–4): 79–84.
- 22. D'Agostino D, Carnicella G, Ciminelli C, Thijs P, Veldhoven PJ, Ambrosius H, Smit M. Low-loss passive waveguides in a generic InP foundry process via local diffusion of zinc. *Optics Express*. 2015;23(19): 25143.
- 23. Blokhin SA, Levin RV, Epoletov VS, Kuzmenkov AG, Blokhin AA, Bobrov MA, Kovach YN, Maleev NA, Andryushkin VV, Vasil'ev AP, Voropaev KO, Ustinov VM. Zn diffusion from vapor phase into InGaAs/InP heterostructure using diethylzinc as a p-dopant source. *Materials Physics and Mechanics*. 2023;51(3): 38–45.
- 24. Zhang L, La X, Zhu X, Guo J, Zhao L, Wang W, Liang S. High Speed Waveguide Uni-Traveling Carrier InGaAs/InP Photodiodes Fabricated By Zn Diffusion Doping. *IEEE Journal of Selected Topics in Quantum Electronics*. 2022;28(2): 1–6.
- 25. Vanhollebeke K, D'Hondt M, Moerman I, Van Daele P, Demeester P. Zn doping of InP, InAsP/InP, and InAsP/InGaAs heterostructures through metalorganic vapor phase diffusion (MOVPD). *Journal of Electronic Materials*. 2001;30(8): 951–959.
- 26. Pitts OJ, Benyon W, Goodchild D, SpringThorpe AJ. Multiwafer zinc diffusion in an OMVPE reactor. *Journal of Crystal Growth*. 2012;352(1): 249–252.
- 27. Van Gurp GJ, Van Dongen T, Fontijn GM, Jacobs JM, Tjaden DLA. Interstitial and substitutional Zn in InP and InGaAsP. *Journal of Applied Physics*. 1989;65(2): 553–560.
- 28. Zou WX, Vawter GA, Merz JL, Coldren LA. Behavior of SiNx films as masks for Zn diffusion. *Journal of Applied Physics*. 1987;62(3): 828–831.
- 29. Hampel CA, Blaauw C, Haysom JE, Glew R, Calder ID, Guillon S, Bryskiewicz T, Puetz N. Metalorganic vapor phase diffusion using DMZn Part II: Determination of the interstitial zinc charge state from secondary ion mass spectroscopy measurements using the Boltzmann–Matano technique. *Journal of Vacuum Science & Technology A*. 2004;22(3): 916.

THE AUTHORS

Blokhin S.A.

e-mail: blokh@mail.ioffe.ru

Epoletov V.S.

e-mail: vadep@yandex.ru

Blokhin A.A.

e-mail: Aleksey.Blokhin@mail.ioffe.ru

Kovach Ya.N. 🗓

e-mail: j-n-kovach@itmo.ru

Nikitina E.V.

e-mail: nikitina@mail.ru

Vasiljev A.P. 🗓

e-mail: Vasiljev@mail.ioffe.ru

Ustinov V.M.

e-mail: vmust@beam.ioffe.ru

Levin R.V.

e-mail: Lev@vpegroup.ioffe.ru

Kuzmenkov A.G. D

e-mail: kuzmenkov@mail.ioffe.ru

Bobrov M.A.

e-mail: bobrov.mikh@gmail.com

Maleev N.A.

e-mail: maleev.beam@mail.ioffe.ru

Andryushkin V.V.

e-mail: vvandriushkin@itmo.ru

Voropaev K.O. 🗓

e-mail: kirill.voropaev@novsu.ru

The effect of ZnO cupping layer on the formation of sol-gel synthesized Ag nanoparticles

Submitted: June 18, 2023

Approved: July 5, 2023

Accepted: July 20, 2023

L.A. Sokura ^{1,2 ™}, A.V. Kremleva ^{1,2}, A.E. Romanov ^{1,3}

¹ Ioffe Institute, St. Petersburg, Russia
² ITMO University, St. Petersburg, Russia
³ Togliatti State University, Togliatti, Russia

⊠ sokuraliliy@itmo.ru

Abstract. Samples containing Ag nanoparticles (NPs) in a ZnO matrix were produced using a sol-gel method, with varying the annealing temperature and the thickness of the ZnO cupping layer. The dependence of the optical and structural properties of the samples on the silver diffusion was studied. As a result of annealing at temperatures of 570-650 °C, a long-wavelength shift of the plasmon absorption peak of NPs was observed due to an increase in their average size, as well as an increase in the intensity of the absorption peak due to a narrower size distribution of NPs. The transformation of the nanoparticle shape and size during annealing was shown to result from the diffusion of silver, whereas the ZnO cupping layer and its thickness was proved to control these processes.

Keywords: Ag nanoparticles; zinc oxide; sol-gel synthesis; plasmonics; scanning electron microscopy; transmission electron microscopy

Acknowledgements. The work was carried out with the support of the Ministry of Science and Higher Education of the Russian Federation (agreement No 075-15-2021-1349).

Citation: Sokura LA, Kremleva AV, Romanov AE. The effect of ZnO cupping layer on the formation of sol-gel synthesized Ag nanoparticles. *Materials Physics and Mechanics*. 2023;51(4): 76-84. DOI: 10.18149/MPM.5142023_7.

Introduction

Uniform arrays of metal nanoparticles (NPs) embedded in a dielectric or semiconductor matrix have unique optical, catalytic, magnetic, electronic, and other properties, which are controlled by plasmonic phenomena. The mentioned properties depend on the composition, size, and shape of the particles, as well as on the distance between them. In recent years, the nanostructures comprised of NPs have been increasingly used as active elements for producing solid-state chemical and biological sensors [1,2], catalytic systems [3], optical devices and other applications [4,5]. Such systems require precise control of the NPs density in the array, also, a two-dimensional array structure with a well-defined geometry is to be formed on the substrate. The size of the NPs can influence the defective structure of the NPs [6–9], which is also important for their functional properties. Conventional methods, including ion implantation, chemical or vacuum deposition, do not appear to produce uniform NP arrays with narrow distributions of particle sizes and the distances between them [10–12]. Therefore, in recent years, various modifications of these methods were developed, for example, colloidal lithography [13], laser interference lithography [14], vapor phase deposition through a mask of a given pattern [15,16], adsorption of NPs from colloidal solutions onto substrates modified by

© L.A. Sokura, A.V. Kremleva, A.E. Romanov, 2023.

Publisher: Peter the Great St. Petersburg Polytechnic University

the self-organizing monolayers of functionalized silanes and thiols [17], microcontact printing [18].

Uniform NPs array fabrication requires a detailed study of their formation processes. Although multiple papers have been published on the topic, a clear physical model of metal NP formation process in a dielectric matrix does not seem to have been reported. However, the NP formation is known to result from sequential addition of metal atoms or ions to each other due to the activation of diffusion processes in the matrix [19–21]. Otherwise, two simultaneous processes of coalescence (the augmentation of the NP sizes and an increase in the distance between them) and evaporation are responsible for the formation of NPs during the thermal decomposition of Ag and Au thin films [22–24].

Our previous research involved experiments for producing silver NP arrays in thin ZnO films deposited on quartz substrates by sol-gel method [25–27]. We showed that the diffusion through annealing in such samples results in significant changes in the morphological and optical properties of the Ag NP arrays. At a fixed annealing time (10-15 minutes), an increase in the annealing temperature from 300 to 650 °C caused an increase in the NP size from 20-30 to 50-70 nm. With a further increase in the annealing temperature up to 700 °C, we observed NPs decomposition and diffusion of silver into the quartz substrate with the formation of small clusters up to 10 nm in diameter in the near-surface layer of the substrate [25]. Besides, there was an increase in the NPs size with an increase in the annealing time from 5 to 20 minutes at a fixed temperature [26]. On the other hand, an increase in the silver concentration in the initial solution, as well as an increase in the number of the solution layers deposited on a substrate, resulted in an increase in the NPs array density while maintaining their size [27].

This paper discusses the effect of the ZnO cupping layer and its thickness on the parameters of the NPs. We produced a series of the samples with the silver NP array in a ZnO matrix, differing in the thickness of the ZnO coat and the annealing temperature. It was suggested that if it is the diffusion of silver in the ZnO layer being influential in the NP array formation, then when the annealing temperature changes while there is no ZnO layer or when its thickness is different, the diffusion processes would occur differently, and the resulting NP arrays will have different optical and structural properties.

Methods

We chose the sol-gel method to produce experimental samples. To study the effect of the ZnO matrix on the diffusion of silver, a series of samples was made that differ from each other in the annealing temperature and the thickness of the ZnO cupping layer.

The solution for making Ag NPs contained silver nitrate (AgNO₃) in 2-Methoxyethanol ($C_3H_8O_2$) in the concentration of 0.05 M. The solution was treated on a magnetic stirrer for 10 minutes at a speed of 500 rpm at room temperature. No aging was required, so the solution was finished immediately before application.

The solution for producing the ZnO layers contained zinc acetate dihydrate $(Zn(CH_3COO)_2 \cdot 2H_2O)$ in the concentration of 0.2 M in 2-Methoxyethanol $(C_3H_8O_2)$. To accelerate the sol aging, monoethanolamine (C_2H_7ON) was added to the solution in a ratio of 1:1 to Zn. The solution was treated on a magnetic stirrer for 60 minutes at a speed of 500 rpm at room temperature, then kept for 24 hours for aging and transition to the sol state.

The layers were coated on polished flat-parallel quartz plates by spin-coating method at a speed of 3500 rpm for 12 seconds. After coating, each layer was exposed to air drying for 3 minutes at 300 °C. To produce the samples for the experiment, the first 5 layers of the ZnO sol were deposited (equivalent to the 50 nm thick ZnO layer) followed by 5 layers of the silver nitrate solution. Further, more ZnO layers were applied on top with 0 (without ZnO coating), 2 or 5 layers of the ZnO sol. The resulting multilayer samples were not annealed, or else they were annealed in a muffle furnace in the air for 15 minutes at temperatures of 570 and 650 °C.

Thus, in total, 9 samples were prepared: without a ZnO cupping layer, with the ZnO cupping layer 20 and 50 nm thick (equivalent to the 2 and 5 ZnO spin-coated layers, respectively), without annealing or annealed at temperatures of 570 and 650 °C (Table 1).

Table 1. Description of produced samples

Sample layout	Sample №	Thickness of the ZnO cupping layer, nm	Annealing temperature, °C
ZnO 50 nm quartz	1	0	300
	2		570
	3		650
ZnO 20/50 nm Ag ZnO 50 nm	4	20	300
	5		570
	6		650
	7	50	300
quartz	8		570
	9		650

The optical absorption spectra of the samples were measured using an Avantes fiber-optic system based on the AvaSpec 2048 spectrometer and the AvaLight-DH-S-BAL radiation source, which provides measuring absorption and transmission spectra in the spectral range of 200–1100 nm.

The structural and morphological properties of the NP arrays in the samples produced were studied using a scanning electron microscope (SEM) Mira 3 Tescan and a transmission electron microscope (TEM) JEM-2100F JEOL. The combination of SEM and TEM methods provided a detailed study of the fabricated samples in the plan view and cross-section geometries.

Thin cross-section samples with Ag NPs in the ZnO matrix for TEM studies were prepared in accordance with the standard procedure, with preliminary mechanical thinning and subsequent polishing by an ion beam (Ar⁺) with energy of 4 keV [28]. The TEM studies were performed using the equipment belonging to the Joint Research Center "Material science and characterization in advanced technology" (Ioffe Institute).

Results and Discussion

Figure 1 shows the absorption spectra of the samples containing Ag NP arrays in a ZnO matrix produced at different thicknesses of the ZnO cupping layer (0 nm - without a ZnO coating, 20 and 50 nm) and at different annealing temperatures (without annealing - after drying at 300 °C, annealing at 570 and 650 °C). Intense absorption at the wavelengths lower than 400 nm corresponds to the edge of the ZnO interband absorption [29].

Absorption peaks with different intensities in the range of 500-700 nm, observed in the samples, appear to be caused by the localized plasmon resonance in Ag NPs [30,31]. Parts (a) to (c) of Fig. 1 show that irrespective of the ZnO cupping layer thickness, the spectra behave similarly when annealing conditions change. After annealing at a temperature of 570 °C (samples N_2 2, 5, 8), the intensity of the NP absorption peak decreases and the peak widens compared to the sample without annealing (samples N_2 1, 4, 7). After annealing at a temperature of 650 °C (samples N_2 3, 6, 9), the intensity of the peak increases sharply, while the shape and the width of the peak remain unchanged.

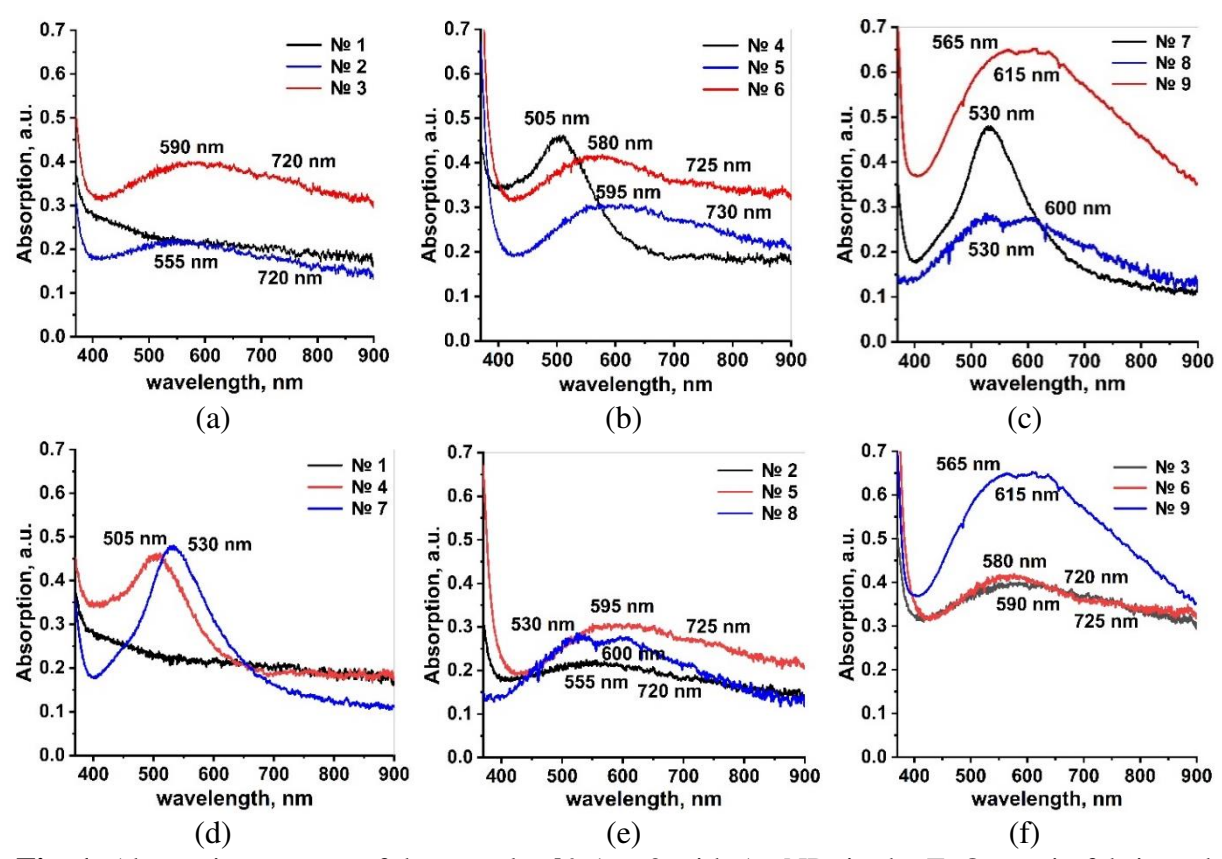


Fig. 1. Absorption spectra of the samples № 1 to 9 with Ag NPs in the ZnO matrix fabricated with different thicknesses of the ZnO cupping layer (0, 20 and 50 nm) and at different annealing temperatures (without annealing, annealing at 570 and 650 °C):

(a) to (c) give a comparison based on the effect of annealing temperature at the same thickness of the ZnO cupping layer, (d) to (f) provide a comparison based on the effect of ZnO coat thickness at the same annealing temperature

Comparison of the spectra in parts (d) to (f) of Fig. 1 shows that ZnO cupping layer and its thickness have negligible effect on the shape and the spectral position of NP plasmon absorption peak. However, the addition of the ZnO cupping layer increases the absorption intensity of the NPs, which is especially noticeable for the samples without annealing (samples N = 4, 7) and those annealed at 650 °C (samples N = 6, 9). In the samples without a cupping layer of ZnO, the NP absorption peak has very low intensity, and in the sample without annealing, there is no peak at all (sample N = 1).

The wavelength values corresponding to the spectral position of the NP absorption peak in the studied samples are marked with respective numbers in Fig. 1. In all samples annealed at 650 °C, the spectral position of the absorption peak is shifted to the long-wavelength region compared to the samples without annealing. In accordance with the theory of Mie [32], which describes the dependence of optical properties on the metal NP size, the shift of the absorption peak to the long-wavelength region indicates that the NP average size in the samples has increased as a result of annealing. All absorption spectra of the samples annealed at 570 and 650 °C are shown to have a long-wavelength shoulder in the range of 600–730 nm, in addition to the absorption peak in the range of 530–590 nm. They may represent a superposition of the absorption spectra of the array of NPs with varying sizes. Moreover, an additional peak appearing as a long-wavelength shoulder of the absorption spectrum, may indicate the possible non-sphericity of the NPs [33], for example, the NPs may become ellipsoidal or elongated in one or more directions.

A combined study of the sample structural properties by SEM and TEM methods detected the presence of two simultaneously existing entries: arrays of silver small NPs and large Ag submicroscopic particles (SMPs). Parts (a) to (c) of Fig. 2 show SEM images of the sample surface with no ZnO cupping layer without annealing (sample N 1) and after it (samples N 2, 3). The images show that immediately after drying at 300 °C (without annealing, sample N 1), a NP array with a high density up to 1.5×10^9 cm⁻² is formed, however, this array has a wide NP size distribution – some NPs with a diameter of 50 to 200 nm are observed, as well as some larger Ag SMPs reaching 500 nm in diameter. It is possible that the observed wide NP size distribution in this sample is responsible for a high absorption level in the whole visible spectrum range and the absence of an obvious NP absorption peak, see Fig. 1(a).

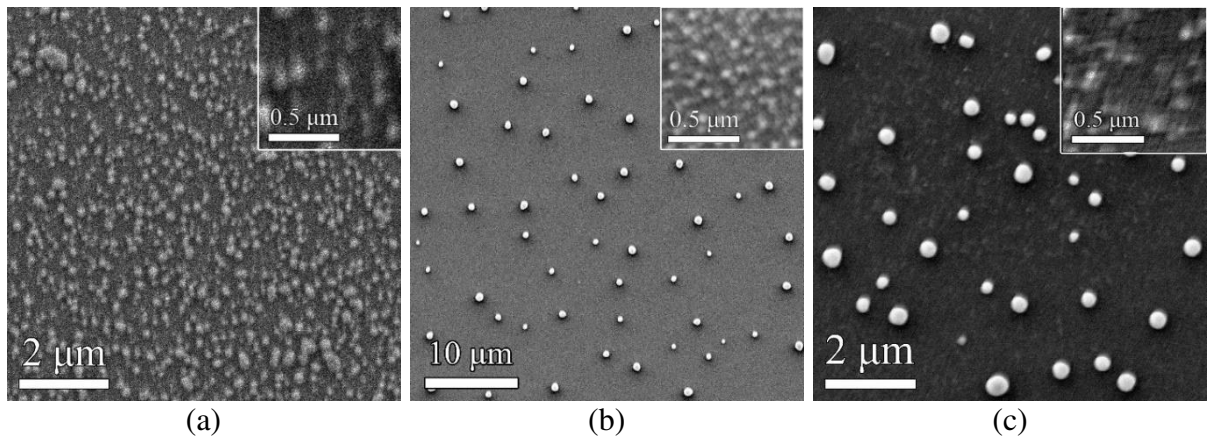


Fig. 2. SEM images of the surfaces samples № 1 to 3 with Ag particles without a ZnO cupping layer produced by sol-gel method: (a) sample № 1 - without annealing, (b) sample № 2 - after annealing at a temperature of 570 °C and (c) sample № 3 - after annealing at a temperature of 650 °C. The inserts show magnified images of NPs

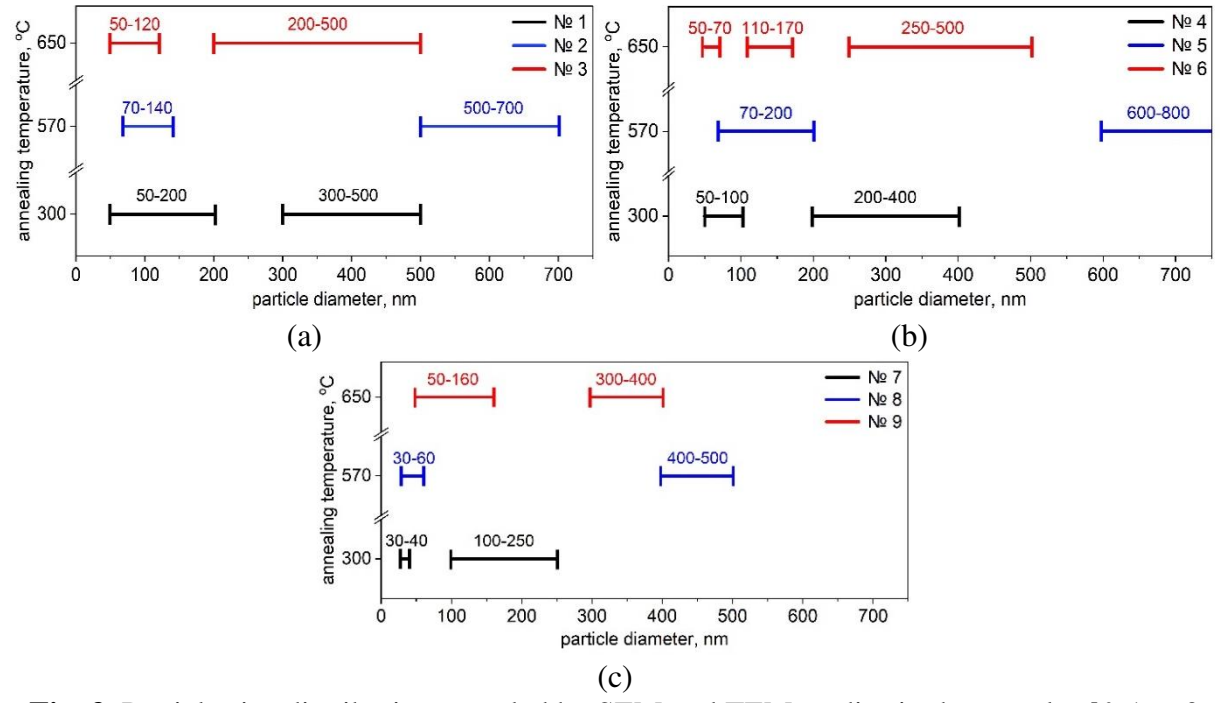


Fig. 3. Particle size distribution revealed by SEM and TEM studies in the samples № 1 to 9 without annealing (300 °C) and after annealing at temperatures of 570 and 650 °C:

(a) samples № 1 to 3 - without a ZnO cupping layer, (b) samples № 4 to 6 – covered with a 20 nm thin ZnO layer and (c) samples № 7 to 9 - covered with a 50 nm thick ZnO layer

As a result of annealing at the temperature of 570 °C (sample № 2), the NPs start being located more uniformly on the substrate surface, see Fig. 2(b). Besides the equidistant distribution of NPs in the array, they also demonstrate a narrower size distribution. In addition to a homogeneous array of ordered large SMPs with a diameter of 500-700 nm, some smaller NPs with a diameter of 70 to 140 nm are also observed in the sample. The number of the large SMPs compared to those in the sample before annealing has decreased by 2 orders - from 3×10^8 to 3×10^6 cm⁻², and the number of small NPs has increased to 8×10^9 cm⁻². Annealing at a temperature of 650 °C (sample № 3) has further decreased the particle size and distribution in arrays – the NP size ranged from 50 to 120 nm, large SMPs – from 300 to 500 nm, while the number of large SMPs has significantly decreased, see Fig. 2(b). For a sake of clarity, the particle sizes in the samples revealed by the results of SEM and TEM studies are shown in the graphs in Fig. 3.

The NP sizes in the samples covered with the ZnO layers demonstrated the changes in Ag NP distributions due to the effect of annealing in a similar way to the NP arrays in the samples without a ZnO cupping layer, see Figs. 3 and 4. First, the average particle size increases as a result of annealing at the temperature of 570 °C (samples $N_{\mathbb{Q}}$ 5 and 8), and after annealing at 650 °C (samples $N_{\mathbb{Q}}$ 6 and 9), it decreases. The addition of the ZnO cupping layer is shown to result in the narrowing of the NP size distribution, and to the reduction of the number and the size of large SMPs in the samples in the case of the largest thickness of the ZnO coating cupping layer (50 nm, samples $N_{\mathbb{Q}}$ 8 and 9). Consequently, it can be concluded that large SMPs are formed during the coagulation of silver, whereas the ZnO cupping layer prevents this.

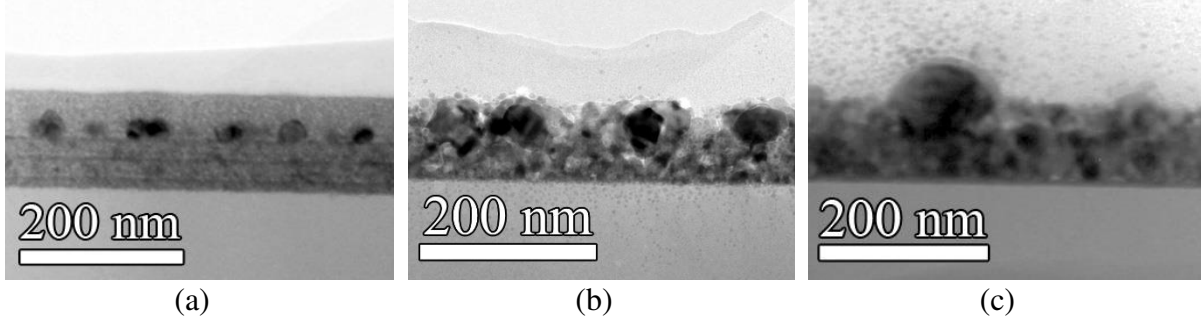


Fig. 4. TEM images of the samples № 7 to 9 with Ag particles with a 50 nm thick ZnO cupping layer produced by sol-gel method: (a) № 7 - without annealing, (b) № 8 - after annealing at a temperature of 570 °C and (c) № 9 - after annealing at a temperature of 650 °C

The sample absorption spectra suggested that the particle size should increase during the annealing process. This assumption is in good agreement with the data obtained from the studies of morphological and structural properties of the samples. The NP average size increased as a result of annealing, however, the size distribution narrowed, which contributed to an increase in the intensity of absorption peaks. An array of larger SMPs observed in the samples might be responsible for the appearance of long-wavelength shoulders in the range of 600–730 nm.

Since the amount of silver deposited is the same in all samples, it is the presence of the ZnO cupping layer that is responsible for the particle size change and the shift of the absorption peak. Referring to the earlier assumption that the transformation of the particle shape and size during annealing occurs due to silver diffusion [25,34], the fact is that the ZnO cupping layer and its thickness affect Ag diffusion to these processes.

Conclusion

Experiments have been conducted to study optical and structural properties of the samples with Ag NPs in a ZnO matrix made by the sol-gel method with different annealing temperature and thickness of the ZnO cupping layer. The absorption spectra of the produced samples did contain Ag NP plasmon absorption peak in the range of 500-700 nm. As a result of annealing at the temperature of 570-650 °C, a long-wavelength shift of the plasmon absorption peak was observed resulting from an increase in the NP average size, as well as an increase in the peak intensity resulting from the narrowing in the NP size distribution. The addition of the ZnO cupping layer led to a narrower NP size distribution, as well as to a decrease in the number and the size of large submicroscopic particles in the samples.

The optical and structural properties of the samples with Ag NPs in the ZnO matrix were shown to be determined by the diffusion of silver passing through the ZnO cupping layer during annealing. The ZnO cupping layer and its thickness affect the above process.

References

- 1. Jiang J, Wang X, Li S, Ding F, Li N, Meng S, Li R, Qi J, Liu Q, Liu GL. Plasmonic nanoarrays for ultrasensitive bio-sensing. *Nanophotonics*. 2018;7(9): 1517–1531.
- 2. Barizuddin S, Bok S, Gangopadhyay S. Plasmonic sensors for disease detection-a review. *Journal of Nanomedicine and Nanotechnology*. 2016;7(3): 1000373.
- 3. Varghese AK, Tamil PP, Rugmini R, Shiva PM, Kamakshi K, Sekhar KC. Green synthesized Ag nanoparticles for bio-sensing and photocatalytic applications. *ACS Omega*. 2020;5(22): 13123–13129.
- 4. Ross MB, Mirkin CA, Schatz GC. Optical properties of one-, two-, and three-dimensional arrays of plasmonic nanostructures. *Journal of Physical Chemistry C.* 2016;120(2): 816–830.
- 5. Wang W, Qi L. Light management with patterned micro-and nanostructure arrays for photocatalysis, photovoltaics, and optoelectronic and optical devices. *Advanced Functional Materials*. 2019;29(25): 1807275.
- 6. Chaldyshev VV, Kolesnikova AL, Bert NA, Romanov AE. Investigation of dislocation loops with As-Sb nanoclusters in GaAs. *Journal of Applied Physics*. 2005;97: 024309.
- 7. Chaldyshev VV, Bert NA, Kolesnikova AL, Romanov AE. Stress Relaxation Scenario for Buried Quantum Dots. *Physical Review B*. 2009;79(23): 233304.
- 8. Gutkin MY, Smirnov AM. Initial stages of misfit stress relaxation in composite nanostructures through generation of rectangular prismatic dislocation loops. *Acta Materialia*. 2015;88: 91–101.
- 9. Gutkin MY, Krasnitckii SA, Smirnov AM, Kolesnikova AL, Romanov AE. Dislocation loops in solid and hollow semiconductor and metal nanoheterostructures. *Physics of the Solid State*. 2015:57: 1177–1182.
- 10. Mizuno A, Ono A. Static and dynamic tuning of surface plasmon resonance by controlling interparticle distance in arrays of Au nanoparticles. *Applied Surface Science*. 2019;480: 846–850.
- 11. Yilmaz M, Senlik E, Biskin E, Yavuz MS, Tamer U, Demirel G. Combining 3-D plasmonic gold nanorod arrays with colloidal nanoparticles as a versatile concept for reliable, sensitive, and selective molecular detection by SERS. *Physical Chemistry Chemical Physics*. 2014;16(12): 5563–5570.
- 12. Liu B, Yao X, Chen S, Lin H, Yang Z, Liu S, Ren B. Large-area hybrid plasmonic optical cavity (HPOC) substrates for surface-enhanced Raman spectroscopy. *Advanced Functional Materials*. 2018;28(43): 1802263.
- 13. Wang Z, Ai B, Möhwald H, Zhang G. Colloidal lithography meets plasmonic nanochemistry. *Advanced Optical Materials*. 2018;6(18): 1800402.
- 14. Bagheri S, Strohfeldt N, Sterl F, Berrier A, Tittl A, Giessen H. Large-area low-cost

- plasmonic perfect absorber chemical sensor fabricated by laser interference lithography. *ACS Sensors*. 2016;1(9): 1148–1154.
- 15. Jeong HH, Mark AG, Lee TC, Son K, Chen W, Alarcón-Correa M, Kim I, Schütz G, Fischer P. Selectable Nanopattern Arrays for Nanolithographic Imprint and Etch-Mask Applications. *Advanced Science*. 2015;2(7): 1500016.
- 16. Terekhin VV, Dement'eva OV, Rudoy VM. Formation of ordered nanoparticle assemblies by block copolymer lithography methods. *Russian Chemical Reviews*. 2011;80(5): 453.
- 17. Saifullina IR, Chiganova GA, Karpov SV, Slabko VV. Preparation of composite films with silver nanoparticles and their fractal aggregates in a polymeric matrix. *Russian Journal of Applied Chemistry*. 2006;79: 1639–1642.
- 18. Kasani S, Curtin K, Wu N. A review of 2D and 3D plasmonic nanostructure array patterns: fabrication, light management and sensing applications. *Nanophotonics*. 2019;8(12): 2065–2089.
- 19. Chentsova IE, Dubovik VI, Kovivchak VS. Synthesis of silver nanoparticles by thermal annealing of thin films. *Herald of Omsk University*. 2012;2: 110–114.
- 20. Ignat'ev AI, Nashchekin AV, Nevedomskii VN, Podsvirov OA, Sidorov AI, Solov'ev AP, Usov OA. Formation of Silver Nanoparticles in Photothermorefractive Glasses during Electron Irradiation. *Technical Physics*. 2011;56(5): 662.
- 21. Stepanov AL, Popok VN, Hole DE, Bukharaev AA. Interaction of high-power laser pulses with glasses containing implanted metallic nanoparticles. *Physics of the Solid State*. 2001;43: 2192–2198.
- 22. Gromov DG, Pyatilova OV, Bulyarskii SV, Belov AN, Raskin AA. Specific features of the formation of arrays of silver clusters from a thin film on a SiO₂ surface. *Physics of the Solid State*. 2013;55: 619–623.
- 23. Ruffino F, Torrisi V, Marletta G, Grimaldi MG. Growth morphology of nanoscale sputter-deposited Au films on amorphous soft polymeric substrates. *Applied Physics A*. 2011;103: 939–949.
- 24. Ranjbar M, Kameli P, Salamati H. Coalescence threshold temperature in Ag nanoisland growth by pulsed laser deposition. *Materials Physics and Mechanics*. 2013;17(1): 21–28.
- 25. Sokura LA, Shirshneva-Vaschenko EV, Kirilenko DA, Snezhnaia ZhG, Shirshnev PS, Romanov AE. Electron-microscopy study of ordered silver nanoparticles synthesized in a ZnO:Al polycrystalline film. *Journal of Physics: Conference Series*. 2019;1410(1): 012170.
- 26. Shirshneva-Vaschenko EV, Sokura LA, Baidakova MV, Yagovkina MA, Snezhnaia ZhG, Shirshnev PS, Romanov AE. Study of the influence of the ZnO:Al polycrystalline film morphology on the silver nanoparticles formation. *Journal of Physics: Conference Series*. 2019;1400(5): 055026.
- 27. Sokura LA, Snezhnaia ZhG, Nevedomskiy VN, Shirshneva-Vaschenko EV, Romanov AE. Ordering mechanism of silver nanoparticles synthesized in a ZnO:Al polycrystalline film by sol gel method. *Journal of Physics: Conference Series*. 2020;1695(1): 012034.
- 28. Rao DVS, Muraleedharan K, Humphreys CJ. TEM specimen preparation techniques. *Microscopy: Science, Technology, Applications and Education*. 2011;2: 1232–1244.
- 29. Denisov NM, Chubenko EB, Bondarenko VP, Borisenko VE. Optical Properties of Multilayered Sol–Gel Zinc-Oxide Films. *Semiconductors*. 2018;52(6): 723–728.
- 30. Muzalev PA, Kosobudskii ID, Kul'batskii DM, Ushakov NM, Podvigalkin VY. Synthesis, structure, and properties of silver nanocomposite materials with poly (hydroxyethyl methacrylate) matrix. *Russian Journal of Applied Chemistry*. 2011;84: 666–669.
- 31. Shirshneva-Vaschenko EV, Sosnin IM, Nuryev RK, Gladskikh IA, Liashenko TG, Bougrov VE, Romanov AE. Electrical and optical properties of transparent conducting ZnO: Al/AgNP multilayer films. *Materials Physics and Mechanics*. 2016;29(2): 145–149.

- 32. Kreibig U, Vollmer M. Optical properties of metal clusters. Berlin: Springer; 1995.
- 33. Ross MB, Blaber MG, Schatz GC. Using nanoscale and mesoscale anisotropy to engineer the optical response of three-dimensional plasmonic metamaterials. *Nature Communications*. 2014;5(1): 4090.
- 34. Sokura LA, Ryabkova EA, Kirilenko DA, Shirshneva-Vaschenko EV. Structural and Optical Properties of Silver Nanoparticles In Situ Synthesized in ZnO Film by Sol–Gel Method. *Reviews on Advanced Materials and Technologies*. 2021;3(4): 29–33.

THE AUTHORS

Sokura L.A. 🗓

e-mail: sokuraliliy@mail.ru

Kremleva A.V. 🗓

e-mail: avkremleva@itmo.ru

Romanov A.E.

e-mail: alexey.romanov@niuitmo.ru

Spin transistor effect in edge channels of silicon nanosandwiches

Submitted: May 16, 2023

Approved: May 23, 2023

Accepted: June 28, 2023

L.E. Klyachkin [™], N.T. Bagraev, A.M. Malyarenko

Ioffe Institute, St. Petersburg, Russia

☑ leonid.klyachkin@gmail.com

Abstract. The conductance dependences of the edge channels of silicon nanosandwich structures (SNS) on the vertical gate voltage $V_{\rm g}$ are studied. The experiments are carried out in such a range of $V_{\rm g}$, in which the two-dimensional density of holes $p_{\rm 2D}$ is stable that made it possible to avoid the changes of the Fermi level position and thereby to unambiguously identify the Aharonov–Casher oscillations. The effect of a spin field-effect transistor at a high temperature ($T=77~\rm K$) is demonstrated, which manifests itself in the form of Aharonov–Casher oscillations of longitudinal conductance depending on $V_{\rm g}$, which controls the Bychkov–Rashba spin-orbit interaction. This experiment became possible due to the high degree of spin polarization of holes and the long spin-lattice relaxation time because of the extremely small width of the silicon quantum well and the narrowness of its edge channels, which is ensured by the properties of the negative-U-barriers limiting them effectively decreasing the electron-electron interaction.

Keywords: silicon nanosandwich; edge channel; Aharonov–Casher oscillations; Bychkov–Rashba spin-orbit interaction; spin field-effect transistor

Acknowledgements. The work was financed within the framework of the State task on the topic 0040-2019-0017 "Interatomic and atomic-molecular interactions in gases and condensed matter; quantum magnetometry and multiphoton laser spectroscopy".

Citation: Klyachkin LE, Bagraev NT, Malyarenko AM. Spin transistor effect in edge channels of silicon nanosandwiches. *Materials Physics and Mechanics*. 2023;51(4): 85-95. DOI: 10.18149/MPM.5142023_8.

Introduction

In the last decades of the 20th century, progress in the field of semiconductor nanotechnologies led to the creation of structures with quasi-one-dimensional (1D) conducting channels with the length less than the inelastic scattering length [1,2], due to which the ballistic transfer of single carriers occurs in them and macroscopic quantum phenomena are observed.

Therefore, such channels provide conditions for spin interference of single carriers due to spontaneous spin polarization of a quasi 1D carrier gas in a zero magnetic field [3,4] and Bychkov–Rashba strong spin-orbit interaction (SOI) [5].

Obviously, such semiconductor nanostructures are promising for solving various problems of high-temperature nano- and optoelectronics, especially for the experimental implementation of electron-wave analogues of electro-optical modulators. The most striking proposal consists in creating a spin field-effect transistor (SFET) [6–10].

The current modulation in the SFET structure occurs due to quantum interference effects, namely, due to the spin precession caused by Bychkov-Rashba SOI in an ultranarrow quantum well, which is the main element of the field-effect transistor. At the same

time, magnetic contacts, which play the role of source and drain, are preferentially used for injection and detection of certain spin orientations (Fig. 1) [6]. In the SFET structure, the source and drain, which are also a polarizer and analyzer, can be made of a ferromagnet, such as iron. At the Fermi level in such materials, the density of states of an electron with one spin orientation greatly exceeds the density of states with another spin orientation, so that the contact preferentially injects and detects electrons with a certain spin direction. The spin polarization of the current, reaching $\sim 50 \%$ in this case, was experimentally demonstrated using contacts made of permalloy (a magnetically soft alloy of Ni with Fe) [11,12]. A contact magnetized in the x direction preferentially emits and detects spin-polarized electrons along the positive x-axis, which is represented as a linear combination of positive z-polarized and negative z-polarized electrons.

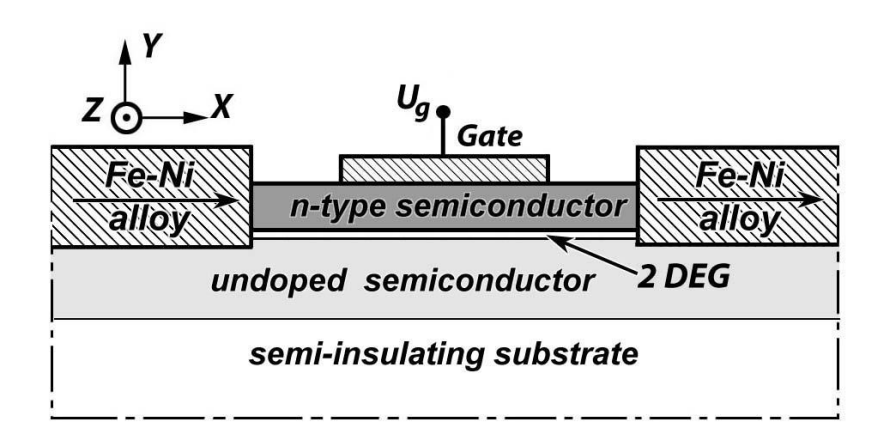


Fig. 1. Diagram of a spin field-effect transistor

By analogy with an electro-optical material, the differential phase shift introduced between +z polarized and -z polarized electrons can be controlled by the vertical gate voltage of the FET, which controls the SOI value in the quantum well [6]. It is assumed that the dominant mechanism of spin energy splitting between electrons with spins up and down in a zero magnetic field, as indicated above, is the Bychkov–Rashba term [13], taken into account in the effective-mass Hamiltonian [6]:

$$H_{R} = \alpha \left(\sigma_{z} k_{x} - \sigma_{x} k_{z} \right), \tag{1}$$

where α is the Rashba SOI parameter, which depending on the type of quantum well conductance is determined by the characteristics of the conduction band or valence band [13–15]. This term is a consequence of the presence of an electric field perpendicular to the plane of the quantum well or the interface of a single heterojunction. Other mechanisms of spin splitting in a zero magnetic field, for example, due to the influence of the inversion center, can also contribute [16]. However, if the quantum well is formed inside the p-n junction, their contribution to the SOI value is much less than the Bychkov–Rashba term. It is easy to see that the Bychkov–Rashba term leads to the fact that +z and -z polarized electrons have the same energy and different wave vectors k_1 and k_2 . Moreover, if we consider an electron moving in the x direction with $k_z=0$ and $k_x\neq0$, the Bychkov–Rashba term H_R is equal to $\alpha\sigma_z k_x$, which increases the energy of +z polarized electrons by αk_x and, respectively, reduces the energy of -z polarized electrons by the same value. A similar change in energy can be achieved if the electron were in a magnetic field B_z proportional to k_x ($\alpha k_x -> \mu_B B_z$, where μ_B is the Bohr magneton).

This energy difference for +z polarized and -z polarized electrons can lead, under the condition of their transport along the x direction, to a differential phase shift, $\Delta\theta$, proportional to the Bychkov–Rashba SOI parameter, the value of which can be varied using the vertical gate voltage

$$E(+z \, pol.) = \hbar^2 \, k_{xl}^2 / 2m^* - \alpha k_{xl}, \tag{2}$$

$$E(-z \, pol.) = \hbar^2 \, k^2_{x2} / 2m^* + \alpha k_{x2}. \tag{3}$$

$$\Delta\theta = (k_{x1} - k_{x2})L = 2m * \alpha L/\hbar^2. \tag{4}$$

Thus, within the framework of the described field-effect transistor structure, current modulation can occur due to spin precession under SOI conditions, thereby identifying the effect of SFET depending on the vertical gate voltage.

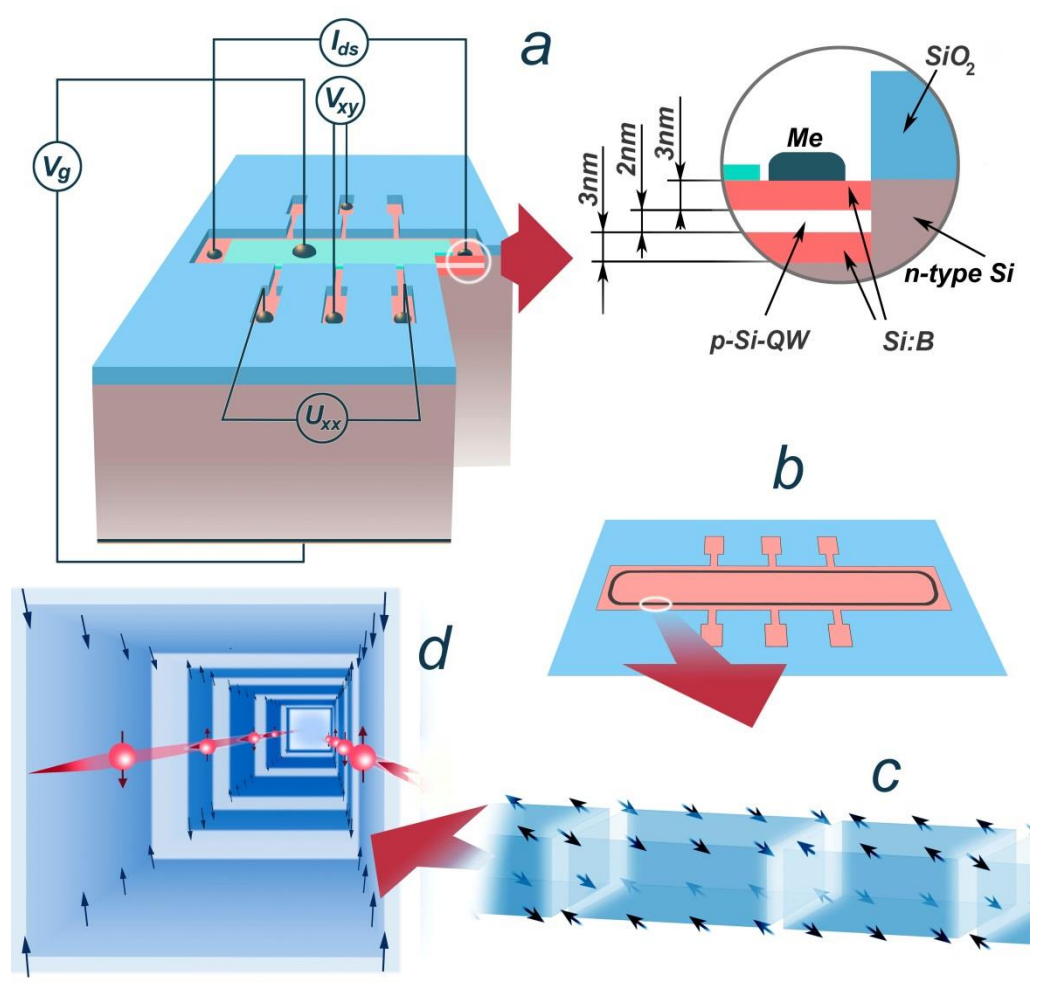


Fig. 2. Experimental SNS made in Hall geometry to demonstrate the SFET effect (a). Topological edge channel of the SNS (b), in which single charge carriers occupy its separate areas, pixels (c). Polarized carriers are transported along opposite pixel walls of the edge channel (d)

The discovery of spin interference in 1D channels contributed to the development of spintronic devices based on the phenomena of spin interference, which are able to demonstrate SFET characteristics even without ferromagnetic electrodes and external magnetic fields in the presence of spin polarization in low-dimensional systems [13,17]. Moreover, it is advisable to create spintronic devices based on topological insulators and superconductors with a control vertical gate, which, in addition to the geometric Berry phase, provides a phase shift between the transmission amplitudes for carriers moving clockwise and counterclockwise [13] (see Fig. 2). This phase shift leads to the observation of Aharonov—

Casher (AC) conductance oscillations, measured by varying the voltage on the vertical gate that controls the transport of single carriers in quasi-one-dimensional channels, even in the absence of an external magnetic field and magnetic electrodes responsible for obtaining and recording the spin polarization of carriers. However, changes in the carrier density that accompany the application of a voltage on a vertical gate can also cause conductance oscillations resulting from changes in the value of the Fermi wave vector, although they are similar in appearance to oscillations in the AC conductance [18,19].

Nevertheless, the unambiguous identification of AC conductance oscillations when controlling the transport of single carriers using a change in the vertical gate, and, consequently, the demonstration of the SFET effect, turned out to be possible when using a silicon nanosandwich structure (SNS) for this purpose.

Methods

In this work, to determine the contribution of the AC effect to the conductance oscillations and to demonstrate the SFET effect, we use an SNS with a diffusion profile depth of 8 nm (according to SIMS data), containing a single quantum well about 2 nm wide. The well is bounded by two δ -barriers consisting of B⁺-B⁻ dipoles with negative correlation energy (negative-U), formed due to the interconnectedness of the electron-vibrational and electron-electron interactions [20]. A similar effect occurs at an ultrahigh concentration of boron dopant in δ -barriers (about 5 10^{21} cm⁻³) [20]. The SNS was made in the Hall geometry and equipped with an additional control electrode, which is used as a vertical gate, to which voltage V_g is applied (Fig. 2(a)). The vertical gate electrode was formed on the surface of a thin (about 20 nm) gate insulator SiO₂ layer preliminarily deposited on the SNS by the plasma-chemical method.

Previous studies of the de Haas–van Alphen (DHVA), Shubnikov–de Haas (SdH) and quantum Hall effects (QHE) [21] showed that in this experimental SNS, the two-dimensional concentration $p_{\rm 2D}$ of single charge carriers in a quantum well bounded by a negative-U δ -barriers is $3\cdot10^{13}$ m⁻². Their behavior is characterized by a long relaxation time and a low value of the effective mass (m* < 10^{-3} m₀) [22].

In addition, it was experimentally demonstrated that the transport of single charge carriers in SNS occurs in topological edge channels (ECs) (Fig. 2(b)), formed in the SNS quantum well by chains of negative-U boron dipole centers [21]. It was shown that it is precisely due to such chains of negative-U dipoles, which form and limit ECs, that conditions are created for the effective suppression of the electron-electron interaction (EEI) in ECs, which, in turn, made it possible to observe the above macroscopic quantum effects in SNS at high temperatures up to the room one [21].

The cross-sectional area of the ECs of the SNS under study is 2×2 nm, since 2 nm is the characteristic distance between the negative-U δ -barriers that form them. Previous experiments showed that the EC of the studied SNS consists of regions of single carrier interference, the length of which is approximately 16 µm, taking into account the value of the 2D density of single carriers determined from Hall measurements [21]. That is, each region of the EC, in which a single carrier ("pixel") is located, consists of layers containing negative-U boron dipoles with an area of $S_{\text{pixel}} = 16 \times 2 \text{ nm}^2$, along which the carrier tunneling occurs (Fig. 2(c)). In this case, the resistance of a single carrier in a pixel is quantized and amounts to $n(h/e^2)$ [21,23].

The spin polarization of single carriers in ECs of such SNSs was observed experimentally, and it was shown that ECs are paired, and the carriers in them have opposite spin orientations [4,21]. Obviously, in such ECs, single carriers have the ability to interfere both in the entire EC (or part of it) and inside a single pixel, since carriers

with different spins move towards each other on opposite sides of the pixel under the action of the field (Fig. 2(d)) [4].

To demonstrate the SFET effect, such an SNS has a number of advantages. First, due to the built-in p-n junction in the QW, the electric field sharply increases, which contributes to an increase in the Bychkov–Rashba SOI. Second, as noted above, the EEI inside the EC is leveled due to the interaction of single carriers with negative-U dipole boron centers, which makes it possible to study the macroscopic phenomena of quantum interference at high temperatures [22]. In addition, it should be noted that, in the SNSs under study, the carriers in ECs are holes, which exhibit a stronger SOI compared to electrons [16].

In order to demonstrate the SFET effect, it is necessary to study the conductance of the SNS EC experimentally by varying the vertical gate voltage $V_{\rm g}$, since in this case it becomes possible to control the Bychkov–Rashba SOI and, thus, the spin polarization of holes in the EC. However, when performing experiments, it should be taken into account that varying the value of $V_{\rm g}$ leads to a change in the concentration and mobility of 2D holes in the QW. This, at first glance, may interfere with the unambiguous identification of the AC conductance oscillations caused by the Bychkov–Rashba SOI, since other effects, such as the influence of the position of the Fermi level, also cause conductance oscillations due to changes in the density and mobility of 2D holes.

The concentration of 2D holes and their mobility in a silicon QW were determined from Hall measurements (Fig. 3) [22]. The initial value of the density of 2D holes $p_{2D} = 4 \cdot 10^{13}$ m⁻² ($V_g = 0$) was controlled by an order of magnitude, between $5 \cdot 10^{12}$ m⁻² and $9 \cdot 10^{13}$ m⁻², by shifting on the vertical gate through the insulator layer, which performs the function p⁺-n junction offsets. It was shown that in the vertical gate voltage range between 150 and 400 mV, p_{2D} is practically independent of V_g . Therefore, this V_g range can be used to identify AC oscillations caused by the Bychkov–Rashba SOI.

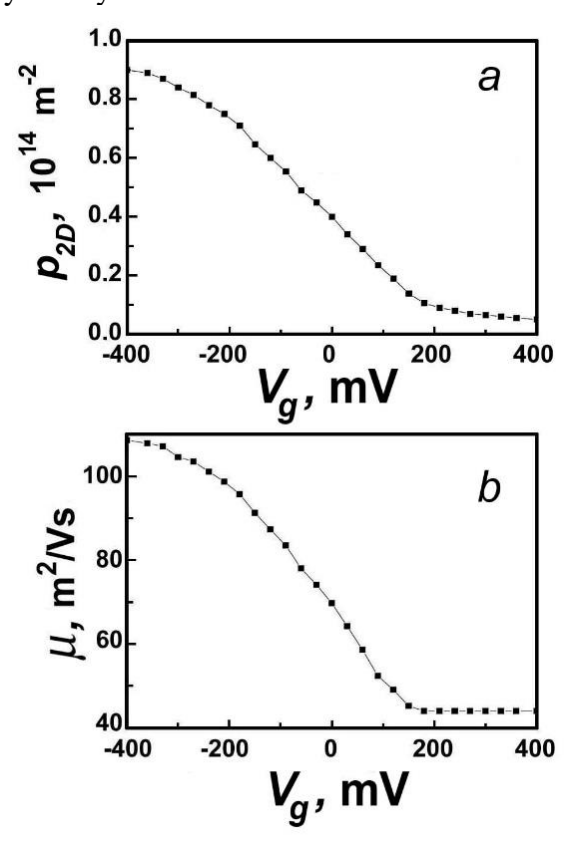


Fig. 3. Density (a) and mobility (b) of a 2D hole gas as a function of vertical gate voltage obtained from measurements of the longitudinal and Hall stresses in the SNS on an n-type Si(100) surface. T=77 K

The experimental conductance dependences on V_g displacement on the vertical gate of the SNS structure made in the Hall geometry (Fig. 2(a)) were obtained at a liquid nitrogen temperature of 77 K. In the experiment, the dependence $U_{xx} = f(V_g)$ was recorded, after which the dependence was calculated $G = f(V_g)$. The measurements were carried out on an experimental bench using Keithley 2182A nanovoltmeters, a Keithley 2010 multimeter, a Keithley 6517A electrometer, and a Keithley 6221 current source. The vertical gate was biased from an independent power source galvanically isolated from the measuring circuit.

As seen in Fig. 2(a), the Hall geometry of the SNS determines its symmetry. For this reason, this article presents the experimental results of measuring U_{xx} for only one pair of the contacts, since U_{xx} measurements on the opposite pair of contacts give equivalent results due to the symmetry of the SNS geometry.

Results

To determine the contribution of the Bychkov–Rashba SOI to the conductance (transmission) of the SNS EC structure, the dependence $U_{xx} = f(V_g)$ was studied under conditions of varying V_g followed by the calculation of the dependence $\Delta G = f(V_g)$. Its analysis made it possible to reveal the spin splitting of holes 44 meV in 1D gas (Fig. 4).

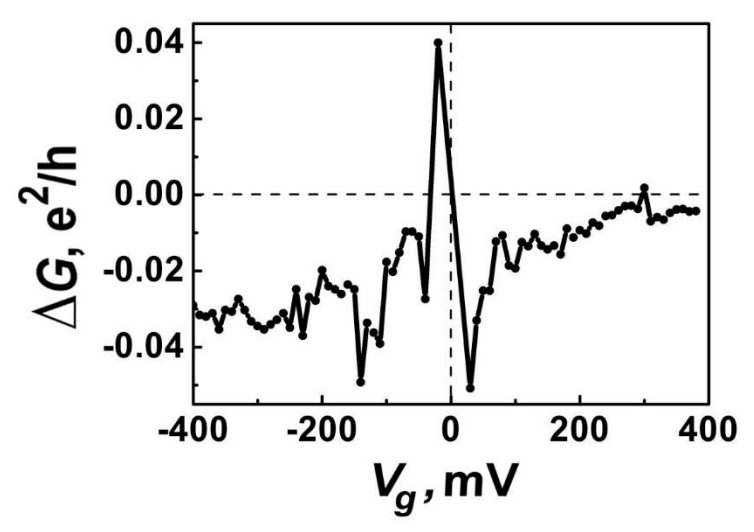


Fig. 4. Conductance change ΔG as a function of the vertical gate voltage applied to the SNS edge channel. T=77 K

The value of the spin splitting 44 meV corresponds to the value of the spin-orbit interaction in the valence band. These data seem to indicate spontaneous spin polarization of heavy holes in the 1D channel due to effective quenching of the kinetic energy by the exchange energy of carriers [4].

Experimental studies of the dependences $\Delta G = f(V_g)$ were carried out in the range $V_g = 150-400$ mV, which makes it possible to unambiguously identify AC oscillations (Fig. 5) caused by the Bychkov–Rashba SOI.

Changes in the phase of the AC oscillations shown in Fig. 5 are apparently caused by the elastic scattering of heavy holes on the quantum point contact inside the EC of SNS. The phase shifts calculated within this model depend on the parameter α determined by the effective magnetic field created by the Bychkov–Rashba SOI [5,6,13–15,18,19,24,25]:

$$\mathbf{B}_{\text{eff}} = \frac{\alpha}{g_B \mu_B} [\mathbf{k} \times \mathbf{e}_z], \tag{5}$$

which affects the conductance modulation [14,15], which is consistent with the oscillations of the AC conductance (Fig. 5). Note that the Bychkov–Rashba SOI in 2D systems cubically depends on the wave vector. However, in a 1D system, it is necessary to average the wave vector components perpendicular to the 1D channel axis. Therefore, the resulting Bychkov–Rashba SOI for 1D hole systems depends linearly on the wave number, as does the Dresselhaus SOI in 1D electron systems [16].

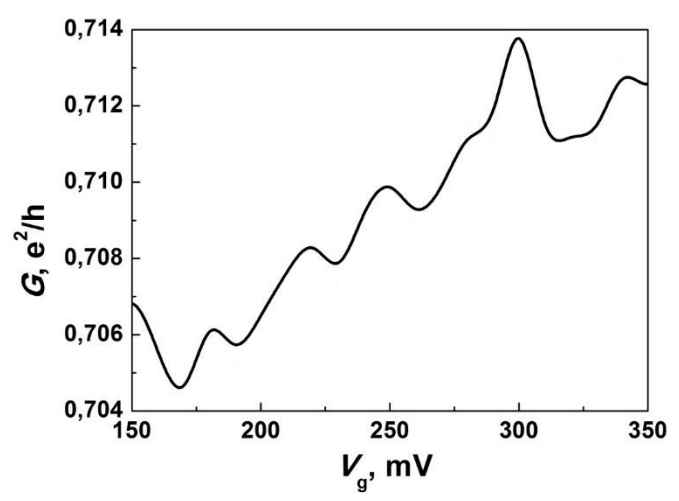


Fig. 5. The Aharonov–Casher conductance oscillations in the edge channel of the SNS. $T=77~\mathrm{K}$

The oscillation period of the AC conductance (ΔV_g), which is determined by the quantum transport of holes through the quantum point contact, can be estimated from the following relations [14,15]:

$$\Delta V_g \approx \frac{h^2 d^2 l}{3\pi^2 R m_{eff} \beta_{hh}},\tag{6}$$

where l is the characteristic length, which provides proportionality between the vertical gate voltage V_g and the electric field, $V_g = Ez \ l$, and is determined by the thickness of the n-type Si(100) plate, l = 300 nm; d is the diameter of the edge channel, 2 nm; R is the effective average pixel radius, the value of which can be controlled by changing the 2D concentration p_{2D} by varying the value of V_g . As mentioned above, to identify the Bychkov–Rashba SOI in these experiments, it is necessary to use a range of V_g values in which the p_{2D} value remains practically unchanged. In this case, the value $R \approx 2500$ nm. The value of β_{hh} is determined by the Bychkov–Rashba parameter α :

$$\alpha_{hh} = -3\beta_{hh} \left\langle k_r^2 \right\rangle E_z \,, \tag{7}$$

$$\beta_{hh} = a\left(\gamma_{2} + \gamma_{3}\right)\gamma_{3}\left[\frac{1}{\varepsilon_{1}^{hh} - \varepsilon_{1}^{lh}}\left(\frac{1}{\varepsilon_{1}^{hh} - \varepsilon_{2}^{lh}} - \frac{1}{\varepsilon_{1}^{hh} - \varepsilon_{2}^{hh}}\right) + \frac{1}{\left(\varepsilon_{1}^{hh} - \varepsilon_{2}^{lh}\right)\left(\varepsilon_{1}^{hh} - \varepsilon_{2}^{hh}\right)}\right]\frac{eh^{4}}{m_{eff}^{2}} \approx 0.02\left[\frac{1}{\varepsilon_{1}^{hh} - \varepsilon_{1}^{lh}}\left(\frac{1}{\varepsilon_{1}^{hh} - \varepsilon_{2}^{lh}} - \frac{1}{\varepsilon_{1}^{hh} - \varepsilon_{2}^{hh}}\right) + \frac{1}{\left(\varepsilon_{1}^{hh} - \varepsilon_{2}^{lh}\right)\left(\varepsilon_{1}^{hh} - \varepsilon_{2}^{hh}\right)}\right]\frac{eh^{4}}{m_{eff}^{2}},$$

$$(8)$$

where the value $\langle k_r^2 \rangle$ is approximately estimated as $\langle k_r^2 \rangle \approx \pi^2/d^2$; d is the diameter of the edge channel $a = \frac{64}{9\pi^2} \approx 0.7$ [11]; $\gamma_2 = -0.18$, $\gamma_3 = -0.1$ are Luttinger parameters for

silicon [26]; $\varepsilon_{1,2}^{lh,hh}$ are the energies of the light and heavy holes in the QW, where the subscript indicates the number of subbands, and the superscript corresponds to a light or heavy hole. Previously, in [27], the results of optical studies were presented, which made it possible to determine the energies of both light and heavy holes in the silicon QW of the SNS used in these experiments: $\varepsilon_1^{hh} = 90 \text{meV}$; $\varepsilon_1^{lh} = 114 \text{meV}$; $\varepsilon_2^{hh} = 307 \text{meV}$; $\varepsilon_2^{lh} = 476 \text{meV}$.

A detailed analysis of the AC conductance oscillations, taking into account the dependence of the 2D hole density $p_{\rm 2D}$ on the vertical gate voltage $V_{\rm g}$ [22], made it possible to determine the values of the effective mass of heavy holes m^* depending on the value of $p_{\rm 2D}$ at the level of $m^* = 10^{-4} - 10^{-3}$ m₀. Note that such a low value of m^* , which is largely a consequence of negative-U δ -barriers limiting the SNS EC, is an important circumstance for the detection of spin-dependent transport at high temperatures (77 K). This makes the properties of SNS similar to those of graphene [28].

Thus, due to the spin polarization of carriers in the edge channels of the SNS, caused by the Bychkov–Rashba SOI, it becomes possible to create a SFET without special ferromagnetic electrodes or any external magnetic fields, while the channel conductance between the source-drain contacts is controlled only by voltage changes at the vertical gate $V_{\rm g}$ (Fig. 6).

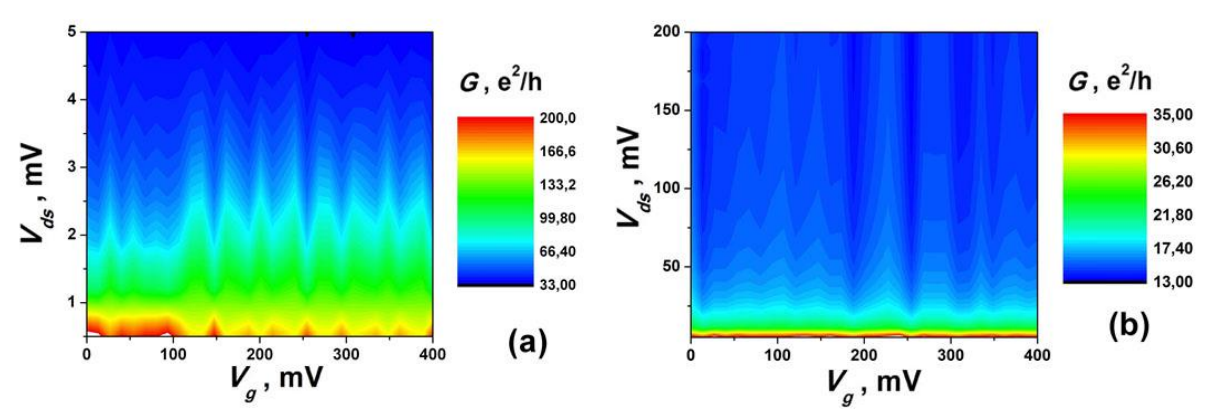


Fig. 6. Diagrams of AC conductance oscillations in a zero magnetic field as a function of the vertical gate voltage V_g , which controls the SOI value, and the source-drain voltage V_{ds} applied to the SNS-based SFET. T=77 K

Oscillations of the AC conductance in the dependence of $G = f(V_g)$, which determine the SFET effect, are described using the relations obtained under the condition of effective backscattering at the quantum point contact [25,29]:

$$G = 2\frac{e^2}{h} \left(1 - \left| B \right|^2 \right),\tag{9}$$

where

$$B(\alpha, E, \Phi) = \frac{\sin^2\left(\frac{\pi m\alpha a}{h^2} + \frac{e\Phi}{2hc}\right)}{1 - \exp\left(2\pi ia\sqrt{\left(\frac{m}{h^2}\right)\left(\frac{m\alpha^2}{h^2} + 2E\right)}\right)\cos^2\left(\frac{\pi m\alpha a}{h^2} + \frac{e\Phi}{2hc}\right)}.$$
(10)

The value of parameter a is determined by the Hall geometry of the contacts and the dimensions of the device structure. In the case of SNS $a=(a_{xx}\cdot a_{xy})^{1/2}$; where a_{xx} and a_{xy} are the distance between contacts XX and XY, $a_{xx}=2$ mm, $a_{xy}=0.2$ mm. These dependences describe conductance oscillations with greater accuracy when varying the value of V_g (also in the case

of a nonzero external magnetic field (Φ =BS)) than a more simplified relation that does not take into account its influence [24]:

$$G = \frac{e^2}{h} \left[1 + \cos\left(2\pi a \frac{\alpha m}{h^2}\right) \right]. \tag{11}$$

The behavior of the AC oscillations shows that the obtained structure is indeed the SFET structure. It should be noted that the magnitude of the amplitude of conductance oscillations at low values of the source-drain voltage ($V_{\rm ds}$) is significantly less than the magnitude of the conductance quantum e^2/h , which may be a consequence of weak localization at a low kinetic energy of low density carriers in the EC (Fig. 5). With an increase in the kinetic energy of carriers in the optimal voltage range $V_{\rm ds}$, the magnitude of the conductance oscillation amplitude corresponds to the conductance value e^2/h (Fig. 6(a)). With a further increase in $V_{\rm ds}$, quenching of conductance oscillations is observed (Fig. 6(b)) as a result of heating of two-dimensional holes and, consequently, a decrease in their spin-lattice relaxation time.

The presented dependences of the conductance (transmission) of the edge channels of the silicon SNS QW $G=f(V_{ds},V_g)$, demonstrating the SFET effect, in fact, are a variant of the AC effect [13,29].

Note that the observation of AC oscillations in hole conduction, illustrating the SFET effect at a high temperature (T = 77 K), became possible due to the high degree of spin polarization of holes and the large time of their spin relaxation. This, in turn, is due to the extremely small width of the silicon QW [30], the narrowness of its ECs, and effective suppression of EEI in them, which is ensured by the properties of the negative-U δ -barriers limiting them.

Conclusions

The paper presents experimental research into dependences of the conductance of the SNS edge channels on the vertical gate voltage $V_{\rm g}$. The studies were carried out in such a range of $V_{\rm g}$, in which the two-dimensional concentration of holes $p_{\rm 2D}$ in the QW is practically independent of the $V_{\rm g}$ value, which makes it possible to avoid the influence of a change in the position of the Fermi level. Therefore, it was possible to avoid the influence of the $p_{\rm 2D}$ change effect in the experiments and ensure unambiguous identification of the AC oscillations.

The effect of a spin transistor at a high temperature (T=77 K) was registered, which manifests itself in the form of the AC oscillations of longitudinal conductance depending on the voltage of the vertical gate, which controls the magnitude of the Bychkov–Rashba SOI.

The observation of AC oscillations in hole conduction, illustrating the effect of a spin transistor at a high temperature (T = 77 K), became possible due to the high degree of spin polarization of holes and the large time of their spin relaxation. This is due to the extremely small width of the silicon QW and its edge channels ensured by the properties of the limiting negative-U-barriers, which effectively suppress EEI.

References

- 1. Wharam DA, Thornton TJ, Newbury R, Pepper M, Ahmed H, Frost JEF, Hasko EG, Peacock EC, Ritchie DA, Jones GAC. One-dimensional transport and the quantisation of the ballistic resistance. *J. Phys. C.* 1988;21(8): L209–L214.
- 2. Van Wees BJ, Van Houten H, Beenakker CWJ, Williamson JG, Kouwenhoven LP, Van der Marel D, Foxon CT. Quantized conductance of point contacts in a two-dimensional electron gas. *Phys. Rev. Lett.* 1988;60(9): 848–850.
- 3. Graham AC, Sawkey DL, Pepper M, Simmons MY, Ritchie DA. Energy-level pinning and the 0.7 spin state in one dimension: GaAs quantum wires studied using finite-bias spectroscopy. *Phys. Rev. B.* 2007;75(3): 035331.

- 4. Bagraev NT, Shelykh IA, Ivanov VK, Klyachkin LE. Spin depolarization in quantum wires polarized spontaneously in a zero magnetic field. *Phys. Rev. B.* 2004;70(15): 155315.
- 5. Bychkov YA, Rashba E I. Oscillatory effects and the magnetic susceptibility of carriers in inversion layers. *J. Phys. C.* 1984;17(33): 6039–6045.
- 6. Datta S, Das B. Electronic analog of the electro-optic modulator. *Appl. Phys. Lett.* 1990;56(7): 665–667.
- 7. Ghiasi TS, Kaverzin AA, Blah PJ, Van Wees BJ, Charge-to-Spin Conversion by the Rashba–Edelstein Effect in Two-Dimensional van der Waals Heterostructures up to Room Temperature. *Nano Lett.* 2019;19: 5959–5966.
- 8. Koch M, Keizer J., Pakkiam P, Keith D, House MG, Peretz E, Simmons MY, Spin readout in atomic qubits in an all-epitaxial three-dimensional transistor. *Nature Nanotech*. 2019;14: 137–140.
- 9. Camenzind LC, Geyer S, Fuhrer A, Warburton RJ, Zumbühl DM, Kuhlmann AV. A hole spin qubit in a fin field-effect transistor above 4 kelvin. *Nat Electron*. 2022;5: 178–183.
- 10. Bhattacharyya K, Debnath D, Chatterjee A. Rashba effect on finite temperature magnetotransport in a dissipative quantum dot transistor with electronic and polaronic interactions. *Sci Rep.* 2023;13: 5500.
- 11. Johnson M, Silsbee RH. Coupling of electronic charge and spin at a ferromagnetic paramagnetic metal interface. *Phys. Rev. B.* 1988;37(10): 5312–5325.
- 12. Meservey R, Paraskevopoulos D, Tedrow PM. Correlation between Spin Polarization of Tunnel Currents from 3d Ferromagnets and Their Magnetic Moments. *Phys. Rev. Lett.* 1976;37(13): 858–860.
- 13. Aronov AG, Lyanda-Geller YB. Spin-orbit Berry phase in conducting rings. *Phys. Rev. Letters.* 1993;70(3): 343–346.
- 14. Winkler R. Rashba spin splitting in two-dimensional electron and hole systems. *Phys. Rev. B.* 2000;62(7): 4245-4248.
- 15. Winkler R, Noh H, Tutuc E, Shayegan M. Anomalous Rashba spin splitting in two-dimensional hole systems. *Phys. Rev. B.* 2002;65(15): 155303.
- 16. Knap W, Skierbiszewski C, Zduniak A, Litwin-Staszewska E, Bertho D, Kobbi F, Robert JL, Pikus GE, Pikus FG, Iordanskii SV, Mosser V, Zekentes K, Lyanda-Geller YB. Weak antilocalization and spin precession in quantum wells. *Phys. Rev. B.* 1996;53(7): 3912–3924.
- 17. Awschalom DD, Loss D, Samarth N. Semiconductor Spintronics and Quantum Computations. Berlin: Springer; 2002.
- 18. König M, Tschetschetkin A, Hankiewicz EM, Sinova J, Hock V, Daumer V, Schäfer M, Becker CR, Buhmann H, Molenkamp LW. Direct Observation of the Aharonov-Casher Phase. *Phys. Rev. Lett.* 2006;96(7): 076804.
- 19. Bergsten T, Kobayashi T, Sekine Y, Nitta J. Experimental Demonstration of the Time Reversal Aharonov-Casher Effect. *Phys. Rev. Lett.* 2006;97(19): 196803.
- 20. Bagraev NT, Gehlhoff W, Klyachkin LE, Naeser A, Rykov S. Quantum-Well Boron and Phosphorus Diffusion Profiles in Silicon. *Defect and Diffusion Forum*. 1997;143–147: 10031008.
- 21. Bagraev NT, Grigoryev VY, Klyachkin LE, Malyarenko AM, MashkovVA, Rul NI. High-temperature quantum kinetic effect in silicon nanosandwiches. *Low Temperature Physics*. 2017;43(1): 132-142.
- 22. Bagraev NT, Galkin NG, Gehlhoff W, Klyachkin LE, Malyarenko AM. Phase and amplitude response of the '0.7 feature' caused by holes in silicon one-dimensional wires and rings. *J. Phys.: Condens. Matter.* 2008;20(16): 164202.

- 23. Klyachkin LE, Bagraev NT, Malyarenko AM. Macroscopic quantum effects of electromagnetic induction in silicon nanostructures. *Mater. Phys. Mech.* 2022;50(2): 252–265.
- 24. Nitta J, Meijer FE, Takayanagi H. Spin-interference device. *Appl. Phys. Lett.* 1999;75: 695–697.
- 25. Shelykh IA, Galkin NG, Bagraev NT. Quantum splitter controlled by Rashba spin-orbit coupling. *Phys. Rev. B.* 2005;72(23): 235316.
- 26. Zitouni O, Boujdaria K, Bouchriha H. Band parameters for GaAs and Si in the 24-k p model. *Semicond. Sci. Technol.* 2005;20(9): 908–911.
- 27. Bagraev NT, Mashkov VA. Danilovsky EY, Gehlhoff W, Gets DS, Klyachkin LE, Kudryavtsev AA, Kuzmin RV. Malyarenko AM, Romanov VV. EDESR and ODMR of Impurity Centers in Nanostructures Inserted in Silicon Microcavities. *Appl Magn Reson*. 2010;39: 113–135.
- 28. Geim AK, Novoselov KS. The rise of graphene. *Nature Mater*. 2007;6(3): 183–191.
- 29. Shelykh IA, Bagraev NT, Galkin NG, Klyachkin LE. Interplay of h/e and h/2e oscillations in gate-controlled Aharonov-Bohm rings. *Phys. Rev. B.* 2005;71(11): 113311.
- 30. Khaetskii AV, Nazarov YV. Spin relaxation in semiconductor quantum dots. *Phys. Rev. B.* 2000;61(19): 12639.

THE AUTHORS

Klyachkin L.E. @

Bagraev N.T.

e-mail: leonid.klyachkin@gmail.com

e-mail: bagraev@mail.ioffe.ru

Malyarenko A.M.

e-mail: annamalyarenko@mail.ru

Gas phase large-scale synthesis of Silicon carbide nanowires by industrial electron accelerator

Submitted: April 16, 2023

Approved: May 8, 2023

Accepted: June 27, 2023

S.P. Bardakhanov ¹⁰ ^{1 ™}, D.Y. Trufanov ¹, I.K. Chakin ², V.R. Gaponenko ¹

¹ Khristianovich Institute of Theoretical and Applied Mechanics of the Siberian Branch of the Russian Academy of Sciences, Novosibirsk, Russia

² Budker Institute of Nuclear Physics of the Siberian Branch of the Russian Academy of Sciences,

Novosibirsk, Russia

☑ bard@itam.nsc.ru

Abstract. This study focuses on the development of a novel and simple catalyst-free one-stage gas phase synthesis process at atmospheric conditions for silicon carbide based nanomaterials. A mixture of high-purity quartz sand and graphite powder is heated as in air as under argon flow at atmospheric pressure using an industrial accelerator of nominal power 100 kW with a relativistic electron beam of continuous action. The carbothermal reduction reaction of silica occurs and micro granular hexagonal silicon carbide powder produced along with cubic phase SiC nanowires (SiCNWs) for different combinations of the process parameters. The mechanism of the formation of SiCNWs under gas flow is proposed, where Si nanoparticles act as an origin for the SiCNWs grow. The observed productivity shows that the process can be used for the large-scale production of high quality SiC nanowires as well as nano and micro powders of SiC.

Keywords: silica; carbon; silicon carbide; nanowires; SiCNWs; industrial electron accelerator

Acknowledgements. Authors are grateful to the Russian Foundation for Basic Research and Novosibirsk Region Government for their support (Grant number 19-43-540013), and V. R. Gaponenko also acknowledges support of this work within the state assignment of Ministry of Science and Higher Education of the Russian Federation.

Citation: Bardakhanov SP, Trufanov DY, Chakin IK, Gaponenko VR. Gas phase large-scale synthesis of Silicon carbide nanowires by industrial electron accelerator. *Materials Physics and Mechanics*. 2023;51(4): 96-106. DOI: 10.18149/MPM.5142023_9.

Introduction

For over a hundred years now, beginning with the Acheson process [1], the carbothermal reduction of silica has been the most widely used method for the synthesis of bulk silicon carbide (SiC) and following production of SiC-based materials at huge industrial scale. Bulk SiC exhibits many preeminent characteristics, including super high hardness and outstanding mechanical robustness, exceptional chemical inertness and corrosion resisting, high melting point (decomposition), low thermal expansion coefficient and excellent thermal stability, suitability for preparation of excellent ceramics, high electron mobility, the last feature is especially useful for highly reliable industrial semiconductor devices.

With regard to obtaining special morphological forms of silicon carbide, the synthesis of SiC nanoparticles started with the nanotechnology era. This trend intensively develops since low dimensionality, quantum confinement and shape effects of SiC nanoparticles demonstrate © S.P. Bardakhanov, D.Y. Trufanov, I.K. Chakin, V.R. Gaponenko, 2023.

Publisher: Peter the Great St. Petersburg Polytechnic University

This is an open access article under the CC BY-NC 4.0 license (https://creativecommons.org/li-censes/by-nc/4.0/)

properties that bulk counterpart cannot possess, what leads to different prospective applications. Respectively, special efforts are devoted to the development of facile methods for the large scale production with cheap raw materials [2,3]. Note, that the gas-phase techniques like plasma synthesis [4,5] and chemical vapor deposition [6], with decomposition of various siloxanes and silanes, are frequently used to produce ultra-small SiC nanoparticles. One can also mention pulsed-laser ablation in liquids [7], but its productivity is not very high.

The growth of elongated whisker-like SiC materials has been a research focus for 50 years now [8,9]. Since the beginning of the 1990s, SiC wires of submicron diameter have been produced using several methods, including the carbothermal reduction of silica [10]. And at the end of the twentieth century, the synthesis of SiC nanowires (SiCNWs) has attracted considerable attention owing to their importance in basic scientific research as well as their potential technological applications [11–13]. The number of papers in this area is about of three hundred now. The availability of large volumes of SiCNWs can lead to immense progress in advanced applications, including photocatalysts, electronics such as emitters, transistors, and sensors, thermal and photoelectric applications, etc.

To date, a variety of methods, both conventional (e.g., carbothermal reduction of silica) and unconventional, used for SiCNW production have been reported [8]. Based on published studies, it can be concluded that most of these methods require the use of expensive raw materials, catalysts, and sophisticated techniques. Additionally, only a few of these studies have reported the synthesis of relatively large quantities of SiCNWs. For instance, the confined reaction method was used for the initial synthesis of carbon nanotubes (CNTs), and the productivity of SiCNWs was 2 g per batch of 15 min [14]. However, the full procedure also included the preparation of a Fe/Ni catalyst and the growth of the CNTs for 1 h. In another study which employed a SiO carbothermal reduction approach using carbon black, relatively specific materials (SiO was commercial and carbon black was treated by arc-discharge plasma for the porosity), were used in 1-h experiments in high-frequency induction furnace, and it was possible to produce 200 g of SiCNWs per day [15]. Other study demonstrated the possibility of synthesizing 3.5 g of SiCNWs within 7 h using expandable graphite (EG) and silicon powder [16]. As the sample of the great efforts to increase the productivity, one could mention the paper [17].

Current research on SiCNWs has been summarized in a recently published book, which highlights the different mechanisms by which SiCNWs can be produced directly from raw materials in the vapor state via the vapor-liquid-solid (VLS) and/or vapor-solid (VS) routes [13]. And in very recent paper [18] it is noted again, that the most of existing methods involve environmentally corrosive and toxic chemicals, or complicated multistep reactions, resulting in much environmental pollution and low efficiency of nanoscale SiC synthesis in a large scale. So, the production of large quantities of high quality SiCNWs using more controllable, predictable, and facile processes is still challenging [13]. Therefore, it is essential to develop a rapid, low-cost, eco-friendly and sustainable preparation strategy for SiC nanowires.

It looks like the carbotermal reduction nowadays could be the most promising base for the large scale production of SiC nanostructures, including SiCNWs. Then the effective heater is necessary to use for this purpose. For our case, it is the electron beam.

It is not widely known, but the electron beam guns are extensively used as concentrated energy source in various material processing applications [19], including welding [20], drilling [21], generation of metal vapor for isotope purification process [22,23] and physical vapor deposition [24]. Therefore, the electron beam is a useful thermal energy source in surface modification, cladding, surfacing, rapid prototyping, engraving as well as texturing, thin film metal and ceramics coating, e.g. [25] preparation technique.

If to say just about welding industry, there are no statistics available to show exactly how many electron beam welding machines are in use worldwide. But it is estimated that the total number of electron beam welding machines is about 3500 in the whole world [21]. Owing to their industrial applications, metal melting and evaporation with e-beam or laser beam systems has been studied extensively in literature, e.g. [26–29].

To emphasize the nanotechnology applications, besides film deposition with nanocrystals [30], the electron beam evaporation (EBE, as with continuous as pulsed beam) is used for high entropy alloys [31], nanoparticles' production [32,33]. In fairness, the papers [34,35] should be noted, where to the best of our knowledge, the first attempt was made to purposefully obtain a noticeable amount of oxide nanopowders using electron beam evaporation. But they used the installation of only 1 kWt with a voltage in the range 15 to 30 kV and oxygen at a pressure of 7 Pa.

But in spite of widespread electron beam technologies, all of them had a serious disadvantage in the sense of large scale production of nanomaterials. The usual energy produced range was not more than 400 keV. Therefore, previous commercial EBE could be used only at vacuum environment or in low-pressure gas, mostly not more than 100 Pa. At non vacuum conditions, the energy of the electrons scatters by gas molecules, and the electron beam without enough energy cannot be used as the powerful heater. In 80s this barrier had been override by introducing the new kind of industrial accelerator developed by Budker Institute of Nuclear Physics with focused electron beam extracted into atmosphere [36]. And we employ this facility since 1992 for the gas phase synthesis of nanomaterials [37–39].

Further, a critical analysis is the following of the pros and cons of our electron beam heating method. Actually, it is almost fully copied from very recent paper [40] of our colleagues. And this analysis compares the laser beam and electron beam heating.

Laser cladding is considered to be an effective process for the fabrication of different coatings. This technology has such advantages as high power density, beam focusing accuracy, and perfect beam position control. At the same time, the laser cladding technology also has a number of disadvantages, such as a low efficiency coefficient and a low depth of radiation penetration, which make it difficult to obtain cladded layers of considerable thickness.

The electron beam as an energy source seems to be an attractive alternative to a laser for applications in cladding technologies. Traditional electron beam processing is carried out in vacuum chambers at a beam energy of 20–400 keV. Around 90 % of the electron beam energy is absorbed by the metals, which is one of the main advantages of the electron beam, especially taking into account that the absorption of the laser radiation may be as low as 3-7 %. However, a convenient electron beam treatment has a number of limitations. Firstly, the processing of large surfaces is quite complicated since the treated items must be placed in a vacuum chamber. The other disadvantage is the relatively small penetration depth of electrons into the material due to the relatively low electron beam energy. For instance, the maximum penetration depth of electrons with an energy of 200 keV in Ti is 0.13 mm, and for electrons with an energy of 400 keV, it reaches 0.66 mm.

The non-vacuum electron beam cladding technology is free of the aforementioned disadvantages. High-energy electron accelerators developed by Budker Institute of Nuclear Physics provide high-power electron beams with an energy of 1.4 MeV. A specially designed vacuum system allows for the direct injection (without any foil) of the electron beams in the air wth atmospheric pressure. Due to the high initial energy, electrons penetrate the material to a depth of about 2 mm (for Ti and other elements with similar atomic numbers), which provides rapid heating of the surface layer [36]. Note, that for the evaporation purpose laser beam is less suitable due to scattering on high concentration vapor, and its efficiency strongly depends on treated target material. The high energy electron beam is free of such disadvantages. As for the gas phase production of nanomaterials (nanoparticles, nanopowders), in difference with

vacuum conditions, such facility allows fully independent control of electron beam power and gas transportation through the evaporation region at arbitrary flow rate in surrounding atmospheric pressure.

Therefore, this study aims at developing a novel and facile catalyst-free one-stage process for the production of large quantities of coarse SiC and SiCNWs powders by employing carbothermal reduction via the vaporization of a mixture of high purity quartz sand (silica) and high purity graphite (carbon) using for the first time an industrial accelerator acting at atmospheric pressure with continuous gas flow.

Methods

The high purity quartz sand and high purity graphite powder were mixed in the ratio of 1:2. Industrial accelerator ELV-6, having a power of 100 kW and a relativistic electron beam with initial energy 1.4 MeV, was used as continuous beam source. This energy value provides a 5 m path in the 101.325 kPa (1 atm) air pressure until the energy is completely dissipated. The scheme of accelerator is presented at Fig. 1. The scale 5 meters denotes the approximate total height of accelerator together with under-beam equipment. H1, H2, H3 are the sections of differential pumping separating inner high vacuum from the outer atmospheric pressure. Notation D is the local electron beam diameter at the certain distance from the accelerator outlet. Design details can be found in paper [40].

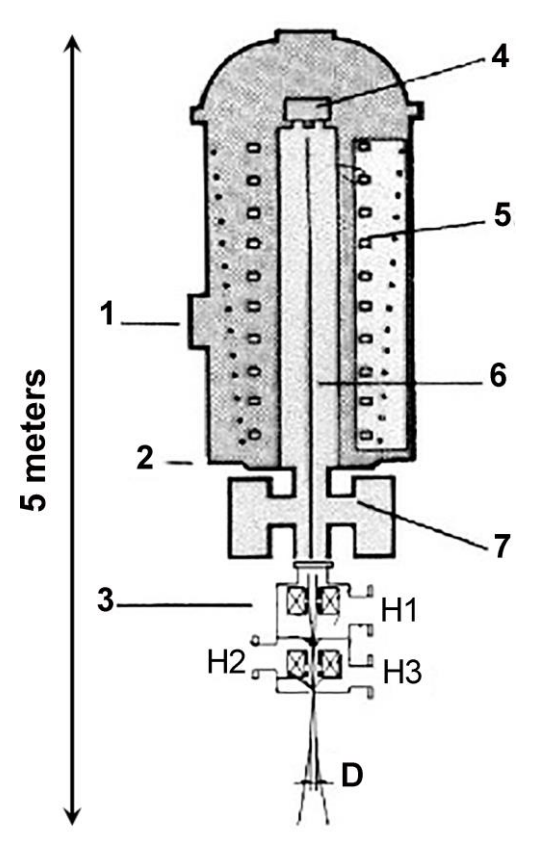


Fig. 1. The scheme of the ELV-6 electron beam accelerator: 1 – power supply system,

- 2 –water cooling system, 3 focused beam release system, 4 electron gun,
- $5-high-voltage\ rectifier,\ 6-accelerating\ tube,\ 7-magnetic\ discharge\ pumps,$

D – local diameter of electron beam

A unique feature of this equipment is the ability to inject a narrow beam directly into the atmosphere, thus, offering the possibility of heating rate more than a thousand degree per second and easy vaporization of any material at normal pressure, in difference with other

electron beam technologies which usually require vacuum in the treatment chamber. It leads to another advantage, consisting of continuous gas flow control independently of electron beam power. Production of nanopowders from raw materials in the gas phase, including the semi-industrial scale (that is still in operation since 2005 with the yield more than 7 kg h⁻¹ at 70 kW for the silica nanopowder) have been reported [37–39]. The measured dependence of yield versus electron beam power is exponential, for instance, at 100 kW it is about 30 kg h⁻¹.

In this study, a medium-size treatment chamber (sublimator) was used. The detailed scheme of facility used for the nanopowder production is presented at Fig. 2. It has been discussed in a previous study [41]. The raw mixture was loaded into the sublimator. The sublimator is a water-cooled closed stainless-steel cylinder into which an electron beam can be injected through a 2 mm diameter hole at the top. The gas passes through sublimator and together with condensed nanoparticles moves along the gas path to filter that capture fine powders.

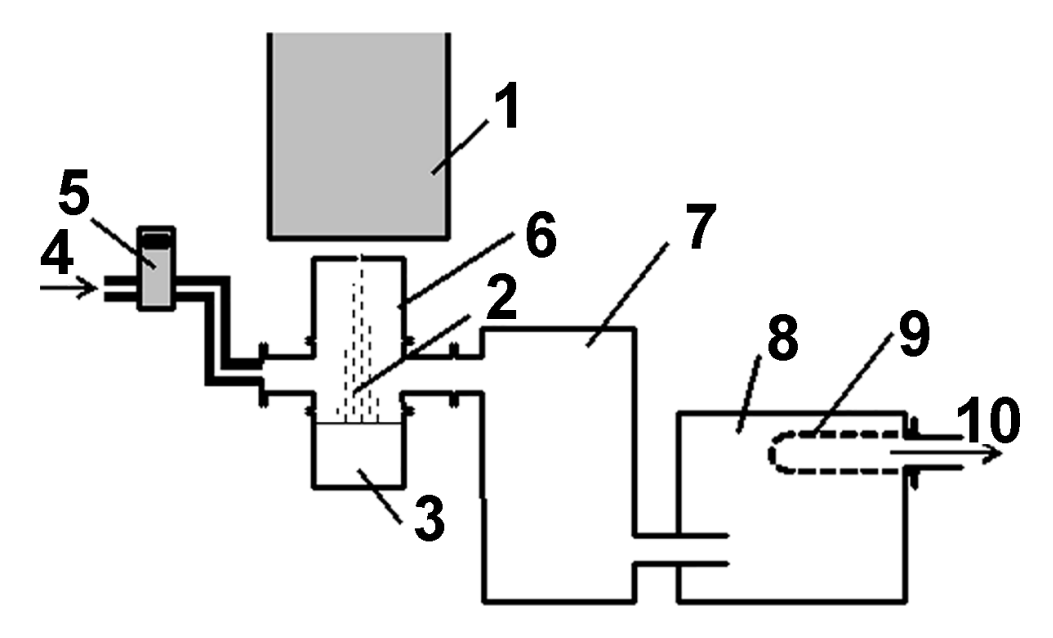


Fig. 2. The scheme of experimental path: 1 - electron accelerator; 2 - electron beam down from accelerator; 3 - target material; 4 - carrier gas supply channel; 5 - electronic flow regulator; 6 - water-cooled sublimator; 7 - coarse fraction separator; 8 - plastic box; 9 - fabric bag filter; 10 - outlet of carrier gas

The series of experiments involved the treatment of the SiO₂/C mixture with forced argon blowdown at a gas flow rate of 12 L min⁻¹ with a beam power of 6 kW. The specific surface area of the powders was measured by Brunauer-Emmett-Teller (BET) method. X-ray diffraction (XRD, Bruker D8 Advance New X-ray diffractometer) and transmission electron microscopy (JEM-2200FS, JEOL Ltd.) with energy-dispersive spectroscopy (EDS) were used for the detailed analysis of the nanomaterials.

Results and Discussion

The pattern of the substance inside the sublimator after experiment is illustrated in Fig. 3. TEM and EDS showed that powder 1, deposited in the region surrounding the beam exposure zone 2, and filament 3, which formed above the heated region, consisted of light-brown, fluffy, and amorphous silicon monoxide (SiO). They condensed from the corresponding vapor resulting from the high-temperature reaction that occurred when the SiO₂/C mixture was heated by the electron beam.

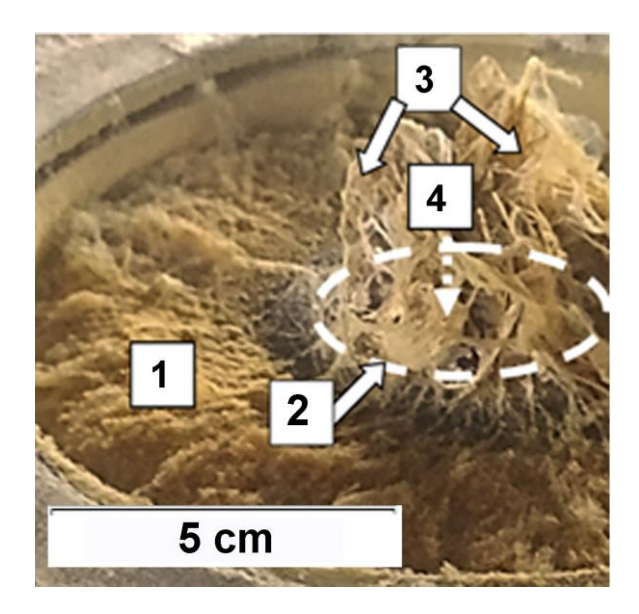


Fig. 3. Pattern of the deposited substance in the sublimator at beam power of 6 kW. 1, zone outside of electron beam; 2, electron beam heating zone; 3, silicon monoxide filaments; 4, electron beam direction

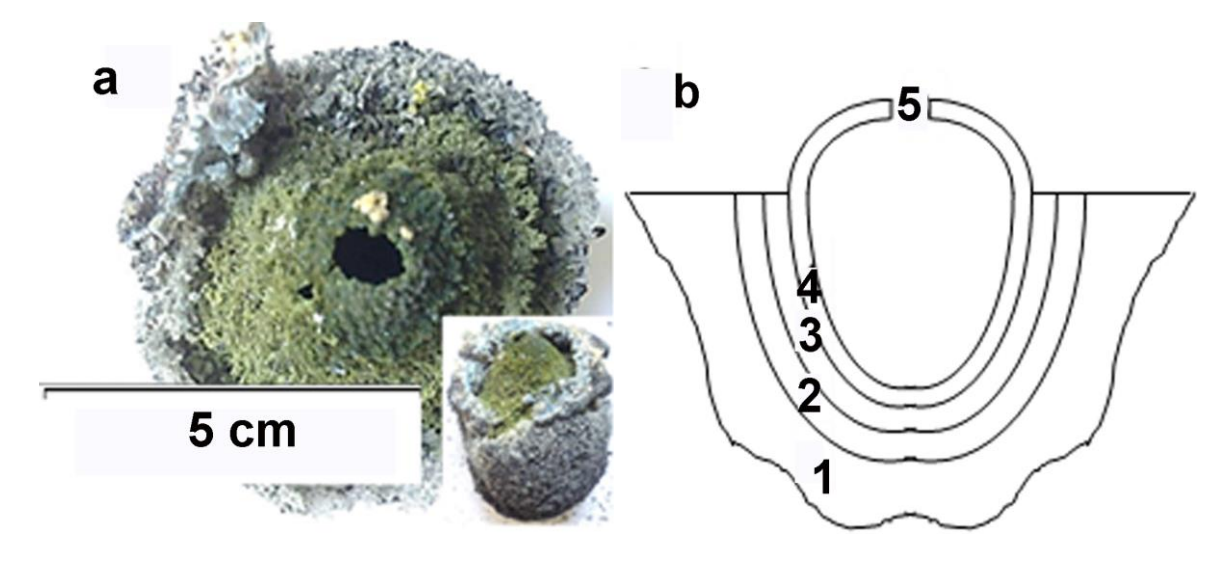


Fig. 4. Egg-like structure: (a) top view (Inset: Typical side view); (b) scheme of internal structure: 1, surrounding raw mixture; 2, sintered layer of quartz sand with graphite; 3, porous black-gray uniform layer of melted silica and carbon; 4, green shell of closed cavity; 5, electron beam entry

The region of exposure close to the center of the sublimator (indicated by arrow 4) had a special structure. Figure 4 shows an egg-like structure that was excavated from the heated area (zone 2, Fig. 3). The top view of the egg-like structure (main field of Fig. 4(a)) revealed its average diameter to be ~ 60 mm. At the center, a hole with diameter within the range of 10-15 mm, representing the point of entry of the electron beam, was observed. The average height of the whole egg-like structure (Inset, Fig. 4(a)) was ~ 70 mm. The internal texture of the egg-like structure is presented in Fig. 4(b). It reveals the presence of constituent layers, of which layer 4 (green shell) was highly porous and could easily be transformed into a microscopic powder. This powder consisted of approximately 100% of SiC hexagonal 6H α structure (JSPDS No. 42–1360).

The powders collected further downstream in the parts of the whole installation (e.g. filter) had a very fluffy texture, and were green-brown in color. The results showed that the samples typically had a specific surface area of $\sim 100~\text{m}^2~\text{g}^{-1}$, and X-ray analysis revealed that they consisted of cubic SiC (JSPDS No. 29–1129). Figure 5(a) shows that the powder predominantly consisted of smoothly curved and entangled rods with diameter in the range of $\sim 15-30~\text{nm}$, and the magnified image of Fig. 5(b) established the "nanocables". EDX spectra also revealed that the inner nanorods consisted of Si and C with the atomic ratio 1:1. The outer cover consists of amorphous silica.

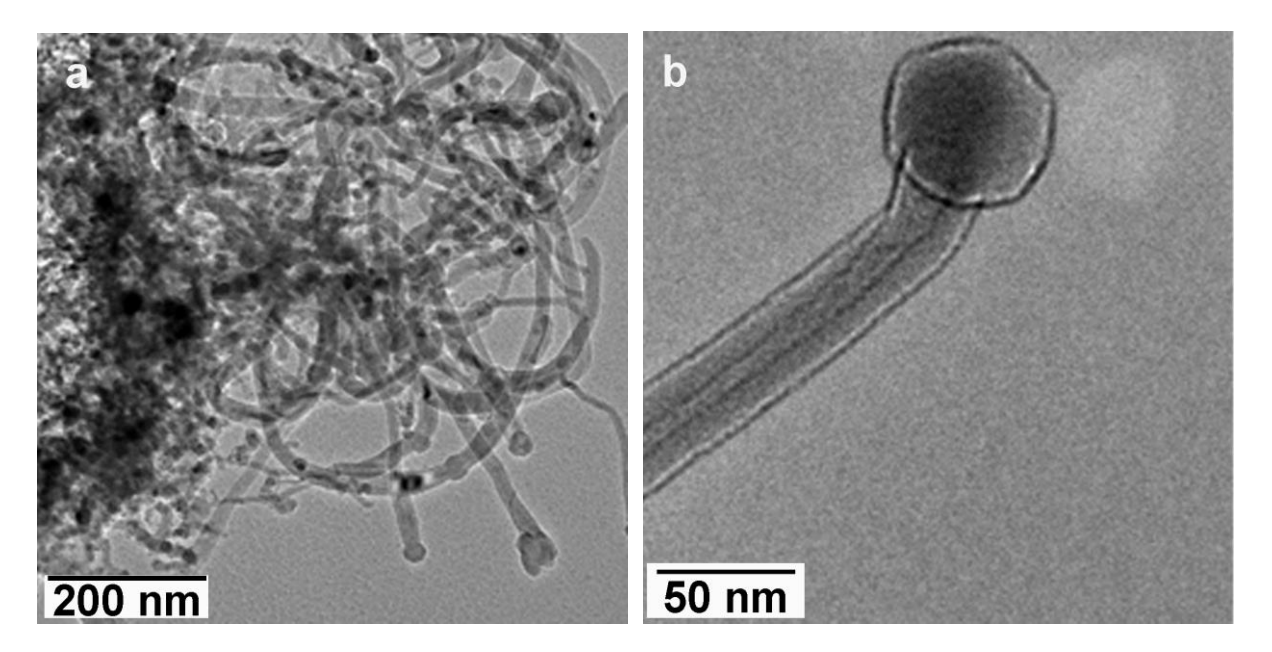


Fig. 5. Species morphology of nanowires:

(a) general view of nanowires; (b) single silicon nanoparticle integrated with SiCNW

In all the samples, free silicon was present as nanoparticles. Firstly, as shown in Fig. 5(b), they appeared as a nanocable head, and secondly, a smaller proportion appeared as relatively detached silicon nanoparticles. Electron-diffraction pattern of them, usually interpreted in the literature as nanocrystalline silicon.

Based on the results of this study, a possible mechanism that highlights a few key events associated with the production of SiCNW has been proposed for the carbothermal reduction under powerful electron beam treatment. Equations (1) and (2) represent solid to vapor reactions that occurred inside the egg-like structure owing to the heating effect of the electron beam:

$$SiO_{2(s)} + C_{(s)} \rightarrow SiO_{(g)} + CO_{(g)} \qquad , \tag{1}$$

$$C_{(s)} \rightarrow C_{(g)}$$
. (2)

Equations (3) and (4) represent the solid-to-liquid and liquid-to-vapor reactions.

$$SiO_{2(s)} + 2C_{(s)} \rightarrow Si_{(l)} + 2CO_{(g)}$$
 (3)

$$Si_{(1)} \rightarrow Si_{(g)}$$
 (4)

Layer 4 of the egg-like structure (Fig. 2(b)) was possibly formed according to Equations (5) and (6), resulting in the deposition of hexagonal SiC.

$$SiO_{(g)} + 3CO_{(g)} \rightarrow SiC_{(s)} + 2CO_{2(g)}$$

$$\tag{5}$$

$$SiO_{(g)} + 2C_{(g)} \rightarrow SiC_{(s)} + CO_{(g)}$$
(6)

The Equation (3) is a well-known overall reaction for the industrial production of silicon by carbothermal reduction in big furnaces. The resulting quantity of liquid Si (which is usually collected from the bottom of the furnace as a target product) depends on the initial ratio of SiO_2

and C. The industrial process also results in production of large quantities of SiO according to Equation (1).

In this study, some quantities of Si and CO were also produced. As for the elementary Si, the results of our earlier studies showed that pure silicon ingots can easily be melted and evaporated by the electron beam according to Equation (4), and with subsequent cooling in inert gases, it is possible to produce large quantities of silicon nanopowders composed of nanoparticles covered by a thin layer of amorphous silica [42]. In this study, we assume that the reduced silicon in liquid phase in the bottom of the egg-like structure, is vaporized by the electron beam.

At the electron beam exposition, the carbon can be evaporated with a large yield of condensed carbon substance [36]. Therefore, Equation (2) yields gaseous carbon. Thus, the generation of SiO, Si, CO and C (as sources of Si and C) is possible in our process.

In this study, the SiC nanorods were not observed inside egg-like structures. This suggests that SiC nanorods originate in the outer gaseous flow. In the flowing argon environment, SiO_(g) and CO_(g) interacted according to Equation (5) and possibly according to Equation (6) as well, forming SiC precursors. Silicon vapor was also generated from the heated zone, and it was considered that in the cooling atmosphere, the solidifying silicon nanoparticles resulting from Equation (4) acted as a catalyst, providing a surface on which SiCNWs grew in the gas stream. The similar supposition was made in paper [43]. The same conjecture was reported for the formation of some quantities of SiC nanorods for the specific ratio SiO₂/CH₄H at the thermal plasma synthesis [44]. We suppose that more recent papers [45-47] also support the probability of topochemical reactions at the surface of solidifying silicon nanoparticles.

The potential yield of SiCNWs could be estimated, based on our current and previous results. The total productivity G was about 0.2 kg h⁻¹ for 6 kW of electron beam power P. Assuming that the function G(P) was linear, the productivity would have been \sim 3 kg h⁻¹ at P = 100 kW. Instead, an exponential relationship was observed when an electron beam was used as a heater, at correspondent scaling the yield would be higher than 5 kg h⁻¹.

Conclusions

In this study, we have proposed a novel and simple catalyst-free one-stage process for synthesis of SiCNWs through carbothermal reduction reaction that employs the relativistic electron beam of a high-power industrial accelerator at atmospheric pressure. The process is continuous and allows the independent control of power and gas flow. The mechanism of SiCNWs formation under gas flow is proposed according to which the SiCNWs grow originates on the Si nanoparticles.

References

- 1. Acheson G. Carborundum. US492767 (Patent) 1893.
- 2. Beke D, Valenta J, Karolyhazy G, Lenk S, Czigany Z, Markus BG, Kamaras K, Simon F, Gali A. Room-temperature defect qubits in ultrasmall nanocrystals. *J. Phys. Chem. Lett.* 2020;11(5): 1675–1681.
- 3. An Z, Xue J, Cao H, Zhu C, Wang H. A facile synthesis of silicon carbide nanoparticles with high specific surface area by using corn cob. *Advanced Powder Technology*. 2019;30(1): 164–169.
- 4. Czosnek C, Bucko MM, Janik JF, Olejniczak Z, Bystrzejewski M, Labedz O, Huczko A. Preparation of silicon carbide SiC-based nanopowders by the aerosol-assisted synthesis and the DC thermal plasma synthesis methods. *Materials Research Bulletin*. 2015;63: 164–172.
- 5. Wang C, Zhou J, Song M, Chen X, Zheng Y, Yang C, Xia W, Xia W. Fabrication of ultra-small SiC nanoparticles with adjustable size, stoichiometry and photoluminescence by AC multi-arc plasmas. *Ceramics International*. 2022;48: 632–641.

- 6. Liu R, Liu M, Chang J. Large-scale synthesis of monodisperse SiC nanoparticles with adjustable size, stoichiometric ratio and properties by fluidized bed chemical vapor deposition. *J. Nanopart. Res.* 2017;19: 26.
- 7. Zhu J, Hu S, Wang W, Xia W, Chen H, Chen X. Luminescent amorphous silicon carbide ultrafine nanoparticles fabricated by pulsed-laser ablation. *Appl. Phys. A*. 2017;123: 244.
- 8. Prakash J, Venugopalan R, Tripathi BM, Ghosh SK, Chakravartty JK, Tyagi AK. Chemistry of one dimensional silicon carbide materials: Principle, production, application and future prospects. *Prog. Solid State Chem.* 2015;43: 98–122.
- 9. Li X, Liu Q, Chen S, Li W, Liang Z, Fang Z, Yang W, Tian Y, Yang Y. Quasi-aligned SiC@C nanowire arrays as free-standing electrodes for high-performance microsupercapacitors. *Energy Storage Mater.* 2020;27: 261–269.
- 10. Liang J, Guo W, Liu J, Qin H, Gao P, Xiao H. Synthesis of in-situ SiC nanowires by self-assembly nanoparticles on carbon fibers and their photoluminescence properties. *J. Alloys and Compd.* 2019;797: 101–109.
- 11. Meng GW, Zhang LD, Qin Y, Mo CM, Phillipp F. Synthesis of beta-SiC nanowires with SiO2 wrappers. *Nanostruct. Mater.* 1999;12: 1003–1006.
- 12. Yang P, Yan R, Fardy M. Semiconductor Nanowire: What's Next? *Nano Lett.* 2010;10(5): 1529–1536.
- 13. Chen S, Li W, Li X, Yang W. Silicon carbide nanowires and electronics. In: Shen G, Chueh YL. (eds.) *Nanowire Electronics: Nanostructure Science and Technology*. Singapore: Springer; 2019. p.237–335.
- 14. Chiu SC, Li YY. SiC nanowires in large quantities: Synthesis, band gap characterization, and photoluminescence properties. *J. Cryst. Growth.* 2009;311(4): 1036–1041.
- 15. Wang FL, Zhang LY, Zhang YF. SiC nanowires synthesized by rapidly heating a mixture of SiO and arc-discharge plasma pretreated carbon black. *Nanoscale Res Lett.* 2009;4: 153–156.
- 16. Chen J, Shi Q, Xin L, Liu Y, Liu R, Zhu X. A simple catalyst-free route for large-scale synthesis of SiC nanowires. *J. Alloys and Compd.* 2011;509(24): 6844–6847.
- 17. Li ZJ, Yu HY, Song GY, Zhao J, Zhang H, Zhang M, Meng AL, Li QD. Ten-gram scale SiC@SiO2 nanowires: high-yield synthesis towards industrialization, in situ growth mechanism and their peculiar photoluminescence and electromagnetic wave absorption properties. *Phys. Chem. Chem. Phys.* 2017;19 (5): 3948–3954.
- 18. Yang B, Sun R, Li X, Ma M, Zhang X, Wang Z, Yi W, Zhang Z, Yang R, Sun H, Gao G, Chu Y, Zhao Z, Liu X. Rapid fabrication of hierarchical porous SiC/C hybrid structure: toward high-performance capacitive energy storage with ultrahigh cyclability. *J. Mater. Sci.* 2021;56 16068–16081.
- 19. Kumar VD, Mazumder A, Alangi N, Mukherjee J, Sethi S. Evaluation of crucible for cold hearth transverse electron beam vapor generator. *Case Studies in Thermal Engineering*. 2021;27: 101318.
- 20. Węglowski MS, Blacha S, Phillips A. Electron beam welding-techniques and trends-review. *Vacuum*. 2016;130: 72–92.
- 21. Leitz KH, Koch H, Otto A, Alexander M, Lower T, Schmidt M. Numerical simulation of drilling with pulsed beams. *Physics Procedia*. 2012;39: 881–892.
- 22. Anklam TM, Berzins LV, Hagans KG, George K, McClelland M.A, Scarpetti RD, Shimer DW. Uranium AVLIS vaporizer development. In: *Proc. SPIE 1859, Laser Isotope Separation* 1993. 1993. p.277–286.
- 23. Greenland PT. Laser isotope separation. *Contemp. Phys.* 1990;31(6): 405–424.
- 24. Singh J, Wolfe D. Review Nano and macro-structured component fabrication by electron beam-physical vapor deposition (EB-PVD). *J. Mater. Sci.* 2005;40: 1–26.

- 25. Oks EM, Tyunkov AV, Yushkov YG, Zolotukhin DB. Ceramic coating deposition by electron beam evaporation. *Surface and Coatings Technology*. 2017;325(25): 1–6.
- 26. Powell A, Pal U, Avyle JVD, Damkroger B, Szekely J. Analysis of multicomponent evaporation in electron beam melting and refining of titanium alloys. *Metall. Mater. Trans. B*. 1997;28(6): 1227–1239.
- 27. Klassen A, Forster VE, Juechter V, Körner C. Numerical simulation of multi-component evaporation during selective electron beam melting of TiAl. *Journal of Materials Processing Technology*. 2017;247: 280–288.
- 28. Zhao Y, Aoyagi K, Yamanaka K, Chiba A. Role of operating and environmental conditions in determining molten pool dynamics during electron beam melting and selective laser melting. *Additive Manufacturing*. 2020;36: 101559.
- 29. Amine T, Newkirk JW, Lioua F. An investigation of the effect of direct metal deposition parameters on the characteristics of the deposited layers. *Case Studies in Thermal Engineering*. 2014;3: 21–34.
- 30. Efremova SL, Salatov AV, Kulikova DP, Kasyanov AA, Bykov IV, Afanasev KN, Tananaev PN, Baryshev AV. On the fabrication of one-dimensional magnetophotonic crystals from various oxides and metal—organic decomposition-made Bi0.5Y2.5Fe5O12. *Journal of Physics D: Applied Physics*. 2021;54(50): 505305.
- 31. Ustinov AI, Polishchuk SS, Demchenkov SA, Melnychenko TV, Skorodzievskii VS. Formation of thin foils of high-entropy CrFeCoNiCu alloys by EB-PVD process. *Surf. Coat. Technol.* 2020;403: 126440.
- 32. Sokovnin SY, Il'ves VG, Zuev MG. Production of complex metal oxide nanopowders using pulsed electron beam in low-pressure gas for biomaterials application. In: Grumezescu AM. (ed.) *Engineering of Nanobiomaterials. Applications of Nanobiomaterials.* 2016;2: 29–75.
- 33. Ilves VG, Gaviko VS, Malova OA, Murzakaev AM, Sokovnin SY, Uimin MA, Zuev MG. Phase transformation in vacuum and basic physicochemical properties of heterophasic amorphocrystalline Bi2O3-based nanopowder produced by pulsed electron beam evaporation. *Journal of Alloys and Compounds*. 2021;881: 160514.
- 34. Ramsay JDF, Avery RG. Ultrafine oxide powders prepared by electron beam evaporation. Part 1 Evaporation and condensation processes. *Journal of Materials Science*. 1974;9: 1681–1688.
- 35. Ramsay JDF, Avery RG. Ultrafine oxide powders prepared by electron beam evaporation. Part 2 Powder characteristics. *Journal of Materials Science* 1974;9: 1689–1695.
- 36. Fadeev SN, Golkovski MG, Korchagin AI, Kuksanov NK, Lavruhin AV, Petrov SE, Salimov RA, Vaisman AF. Technological applications of BINP industrial electron accelerators with focused beam extracted into atmosphere. *Radiation Physics and Chemistry*. 2000;57(3–6): 653–655.
- 37. Lukashov VP, Bardakhanov SP, Salimov RA, Korchagin AI, Fadeev SN, Lavruhin AV. A way to obtain the ultrafine silica powder, device for its realization and ultrafine silica powder. RU2067077 (Patent) 1994.
- 38. Bardakhanov SP. The formation of fine silica powder after vaporization of quartz. In: *Proc. 5th Int. Conf. Computer Aided Design of Adv. Materials and Technologies (CADAMT'97), Baikal Lake, Russia.* 1997. p.88–89. (In-Russian)
- 39. Bardakhanov SP, Korchagin AI, Kuksanov NK, Lavrukhin AV, Salimov RA, Fadeev SN, Cherepkov VV. Nanopowder production based on technology of solid raw substances evaporation by electron beam accelerator. *Mater Sci Eng B.* 2006;132: 204–208.
- 40. Ruktuev AA, Golkovski MG, Lazurenko DV, Bataev VA, Ivanov IV, Thommes A, Bataev IA. Ti–Ta–Nb clads produced by electron beam surface alloying in regular air at

atmospheric pressure: Fabrication, structure, and properties. *Materials Characterization*. 2021;179: 111375.

- 41. Zavjalov AP, Zobov KV, Chakin IK, Syzrantsev VV, Bardakhanov SP. Synthesis of copper nanopowders using electron-beam evaporation at atmospheric pressure of inert gas. *Nanotechnologies in Russia.* 2014;9: 660–666.
- 42. Efremov MD, Volodin VA, Marin DV, Arzhannikova SA, Goryainov SV, Korchagin AI, Cherepkov VV, Lavrukhin AV, Fadeev SN, Salimov RA, Bardakhanov SP. Visible photoluminescence from silicon nanopowders produced by silicon evaporation in a high-power electron beam. *JETP Lett.* 2004;80: 544–547.
- 43. Latu-Romain L, Ollivier M, Mantoux A, Auvert G, Chaix-Pluchery O, Sarigiannidou E, Bano E, Pelissier B, Roukoss C, Roussel H, Dhalluin F, Salem B, Jegenyes N, Ferro G, Chaussende D, Baron T. From Si nanowire to SiC nanotube. *J. Nanopart. Res.* 2011;13: 5425–5433.
- 44. Ramachandran M, Reddy RG. Thermal plasma synthesis of SiC. *Adv. Manuf.* 2013;1: 50–61.
- 45. Kukushkin, SA, Osipov AV. Phase equilibrium in the formation of silicon carbide by topochemical conversion of silicon. *Phys. Solid State*. 2016;58: 747–751.
- 46. Grashchenko AS, Kukushkin SA, Osipov AV, Redkov AV. Formation of composite SiC-C coatings on graphite via annealing Si-melt in CO. *Surface and Coatings Technology*. 2021;423: 127610.
- 47. Kukushkin SA, Osipov AV. Thermodynamics, kinetics, and technology of synthesis of epitaxial layers of silicon carbide on silicon by coordinated substitution of atoms, and its unique properties. A review. *Condensed Matter and Interphases*. 2022;24(4): 407–458.

THE AUTHORS

Bardakhanov S.P. 🗓

e-mail: bard@itam.nsc.ru

Chakin I.K.

e-mail: chak_in2003@bk.ru

Trufanov D.Y.

e-mail: trufanov@itam.nsc.ru

Gaponenko V.R.

e-mail: vasko-nsk@yandex.ru

Laser induced modification of nickel surface for non-enzymatic glucose detection

Submitted: February 18, 2023

Approved: June 1, 2023

Accepted: July 3, 2023

A.S. Kondrateva ^{10 1 ∞}, D.A. Strekalovskaya ^{10 2}, B.V. Babuyk ², A. Kuznetsov ³,

L.A. Filatov ², P.G. Gabdullin ¹⁰

¹ St. Petersburg Academic University of the Russian Academy of Sciences, St. Petersburg, Russia

² Peter the Great St. Petersburg Polytechnic University, St. Petersburg, Russia

☐ freyanasty@ya.ru

Abstract. This article proposes for consideration the experimental results of applying the method of laser surface modification for the manufacture of a highly sensitive enzyme-free sensitive layer of the working electrode of a glucose sensor using nickel oxide as an example. This technology can be integrated into the lab-on-a-chip concept. Using cyclic voltammetry, the sensitivity of the proposed system to the addition of microdoses of glucose to the solution for unmodified and laser-modified nickel surfaces was studied. The formed structure of metal oxide sensors was studied for the determination of D-(+)-glucose in the range of analyte concentrations up to 1.5 μ M. In addition, the sensitive layers made using the proposed technology showed durability and reproducibility of properties. This allows us to conclude that the demonstrated method of laser-induced metal surface modification is suitable for the production of a wide range of enzyme-free glucose sensors.

Keywords: surface modification; laser-driven surface alteration; nickel surface; glucose detection; electrocatalytic oxidation

Acknowledgements. The research is partially funded by the Ministry of Science and Higher Education of the Russian Federation as part of World-class Research Center program: Advanced Digital Technologies (contract No. 075-15-2020-934 dated 17.11.2020).

Citation: Kondrateva AS, Strekalovskaya DA, Babuyk BV, Kuznetsov A, Filatov LA, Gabdullin PG. Laser induced modification of nickel surface for non-enzymatic glucose detection. *Materials Physics and Mechanics*. 2023;51(4): 107-117. DOI: 10.18149/MPM.5142023_10.

Introduction

Quantitative glucose monitoring is of great world-wide interest because it might significantly diminish the risk of such adverse health effects as various heart trouble, renal failure, or cecity and thus considerably improve the life quality of people with diabetes [1]. Which is one in the SARS-CoV-2 post-pandemic situation, with a large number of diabetic patients infected with COVID-19, has enlarged the interest in real-time glucometer devices [2]. In retrospect, elevated levels of glucose in the blood and urine is one of the key occasions of disability or even death. This metabolic malady occurs when blood insulin concentrations fall below 3.9-6.2 μ M (fasting glucose level) or 3.9-7.8 μ M (2 hours after food ingestion). In the case of using other biological fluids (sweat, tear, or saliva [3–9]) as analytes, it is necessary to determine significantly lower glucose concentrations: 0.02-0.6, 0.1-0.6, and 0.05-1 μ M, respectively. It takes 15-30 minutes to establish a steady-state concentration when analyzing sweat or tear liquid. In the case of

saliva investigation, the measured glucose level can be immediately correlated with that in blood. Generally, methods such as mid-infrared spectroscopy, liquid spectrophotometry, and voltamperometria are applied for glucose levels monitoring, and the choice is made taking into account the specifics of each of the approaches. Among the mentioned methods, electrochemical approach offers the advantages of high accuracy, facile scalability, and ease of analysis of the received measurement signal.

The conventional model of glucose oxidation can be described as follows: at low potentials, the process begins with the anomeric carbon's hydrogen removing. A gluconate ion is formed on the surface at low potentials, while the formation of δ -gluconolactone corresponds to high potentials. As a result of particle desorption and subsequent hydrolysis, only the gluconate remains in the solution [10]. The electrocatalysis process starts with the analyte's adsorption on the electrode surface [11–13]. The superficies of the sensing area play a crucial role [14]. Pletcher suggested that the catalytic process of hydrogenation occurs contemporaneously with the organic substances adsorption. Indeed, the elimination of the hemiacetal hydrogen is presumed to be the limiting step in glucose electrooxidation [15]. In addition, chemisorbed hydroxyl radicals are supposed to participate in the slow stage of the process [16]. Thus, non-enzymatic glucose determination is a pH-controlled process, and OH-containing fluids are suitable for it. This is the reason for the higher sensitivity of non-enzymatic glucose sensors in higher pH environments. Consequently, both electronic and geometric factors must be considered in the manufacture and study of electrocatalysts to take full advantage of the possible improvements of the sensor from the kinetics point of view.

Among various materials [17–18], nickel-oxide-based structures with a developed surface have attracted considerable interest due to their sufficient susceptibility and selectivity to D-(+)-glucose detection. The oxidative activity of nickel-based materials in the glucose determination arises as a result of the rapid transformation of NiO / NiOOH redox pairs formed on the top of electrode surfaces in fluids. Nickel trivalent particles act as the catalyst in the oxidation reaction, which produces a flux of electrons into the surface. However, since nickel oxides and oxyhydroxides have high electrical resistivity, it is often precipitated on the electrode surface. Nevertheless, this additional layer has ensured more efficient electron transfer [19]. Despite the high sensitivity of nickel oxide and advanced state of knowledge regarding the catalytic reactions on its surface, fabrication of sensing metal-based nanostructures mostly requires aggregate chemical synthesis and time-consuming and expensive production techniques.

A wide spectrum of NiO layer formation techniques has been investigated including physical (magnetron sputtering, pulsed laser deposition, thermal deposition), and chemical (reactive evaporation, spray pyrolysis, and chemical vapor deposition) approaches [20]. All proposed methods require a large amount of time: from several hours to days (if additional post-processing is required). Among the various techniques of laser-driven local alteration of metal, foils make it possible to overcome aforecited disadvantage, providing the possibility of direct formation of functional coatings on Ni electrode surface. According to Wagner's model, as a result of laser radiation and thick metal layer interaction, a parabolic profile of oxygen penetration into the layer is formed [21]. Laser-driven oxidation methods make it possible to obtain almost any thermodynamic stable metal oxides and gradient layers with thicknesses up to 200 µm [22].

The paper analysis indicates that publications on electrocatalysts for amperometric glucose detection in the overwhelming majority of cases do not resemble scientific research in the field of synthesis of new substances. There are no usual attributes, such as patterns of morphology and phase characteristics from the synthesis conditions, kinetic patterns, chemical and phase analysis, the relationship of the surface structure with the material's analyte sensitivity, the proposal of synthesis models, or the response to the disturbance (here

electrocatalytic properties) of the material and their verification, etc. A feature of this work is the choice of the laser-driven surface alteration as a technology that makes it possible to vary the synthesis conditions over a wide range. The main goal of this paper is to estimate how the structure and composition effects on the catalytic properties of the nickel-based materials for potential use in enzymeless measurements of glucose by the electrochemical method.

Methods

Sodium hydroxide (NaOH) pellets (99.5 %), D-(+)-glucose (99.5 %) were purchased from Vecton LLC. Both background and stock solutions of glucose were prepared by dissolving the reagents in deionized water. Nickel foil (99.6 %) sample with a working size of 10 mm. sqr. was supplied by Contact LLC.

A novel laser-driven surface alteration technique for non-enzymatic glucose sensor's working electrode preparation was used. Laser processing of the Ni foil was carried out using a pulsed laser (Minimarker-2, CNI LOT) generating 1064 nm wavelength with a pulse duration of $4 \div 200$ ns. The beam profile followed a Gaussian distribution with a spot of 1 mm and a repetition frequency of 30 kHz, resulting in 50 % overlap. Laser energy fluence was from 30 to 240 mJ·cm⁻². The experiments were made in the atmospheric air at ambient temperature. For cyclic voltammetry (CV) experiments, the backsides of samples were passivated by rosin, with a 10×10 mm² window.

All electrochemical measurements were performed using electrochemical potentiostat VersaStat 4 Princeton Applied Research. For CV measurements, a three-electrode system has been employed. NiO-Ni sample was used as a working electrode, Pt wire was used as a counter electrode, a silver-chloride electrode (Ag/AgCl) with a KCl solution was used as a reference electrode. The Ag/AgCl reference electrode was separated from the electrochemical cell with 0.1 M NaOH electrolyte using a salt bridge. CV curves were scanned with different voltage scan rates varying between 3 and 80 mV·s⁻¹ under magnetically stirred conditions. Recording the CV scans repeatedly up to 3000 cycles showed high stability of the studied electrode.

A detailed description of the methodology, choice of modes and materials is presented in more detail in a previously published work [26].

Results and Discussion

SEM images of the boundary between the processed and unprocessed (pristine) regions of a nickel electrode are given in Fig. 1. The pristine region is essentially a smooth Ni surface. It can be seen that the treatment by laser irradiation results in alteration of the surface. EDX analysis indicates that the laser-induced modification adduced to a change of Ni/O ratio on the surface from $95.96 \pm 0.04/4.04$ to $92.02 \pm 0.06/7.98$, which is evidence of surface oxidation induced by laser irradiation in an oxygen-containing medium. This evidence is also supported by the results of Raman spectroscopy.

The Raman spectra are shown in Fig. 2. For the processed metal, characteristic NiO peaks are observed with maxima at 512 cm⁻¹ (longitudinal optical vibrations, LO, which is due to the presence of defects and is absent in the spectrum of crystalline NiO according to [23] and 960 cm⁻¹ (2LO) [24] alongside peaks related to carbon inclusions (1332, 1601, 2920 cm⁻¹), the latter probably due to surface contamination of the sample with carbon [25]. Thus, the described laser modification of the nickel surface leads to the formation of an oxide layer.

Although the nickel foil treatment was carried out in an atmosphere containing about 20 % oxygen, the amount of oxygen in the altered layer remains rather low. This may be due to the peculiarities of the selected mode of surface alteration when a protective atmosphere of evaporated nickel was formed during laser treatment, which prevented the penetration of oxygen to the surface. In this case, evaporation and condensation of the material occurred,

which did not lead to its significant loss. This is confirmed by the SEM results, which show the absence of porous structures.

The SEM and Raman spectroscopy results indicate the fundamental possibility of producing oxide layers in solution through the described laser-driven surface alteration. The considered fabrication method makes it possible to obtain a developed oxidized metal surface quickly and reproducibly.

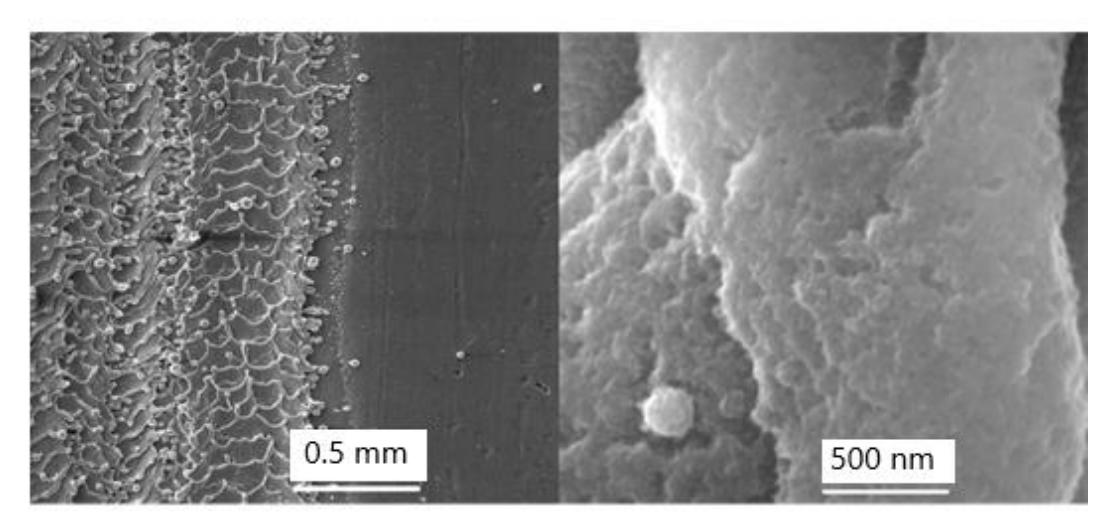


Fig. 1. SEM images of vicinities of the boundary between the processed and unprocessed regions of a nickel electrode surface at different magnifications

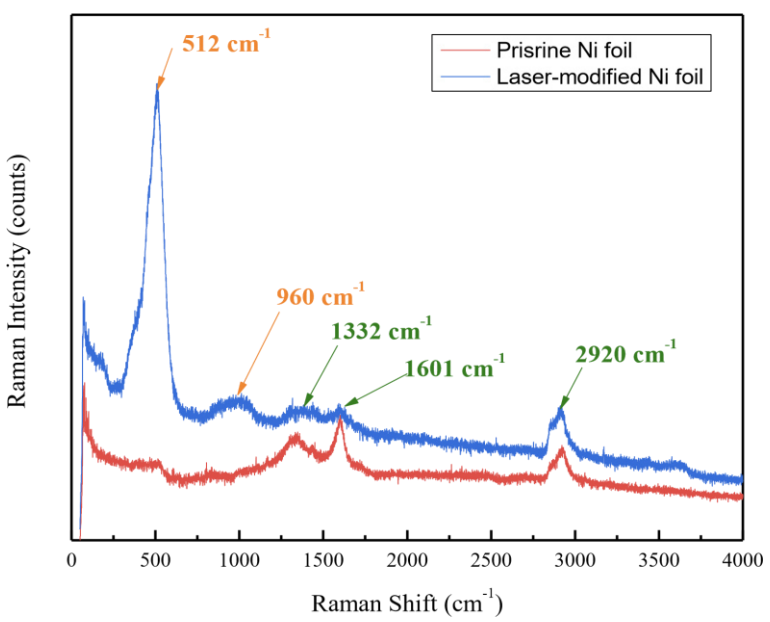


Fig. 2. Raman spectra obtained from the boundary region between the processed and unprocessed areas of a nickel electrode

Study of the electrooxidative activity of pristine Ni foil. At the first stage, the behavior of pristine Ni foil in 0.1M NaOH was studied. The characteristic peaks of the transition Ni (III) / Ni (II) [26] were not observed (Fig. 3). Additional electrochemical treatment (anodic, 1.5 V, 60 s), etching, and mechanical activation of the surface of the initial foil lead to the appearance of transition corresponding peaks on the CV. Upon increasing the analyte concentration from 0.1 to 1.5 μ M, both anodic and cathodic peaks current (Fig. 3, inset) was increased, which can indicate the surface oxidation of glucose molecules. The slight variation

of the anodic and cathodic peak positions is likely due to the crystal structures of the electrochemical formed surface layers change [27,28].

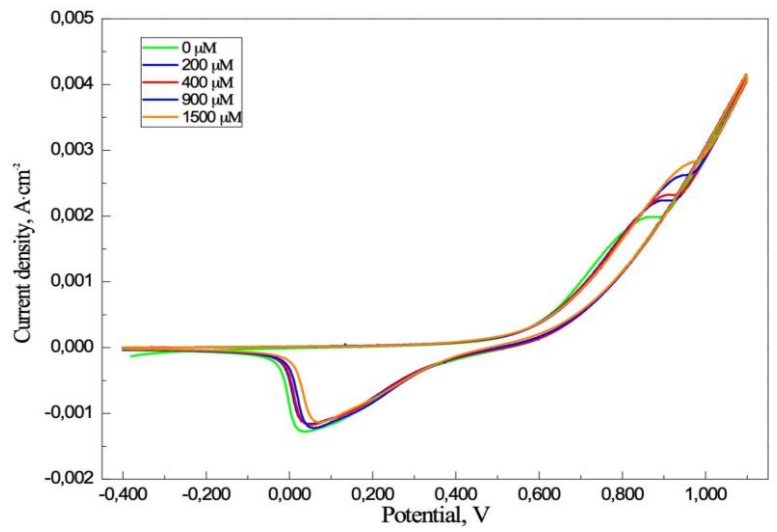


Fig. 3. Cyclic voltammograms of pristine Ni and NiO in 0.1 M NaOH solutions at scan rate of $20 \text{ mV} \cdot \text{s}^{-1}$

The most likely reaction scheme can be supported by electrochemical activation of NiO followed by the redox reactions on the NiOOH surface, which were discussed elsewhere [29,30]. On the NiOOH surface, glucose oxidizes to gluconolactone which reacts with a water molecule to form gluconate and hydronium ions.

Study of the electrooxidative activity of modified NiO-Ni layer toward glucose. For non-enzymatic sensing study, CV measurements have been carried out with NiO-Ni sample as the working electrode at a scan rate of 20 mV·s⁻¹ in the presence and absence of glucose, in the 0.1 M NaOH electrolyte as demonstrated in Fig. 4. When a preliminary laser-activated nickel foil is used as a working electrode in 0.1 M NaOH media, characteristic peaks of the Ni (III) / Ni (II) transition are observed on CV at potentials of about 0.4 V. In the region of high glucose level, an anodic peak intensity decrease is also observed. It is likely due to the poisoning of the work surface. In this case, the intensity observed for laser-modified nickel is higher than for the oxide formed by anodic treatment.

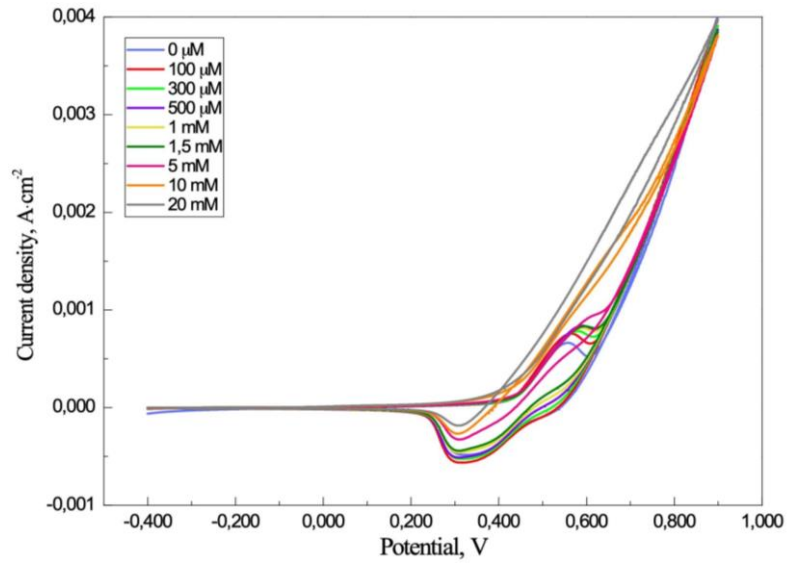


Fig. 4. Cyclic voltammograms of NiO-Ni sensitive layer in 0.1 M NaOH solutions in the presence of D-(+)-glucose concentrations up to 20 mM

The effect of scan rate on the anodic and cathodic peaks current (I_a and I_c) of 1 μ M D-(+)-glucose was measured in the range of 3 to 80 mV·s⁻¹ (Fig. 5). It was detected that both the anodic and cathodic peaks current (I_a and I_c) gains linearly with the scan rate's square root ((mV·s⁻¹)^{1/2}). The glucose oxidation in those conditions is limited by diffusion. The diffusion coefficient was counted for the pseudo plane electrode in reversible charge transfer mode and was 1.8×10^{-2} cm²·s⁻¹. This value is higher than the previously described quantity [31].

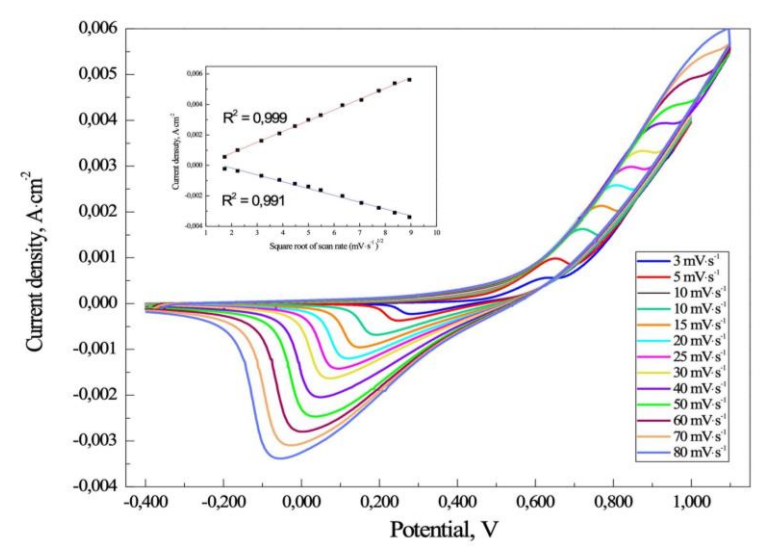


Fig. 5. Cyclic voltammograms of NiO-Ni sensitive layer in 0.1 M NaOH solutions in the presence of 1 μ M of D-(+)-glucose at different scan rates. Inset: anodic and cathodic current versus the square root scan rate

Amperometric study for NiO-Ni sensitive layer. The electrocatalytic behavior of the NiO-Ni sensitive layer on glucose oxidation was examined by monitoring a current replication on glucose adjunction at a fixed potential (Fig. 6). Firstly, the working potential was determined by the dropwise adjunction of 0.1 μ M glucose in 0.1 M NaOH. At a potential of 0.4 V, a sufficient signal-to-noise ratio, adequate correlation coefficient value, and current response were measured. All results are in an agreement with the corresponding value obtained in [32]. At a potential of 0.4 V, the current response increases linearly with analyte quantity in the range of 0.1 – 1.5 μ M. A correlation coefficient is counted to be of 0.996. Taking into account the slope (0.005 mA·mM⁻¹) and electrochemical area (1.2 cm⁻²) of the formed sensitive layer, the susceptibility of the structure was calculated as 0.4 mA· μ M⁻¹·cm⁻². The limit of detection (LOD) (0.4 μ M) and the limit of quantification (LOQ) (1 mM) also were calculated.

The current value does not diverge from linearity at higher analyte quantity. This fact indicates that neither poisoning of the electrode nor glucose isomers formation is affected, which is an opposite situation compared to that known to occur in high-pH solutions [33], which could be attributed to low D-glucose concentrations. The performance of the reported NiO-Ni structures in the range of $0.6-2~\mu M$ D-glucose concentration allows us to suggest their use as sensitive elements for determining the glucose level in blood. Usage of the formed structures for the analysis of saliva, tears, or sweat requires improvement of the detection limit and the limit of quantification, for example, by increasing the electrochemical area.

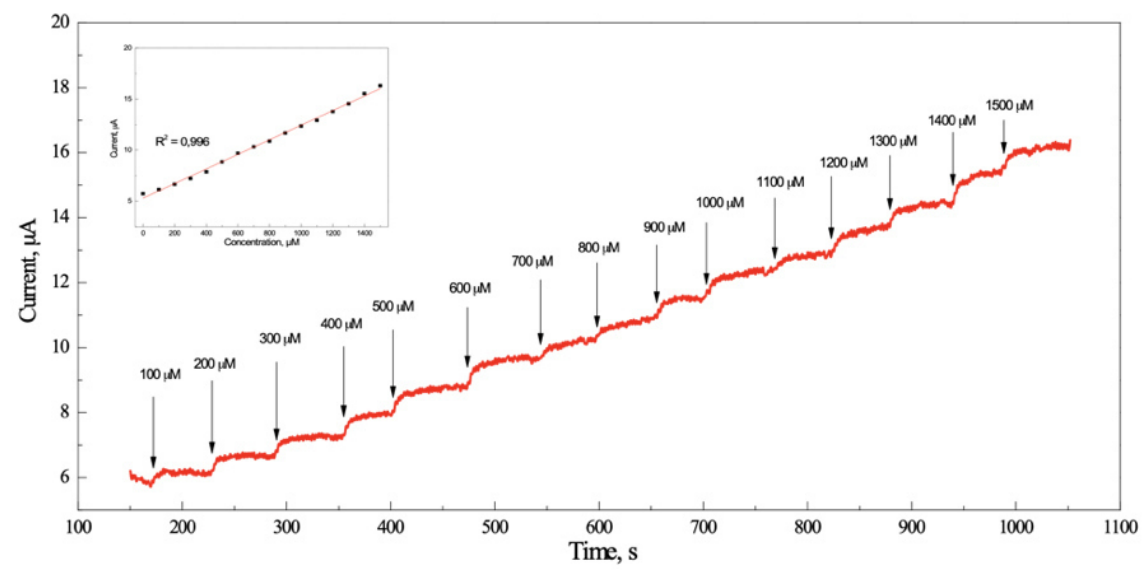


Fig. 6. Amperometry of D-(+)-glucose on NiO-Ni sensitive layer in 0.1 M NaOH solutions with $E_{st} = 0.4 \text{ V}$ under continuous agitation. Inset: the anodic and cathodic peaks current versus the D-(+)-glucose concentration

Table 1 shows the comparison of working detection potentials, sensitivity, LOD, preparation time of the currently prepared NiO-Ni sensitive layer with previously cited nickelbased structures in terms of working potential range, sensitivity, limits of detection, and fabrication complexity. The proposed method of laser modification is a much simpler and faster technique compared to standard methods of sol-gel synthesis, sintering, and pressing. In spite of the simplicity of the proposed NiO-Ni sensitive layer fabrication methodology, it shows comparable D-glucose detection performance. At the same time, the samples obtained using this technology showed comparable sensitivity and detection limits. It is planned to further increase the detection limit and sensitivity of the element by introducing additives of other materials (copper, iron, carbon in various forms), which is planned as a continuation of work on this topic.

Table 1. Comparison of working detection potentials, sensitivity, LOD, preparation time of this

work with previously reported studies for glucose detection.

Sensing layer	Working potential, V	Sensitivity, mA·μM ⁻¹ ·cm ⁻²	LOD, mM	Preparation time, h	Reference
Ni-Cu-Vulcan carbon	0.5	1.5	0.02	10-12	[30]
Ni/Au nanowires	0.6	1.9	0.1	10-12	[34]
NiCo ₂ S ₄ / Ni	0.45	0.2	6	0.5	[35]
NiO/MWCNT composite	0.5	0.1	0.01	5	[36]
Ni(OH)2 and NiO	0.58	0.1	0.7	30	[37]
NiO-Ni	0.4	0.6	0.6	1/3	This work

Repeatability and stability of NiO-Ni sensitive layer. Reproducibility and consistency of results are the main parameters for the performance of the device. Cyclic voltammetry is known as a precision and accurate method [38]. Repeatability is an important goal for sensor performance. The reproducibility of the readings of the system under study was studied by analyzing the CV of three groups of layers, sensitive to NiO-Ni, prepared in different experiments. All samples were investigated under cyclic conditions in a 0.1 M NaOH solution to 0.1 μ M D-glucose response with continuous stirring. The Figure 7 shows the averaged data for 6 samples: 3000 cyclic voltammograms, which were obtained on NiO-Ni sensitive layers. Repeatability of standard derivation was measured to be 4 %. It shows that the formed structure is not poisoned by the reaction products formed during the whole course of the process.

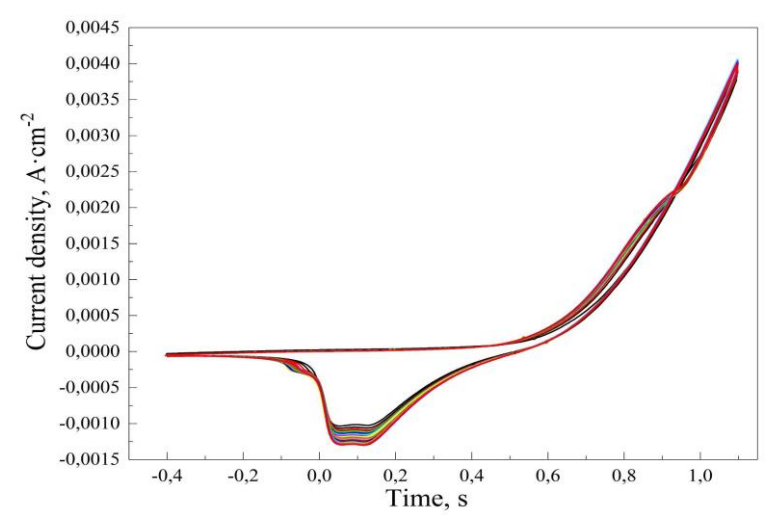


Fig. 7. 3000 cyclic voltammograms of NiO-Ni sensitive layer in 0.1 M NaOH solutions in the presence of 0.1 μ M of D-(+)-glucose at scan rate of 50 mV·s⁻¹

The stability of the prepared oxide layer was also evaluated by keeping a NiO-Ni sensitive layer for 100 days at ambient conditions. The measured current remains 85 % of the initial value after 100 days. This demonstrates that the prepared non-enzymatic glucose sensor has a high shelf-life stability. A decrease in the anodic and cathodic currents during long-term cyclic measurements can be related to the formation of γ -NiOOH, in which the volume of the working surface of the electrode increases up to the formation of microcracks. Physical destruction of the working surface is known to occur [39]. The results convincingly indicate the high reproducibility and high stability of the preliminarily prepared sensitive layer of NiO-Ni for the enzyme-free determination of D-(+)-glucose.

Conclusions

Nickel-based oxide nanostructure was formed on a metallic nickel surface by laser-driven modification approach. Formed structures were examined to be sensing electrodes for non-enzymatic glucose detection. The formed NiO-Ni structure morphology and chemical composition were investigated. Electrochemical analysis of NiO-Ni electrode behavior in alkaline solution confirmed the glucose-sensitive oxide layer to be presented on the top of the electrode. The electrochemical glucose detection results indicate enhancement of the electrode performance after laser modification as compared to Nickel foil.

A linear sensitivity of $0.4~\text{mA}\cdot\mu\text{M}^{-1}\cdot\text{cm}^{-2}$ with a correlation coefficient of 0.996~was obtained. Reproducibility and stability of the proposed non-enzymatic D-(+)-glucose sensor were established by long-term measurements. These results reveal the potentiality of producing advanced functional materials (in the present case, NiO-Ni structures with a modified surface) for competitive glucose sensors by implementing low-cost lasers to perform the metal oxidation and surface activation processes.

References

- 1. Kang S, Zhao K, Yu DG, Zheng X, Huang C. Advances in biosensing and environmental monitoring based on electrospun nanofibers. *Advanced Fiber Materials*. 2022;4(3): 404–435.
- 2. Levshakova AS, Khairullina EM, Panov MS, Ninayan R, Mereshchenko AS, Shishov A, Tumkin II. Modification of nickel micropatterns for sensor-active applications from deep eutectic solvents. *Optical and Quantum Electronics*. 2023;55(3): 267.
- 3. Bariya M, Nyein HY, Javey A. Wearable sweat sensors. *Nat. Electron.* 2018;1: 160–171.
- 4. Kim J, Campbell AS, de Ávila BE, Wang J. Wearable biosensors for healthcare monitoring. *Nat. Biotechnol.* 2019;37(4): 389–406.
- 5. Mannoor MS, Tao H, Clayton JD, Sengupta A, Kaplan DL, Naik RR, Verma N, Omenetto FG, McAlpine MC. Graphene-based wireless bacteria detection on tooth enamel. *Nat. Commun.* 2012;3(1): 763.
- 6. Wei M, Qiao Y, Zhao H, Liang J, Li T, Luo Y, Lu S, Shi X, Lu W, Sun X. Electrochemical non-enzymatic glucose sensors: Recent progress and perspectives. *Chem. Commun.* 2020;56(93): 14553–14569.
- 7. Qiao Y, Liu Q, Lu S, Chen G, Gao S, Lu W, Sun X. High-performance non-enzymatic glucose detection: using a conductive Ni-MOF as an electrocatalyst. *Journal of Materials Chemistry B*. 2020;8(25): 5411–5415.
- 8. Wang Z, Cao X, Liu D, Hao S, Kong R, Du G, Asiri AM, Sun X. Copper-nitride nanowires array: an efficient dual-functional catalyst electrode for sensitive and selective non-enzymatic glucose and hydrogen peroxide sensing. *Chemistry–A European Journal*. 2017;23(21): 4986–4989.
- 9. Liu Y, Cao X, Kong R, Du G, Asiri AM, Lu Q, Sun X. Cobalt phosphide nanowire array as an effective electrocatalyst for non-enzymatic glucose sensing. *Journal of Materials Chemistry B*. 2017;5(10): 1901–1904.
- 10. Hwang DW, Lee S, Seo M, Chung TD. Recent advances in electrochemical non-enzymatic glucose sensors—a review. *Analytica Chimica Acta*. 2018;1033: 1–34.
- 11. Heller A, Feldman B. Electrochemical glucose sensors and their applications in diabetes management. *Chemical Reviews*. 2008;108(7): 2482–2505.
- 12. Pletcher D. Electrocatalysis: present and future. *J. Appl. Electrochem.* 1984;14(4): 403–415.
- 13. Tian K, Prestgard M, Tiwari A. A review of recent advances in nonenzymatic glucose sensors. *Materials Science and Engineering: C.* 2014;41: 100–118.
- 14. Kokkindis G, Leger JM, Lamy C. Structural effects in electrocatalysis: oxidation of D-glucose on pt (100),(110) and (111) single crystal electrodes and the effect of upd adlayers of Pb, Tl and Bi. *Journal of Electroanalytical Chemistry and Interfacial Electrochemistry*. 1988:242(1-2): 221–242.
- 15. Hsiao MW, Adžić RR, Yeager EB. Electrochemical oxidation of glucose on single crystal and polycrystalline gold surfaces in phosphate buffer. *Journal of the Electrochemical Society*. 1996;143(3): 759.
- 16. Pessoa AM, Fajín JL, Gomes JR, Cordeiro MN. Ionic and radical adsorption on the Au (hkl) surfaces: A DFT study. *Surface Science*. 2012;606(1-2): 69–77.
- 17. Niu Q, Lu W, Bao C, Wei M, Chen ZA, Jia J. Glucose-sensing abilities of mixed-metal (NiCo) Prussian blue analogs hollow nanocubes. *Journal of Electroanalytical Chemistry*. 2020;874: 114507.
- 18. Bariya M, Shahpar Z, Park H, Sun J, Jung Y, Gao W, Nyein HY, Liaw TS, Tai LC, Ngo QP, Chao M. Roll-to-roll gravure printed electrochemical sensors for wearable and medical devices. *ACS Nano*. 2018;12(7): 6978–6987.

- 19. Mahadevan A, Fernando S. Inorganic iron-sulfur clusters enhance electron transport when used for wiring the NAD-glucose dehydrogenase based redox system. *Microchimica Acta*. 2018;185: 1–8.
- 20. Kondrateva AS, Mishin M, Shakhmin A, Baryshnikova M, Alexandrov SE. Kinetic study of MOCVD of NiO films from bis-(ethylcyclopentadienyl) nickel. *Physica Status Solidi (C)*. 2015;12(7): 912–917.
- 21. Atkinson A. Transport processes during the growth of oxide films at elevated temperature. *Reviews of Modern Physics*. 1985;57(2): 437.
- 22. Nánai L, Vajtai R, George TF. Laser-induced oxidation of metals: state of the art. *Thin Solid Films*. 1997;298(1-2): 160–164.
- 23. George G, Anandhan S. Synthesis and characterisation of nickel oxide nanofibre webs with alcohol sensing characteristics. *Rsc Advances*. 2014;4(107): 62009–62020.
- 24. Bose P, Ghosh S, Basak S, Naskar MK. A facile synthesis of mesoporous NiO nanosheets and their application in CO oxidation. *Journal of Asian Ceramic Societies*. 2016;4(1): 1–5.
- 25. Guedes-Silva CC, Rodas AC, Silva AC, Ribeiro C, Carvalho FM, Higa OZ, Ferreira TD. Microstructure, mechanical properties and in vitro biological behavior of silicon nitride ceramics. *Materials Research*. 2018;21(6): e20180266.
- 26. Kondrateva A, Babyuk V, Strekalovskaya D, Filatov L, Gabdullin P, Kvashenkina O, Prokopenko Y, Gruzdev A, Petruhno K, Kuznetsov A. Laser-driven metal alteration for glucose detection sensor. *Materials Physics and Mechanics*. 2021;47(5): 767–779.
- 27. Zhao C, Shao C, Li M, Jiao K. Flow-injection analysis of glucose without enzyme based on electrocatalytic oxidation of glucose at a nickel electrode. *Talanta*. 2007;71(4): 1769–1773.
- 28. Kwan KW, Hau NY, Feng SP, Ngan AH. Electrochemical actuation of nickel hydroxide/oxyhydroxide at sub-volt voltages. *Sensors and Actuators B: Chemical*. 2017;248: 657–664.
- 29. Fleischmann M, Korinek K, Pletcher D. The oxidation of organic compounds at a nickel anode in alkaline solution. *Journal of Electroanalytical Chemistry and Interfacial Electrochemistry*. 1971;31(1): 39–49.
- 30. Nisar S, Tariq M, Muhammad S, Saqib M, Akbar F. Electrocatalytic efficacy of Ni-Cu@ VC-72: Non-enzymatic electrochemical detection of glucose using Ni-Cu nanoparticles loaded on carbon black. *Synthetic Metals*. 2020;269: 116578.
- 31. Kim S, Muthurasu A. Metal-organic framework—assisted bimetallic Ni@ Cu microsphere for enzyme-free electrochemical sensing of glucose. *Journal of Electroanalytical Chemistry*. 2020;873: 114356.
- 32. Zhang X, Wang Y, Ning X, Chen J, Shan D, Gao R, Lu X. Three-dimensional porous self-assembled chestnut-like nickel-cobalt oxide structure as an electrochemical sensor for sensitive detection of hydrazine in water samples. *Analytica Chimica Acta*. 2018;1022: 28–36.
- 33. Shamsipur M, Najafi M, Hosseini MR. Highly improved electrooxidation of glucose at a nickel (II) oxide/multi-walled carbon nanotube modified glassy carbon electrode. *Bioelectrochemistry*. 2010;77(2): 120–124.
- 34. Qin L, He L, Zhao J, Zhao B, Yin Y, Yang Y. Synthesis of Ni/Au multilayer nanowire arrays for ultrasensitive non-enzymatic sensing of glucose. *Sensors and Actuators B: Chemical*. 2017;240: 779–784.
- 35. Babu KJ, Raj Kumar T, Yoo DJ, Phang SM, Gnana Kumar G. Electrodeposited nickel cobalt sulfide flowerlike architectures on disposable cellulose filter paper for enzyme-free glucose sensor applications. *ACS Sustainable Chemistry & Engineering*. 2018;6(12): 16982–16989.
- 36. Prasad R, Bhat BR. Multi-wall carbon nanotube—NiO nanoparticle composite as enzyme-free electrochemical glucose sensor. *Sensors and Actuators B: Chemical*. 2015;220: 81–90.

- 37. Pal N, Banerjee S, Bhaumik A. A facile route for the syntheses of Ni (OH) 2 and NiO nanostructures as potential candidates for non-enzymatic glucose sensor. *Journal of Colloid and Interface Science*. 2018;516: 121–127.
- 38. Lerke SA, Evans DH, Feldberg SW. Digital simulation of the square scheme in cyclic voltammetry: A comparison of methods. *Journal of Electroanalytical Chemistry and Interfacial Electrochemistry*. 1990;296(2): 299–315.
- 39. Singh D. Characteristics and effects of γ -NiOOH on cell performance and a method to quantify it in nickel electrodes. *Journal of the Electrochemical Society*. 1998;145(1): 116.

THE AUTHORS

Kondrateva A.S. 🗓

e-mail: freyanasty@ya.ru

Babuyk B.V.

e-mail: vladislavbabyuk@gmail.com

Filatov L.A.

e-mail: balldr@mail.ru

Strekalovskaya D.A. 🗓

e-mail: darya.strek@gmail.com

Kuznetsov A.

e-mail: leshiy2698@mail.ru

Gabdullin P.G. (10)

e-mail: pavel-gabdullin@yandex.ru

Structural and mechanical relaxation on annealing in glass-metal layered composites

Submitted: December 14, 2022

Approved: December 28, 2022

Accepted: April 22, 2023

M.A. Barbotko [™], O.N. Lyubimova [®], M.V. Ostanin [®]

Far Eastern Federal University, Vladivostok, Russia

☐ barbotko_ma@dvfu.ru

Abstract. The technological modes of annealing of the layered glass-metal composite material – glass-metal composite – which include heating-up to the glass softening point and aftercooling with annealing are investigated. The mathematical model of stress evolution is considered. The complexity in modeling is caused by the combined deformation of the glassy layer and the elastic-plastic layer with non-uniform temperature changes. Structural and mechanical relaxation processes in the glass transition interval are described within the framework of the relaxation kinetic theory of glass transition. The algorithm for calculations of technological and residual stresses in glass-metal composite, at different modes, is proposed. A comparison of the numerical method with the analytical solution obtained for constant thermomechanical parameters of materials is presented. The practical implications are in the possibility of modeling technological and residual stresses in laminated structural cylindrical systems functioning during cyclic heating-cooling to high temperatures, including glass transition and plastic deformation of the layers.

Keywords: glass-metal composite; structural and mechanical relaxation

Acknowledgements. The reported study was funded by FEFU, project number 22-07-01-007.

Citation: Barbotko MA, Lyubimova ON, Ostanin MV. Structural and mechanical relaxation on annealing in glass-metal layered composites. *Materials Physics and Mechanics*. 2023;51(4): 118-129. DOI: 10.18149/MPM.5142023_11.

Introduction

Advanced approaches to the simulation of new materials stand out the tendency of producing materials that combine the properties of glass and metal, which are called glass-metal composites: bioactive glass coatings in biomedicine [1], glass microspheres reinforced metal matrix [2–3], glass-metal nanocomposites, layered structural materials based on metal and glass fabric [4–6] or glass monolayers [7–8]. Manufacturing of glass-metal composites based on glass and metal monolayers is associated with heat treatment, during which glass layers are brought to a viscous liquid state, and then during cooling due to the difference in thermal coefficients of expansion, certain compressive stresses are formed in them, which are the reason for increasing the strength of glass layers.

The formulation of the mathematical model forecasting the mechanical behavior of the material with due regard to the glass transition process and plastic yield in metal in the course of heat treatment is essential.

The studies of the glass transition phenomenon have not yet allowed to develop a general theoretical understanding of the process, there are several basic theoretical approaches, among which the relaxation theory (transition theory within the two-state model) stands out as the most

experimentally tested one [10–12]. In the relaxation theory, glass transition is modeled as a transition of a medium from equilibrium (liquid) state to metastable (glassy) state through the change of a structural parameter characterizing the system state - "fictitious" temperature T_f [12–17]. The methods of calculating stresses in the course of heat treatment of, for example, flat leak-proof two-layered soldered joints of glass with metal, which are effectively used for calculations of stresses in amorphous coatings, are known [18–20]. Meantime, in the course of the glass-metal composite manufacture, the development of the elastoplastic strenuously-deformed state (in metal) resulting sometimes in destruction of the metal layer in case of mismatched parameters of the technological process and dimensions of metal layer is possible. The attempts to describe a change in the geometry of soldered joints under consideration and elastoplastic deformation of the metal element of a soldered joint require complication of the problem and adjustment of calculation methods of stress relaxation when passing through the glass transition interval, which determines the objective of this paper.

Statement of the Problem and mathematical model

The thermal regime of manufacturing the glass-metal composite (Fig. 1(a)) includes intervals of heating-up I_a , exposure I_b , cooling I_c and annealing, which is carried out either immediately at the cooling stage and associated with control of the rate of temperature change and exposure at the glass transition temperature or on reheating I_a^0 and following stages of controlled cooling I_b^0 and I_c^0 . Simulation of controlled cooling is necessary for monitoring and regulating of technological and residual stresses. On cooling from a temperature which can coincide with the glass-melting temperature or be not so many as it, the structure and properties of the glass change continuously. Such process is termed as glass transition, and it proceeds in certain interval $\left(T_g^-, T_g^+\right)$ (Fig. 1(b)). The average temperature of the glass transition interval is referred the glass transition temperature T_g . The position of glass transition interval depends on the cooling rate and the prehistory of temperature treatment while the boundaries of glass transition interval T_g^- and T_g^+ are usually associated with those of hysteresis loop characterizing change of enthalpy under uniform cooling and heating-up from the equilibrium condition of the liquid melt to the frozen structure.

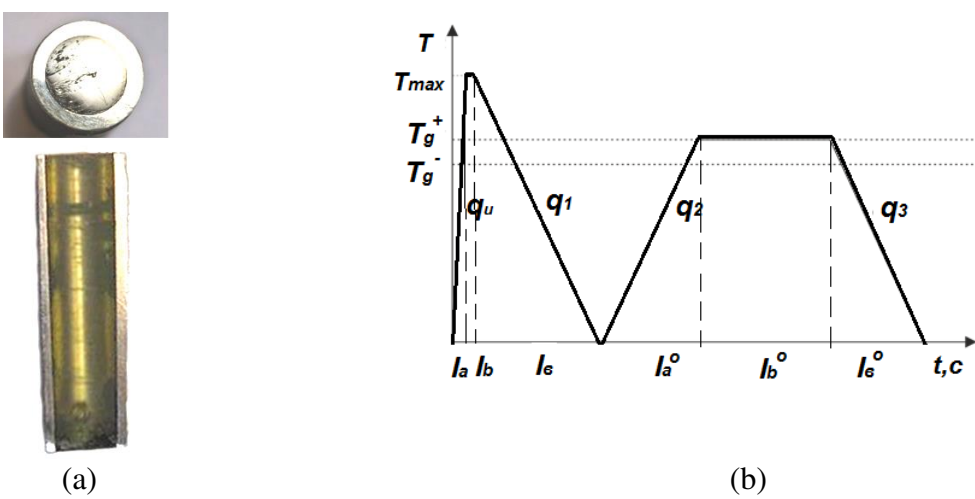


Fig. 1. Photographs of the experimental samples (a); temperature conditions of annealing (b)

When passing through the glass transition interval, the specificity of structure change, and mechanical relaxation is described by changing the fictitious (structural) temperature and the rate of its change relative to temperature, an analytical expression in the form of the Tule-Nayaranaswamy-Moynihan formula [13–15]:

$$T_{f} = T_{0} + \int_{0}^{t} \left(1 - M_{s}(\xi - \xi')\right) \frac{dT}{d\xi'} d\xi', \tag{1}$$

here $T_0 = T_{\text{max}}$, the function of the structural relaxation of glass properties is well described by the function of Kohlrausch [18]:

$$M_{s}(\xi) = e^{-(\xi/\tau_{r})^{b}} = e^{-(\xi K_{r}/\eta_{r})^{b}},$$
 (2)

where b is a constant for the glasses having fixed compositions (0 < b < 1), ξ is a "true" time, which being a temperature-invariant characteristic of viscoelastic properties, can be written as

$$\xi(t) = \int_{0}^{t} \frac{\eta_r}{\eta(t')} dt'$$
, where η_r — shearing viscosity at arbitrarily chosen comparison temperature T_r ,

$$\eta(t)$$
 — is current viscosity, $K_r = \eta_r/\tau_r$, τ_r — is relaxation time at the comparison temperature.

The analytical dependences of the change in viscosity and the thermal coefficient of linear expansion can be written as (3) and (4) commonly used for calculating thermal stresses in the flat soldered joint of glass with metal in the algorithm called "IHS calculation method (Institute of Silicate Chemistry)".

$$\lg \frac{\eta}{\eta_0} = B_e \left(T_f^{(-1)} - T_0^{(-1)} \right) + B_f \left(T^{(-1)} - T_f^{(-1)} \right), \tag{3}$$

$$\alpha = \alpha_e + \left(\alpha_f - \alpha_e\right) \left(\frac{dT_f}{dT}\right),\tag{4}$$

where η_0 is viscosity at T_0, B_e, α_e , B_f, α_f are coefficients characterizing the temperature dependences of η and α under conditions of the equilibrium and frozen structures, respectively.

The change of fictitious temperature (1), its rate and physical and chemical properties of liquid glass melt (2)-(4) during temperature treatment is determined from the solution of the heat and mass transfer problem, which is considered in work [21] for different methods of heating and cooling.

In mathematical simulation of the evolution of stresses in the glass-metal composite, different ways of thermomechanical deformation of the materials of which it composes – thermo-visco-plastic one with structural changes in the glass component and thermo-elastic-plastic one in the metal were taken into account. Simulation has been performed for a specific geometry representing composite stems: a glassy core and a steel shell. Assuming an axisymmetric, uniform heating along generatrix at small deformations in the cylindrical coordinate system, the components of the displacement tensor can be written in the form of the following unknown functions: $u_r = u(r,t)$, $u_{\omega} = 0$, $u_z = w(z,t)$, and deformation tensors has

a diagonal form and the components:
$$\varepsilon_{rr} = \frac{\partial u}{\partial r}$$
, $\varepsilon_{\varphi\varphi} = \frac{u}{r}$, $\varepsilon_{zz} = \frac{\partial w}{\partial z} = \varepsilon_z(t)$, $\varepsilon_{r\varphi} = \varepsilon_{rz} = \varepsilon_{\varphi z} = 0$.

Equations of state for glass can be described on the basis of the Boltzmann-Volterra superposition principle [22] and the absence of bulk relaxation properties condition

$$s_{i} = 2G\left(e_{i} - \int_{0}^{t} M\left(\eta(t, t')\right) e_{i} dt'\right), \ i = r, \varphi, z,$$

$$(5)$$

$$\sigma(r,t) = 3K\theta, \tag{6}$$

here
$$\sigma = (\sigma_r + \sigma_\varphi + \sigma_z)/3$$
, $\varepsilon = (\varepsilon_r + \varepsilon_\varphi + \varepsilon_z)/3$, $\theta = 3\varepsilon - \int_{T_0}^{T} \alpha(T) dT$, $s_i = \sigma_i - \sigma$, $e_i = \varepsilon_i - \varepsilon$,

G is the shear modulus, K is bulk modulus; is the relaxation core characterizing the decrease by the time t in shearing stresses caused by deformation at time t' the analytic record of which is non-exponential as in (2), at that, the parameters b and K_r are different from values used for determination of the structural parameter T_f ; $\alpha(T)$ is the thermal coefficient of linear expansion determined from the solution of the temperature problem according to formula (4).

The constitutive relations for the outer cylinder are written in line with the Prandtl-Reuss model with respect to thermal phenomena and division of small deformations into the convertible (elastic ε^e) and irreversible (plastic ε^p) components

$$\varepsilon_i = \varepsilon_i^e + \varepsilon_i^p \ . \tag{7}$$

The elastic state in stress space will be limited by the surface of limiting state of Mises and condition of active loading:

$$f(\sigma,T) = (\sigma_r - \sigma_\varphi)^2 + (\sigma_z - \sigma_\varphi)^2 + (\sigma_r - \sigma_z)^2 - 2\sigma_T^2(T) = 0$$

$$\frac{\partial f}{\partial \sigma_r} \dot{\sigma}_r + \frac{\partial f}{\partial \sigma_r} \dot{\sigma}_r + \frac{\partial f}{\partial \sigma_r} \dot{\sigma}_r + \frac{\partial f}{\partial T} \dot{T} > 0,$$
(8)

where maximum tensile stress $\sigma_T(T)$ depends only on temperature. The plastic components of the deformation tensor are determined in accordance with the law of associated flow:

$$\dot{\mathcal{E}}_{r}^{p} = \Lambda \frac{\partial f}{\partial \sigma_{r}}, \, \dot{\mathcal{E}}_{\varphi}^{p} = \Lambda \frac{\partial f}{\partial \sigma_{\varphi}}, \, \dot{\mathcal{E}}_{z}^{p} = \Lambda \frac{\partial f}{\partial \sigma_{z}},$$

$$(9)$$

here, Λ has meaning of Langrangian multiplier while finding the maximum specific capacity of deformation with restriction (8).

Considering the relation (7) and the assumptions about the displacements the elastic deformations are rewritten as:

$$\varepsilon_r^e = \frac{\partial u}{\partial r} - \varepsilon_r^p, \varepsilon_\varphi^e = \frac{u}{r} - \varepsilon_\varphi^p, \varepsilon_z^e = \varepsilon_z - \varepsilon_z^p. \tag{10}$$

The boundary conditions are determined according to no-load conditions at the outer surfaces of the stem and equality of radial stresses and displacements when passing through the glass-metal boundary in case of perfect contact, without slippage along the cylinder axis $\left(\varepsilon_{s}^{g} = \varepsilon_{s}^{m}\right)$:

$$u(R_{1}-t) = u(R_{1}+t), \ \sigma_{r}(R_{1}-t) = \sigma_{r}(R_{1}+t),$$

$$\sigma_{r}(R_{2},t) = 0,$$

$$\int_{0}^{R_{1}} \sigma_{z}(r,t)rdr + \int_{R_{1}}^{R_{2}} \sigma_{z}(r,t)rdr = 0.$$
(11)

Here R_1 radius of the glassy stem, $R_2 - R_1$ thickness of metal layer. Using the expressions (5)-(6), the displacement equation of equilibrium at $0 < r < R_1$:

$$\left(\frac{4}{3}G + K\right)\left(\frac{\partial^{2}u}{\partial r^{2}} + \frac{1}{r}\frac{\partial u}{\partial r} - \frac{u}{r^{2}}\right) - \frac{2}{3}G\int_{0}^{t}M\left(t, t'\right)\left(\frac{\partial^{2}u}{\partial r^{2}} + \frac{1}{r}\frac{\partial u}{\partial r} - \frac{u}{r^{2}}\right)dt' = 0$$
(12)

at the same time, for $R_1 < r < R_2$ with regard to (10) will be written as:

$$\frac{\partial^2 u}{\partial r^2} + \frac{1}{r} \frac{\partial u}{\partial r} - \frac{u}{r^2} = \frac{2G}{\frac{4}{3}G + K} \left(\frac{\partial \left(\varepsilon_r^p + \varepsilon_\varphi^p \right)}{\partial r} + \frac{\varepsilon_r^p - \varepsilon_\varphi^p}{r} \right). \tag{13}$$

When the plastic flow in the outer cylindrical layer is described by the Mises' equation of yielding (8) while the visco-elastic deformation, with consideration for the structural changes, is determined by the Kohlrausch relaxation core (2) and (5), at the moment, it seems to be impossible to achieve the analytic solution of the problem (5)-(13) even on the basis of all adopted simplications. Based on the finite-difference method, the numerical analytic method of the problem is proposed in this paper.

Numerical-analytical method

The characteristic property of the problem (5)-(13) consists in its dependence on loading history, therefore, for numerical implementation, all equations were rewritten in small increments in time. The approximation of all defining relations with the use of the finite-difference method is accurately described, for example, in the work [23], therefore, we will highlight only distinctive features of the approach developed by authors in this paper.

In each temporal layer, the increments of displacements at $0 < r < R_1$ are written as the known coordinate functions, in which only the increment of integration constant $\Delta u^k = \Delta C_1^k \cdot r$ should be found. The increments of displacements at $R_1 < r < R_2$ are considered as the grid functions Δu_j^k , being determined from the system solution obtained as a result of finite-difference writing of equation (13). Herewith, the increment of constant ΔC_1^k can be found from solution of the consistent system resulting from the finite-difference presentation of equations (11) and (13). It is suggested to find the influence of the relaxation processes on the stresses in the form of the difference of the sums of the stress deviator components increments in all preceding time layers and "relaxation correcting" stress deviator components in the current layer.

When determining of the plastic deformations, the method of additional strains [24] is used, in which the iterative procedure of calculating the plastic deformation starts at each time step after the zero increments of stresses and strains are determined if the conditions (8) are met, when the plastic deformation "correcting" the stresses emerges.

With consideration for structural changes when passing through the glass transition phase and elastic-plastic stresses in the metal at (in) each time layer, under initial conditions of no increments of displacements, deformations and stresses, the calculation algorithm of combined visco-elastic stresses in the glass is:

1. When solving the temperature problem, the structural parameters (1)-(4) are determined:

$$\begin{split} T_f^k &= T^0 + \sum\nolimits_{k_1 = 1}^k \left(1 - \exp \left(-\left(\frac{\left(\xi^k - \xi^{k_1} \right) K_{rs}}{\eta_r} \right)^{b_s} \right) \right) \Delta T^k, \\ \xi^k &= \xi^{k-1} + \sum\nolimits_{k_1 = 1}^k \frac{\eta_r \Delta t}{\eta^{k_1 - 1}}, \\ \lg \eta^k &= \lg \eta^0 + B_e \left(\left(T_f^k \right)^{-1} - \left(T^0 \right)^{-1} \right) + B_f \left(\left(T^k \right)^{-1} - \left(T_f^k \right)^{-1} \right), \\ \alpha^k &= \alpha_e + \left(\alpha_f - \alpha_e \right) \frac{\Delta T_f^k}{\Delta T^k}. \end{split}$$

2. The displacements in the region $0 < r < R_1$ are determined as solutions of the Euler equation, which is a consequence of the integro-differential equation (12), provided that the relaxation core (2) is independent on the r:

$$\Delta u_j^k = \Delta C^k r_j;$$

at $R_1 \le r \le R_2$ the displacement increments are determined from the system:

$$\begin{split} &\left(\frac{\Delta r_m}{2r_j}+1\right)\Delta u_{j+1}^k - \left(\frac{\Delta r_m^2}{r_j^2}+2\right)\Delta u_j^k + \left(1-\frac{\Delta r_m}{2r_j}\right)\Delta u_{j-1}^k = \\ &= \frac{2G_m\Delta r_m^2}{4\sqrt{3}G_m+K_m}\left(\frac{\Delta \mathcal{E}_{r\ j+1}^{pk-1}-\Delta \mathcal{E}_{r\ j-1}^{pk-1}}{2\Delta r_m}+\frac{\Delta \mathcal{E}_{r\ j}^{pk-1}-\Delta \mathcal{E}_{\varphi\ j}^{pk-1}}{r_j}\right), \end{split}$$

in general, at each temporal layer the displacements in the whole area are determined as $u_i^k = u_i^{k-1} + \Delta u_i^k$

3. Determination of the stress increments is carried out using an iterative procedure that should contain at least two iterations: at the zero step for finding the increments ΔC_j^k , Δu_j^k , $\Delta \varepsilon_z^k$ the system (11) and (13) is solved in finite difference approximation, and at the interface of the layers the condition of continuity of displacements are written as

$$\Delta C^k = \frac{\Delta u_{j_0}^k}{J_0 \Delta r_a}$$

here $J_0\Delta r_g$ – layer interface. After determining the displacement and stress increments using finite-difference analogues (5) and (6) as

$$\Delta \sigma_r^k = \Delta \sigma_\varphi^k = \left(\frac{2}{3}G_g + 6K_g\right) \Delta C^k + \left(3K_g - \frac{2}{3}G_g\right) \Delta \varepsilon_z^k - 3K_g \Delta \tilde{\alpha}_g^k,$$

$$\Delta \sigma_z^k = 2\left(3K_g - \frac{2}{3}G_g\right) \Delta C^k + \left(3K_g + \frac{2}{3}G_g\right) \Delta \varepsilon_z^k - 3K_g \Delta \tilde{\alpha}_g^k,$$
(14)

we determine the increments of the stress deviator components and calculate the correction part that takes into account the mechanical relaxation in the layer

$$\Delta S_r^k = \frac{2}{3} \Delta \sigma_{rj}^k - \frac{1}{3} \left(\Delta \sigma_{\varphi j}^k + \Delta \sigma_{zj}^k \right), \ \Delta S_{\varphi}^k = \frac{2}{3} \Delta \sigma_{\varphi j}^k - \frac{1}{3} \left(\Delta \sigma_{rj}^k + \Delta \sigma_{zj}^k \right),$$
$$\Delta S_r^k = \frac{2}{3} \Delta \sigma_{zj}^k - \frac{1}{3} \left(\Delta \sigma_{\varphi j}^k + \Delta \sigma_{rj}^k \right),$$

$$\Delta S_{cor,i}^{k} = \sum_{k_{1}=1}^{k-1} \left(1 - e^{\left(-\left(\frac{\left(\xi^{k} - \xi^{k_{1}}\right)K_{r\sigma}}{\eta_{r}}\right)^{b\sigma} \right)} \right) \Delta S_{i}^{k_{1}} - \sum_{k_{1}=1}^{k-2} \left(1 - e^{\left(-\left(\frac{\left(\xi^{k-1} - \xi^{k_{1}}\right)K_{r\sigma}}{\eta_{r}}\right)^{b\sigma} \right)} \right) \Delta S_{i}^{k_{1}},$$

$$\Delta S_i^k = \Delta S_i^k - \Delta S_{cor,i}^k \Delta C_i^k$$

here
$$\Delta \tilde{\alpha}_g^k = \alpha_g^k \cdot \Delta T$$
, $\alpha_g^k = \alpha_g (T^k)$.

At the next iteration, with consideration of the corrected deviatoric part of the stresses, we redefine the , Δu_j^k , $\Delta \mathcal{E}_z^k$ from the repeated solution of the finite-difference analog of the system (11) and (13). We redefine the stress increments $0 \le r \le R_1$ with the use of formulas (14) and for $R_1 \le r \le R_2$ as

$$\begin{split} & \Delta \sigma_{rj}^{k} = \left(\frac{4}{3}G_{m} + 3K_{m}\right) \frac{\Delta u_{j+1}^{k} - \Delta u_{j-1}^{k}}{2\Delta r_{m}} + \left(3K_{m} - \frac{2}{3}G_{m}\right) \left(\frac{\Delta u_{j}^{k}}{r_{j}} + \Delta \varepsilon_{z}^{k}\right) - 3K_{m}\Delta \tilde{\alpha}_{m}^{k} - 2G_{m}\Delta \varepsilon_{rj}^{pk}, \\ & \Delta \sigma_{\varphi j}^{k} = \left(\frac{4}{3}G_{m} + 3K_{m}\right) \frac{\Delta u_{j}^{k}}{r_{j}} + \left(3K_{m} - \frac{2}{3}G_{m}\right) \left(\frac{\Delta u_{j+1}^{k} - \Delta u_{j-1}^{k}}{2\Delta r_{m}} + \Delta \varepsilon_{z}^{k}\right) - 3K_{m}\Delta \tilde{\alpha}_{m}^{k} - 2G_{m}\Delta \varepsilon_{\varphi j}^{pk}, \end{split}$$

$$\Delta \sigma_{zj}^{k} = \left(\frac{4}{3}G_{m} + 3K_{m}\right) \Delta \varepsilon_{z}^{k} + \left(3K_{m} - \frac{2}{3}G_{m}\right) \left(\frac{\Delta u_{j+1}^{k} - \Delta u_{j-1}^{k}}{2\Delta r_{m}} + \frac{\Delta u_{j}^{k}}{r_{j}}\right) - 3K_{m}\Delta \tilde{\alpha}_{m}^{k} - 2G_{m}\Delta \varepsilon_{zj}^{pk},$$

where $\Delta \tilde{\alpha}_m^k = \alpha_m^k \cdot \Delta T$, $\alpha_m^k = \alpha_m (T^k)$, j-coordinate step number.

4. The increment of plastic deformation is calculated by method of additional deformations [23-24], if the stresses at k - th step satisfy the conditions (8) in time then in the process of additional iterations: at $0 \le r \le R_1$ let's specify ΔC^k , $\Delta \varepsilon_z^k$ are improved and the stress increments are redefined according to the algorithm described in step 3 for every iteration; at $R_1 \le r \le R_2$, at the zero step of iteration, the increment of the plastic deformation intensity $\Delta \varepsilon_i^P$ is defined as:

$$\Delta \varepsilon_{ij}^{p0} = \frac{\sqrt{2}}{3} \sqrt{\left(\Delta \varepsilon_{rj}^{0} - \Delta \varepsilon_{\varphi j}^{0}\right)^{2} + \left(\Delta \varepsilon_{\varphi j}^{0} - \Delta \varepsilon_{zj}^{0}\right)^{2} + \left(\Delta \varepsilon_{rj}^{0} - \Delta \varepsilon_{zj}^{0}\right)^{2}},$$

where

$$\Delta \varepsilon_{\mathit{rj}}^{0} = \frac{\frac{2}{3} \Delta \sigma_{\mathit{rj}}^{0} - \frac{1}{3} \left(\Delta \sigma_{\varphi \mathit{j}}^{0} + \Delta \sigma_{\mathit{zj}}^{0} \right)}{2G_{\mathit{m}}} \,, \; \Delta \varepsilon_{\varphi \mathit{j}}^{0} = \frac{\frac{2}{3} \Delta \sigma_{\varphi \mathit{j}}^{0} - \frac{1}{3} \left(\Delta \sigma_{\mathit{rj}}^{0} + \Delta \sigma_{\mathit{zj}}^{0} \right)}{2G_{\mathit{m}}} \,,$$

$$\Delta arepsilon_{zj}^0 = rac{rac{2}{3}\Delta\sigma_{zj}^0 - rac{1}{3}ig(\Delta\sigma_{arphi j}^0 + \Delta\sigma_{rj}^0ig)}{2G_{vv}}\,,$$

then the increment of the plastic deformations are determined as

$$\Delta \varepsilon_{rj}^{p0} = \frac{3\Delta \varepsilon_{ij}^{p0}}{2\sigma_T} \left(\frac{2}{3} \Delta \sigma_{rj}^0 - \frac{1}{3} \left(\Delta \sigma_{\varphi j}^0 + \Delta \sigma_{zj}^0 \right) \right),$$

$$\Delta \varepsilon_{\varphi j}^{p0} = \frac{3\Delta \varepsilon_{ij}^{p0}}{2\sigma_{T}} \left(\frac{2}{3} \Delta \sigma_{\varphi j}^{0} - \frac{1}{3} \left(\Delta \sigma_{rj}^{0} + \Delta \sigma_{zj}^{0} \right) \right),$$

$$\Delta \varepsilon_{zj}^{p0} = \frac{3\Delta \varepsilon_{ij}^{p0}}{2\sigma_{T}} \left(\frac{2}{3} \Delta \sigma_{zj}^{0} - \frac{1}{3} \left(\Delta \sigma_{\varphi j}^{0} + \Delta \sigma_{rj}^{0} \right) \right).$$

Determined $\Delta \varepsilon_{rj}^{p0}$, $\Delta \varepsilon_{\varphi j}^{p0}$, $\Delta \varepsilon_{zj}^{p0}$ are inserted into the equations of the previous steps 2 and 3 and the increments of displacements are determined, and the stresses are redefined. Further, the iterative process of calculating the deformation increments is performed:

$$\Delta \varepsilon_{rj}^{p1} = \frac{3\Delta \varepsilon_{ij}^{p0}}{2\sigma_{T}} \left(\frac{2}{3} \Delta \sigma_{rj}^{k_{1}} - \frac{1}{3} \left(\Delta \sigma_{\varphi j}^{1} + \Delta \sigma_{zj}^{1} \right) \right),$$

$$\Delta \varepsilon_{\varphi j}^{p1} = \frac{3\Delta \varepsilon_{ij}^{p0}}{2\sigma_{T}} \left(\frac{2}{3} \Delta \sigma_{\varphi j}^{1} - \frac{1}{3} \left(\Delta \sigma_{rj}^{1} + \Delta \sigma_{zj}^{1} \right) \right),$$

$$\Delta \varepsilon_{zj}^{p1} = \frac{3\Delta \varepsilon_{ij}^{p0}}{2\sigma_{x}} \left(\frac{2}{3} \Delta \sigma_{zj}^{1} - \frac{1}{3} \left(\Delta \sigma_{\varphi j}^{1} + \Delta \sigma_{zj}^{1} \right) \right),$$

$$\Delta \varepsilon_{ij}^{p1} = \frac{\sqrt{2}}{3} \sqrt{ \left(\Delta \varepsilon_{rj}^{p1} - \Delta \varepsilon_{\varphi j}^{p1} \right)^2 + \left(\Delta \varepsilon_{\varphi j}^{p1} - \Delta \varepsilon_{zj}^{p1} \right)^2 + \left(\Delta \varepsilon_{rj}^{p1} - \Delta \varepsilon_{zj}^{p1} \right)^2} \,.$$

The iterative process is ceased subject to the condition: $\frac{\left|u_{j}^{l}-u_{j}^{l-1}\right|}{\left|u_{j}^{l}\right|} \leq \varepsilon$,

the transition to the next time layer takes place (ε is the prescribed accuracy).

Calculation results

When investigating different modes of annealing, the following data were used for borosilicate glass [25]: $\eta_0 = 10^{4.25}$ MPa·s; $\theta_e = 28726.85$ °C; $\theta_f = 13726.85$ °C; $\theta_f = 13726.85$ °C; $\theta_f = 10^{10.7}$; $\theta_s = 0.65$; $\theta_f = 10^{3}$ MPa·s; $\theta_f = 52 \times 10^{-7}$ °C⁻¹; $\theta_f = 210 \times 10^{-7}$ °C⁻¹; $\theta_f = 10^{4.7}$; $\theta_f = 0.5$; $\theta_g = 0.24 \times 10^5$ MPa; $\theta_g = 0.4 \times 10^5$ MPa;

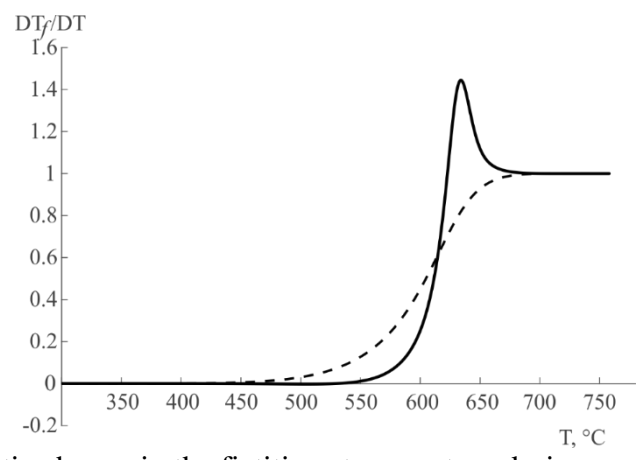


Fig. 2. Characteristic change in the fictitious temperature during cooling and heating up

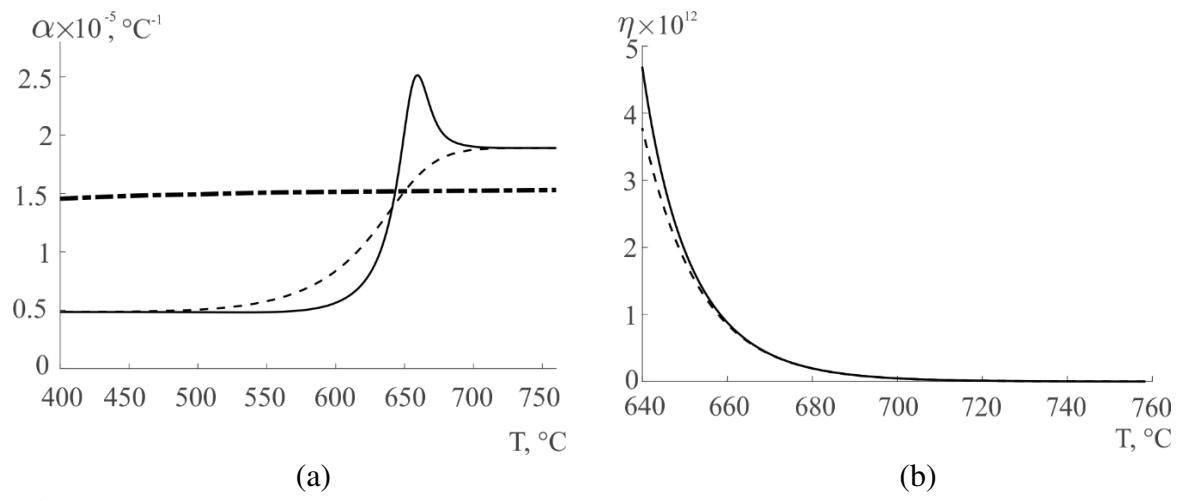


Fig. 3. Temperature dependence of the thermal coefficient of linear expansion (a) and viscosity (b): - heating up, -- cooling; --- thermal coefficient of linear expansion of the metal

In Figure 3(a) it is possible to identify the temperature at which the graphs of thermal coefficients of linear expansion of glass and metal on heating up and cooling have points of intersection for certain mode. At this temperature the stress in the soldered joint changes the sign, for flat soldered joints [19–20] it is accepted to choose the cooling rate (q_3) in the area

between the upper temperature of annealing and the intersection point of graphs of thermal coefficients of linear expansion of glass and metal, as much as possible reduced at least by the increase of compressive stresses.

The following Figs. 4-5 show graphs of stress changes as a function of temperature in the 1st layer (glass) and at the interface between the layers in the 2nd layer (metal), the beginning of the process was assumed as cooling after obtaining the soldered joint from 650 °C (1st stage at a constant rate $q_1 = 3$ °C/min), then annealing was carried out according to the scheme of stage 2 - heating up to the annealing temperature (after pre-calculations, a temperature of 560 °C was taken), exposure at 560 °C for 2 h and cooling; $q_2 = q_3 = q_4 = 3$ °C/min.

From the graphs in Fig. 4, the temperature range and the stress level at which plastic flow develops in the 2nd layer is noticeable; on the graph of the intensity change at all stages in this interval, the graphs merge and correspond to the graph of the change in the yield stress (Fig. 4, lower right graph).

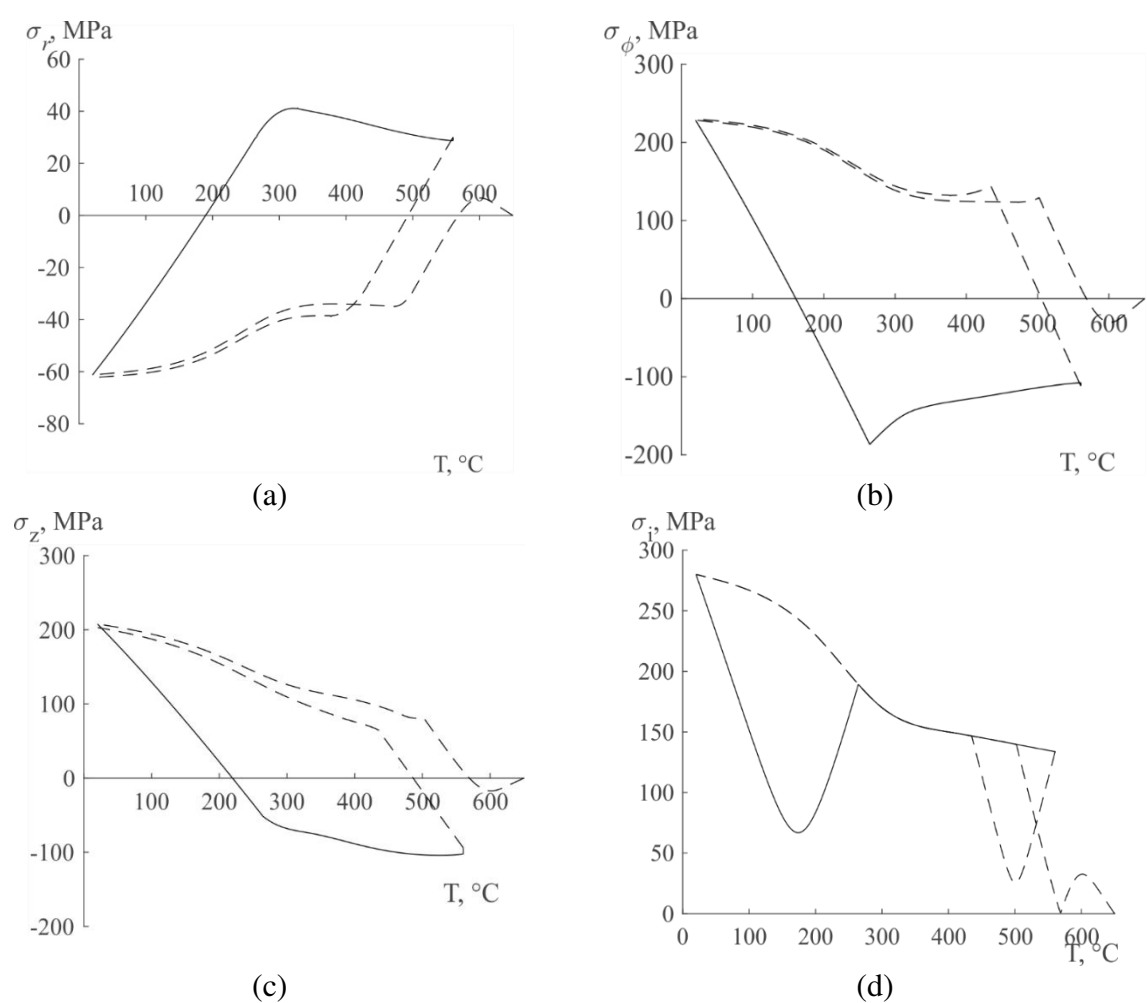


Fig. 4. Change of stress and intensity in the 2nd layer (metal) at the interface of the connection with the glass: (a) $\sigma_r(T)$; (b) $\sigma_{\omega}(T)$; (c) $\sigma_z(T)$; d) $\sigma_i(T)$

In the graphs of stress changes in the 1st layer (glass) (Fig. 5) it is noticeable that after cooling during annealing the stress level changes (highlighted area in σ_z) and is controlled not only by annealing but also by the cooling rate after exposure. It is proved that the stress level and the value of exposure, besides the cooling rate, are also influenced by the heating rate (Figs. 5 and 6). Let's note that such effects are not revealed either at analytical solution for the case of simple Maxwell type cores, or moreover at elastic approximation.

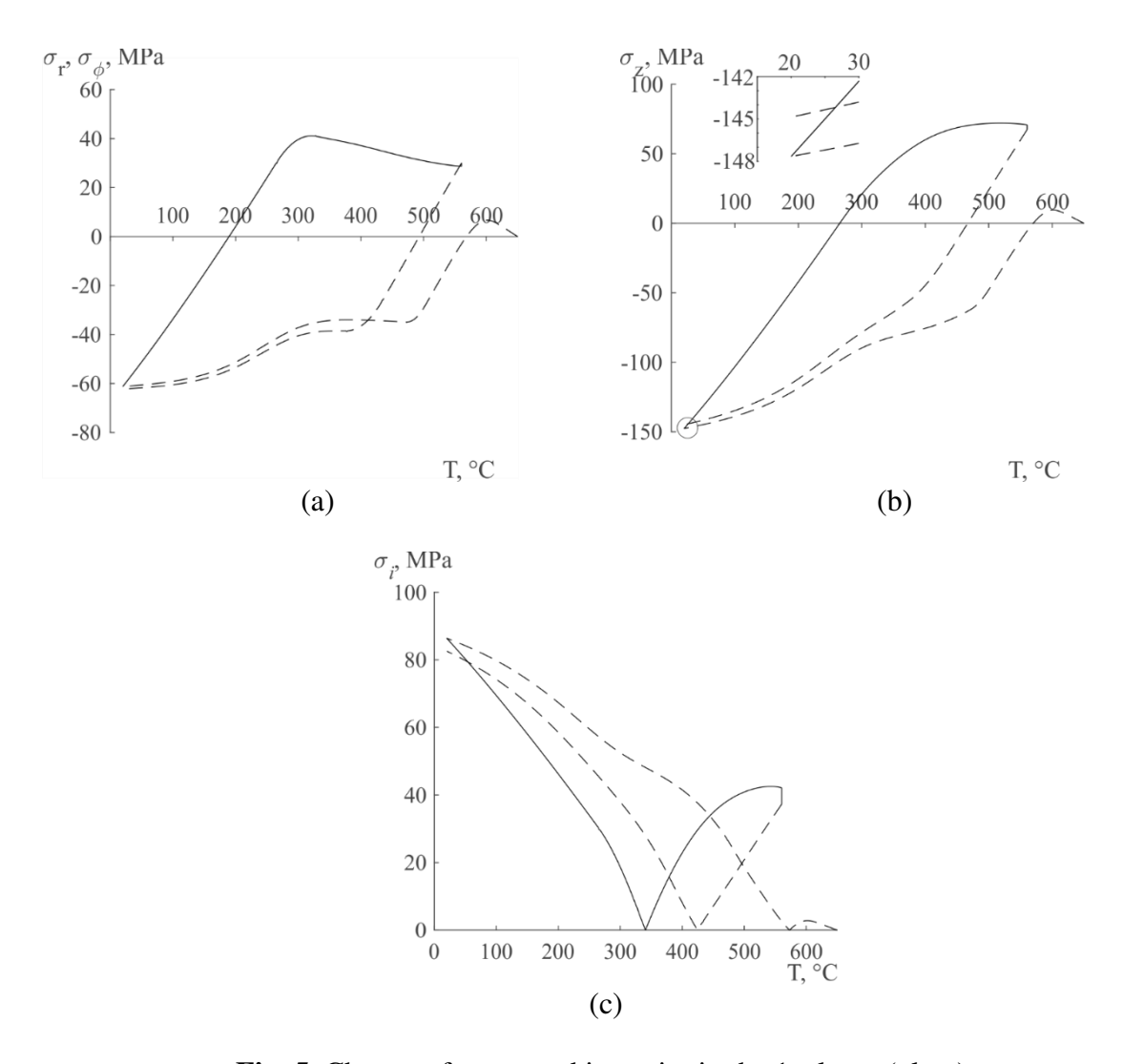


Fig. 5. Change of stress and intensity in the 1st layer (glass): (a) $\sigma_r(T)$ $\bowtie \sigma_{\varphi}(T)$; (b) $\sigma_z(T)$; (c) $\sigma_i(T)$

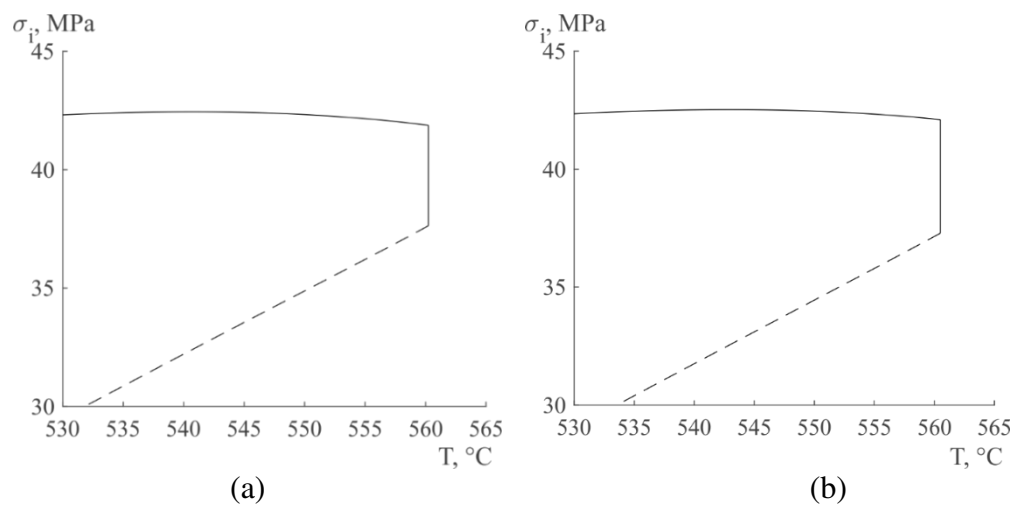


Fig. 6. Fragments of graphs for the layer (1) in the area of exposure at the heating rate $q_1 = 10$ °C/min and cooling at $q_3 = q_4 = 1.5$ °C/min (a), at $q_3 = q_4 = 3$ °C/min (b)

Conclusion

The problem of determining the change in parameters of the strenuously-deformed state in the two-layer cylindrical glass-metal composite in the course of annealing with consideration for glass transition process in the inner glass layer and plastic deformation of the outer metal layer was set and solved. The algorithm of calculation of the cylindrical vitrified layer connected to the plastically deformed non-vitrified layer was proposed. The calculations in accordance with the proposed algorithm allow us to determine the technological stresses with consideration for structural and mechanical relaxation processes. The numerical method suggested in the paper can be applied to the case of several vitrified cylindrical layers.

References

- 1. Sergi R, Bellucci D, Cannillo, V. A Comprehensive Review of Bioactive Glass Coatings: State of the Art, Challenges and Future Perspectives. *Coatings*. 2020;10: 757.
- 2. Thiyagarajan R, Senthil Kumar M. Enhanced energy absorption and microstructural studies on hollow glass microsphere filled closed cell aluminum matrix syntactic foam. *Proceedings of the Institution of Mechanical Engineers, Part C: Journal of Mechanical Engineering Science*. 2022;237(8): 1887–1900.
- 3. Mingming Su, Han Wang, Hai Hao, Thomas Fiedler. Compressive properties of expanded glass and alumina hollow spheres hybrid reinforced aluminum matrix syntactic foams. *Journal of Alloys and Compounds*. 2020;821: 153233.
- 4. Caprino G, Lopresto V, Iaccarino P. A simple mechanistic model to predict the macroscopic response of fibreglass—aluminium laminates under low-velocity impact. *Composites Part A: Applied Science and Manufacturing.* 2007;38: 290–300.
- 5. Boussu F, Provost B, Lefebvre M, Coutellier D. New textile composite solutions for armouring of vehicles. *Adv. Mater. Sci. Eng.* 2019;2019: 7938720. 2019.
- 6. Karpov EV, Demeshkin AG. Strain and fracture of glass-fiber laminate containing metal layers. *J. Appl. Mech. Tech. Physics*. 2018;59(4): 699–705.
- 7. Pikul' VV. Efficiency of glass-metal composite. Moscow: Perspektivnyye materialy; 2000. (In-Russian)
- 8. Lyubimova ON, Dryuk SA. Simulation parameters of temperature in the process of manufacturing a glass-metal composite. *Thermophysics and Aeromechanics*. 2017;24(1): 125–133.
- 9. James PF, Chen M, Jones FR. Strengthening of soda-lime silica glass by sol-gel and melt-derived coatings. *Journal of Non-Crystalline Solids*. 1993;155(2): 99–109.
- 10. Lyubimova ON, Morkovin AV, Dryuk SA, Nikiforov PA. Structure and constitution of glass and steel compound in glass-metal composite. *AIP Conference Proceedings*. 2014;1623: 379–382.
- 11. Tropin TV, Schmelzer JW, Aksenov VL. Modern aspects of the kinetic theory of glass transition. *Physics-Uspekhi*. 2016;59: 42–66.
- 12. Schmelzer J.W.P. Kinetic criteria of glass formation and the pressure dependence of the glass transition temperature. J. Chem. Phys. 2012;136: 074512.
- 13. Startsev YK. Phenomenological description of the glass transition and structural relaxation processes. In: *Vol 7 Physical and chemical aspects of studying clusters, nanostructures and nanomaterials*. Tver': Tver. gos. un-t; 2015. p.494–504. (In-Russian)
- 14. Tool AQ. Relation between inelastic deformability and thermal expansion of glass in its annealing range. *J. Am. Ceram. Soc.* 1946;29(9): 240–253.
- 15. Narayanaswami OS. A model of structural relaxation in glass. *J. Am. Ceram. Soc.* 1971;54(10): 491–498.

- 16. Moynihan CT, Macedo PB, Montrose CJ, Montrose CJ, Gupta PK, DeBolt MA, Dill JF, Dom BE, Drake PW, Easteal AJ, Elterman PB, Moeller RP, Sasabe H, Wilder JA. Structural relaxation in vitreous material. *Ann. New York Acad. Sci.* 1976;279: 15–35.
- 17. Ojovan MI, Tournier RF. On structural rearrangements near the glass transition temperature in amorphous silica. Mater. 2021;14(18): 5235.
- 18. Mazurin OV. *Glass transition*. Lenindrad: Nauka; 1986. (In-Russian)
- 19. Mazurin OV. Annealing of glass-to-metal junctions. Leningrad: Energia; 1980. (In-Russian)
- 20. Gonchukova NO. Calculation of stresses in amorphous nickel–phosphorus coatings on metallic substrates. *Glass Physics and Chemistry*. 2004;8(1): 356–358.
- 21. Kalgin AV. Structural relaxation in an amorphous phase of the thin-film nanogranular composite (x)Ni (1–x)PNBZT. *Ferroelectrics*. 2020; 561: 1–11.
- 22. Lybimova ON, Barbotko MA. Modeling of heat transfer due to induction heating of laminated glass-metal materials. *Thermophysics and Aeromechanics*. 2021;28: 87102.
- 23. Bartenev GM, Sanditov DS. *Relaxation processes in glassy systems*. Novosibirsk: Nauka; 1986. (In-Russian)
- 24. Galanin MP, Guzev MA, Nizkaya TV. *Numerical solution of the thermoplasticity problem with additional state parameters*. To be published in: *Inst. Appl. Math.* [Preprint] 2007. Available from: https://keldysh.ru/papers/2007/prep08/prep2007_08.html [Accessed 1th June 2023].
- 25. Rodriguez-Tinoco C, Gonzalez-Silveira M, Ramos MA, Rodriguez-Viejo J. Ultrastable glasses: new perspectives for an old problem. *Riv. Nuovo Cim.* 2022;45: 325–406.

THE AUTHORS

Barbotko M.A.

e-mail: barbotko_ma@dvfu.ru

Lyubimova O.N.

e-mail: berms@mail.ru

Ostanin M.V.

e-mail: maximostanin91@yandex.ru

The influence of the altered structure zone characteristics after the material jet treatment on the samples stress state during tensility

Submitted: September 8, 2022

Approved: March 16, 2023

Accepted: May 5, 2023

A.I. Verameichyk [™], M.V. Neroda [™], B.G. Holodar [™]

Brest State Technical University, Brest, Belarus

☑ vai_mrtm@bstu.by

Abstract. The article investigates the influence of the mechanical characteristics (elasticity module, Poisson coefficient) of the material altered structure zones, which arise after heat treatment by concentrated high-energy impact. For rectangular samples, two forms of the structure formation zone are analyzed - rectangular and crescent-shaped with a zone of processed material in the form of a semicircle. MSC NASTRAN and ANSYS Workbench software packages were used as calculation packages. A computer simulation of the stress-strain state of samples with one or more treated tracks (along the entire length and on the part of the length) under tension was carried out. The influence of the zone size and the distance between them is investigated. An insignificant effect of the distance between the tracks on the voltages has been established. The stress concentration coefficients in the vicinity of the treatment zones are determined. The transverse stresses are studied depending on the mechanical characteristics of the material.

Keywords: mechanical characteristics of the material; stress-strain state; stress concentration coefficient; finite element method; local impact

Acknowledgements. The work is carried out within the framework of task 3.2.8 of Scientific and Research Work No. 1 "Study of mechanical properties of machine component elements after laser-plasma treatment" of the sub-programme "Electromagnetic, beam-plasma and foundry deformational technologies for material treatment and creation" of the Scientific Research State Programme "Materials study, new materials and technologies" (Belarus).

Citation: Verameichyk AI, Neroda MV, Holodar BG. The influence of the altered structure zone characteristics after the material jet treatment on the samples stress state during tensility. *Materials Physics and Mechanics*. 2023;51(4): 130-141. DOI: 10.18149/MPM.5132023_12.

Introduction

It is known that various inclusions that in some way have arisen in a homogeneous body affect the local stress-strain state (SSS) of the material in its vicinity [1–3]. This effect can be characterized either by way of the stress concentration coefficients or by way of the parameters used in the destruction mechanics (see, for example, [3–8]).

With laser, plasma and other high-energy methods of concentrated impact on the component, zones of altered structure of the source material appear – the target impact zone and the thermal influence zone surrounding it [9]. In the latter, the structure differs markedly from both the processing zone structure and the structure of the base material, and the management of its properties is limited due to the lack of the possibility of direct influence on the structure formation in this area. Data on the properties of the material in these areas are limited, there are no unambiguous analytical dependencies between their mechanical

characteristics, therefore there is a large uncertainty in their values [10], which is a significant drawback in predicting the behavior of a real object in operating conditions.

Numerous works of domestic and foreign scientists have been devoted to the study of the component properties and SSS during heat treatment by a local highly concentrated heating source [11-20]. In [13] some regularities and interrelations between technological factors determining the features of short-term local thermal impacts and the nature of structural changes and properties of low-alloy steels were established, and in [14] – for steel with reduced calcination of 60RC. In [15], the influence of the laser treatment process on the microstructure peculiarities and the formation of the cast iron thermal influence zone is considered. In the article [16], the influence of heat treatment (annealing, normalization, hardening, tempering) during quenching on the mechanical properties and microstructure of steel ST 37-2 was studied. In [17], a method for assigning surface hardening modes is given, which differs from the known ones in that heat treatment modes are set taking into account not only the specified depth and hardness of the hardened layer, but also the nature of the distribution of the remaining stresses in the material. The article [18] describes a mathematical model for calculating the SSS of elements of composite structures under the impact of a local heating source. In [19] computer simulation of tensile tests of a rod with rectangular zones that have arisen during heat treatment by a moving highly concentrated heat source, the material characteristics of which differ from the properties of the base material, is considered. In [20] for the first time, the analytical method solved the problem of changing the stress-strain state of a polymer material during its orientation extraction.

Instrumental studies conducted by domestic and foreign scientists in the field of sample properties after an exposure to a local heating source are mainly aimed at establishing the nature of structural transformations and hardness of materials [21–25]. The results of studying the mechanical characteristics of the material of the treated zone, in particular, elasticity modules and Poisson coefficients, are not sufficiently presented. Accordingly, the results of studies of the impact of emerging differences in these indicators on the SSS of machine components are not sufficiently represented. Therefore, the issue discussed in the article is relevant.

Materials and Methods

Studies show that the depth of surface hardening is small compared to the thickness of the component, so it is most natural to assess the effect of changes in material parameters for the case when there was no stress gradient in the volume of the untreated material, for example, during axial straining of the sample. Therefore, to assess the degree of influence of the differences in the elasticity module and Poisson coefficient of the zones of the component with analtered structure compared to the characteristics of the base material, a finite element simulation of the problem of straining a rod with the tracts of the treated material surrounded by an intermediate zone of thermal influence was carried out.

Two cases of track length are considered – a continuous one along the length of the sample and a shortened one (to account for the influence of its butt-end area). The geometry of the zones, the number of tracks and the distances between them varied during the calculations. The length of the shortened section of the track was 5/11 of the length of the selected section of the rod. During heat treatment, depending on the modes, the thickness of the intermediate layer may vary, so the calculations were carried out for different values of this parameter. In view of the symmetry of the problem, the selected quarter of the sample was considered during modeling (Fig. 1).

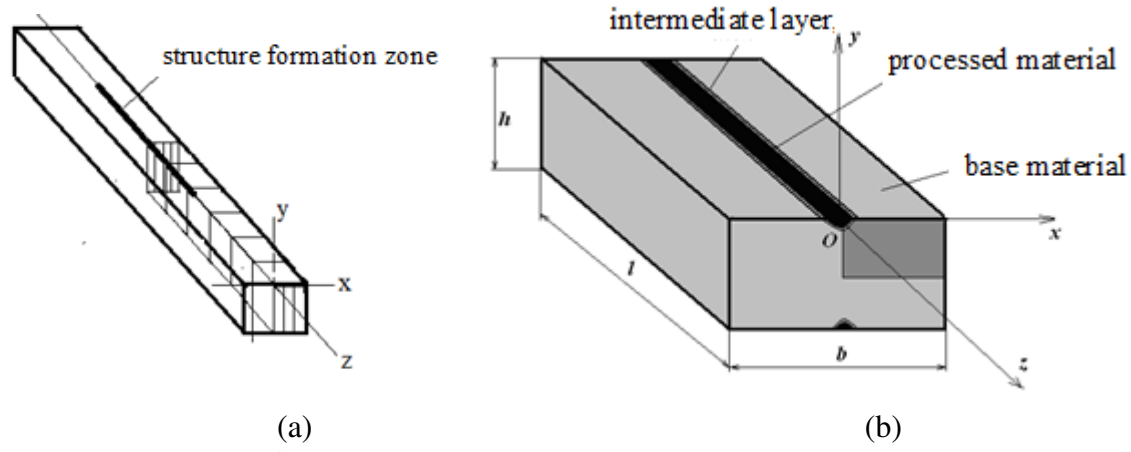


Fig. 1. The sample (a) and the marked element (b)

Two forms of the structure formation zone are analyzed – a rectangular one 0.8×0.4 mm and a crescent-shaped one with a zone of the treated material in the form of a semicircle with a radius of 0.4 mm. The MSC NASTRAN programming complex was used as a calculation package for a model with a rectangular cross-section of the zone, and ANSYS Workbench was used for a crescent-shaped zone.

The finite element model of the sample in the presence of one track is shown in Fig. 2. This volume is comprehensively surrounded by a 0.2 mm thick transition area with a possibility of reducing it to zero. The rest of the volume is occupied by the source (main) material. Overall dimensions of the model are $2.0 \times 2.6 \times 4.4$ mm.

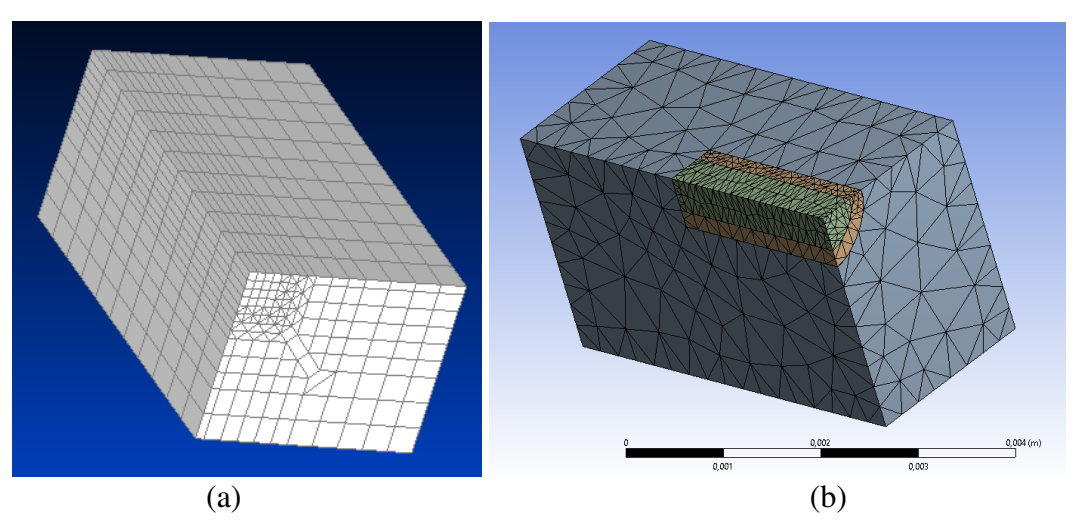


Fig. 2. Finite element models: a) rectangular, b) crescent-shaped

Boundary conditions for displacements were set in the form of a movement restriction in the direction of the axis Oy ($V_y = 0$) at the points of the upper facet of the body, $W_z = 0$ on the rear facet, $U_x = 0$ on the left facet. On the right longitudinal face, boundary conditions of 2 types were set $U_x \neq 0$ (imitation of a rod sample) and $U_x = 0$ (imitation of constrained deformation, which is true, for example, for plates).

The module of elasticity of the initial material was assumed to be equal to $E = E_{bas} = 200$ GPa, the Poisson coefficient $\mu = \mu_{bas} = 0.3$. The elasticity modules of the intermediate and treated layers and their Poisson coefficients varied, but it was assumed that after treatment, the body material at all its points remains in the elastic area of operation, which corresponds to most realizable cases of operation of machine components and mechanisms. SSS in the process of the body cooling directly after heat treatment was not

considered. The indices "bas", "int", "pr" hereafter refer respectively to the source material, the intermediate layer and the treated volume.

Loading was carried out by setting the displacement of the front butt-end section by the value $W_z = 0.0044$ mm, which is determined from the condition of equality of axial stresses $\sigma_z = 200$ MPa for a homogeneous rod. The calculations have shown that the selected rod length is sufficient to equalize the stress state by its volume. The ratio of the elasticity modules of the treated material to the modules of the source material varied within the limits of $K_E = E_{pr}/E_{bas} = 0.8, ..., 1.5$, Poisson coefficients – within the limits of $K_{\mu} = \mu_{pr}/\mu_{bas} = 0.7, ..., 1.4$.

Results and Discussion

A study of the samples SSS with two zones of modified material structure of rectangular and crescent sections for different boundary conditions, the number and size of zones, and material characteristics was carried out. As examples, Figs. 3, 4 show the distributions of equivalent stresses σ_i over the volume of the body for the considered material characteristics and conditions concerning the geometry of treatment. Comparing them, it is possible to determine the direction of change in the material SSS depending on these parameters. The calculated stress values are the average in the corresponding elements. Their values at the angular points of the elements are not used, since due to the small size of the finite elements compared to the overall dimensions of the body, the maximum values in them are quite close to the average. The main stresses σ_I in this problem are close to the longitudinal stresses σ_z .

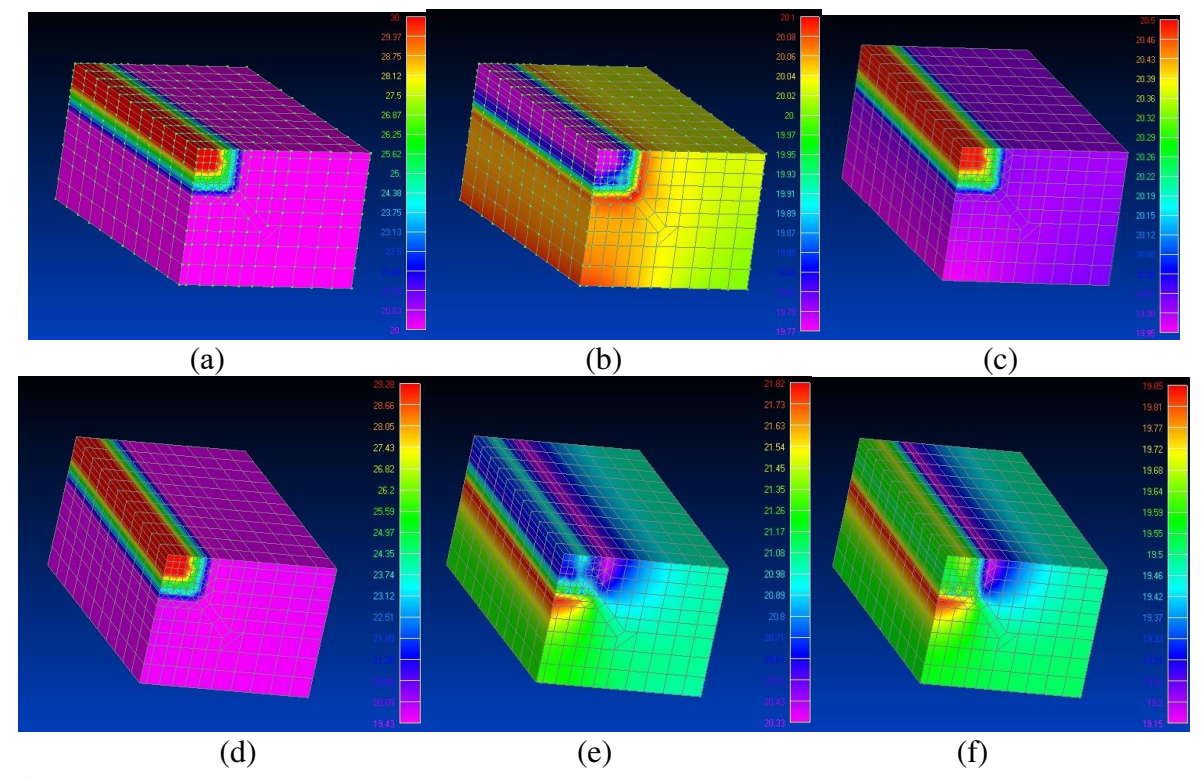


Fig. 3. Distribution of equivalent stresses according to the Mises criterion σ_i for a sample with a rectangular zone [19] with a free (a–c) and a fixed (d–f) right face, thickness of the intermediate layer is 0.2 mm

(a, d)
$$E_{bas} = 200 \,\text{GPa}$$
, $E_{int} = 250 \,\text{GPa}$, $E_{pr} = 300 \,\text{GPa}$, $\mu_{bas} = \mu_{int} = \mu_{pr} = 0.3$,
(b, e) $E_{bas} = E_{int} = E_{pr} = 200 \,\text{GPa}$, $\mu_{bas} = 0.3$, $\mu_{int} = 0.36$, $\mu_{pr} = 0.42$
(c, f) $E_{bas} = E_{int} = E_{pr} = 200 \,\text{GPa}$, $\mu_{bas} = 0.3$, $\mu_{int} = 0.24$, $\mu_{pr} = 0.21$

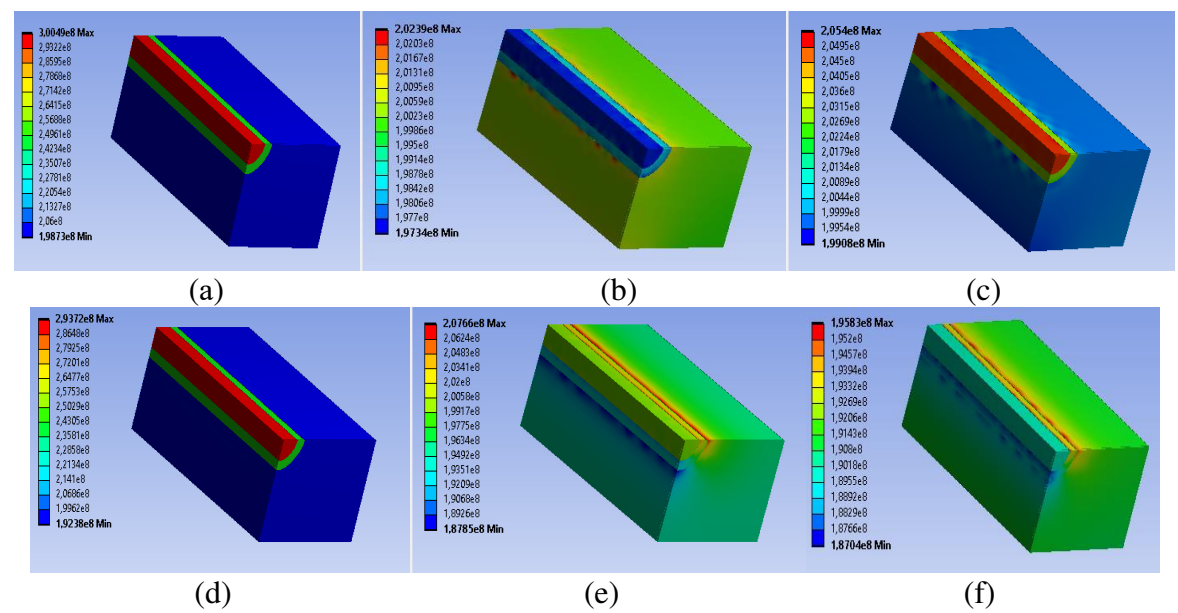


Fig. 4. Distribution of equivalent stresses according to the Mises criterion σ_i for a sample with a crescent-shaped zone with a free (a–c) and a fixed (d–f) right face, thickness of the intermediate layer is 0.2 mm

(a, d)
$$E_{bas} = 200 \,\text{GPa}$$
, $E_{int} = 250 \,\text{GPa}$, $E_{pr} = 300 \,\text{GPa}$, $\mu_{bas} = \mu_{int} = \mu_{pr} = 0.3$, (b, e) $E_{bas} = E_{int} = E_{pr} = 200 \,\text{GPa}$, $\mu_{bas} = 0.3$, $\mu_{int} = 0.36$, $\mu_{pr} = 0.42$ (c, f) $E_{bas} = E_{int} = E_{pr} = 200 \,\text{GPa}$, $\mu_{bas} = 0.3$, $\mu_{int} = 0.24$, $\mu_{pr} = 0.21$

The results of the calculations show that any deviation from the initial parameters leads to a change in the stress distribution over the volume of the part. Their maximum can be realized both in the processed layer, and in the main material, intermediate layer or at the boundaries of layers. For the shortened zone, the greatest stresses occur in the area of the treated material adjacent to the main one. When the modulus of elasticity of the treated layer increases over the modulus of the initial material, there is always an increase in the maximum stresses σ_i and σ_z , while the minimum σ_i and σ_z arising at the boundary of the transition zone and the base material do not obey this pattern. When the modulus of elasticity of the treated zone decreases with respect to the modulus of elasticity of the base material, the stress concentration occurs in the base material, as a result of which the maximum stresses are close to the nominal ones. The main difference for the crescent-shaped zones is that the maximum stress occurs on the axis of symmetry of the segment.

It is established that the influence of Poisson coefficient on the stresses is nonlinear. Its deviation for the treated zone from the coefficient for the initial (base) material in any direction leads to an increase in maximum stresses, but it can affect the minimum level in different ways. The results of the research are presented by the graphs in Figs. 4, 5. When Poisson coefficient of the source material changes, the structures in these figures will also change in a certain way. These observations regarding the influence of Poisson coefficients correspond to [1, pp. 546-573].

Figures 5-9 show the values of the ratios σ_z^{max} to the reference value $\sigma_z = 200$ MPa, which represent the stress concentration coefficients for this problem $K_{\sigma} = \sigma_z^{\text{max}}/\sigma_z$, depending on the ratios of the material parameters $K_E = E_{pr}/E_{bas}$ or $K_{\mu} = \mu_{pr}/\mu_{bas}$. Figures 4 and 5 illustrate the case of a rectangular-shaped zone of the structure formation, Figs. 6-8 – the case of a crescent-shaped one. Light signs relate to the case of a free right facet $U_x \neq 0$ (the

case of the rod), and the dark ones – to the case of a fixed facet $U_x = 0$ (constrained deformation).

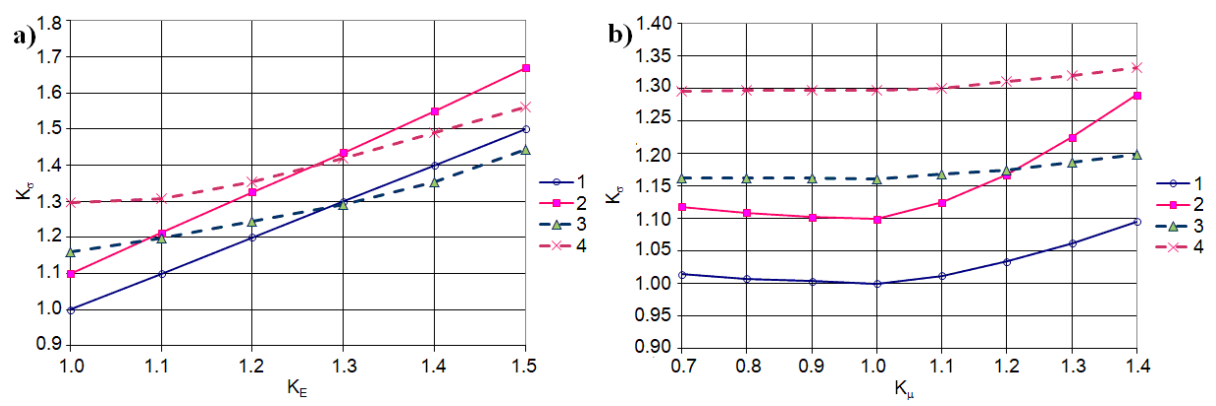


Fig. 5. Influence of elasticity module (a) and Poisson coefficient (b) on longitudinal stresses; intermediate layer is 0.2 mm thick:

1 – long zone, free right facet; 2 – long zone, fixed right facet; 3 – shortened zone, free right facet; 4 – shortened zone, fixed right facet

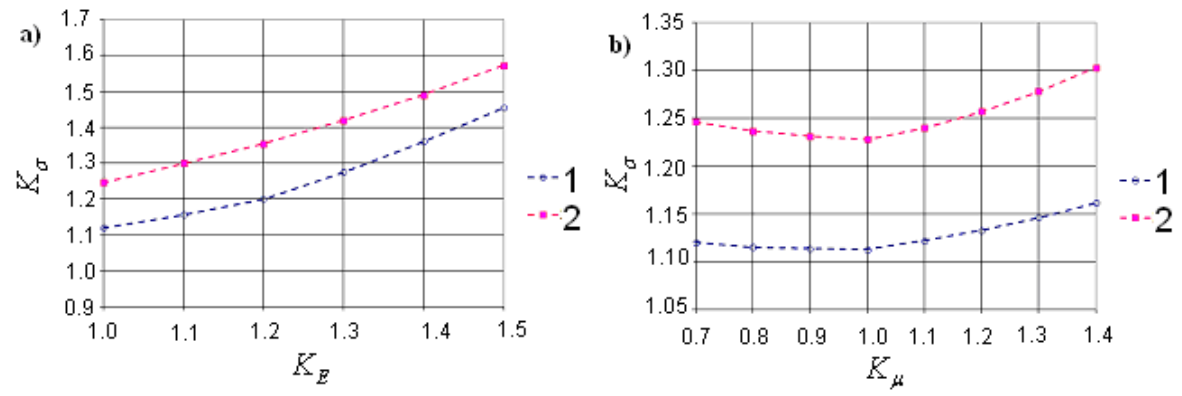


Fig. 6. Influence of the elasticity module (a) and Poisson coefficient (b) on longitudinal stresses in a shortened track with an intermediate layer 0.1 mm thick:

1 – free right facet, 2 – fixed right facet

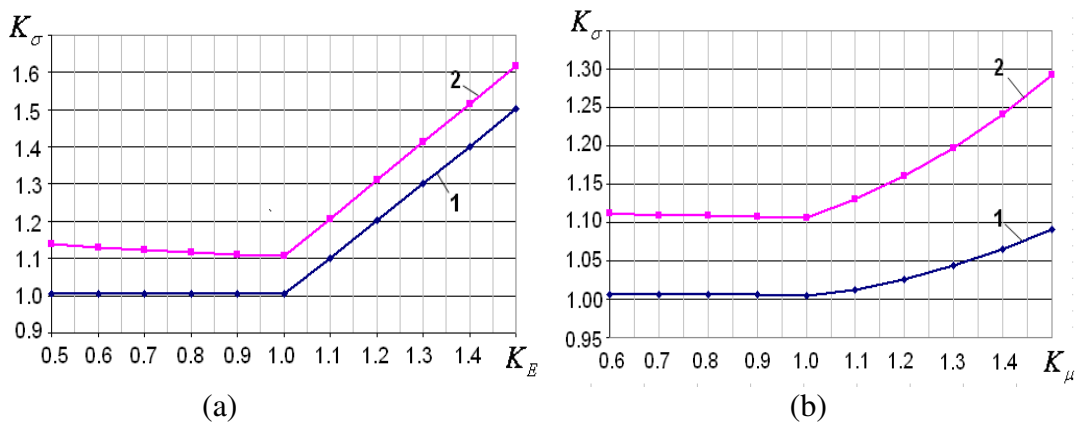


Fig. 7. Dependence of the stress concentration coefficient on K_E (a) and K_{μ} (b) for a sample with a crescent-shaped zone along the entire length:

1 – rod pattern (right facet is free), 2 – constrained deformation (right facet is fixed)

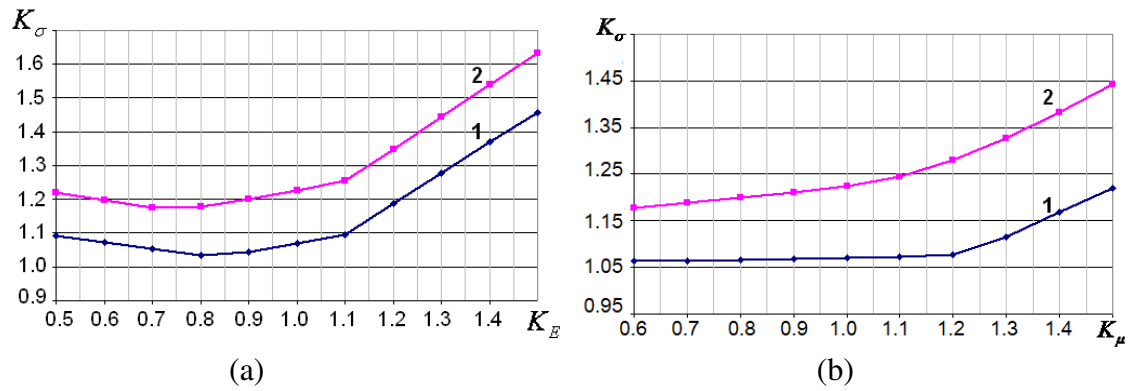


Fig. 8. Dependence of the stress concentration coefficient on K_E (a) and K_{μ} (b) for a sample with a shortened crescent-shaped track:

1 – rod sample (right facet is free), 2 – constrained deformation (right facet is fixed)

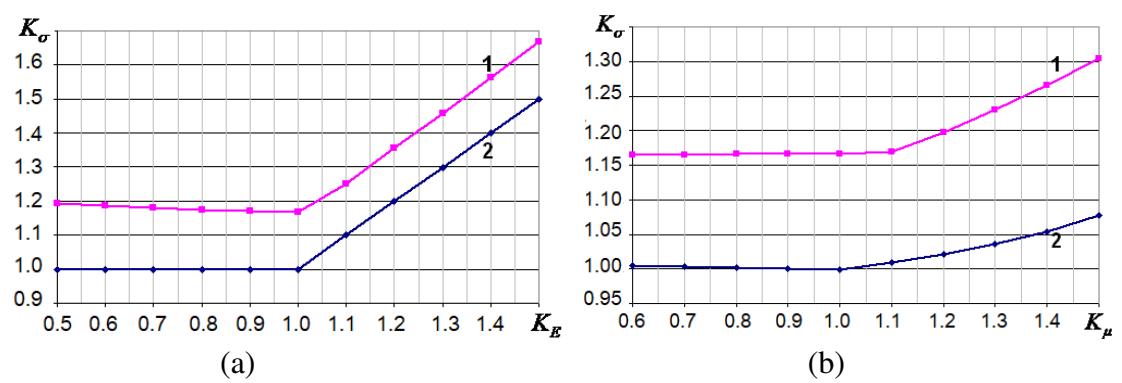


Fig. 9. Dependence of the stress concentration coefficient K_E (a) and K_μ (b) for samples with two crescent-shaped track along the entire length and the distance between them $\delta = 0.4$ mm: 1 - rod sample (right facet is free), 2 - constrained deformation (right facet is fixed)

In the case of constrained deformation, the stresses in all the cases considered are higher than in the case of free deformation. The stress concentration coefficients for the rectangular and crescent-shaped zones of the altered structure differ insignificantly, but the values for the rectangular zone are higher.

For a diagram with a shortened track, when reducing the intermediate layer thickness to zero, a change in Poisson coefficient relative to the value for the source material leads to a slight decrease in stress concentration.

The case of the presence of three parallel tracks along the entire length of the sample, arranged symmetrically at distances $\delta = 0.0$ -0.6 mm from each other, is also considered. As an example for a rectangular track, Figs. 10-13 show the distribution of equivalent stresses σ_i according to Mises for the case when the distance between the roads is 0, 0.1 and 0.6 mm.

The research results and their comparison with the data given in [20] for δ = 0.2 mm show an insignificant effect of the distance δ on the stress concentration factor. Therefore the influence of mechanical and geometric parameters change of materials on the SSS of the body when exposed to a high-energy jet can be carried out based on the results of calculations for a single track. The difference in results does not exceed several percent. A variation in the distance between the tracks for a crescent-shaped zone of structure formation does not affect the values of the stress concentration coefficient, either.

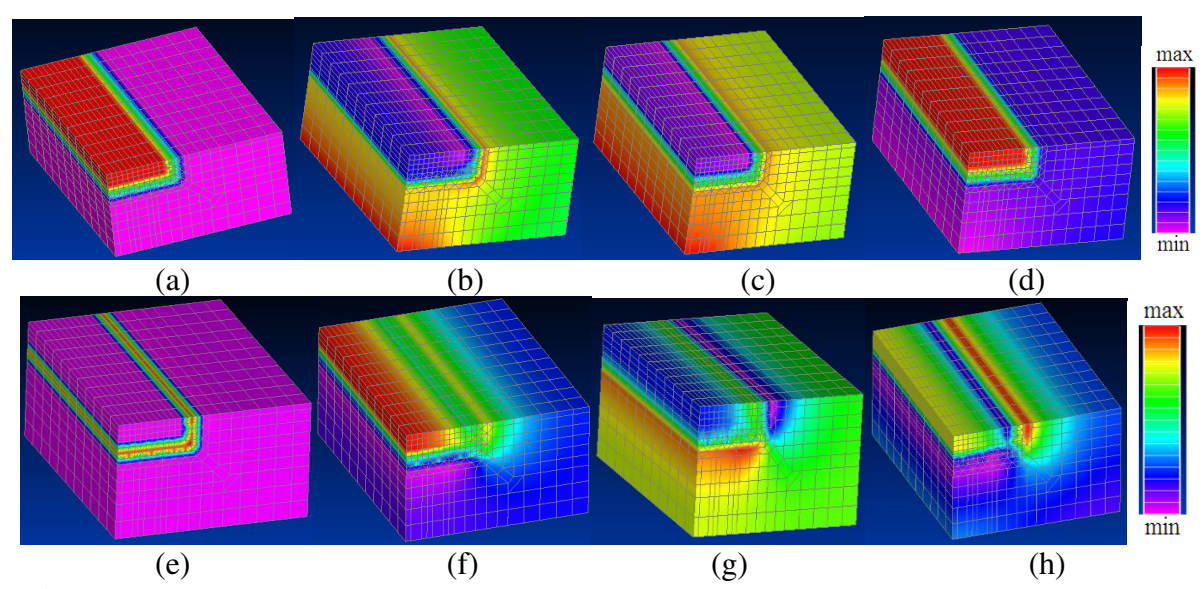


Fig. 10. Distribution of equivalent stresses according to Mises σ_i with a free (a–d) and fixed (e–h) right facet ($\delta = 0$ mm, rectangular-shaped zone):

(a, e)
$$E_{bas} = 200$$
 GPa, $E_{int} = 250$ GPa, $E_{pr} = 300$ GPa, $\mu_{bas} = \mu_{int} = \mu_{pr} = 0.3$
(b, f) $E_{bas} = E_{int} = E_{pr} = 200$ GPa, $\mu_{bas} = 0.3$, $\mu_{int} = 0.36$, $\mu_{pr} = 0.42$
(c, g) $E_{bas} = E_{int} = E_{pr} = 200$ GPa, $\mu_{bas} = 0.3$, $\mu_{int} = 0.24$, $\mu_{pr} = 0.21$
(d, h) $E_{bas} = E_{int} = E_{pr} = 200$ GPa, $\mu_{bas} = 0.21$, $\mu_{int} = 0.24$, $\mu_{pr} = 0.3$

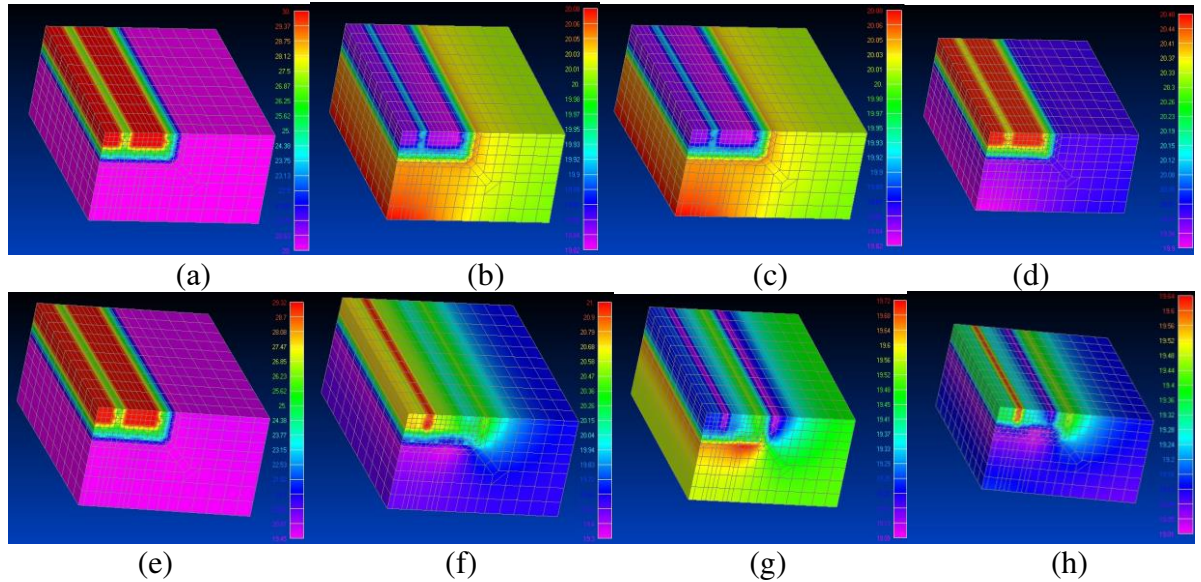


Fig. 11. Distribution of equivalent stresses according to Mises σ_i with a free (a–d) and fixed (e–h) right facet ($\delta = 0.1$ mm, rectangular-shaped zone):

(a, e)
$$E_{bas} = 200 \,\text{GPa}$$
, $E_{int} = 250 \,\text{GPa}$, $E_{pr} = 300 \,\text{GPa}$, $\mu_{bas} = \mu_{int} = \mu_{pr} = 0.3$
(b, f) $E_{bas} = E_{int} = E_{pr} = 200 \,\text{GPa}$, $\mu_{bas} = 0.3$, $\mu_{int} = 0.36$, $\mu_{pr} = 0.42$
(c, g) $E_{bas} = E_{int} = E_{pr} = 200 \,\text{GPa}$, $\mu_{bas} = 0.3$, $\mu_{int} = 0.24$, $\mu_{pr} = 0.21$
(d, h) $E_{bas} = E_{int} = E_{pr} = 200 \,\text{GPa}$, $\mu_{bas} = 0.21$, $\mu_{int} = 0.24$, $\mu_{pr} = 0.3$

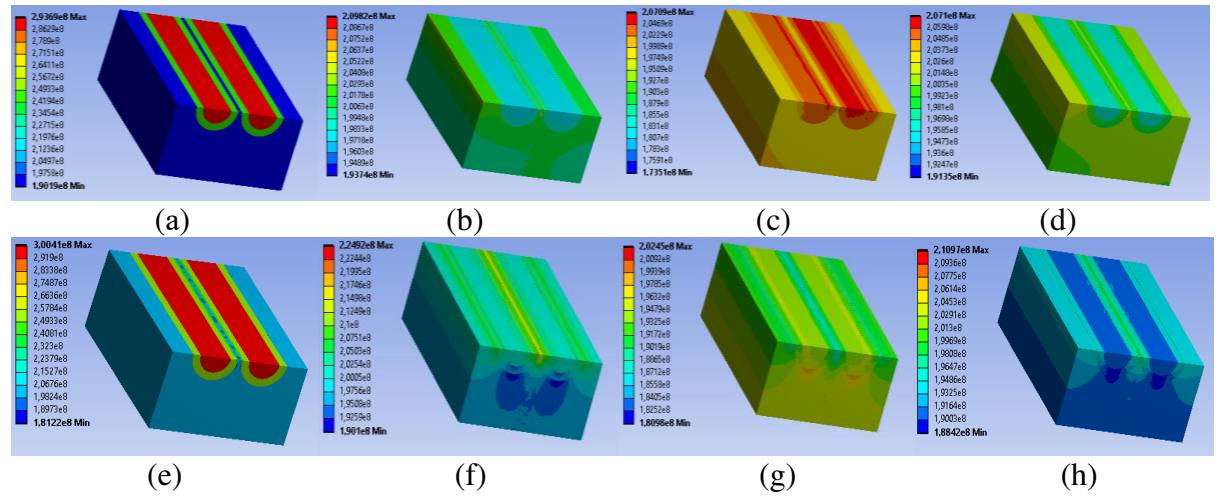


Fig. 12. Distribution of equivalent stresses according to Mises σ_i with a free (a–d) and fixed (e–h) right facet ($\delta = 0.1$ mm, crescent-shaped zone):

(a, e)
$$E_{bas} = 200$$
 GPa, $E_{int} = 250$ GPa, $E_{pr} = 300$ GPa, $\mu_{bas} = \mu_{int} = \mu_{pr} = 0.3$
(b, f) $E_{bas} = E_{int} = E_{pr} = 200$ GPa, $\mu_{bas} = 0.3$, $\mu_{int} = 0.36$, $\mu_{pr} = 0.42$
(c, g) $E_{bas} = E_{int} = E_{pr} = 200$ GPa, $\mu_{bas} = 0.3$, $\mu_{int} = 0.24$, $\mu_{pr} = 0.21$
(d, h) $E_{bas} = E_{int} = E_{pr} = 200$ GPa, $\mu_{bas} = 0.21$, $\mu_{int} = 0.24$, $\mu_{pr} = 0.3$

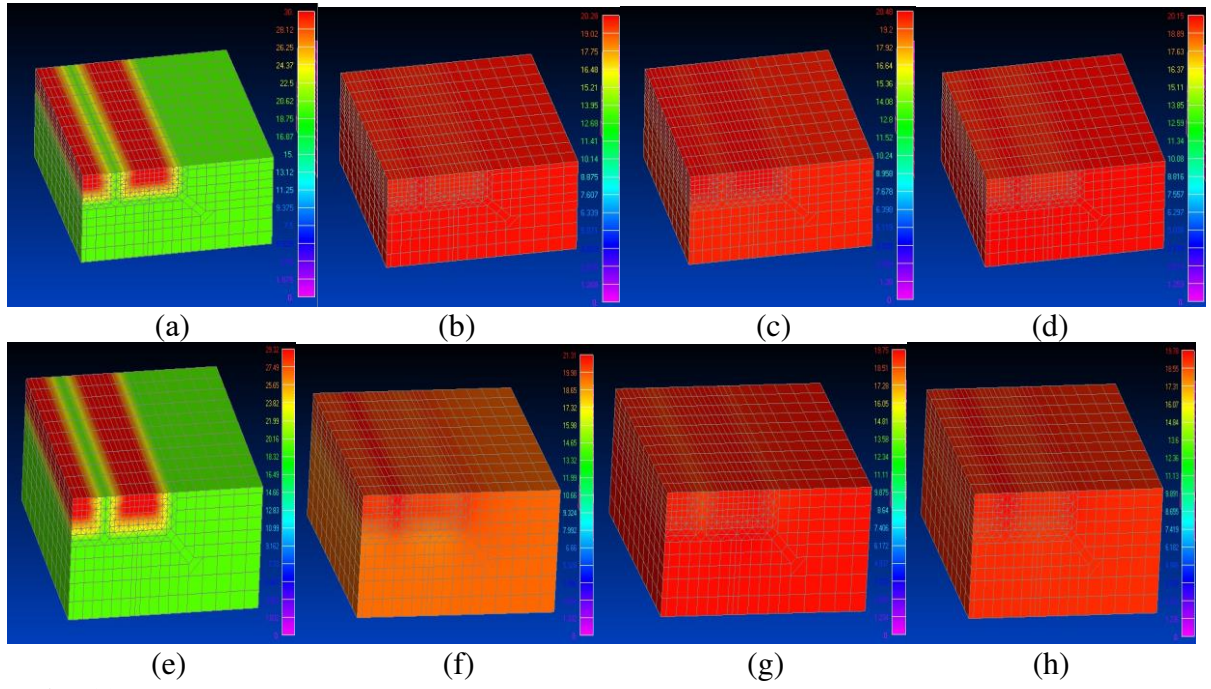


Fig. 13. Distribution of equivalent stresses according to Mises σ_i with a free (a–d) and fixed (e–h) right facet ($\delta = 0.6$ mm, rectangular-shaped zone):

(a, e)
$$E_{bas} = 200$$
 GPa, $E_{int} = 250$ GPa, $E_{pr} = 300$ GPa, $\mu_{bas} = \mu_{int} = \mu_{pr} = 0.3$
(b, f) $E_{bas} = E_{int} = E_{pr} = 200$ GPa, $\mu_{bas} = 0.3$, $\mu_{int} = 0.36$, $\mu_{pr} = 0.42$
(c, g) $E_{bas} = E_{int} = E_{pr} = 200$ GPa, $\mu_{bas} = 0.3$, $\mu_{int} = 0.24$, $\mu_{pr} = 0.21$
(d, h) $E_{bas} = E_{int} = E_{pr} = 200$ GPa, $\mu_{bas} = 0.21$, $\mu_{int} = 0.24$, $\mu_{pr} = 0.3$

It was found that with an increase in δ , the change in the Poisson's ratio of the zones of the modified structure in any direction with respect to the value for the base material practically does not affect the equivalent stresses (Fig. 13).

Transverse stresses σ_x arising during loading depend on geometric conditions and differences in the parameters E and μ , increasing with the growth of ratios E_{pr} / E_{bas} and μ_{pr} / μ_{bas} . The main role is played by the presence constraint of deformation.

In its absence (U_x = var), the stresses are insignificant, vary from zero to several MPa units and can arise both in the treated layer itself and under it at the boundary with the base material. If there are several tracks σ_x in the treated layer, they can be both positive ($\mu_{pr}/\mu_{bas} > 1$) and negative ($\mu_{pr}/\mu_{bas} < 1$) regardless of the distance between the tracks. Their maximum level in the calculations was 3.82 MPa.

If $U_x=0$, then the stresses σ_x in the treated layer are tensile. At $\mu_{pr}/\mu_{bas}<1$ they are slightly below the level $\sigma_z/3$, but they increase at $\mu_{pr}/\mu_{bas}>1$ while remaining below the value $\sigma_z/2$. In case of several tracks, their maximum depends on the distance between them $(\delta=0.2 \text{ mm}, \ \sigma_{max}=11.82 \text{ MPa} \text{ at } \sigma_z=25.42 \text{ MPa}, \ \mu_{pr}=0.42)$.

The levels of transverse stresses σ_x for samples with a crescent-shaped structure formation both qualitatively and quantitatively correspond to the case of a rectangular zone and are shown in Fig. 14.

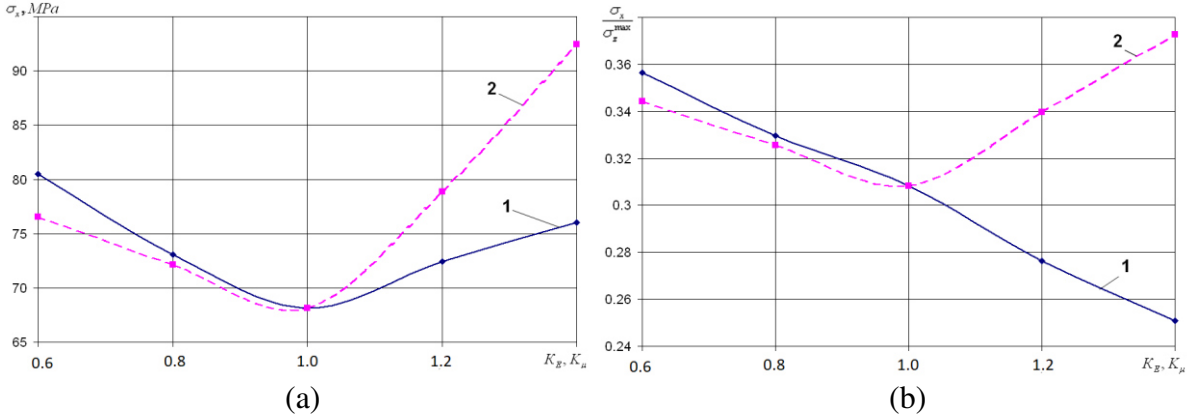


Fig. 14. Dependence of transverse stresses σ_x (a) and their relations to the maximum longitudinal stresses (b) for the case of a sickle-shaped track at E=var(1) and $\mu=var(2)$

Conclusion

The influence of the characteristics of the zones of the altered structure of the source material arising after the heat treatment of samples by a moving highly concentrated heat source on the stress-strain state under tension has been studied. Two forms of the zone of structure formation are considered – rectangular and crescent. Based on the results of finite element calculation in a wide range of values of the elasticity module and Poisson coefficient, the SSS of samples with one or more zones of the material altered structure along its entire length and on the part of the length was determined. Stress concentration coefficients in the vicinity of treatment zones for various boundary conditions, sizes of zones and distances between them are determined. An insignificant influence of the distance between the tracks on the stress concentration coefficient has been established. Transverse stresses depending on the mechanical characteristics of the treated and source material have been investigated.

The obtained values of the concentration coefficients, although they reflect the general trends of SSS transformation in the presence of local material treatment, are not

unambiguous, but depend on geometric and mechanical characteristics of an object (the relations of the treated zone sizes and the initial component, the thickness of the intermediate layer, elasticity modules and Poisson coefficients of the layer materials).

The research results show both the importance of knowing the exact values of the material mechanical characteristics in the field of local impact, and the necessity of carrying out calculations for the hardened part, taking into account the presence of this impact, without which it is impossible to choose an optimal treatment mode for ensuring the required product performance qualities.

References

- 1. Muskhelishvili NI. Some basic problems of the mathematical theory of elasticity. Moscow: Science; 1966. (In-Russian)
- 2. Neiber G. Stress concentration. Moscow: Gostekhizdat; 1947.
- 3. Savin GN. Stress concentration near holes. Moscow: State Publishing House of technology-theoretical lit.; 1951. (In-Russian)
- 4. Birger IA, Panovko YG. (ed.) *Strength, stability, vibrations*. Moscow: Mechanical Engineering. 1968. p.463. (In-Russian)
- 5. Peterson R. Stress concentration coefficients. Graphs and formulas for calculating structural elements for strength. Moscow: World; 1977. (In-Russian)
- 6. Ito Y, Murakami Y, Hasebe N. *Handbook of stress intensity coefficients*. Moscow: World; 1990.
- 7. Cherepanov GP. *Mechanics of brittle fracture*. Moscow: Science; 1974. (In-Russian)
- 8. Berezhnitsky LT, Delyavsky MV, Panasyuk VV. *Bending of thin plates with crack-type defects.* Kiev: Scientific Thoughts; 1979. (In-Russian)
- 9. Grigoriev SN, Ivannikov AY, Prozhega MV, Zakharov IN, Kuznetsova OG, Levin AM. The influence of the highly concentrated energy treatments on the structure and properties of medium carbon steel. *Metals*. 2020;10(12): 1669.
- 10. Gulyaev AP. *Metallovedenie*. Moscow: Book on demand; 2020. (In-Russian)
- 11. Dinesh BP, Balasubramanian KR, Buvanashekaran GH. Laser surface hardening. *International Journal of Surface Science and Engineering*. 2011;5(2/3): 131-151.
- 12. Bely AV, Makushok EM, Pobol IL. Surface hardening treatment with the use of concentrated energy flows. Minsk: Science and technology; 1990. (In-Russian)
- 13. Sharapova DM. Evolution of structure and properties of structural low-alloy steels under short-term local thermal effects by concentrated heat sources. Dissertation of the PhD of Technical Sciences. St. Petersburg, 2018. (In-Russian)
- 14. Gordienko AI, Michluk AI, Ivashko VV, Vegera II The influence of heating modes on the structure and mechanical properties of 60PP steel. *Casting and Metallurgy*. 2011;1(59): 146-153.
- 15. Voitovich ON, Sokolov IN. Investigation of the influence of laser heat treatment parameters on the properties of hardened surface layers. *Bulletin of the Belarusian-Russian University*. 2013;2: 6-14.
- 16. Fadara TG, Akanbi OY, Fadare DA. Effect of heat treatment on mechanical properties and microstructure of NST 37-2 steel. *Journal of Minerals & Materials Characterization & Engineering*. 2011;10(3): 299-308.
- 17. Ivantsievsky VV. Control of the structural and stressed state of the surface layers of machine parts during their hardening using concentrated sources of heating and finishing grinding. Dissertation of the Doctor of Technical Sciences. Novosibirsk; 2012. (In-Russian)
- 18. Gulakov SV, Shcherbakov SV, Zavarika NG. Computer modeling of the stress-strain state of elements of composite structures under the influence of a local heating source. *Bulletin of Pryazovsky State Technical University*. 2004;14: 223-226.

- 19. Verameichyk AI, Neroda MV, Holodar' BG. Konechno-elementnoe modelirovanie zadachi o rastyazhenii materiala s zonami izmenennoj struktury. *Mekhanika mashin, mekhanizmov I materialov*. 2022;3(60): 77–84. (In-Russian)
- 20. Skyba MY, Synyuk OM, Zlotenko BM. Model of changing the stressed-deformed state of a polymer sheet during stretching. *Scientific Bulletin of National Mining University*. 2019;1: 83-89.
- 21. Tkacheva AV, Abashkin EE. Impact of forced cooling of the joint zone and thermal effect on the distribution values of residual stress generated by arc welding. *Materials Physics and Mechanics*. 2022;50(3): 509-517.
- 22. Dowden J, Schulz W. The Theory of Laser Materials Processing. In: *Heat and Mass Transfer in Modern Technology*. Springer; 2017.
- 23. Ruzankina JS, Vasiliev O, Tarasov S. Investigation of functional properties of metal surfaces after laser treatment. *Journal of Physics: Conference Series.* 2019;1410: 012171.
- 24. Bartkowska A. Kuklinski M, Kieruj P. The influence of laser heat treatment on the geometric structure of the surface and condition of the surface layer and selected properties of Waspaloy. *MATEC Web of Conferences*. 2017;121: 03006.
- 25. Muthukumaran G, Dinesh Babu P. Laser transformation hardening of various steel grades using different laser types. *Journal of the Brazilian Society of Mechanical Sciences and Engineering*.2021;43(2): 103.

THE AUTHORS

Verameichyk A.I. © e-mail: vai_mrtm@bstu.by

Neroda M.V.

e-mail: nerodamv@mail.ru

Holodar B.G. be-mail: hbg@list.ru

The effect of mass collapse under hypervelocity impact of solid paraboloid into a thin screen

Submitted: November 24, 2022

Approved: December 19, 2023

Accepted: January 30, 2023

A.F. Nechunaev ⁽¹⁾, N.V. Naumova ⁽¹⁾, N.P. Dorofeev ⁽¹⁾

St. Petersburg State University, St. Petersburg, Russia

☑ nickdorof60@gmail.com

Abstract. In this article, an impact of a solid-paraboloid at a speed of 4190 m/s into a thin aluminum plate is numerically simulated. Such high-speed impacts are dangerous as they can damage the second screen of the Whipple shield. Whipple shield, so-called dual-wall system, is widely used to protect spacecraft from space debris. This paper reviews the mechanism of the interaction between the projectile and bumper, the movement and diffusion of the debris cloud. Numerical simulation for high-speed impact of a hyperboloid on an aluminum alloy plate is presented. Central and non-central impacts are discussed. It is shown that some types of collisions are very dangerous because significant mass of fragments is concentrated on the impact axis. The same calculations were conducted for the sphere of comparable mass, results were compared.

Keywords: hypervelocity impact; space debris; mass collapse effect

Citation: Nechunaev AF, Naumova NV, Dorofeev NP. The effect of mass collapse under hypervelocity impact of solid paraboloid into a thin screen. *Materials Physics and Mechanics*. 2023;51(4): 142-159. DOI: 10.18149/MPM.5142023_13.

Introduction

With the development of human space activities, the volume of technogenic space debris in orbits of different heights is rapidly progressing. As of 2021, more than 130 million objects with a size of 0.1-1 cm are known [1]. Among them: spent rocket stages, fragments from the collision of satellites, particles covering spacecraft, particles of rocket fuel, and other debris. If particles collide with a spacecraft at velocities exceeding 4-7 km per second, they can cause irreversible destruction of the covering, depressurization or damage expensive devices and mechanisms.

Usually, to protect a spacecraft against hypervelocity impacts, so-called Whipple shield is used [2]. When a dangerous particle collides with the first screen of Whipple shield, fragments of a spherical- or pear-shape form a cloud and move to the second screen of Whipple shield [3]. The impact of a debris cloud on the second Whipple shield is less dangerous than the impact of a compact projectile.

Methods for modeling such interactions are well known. Among them: SPH method (smoothed-particle hydrodynamics) [4–16], the discrete elements method [17,18], the finite element method [19–21]. As the velocities of both one SPH particle and a group of such particles have often been studied, we will focus on the SPH method.

In the paper, numerical simulation was conducted using SPH method (smoothed-particle hydrodynamics). This method is successfully used to simulate significant displacements and deformations not only on low-velocity interactions (100-1000 m/s), but, as was shown in [24–26], on interactions at higher speeds. For creating a geometry of SPH-bodies and defining

material models, preprocessor LS-Pre-Post was used [19]. As a solver we used a widely known software package ANSYS/LS-DYNA.

Methods

The first phase of a given study is to test simulation parameters at a speed of, 4190 m/s. This was achieved by comparing results of numerical simulation with the results of the experiment – "two-stage light gas guns" according to Fa-wei Ke and others [22]. Numerical simulation was made for the impact of a sphere out of Al-1100 against a thin Al-6061-T6 aluminum plate with the speed given above. Sphere diameter matched the diameter of the sphere studied in the experiment and was equal to 5.01 mm. Thicknesses of the plates were also identical and were 1 mm. During simulation, the plate was supported by a fixed ring (Fig. 1).

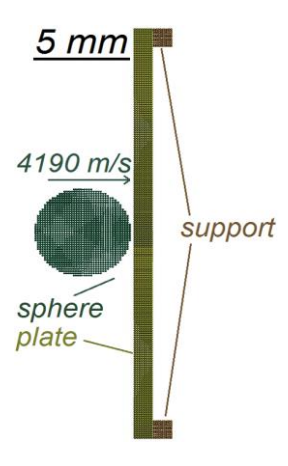


Fig. 1. Problem statement for verification of model's parameters. High velocity impact of a sphere against a thin plate. Plane cut along the main axis of a model is shown

Figures 2 and 3 show the resulting debris clouds at 16 and 24 microseconds times of impact. Computational simulations with the parameters shown in Tables 1-3 show good agreement with the experiment of author Fa-wei Ke and other scientists, who carried out the fixation of the debris cloud evolution with laser shadowgrams. The ratio of fragment cloud length to maximum cloud diameter is 1.58 for the computational simulation and 1.53 for the experiment at a time of 16 microseconds. Accordingly, a discrepancy of about 3.5 % with the experiment was obtained. At the time point of 24 microseconds, this ratio is 1.58 for the computational modelling and 1.59 for the experiment. Correspondingly, the discrepancy with the experiment was 0.5 % [23].

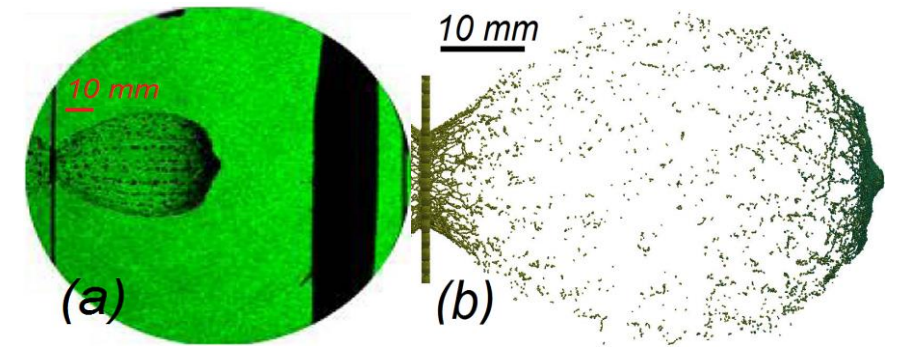


Fig. 2. View of the cloud of fragments at a time of 16 μ s after the impact: (a) – experiment by F. Ke and other scientists [22]; (b) – numerical simulation. Initial impact velocity was V = 4190 m/s, sphere material is Al-1100, sphere diameter is 5.01 mm, barrier material is Al-6061-T6, h = 1 mm

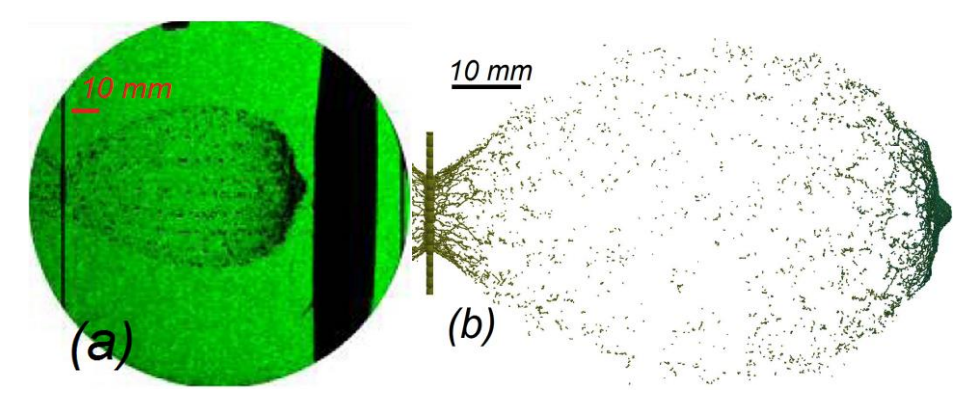


Fig. 3. View of the cloud of fragments at 24 μ s after the impact: (a) – experiment according to Fa. Ke and other scientists [22]; (b) – numerical simulation. Initial impact velocity was V = 4190 m/s, sphere material is Al-1100, sphere diameter is 5.01 mm, barrier material is Al-6061-T6, h = 1 mm

Table 1. Materials' Constants and Parameters [22]

Table 1. Materials Constants and Latameters			
Parameter	Unit.	Al-1100	Al 6061-T6
Density ρ	kg/m ³	2770	2750
Modulus of shearing G	Pa	25.9×10^9	25×10^{9}
Yield stress A	Pa	4.1×10^{7}	3.241×10^{8}
Material hardening B	Pa	1.25×10^{8}	1.138×10^{8}
exponent n	-	0.183	0.42
Johnson-Cook constant c		0.001	0.002
Thermodynamic parameter <i>m</i>		0.859	1.34
Testing temperature	K	293	293
Melting temperature	K	893	893
Testing strain rate	1/s	1	1
Specific heat capacity, C_p	J/(kg·K)	910	910
Coefficients in the Johnson-Cook destruction model D_1		0.071	-0.77
D_2		1.248	1.45
D_3		-1.142	-0.47
D_4		0.0097	0
D_5		0	1.6

Table 2. Linear polynomial equation of state coefficients [22]

C_0	C_{l} , GPa	C_2 , GPa	C_3 , GPa	C_4	C_5	C_6	E_0	V_{0}
0	74.2	60.5	36.5	1.96	0	0	0	1

Table 3. Mie-Gruneisen equation of state coefficients [22]

C_0 , m/s	S_{I}	S_2	S_3	а	E_0	Γ_0	V_{O}
3935	1.578	0	0	0	0	1.69	1

In the second stage of the present study, a computational simulation of a high-speed impact of a solid paraboloid of rotation, the geometrical dimensions of which are shown in Fig. 5, with a similar initial velocity $V=4190\,\text{m/s}$ was performed. The geometric dimensions of the solid-paraboloid were chosen so that the number of particles, and thus the mass of the paraboloid, were comparable with the dimensions and mass of the sphere from the first stage of the present study.

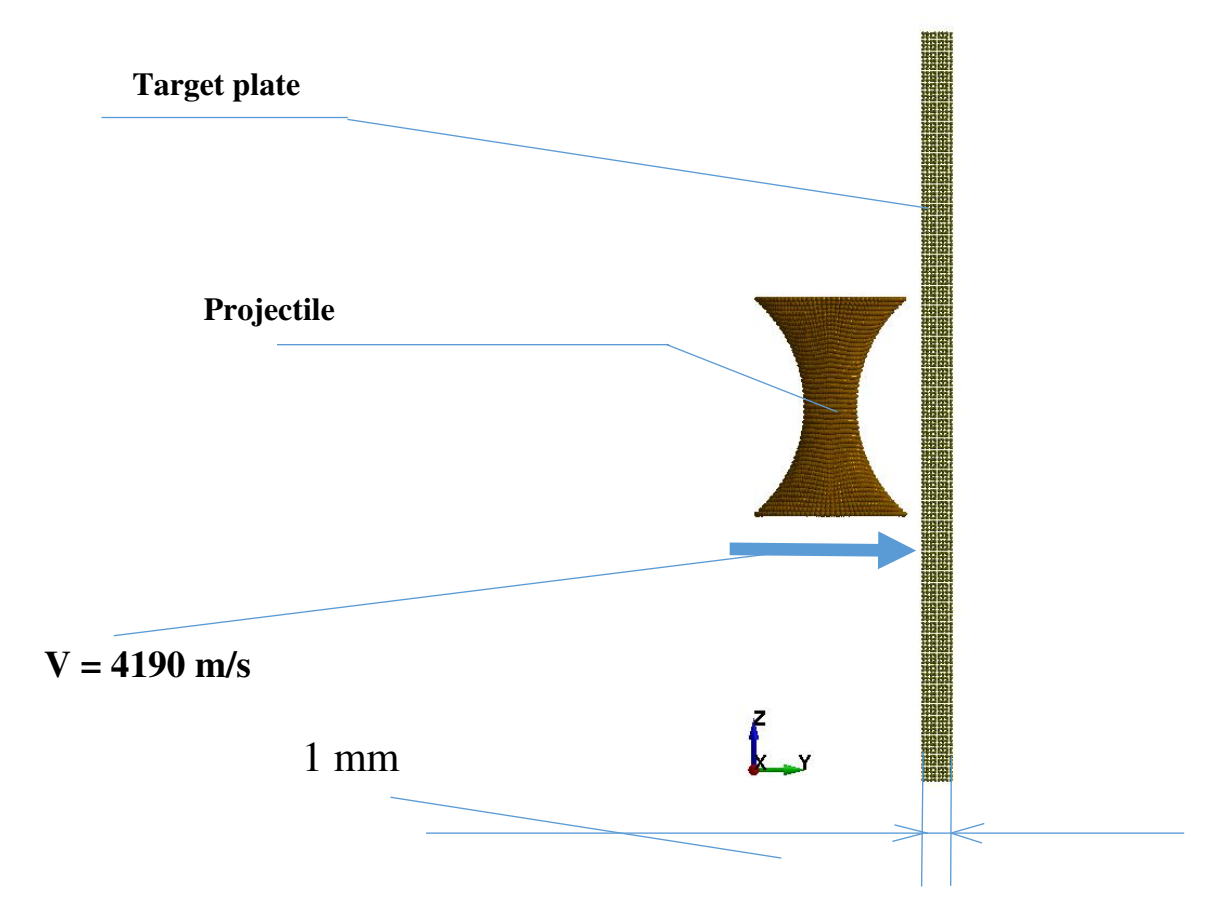


Fig. 4. Problem statement. Solid paraboloid of rotation material is Al. Barrier material is Al-6061-T6, h = 1 mm.

The number of SPH particles of the shock (rotational paraboloid) was 41000. For comparison, the number of SPH particles of the sphere from the first stage of this study was 33000. A 3D view of the computational model before the calculation, which does not show the reference ring, is shown in Fig. 6.

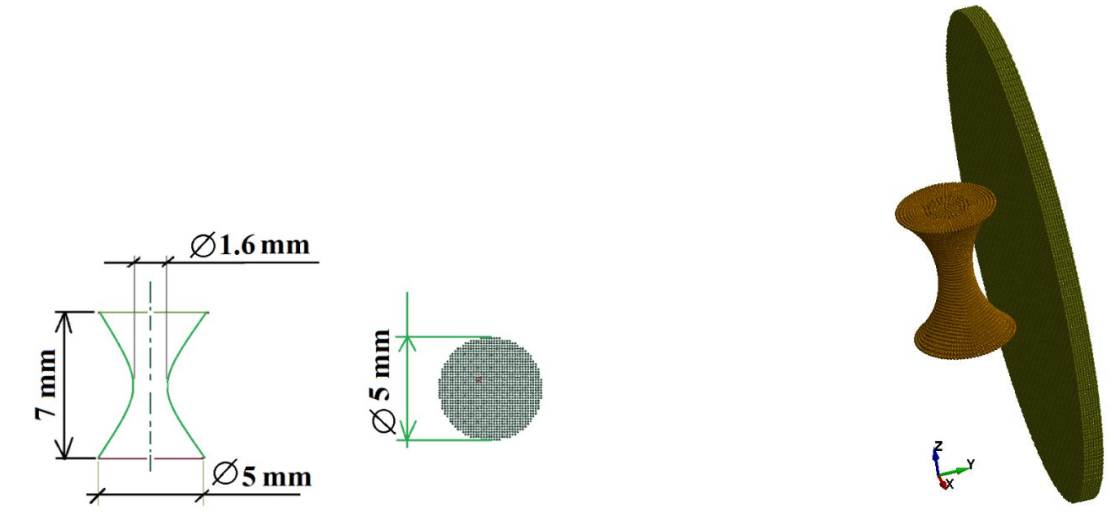


Fig. 5. Comparison of the sphere from the first phase of the study with the solid paraboloid of rotation

Fig. 6. 3D view of the model

The calculated mass of the aluminum sphere considered in the first stage of this study was 183 mg. The mass of the rotation paraboloid was 119.7 mg at Preprocessor Ls-Pre-Post.

Figure 7 shows the evolution of the debris cloud during the interaction of a solid-paraboloid of rotation with a thin 1-mm plate at time moments $t = 0, 1.7, 3.4, \text{ and } 5.5 \,\mu\text{s}$.

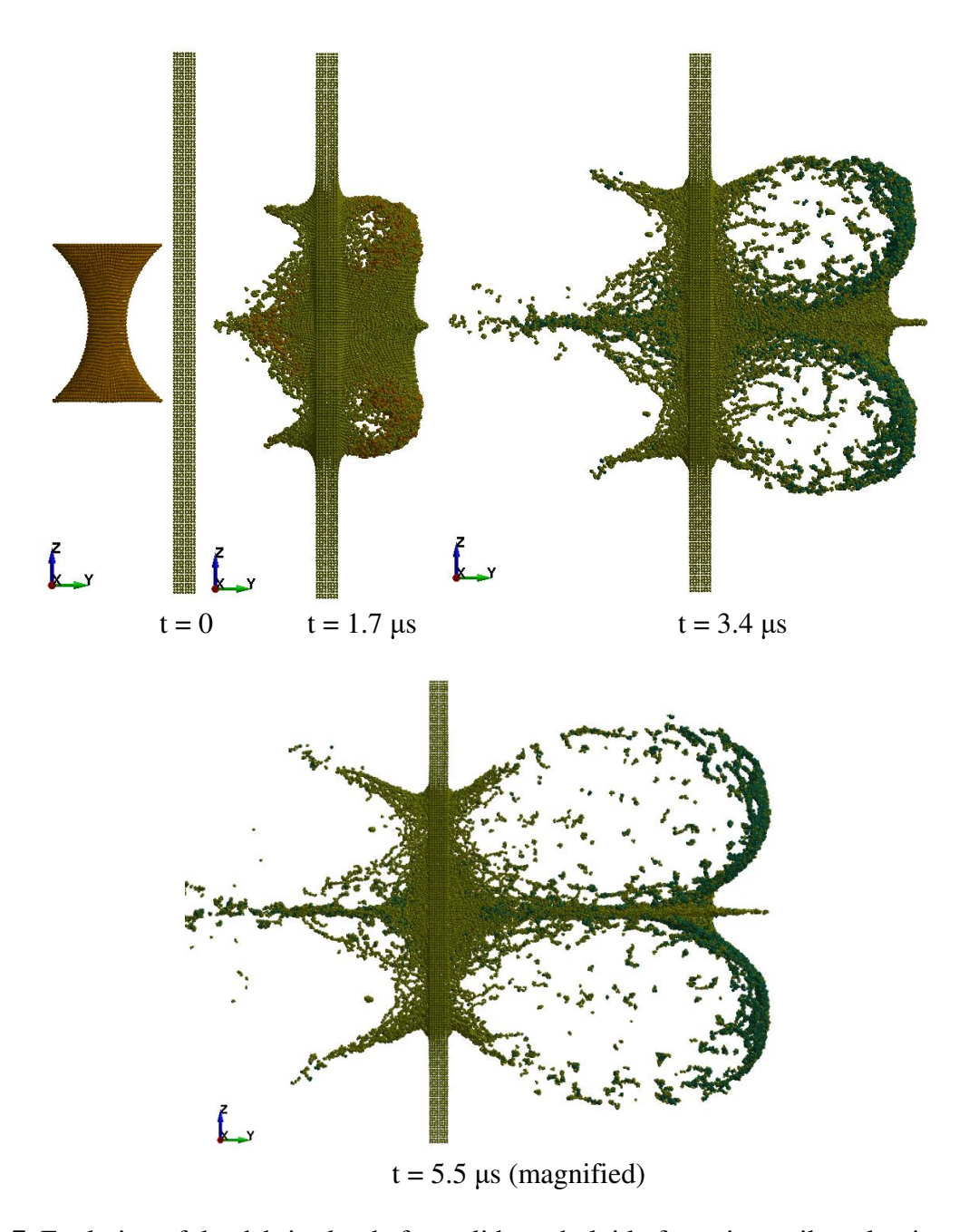


Fig. 7. Evolution of the debris cloud after solid paraboloid of rotation strikes aluminum thin 1-mm plate

At $5.5~\mu s$ (Fig. 7) we can clearly observe that oval clouds' velocity became equal to velocity of a central "spike-like" cloud which is located on the impact axis and leads to faster evolution of these clouds compared to central SPH-particles.

In the next step of the computational modelling, we will carry out the calculation of the mass of the "spike". The "spike" consisting of SPH particles is highlighted by the red box in Fig. 8. The mass of sphere from the first stage of the study is 183 mg, which is informatively given by the LS-Pre-Post preprocessor. Then the mass of 1 SPH particle is

183 mg / 33000 = 0.00555 mg. In the "spike" 34,188 particles were isolated. Then the mass of the spike = 190 mg (that is 34188 multiplied by 0.00555). I.e. the mass of the spike in this problem is comparable to the mass of the sphere from the first step.

Conclusion: Normal impact of solid paraboloid of rotation is as dangerous for the second screen of Whipple shield (after passing through the first one). This is clearly visible in the Figs. 8 and 10 (shape of the cloud of fragments at $t = 10.6 \,\mu s$ (view from above)).

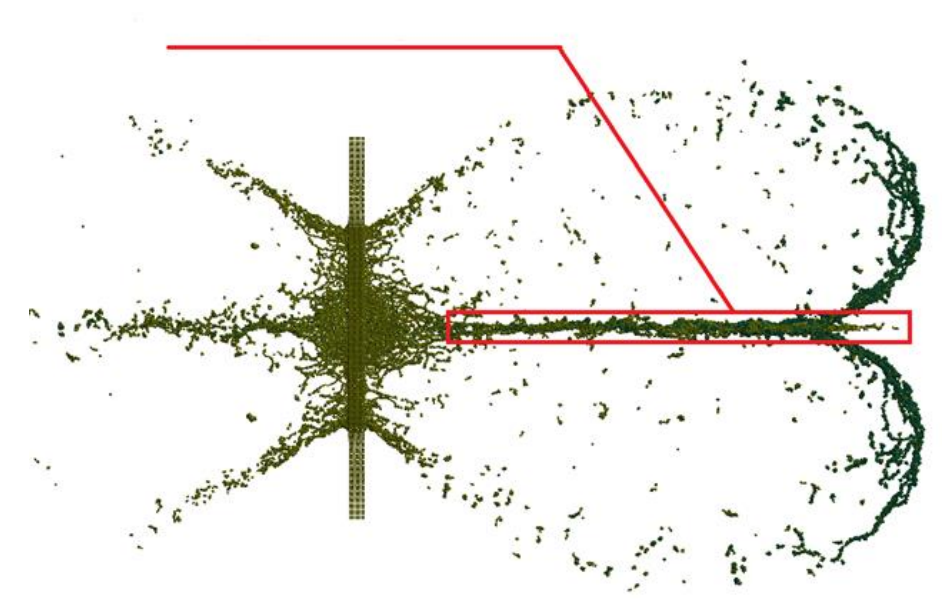


Fig. 8. Time $t = 10.6 \mu s$. Region of SPH particles is selected to estimate number of particles

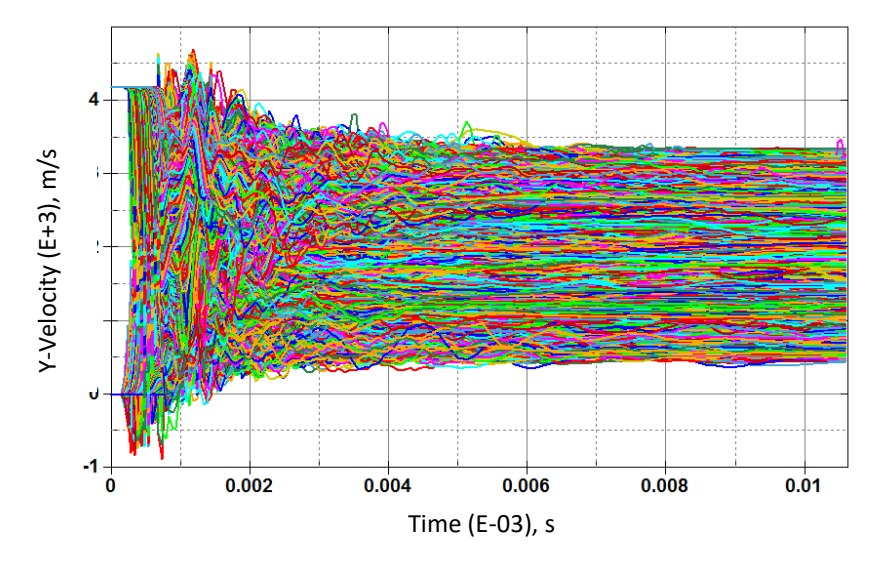


Fig. 9. Group diagram of particles' velocities inside the spike

Group diagram (Fig. 9) shows velocity spectrum of particles located inside the "spike" starting from ~ 400 m/s and ending with ~ 3300 m/s. This group diagram provides clear image that some particles came to the "spike" from the striker (initial velocities at t = 0 from 4190 m/s mark, while some of them were in a state of rest - V = 0 m/s at t = 0). After 6 μ s cloud motion stabilizes, wave oscillations of the particles' velocities reduce and eventually disappears – curves of the velocities of particles are practically parallel to x-axis.

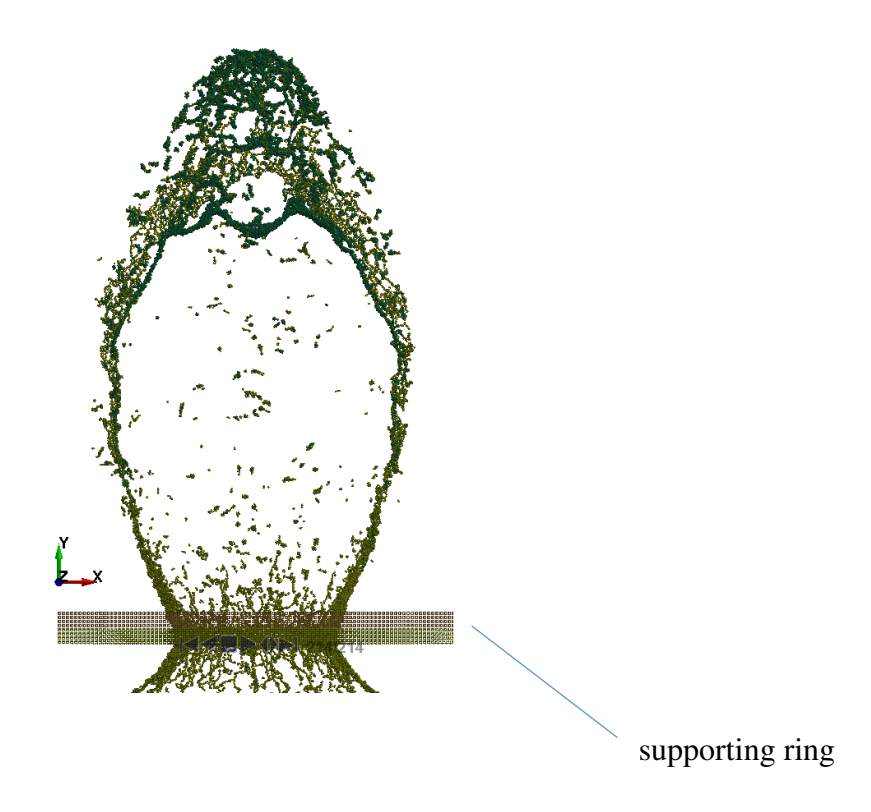


Fig. 10. Shape of the cloud of fragments at $t = 10.6 \mu s$ (view from above)

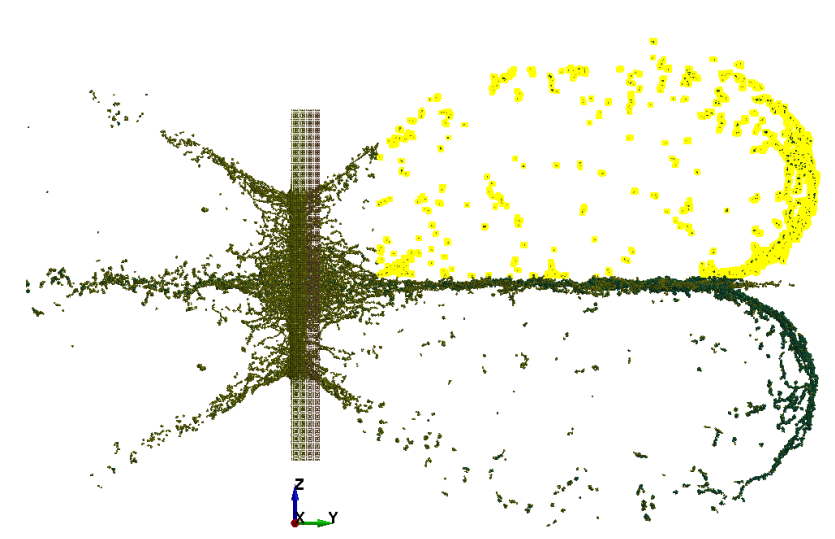


Fig. 11. Top cloud particles selection (shown in yellow) to calculate mass of the cloud

Let us establish the number of particles in each cloud (Fig. 11). This would be 11563 SPH. Given that there are 34,000 particles concentrated in the center (spike), we conclude that each cloud is low hazard, especially since the impact in the second Whipple shield screen would be a "spot" rather than a point impact.

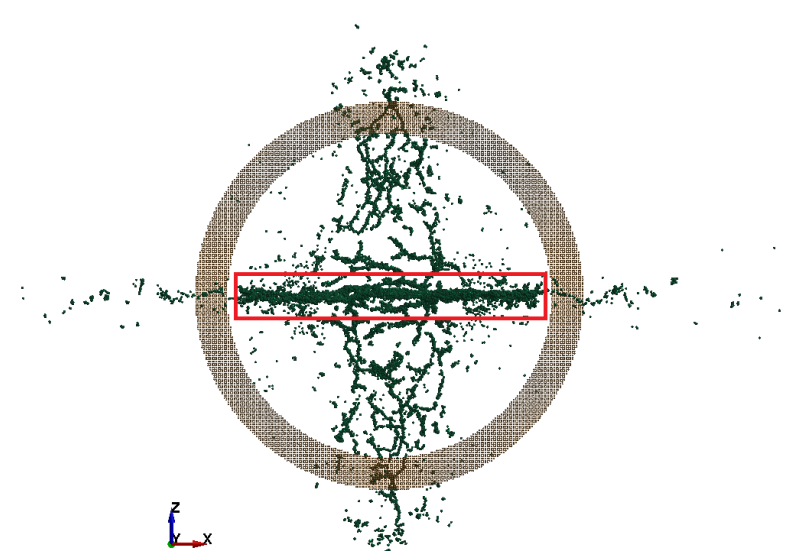


Fig. 12. Dangerous vanguard of clouds, view from the front

During the third step of the study let us split the cloud of debris, formed after the impact of paraboloid, into speed zones.

Zone 1. Low speed zone (near the impact axis, simultaneously it is located right after free surface of a barrier).

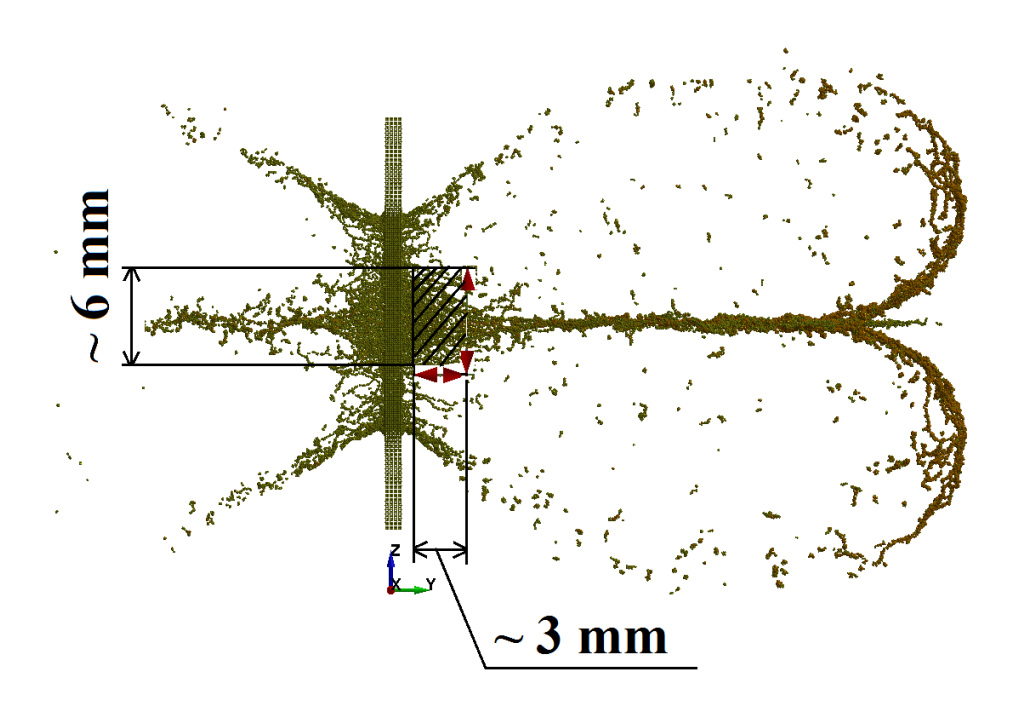


Fig. 13. Selection of SPH particles from the low velocity zone 1 to establish a picture of evolution of debris clouds at $t = 10 \mu s$. Zone 1 is hatched. Supporting ring is hidden

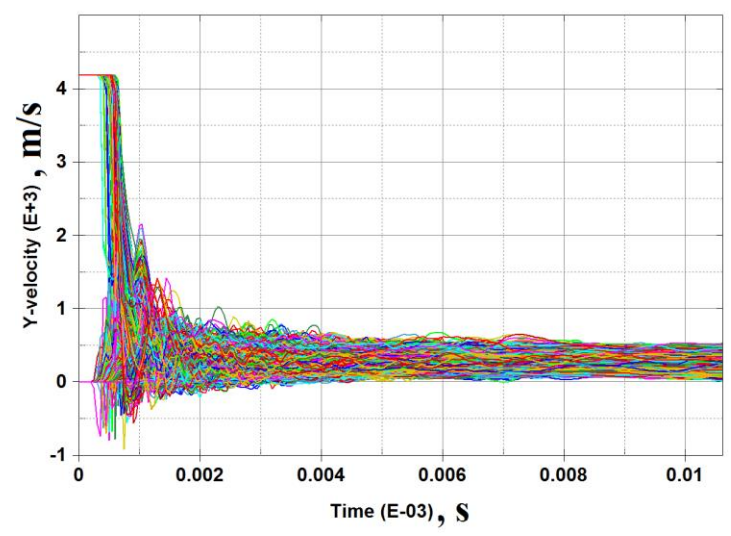


Fig. 14. Velocity diagram of cloud of fragments from low-speed zone

Zone 2. Medium velocity area (in proximity to the impact axis, located between low-velocity area 1 and high-velocity area 3).

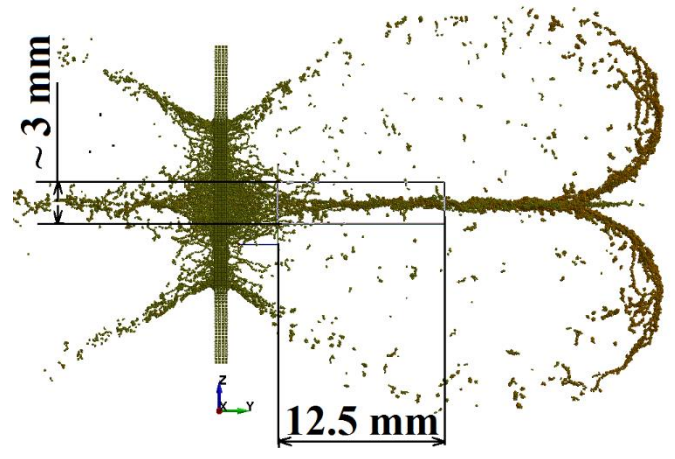


Fig. 15. Selection of SPH particles from medium-speed zone 2 to define a shape of evolution of the debris cloud at $t = 10 \mu s$. Supporting ring is hidden

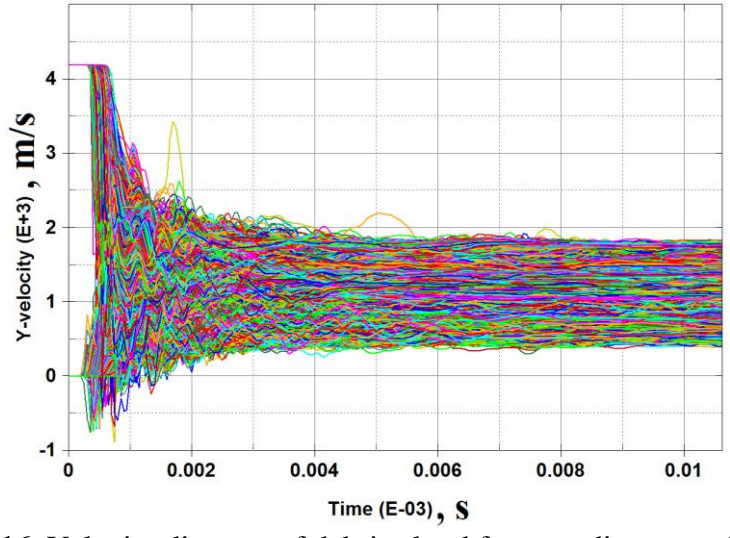


Fig. 16. Velocity diagram of debris cloud from medium-speed area

We consider low-velocity area to be an area with particle velocities varying from 0 m/s to 500-600 m/s. Particles from this zone are scattered and do not have any effect on the integrity of the second screen of Whipple shield. Dimensions of a rectangle which contain low-velocity area are shown in Fig. 13, a velocity diagram of this area is presented in Fig. 14. Dimensions of a rectangle which contain medium-velocity area are shown in Fig. 15, a velocity diagram of this area is presented in Fig. 16. Figure 16 indicates that, velocity of particles located in this zone does not exceed 2 km/s and do not pose a substantial threat in space in case of a relatively small mass of particles (fragments). We base our conclusions on findings of [28]. It states that maximum velocity of collision of a striker against a barrier exists. If collision occurs at a higher velocity and the striker penetrates the barrier, the deformation of a striker of any form is accompanied by fluidity. For ordinary materials, evidently, this maximum speed has an order of magnitude of 2 km/s.

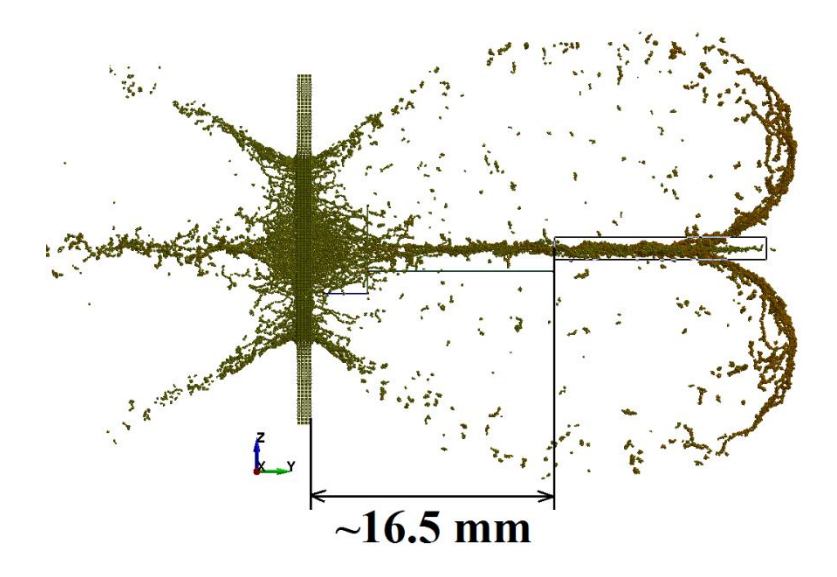


Fig. 17. Selection of SPH particles from high-speed zone 3 to define a shape of evolution of the debris cloud at $t = 10 \mu s$. Supporting ring is hidden

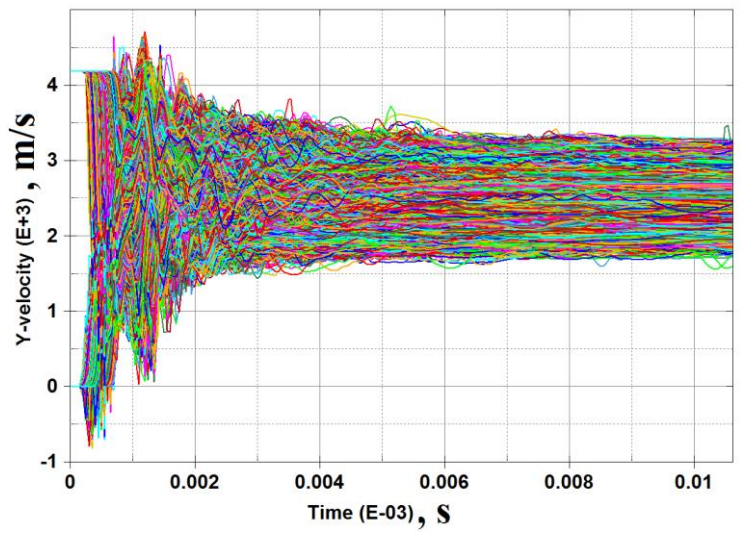


Fig. 18. Velocity diagram of cloud of fragments from high-speed area

Zone 3. High velocity area (in proximity to the impact axis, the most remote area from the barrier surface). Choice of this zone is shown in Fig. 17. The rectangle height along Z in this case is ~ 1.5 mm. The velocity diagram of particles from this zone, presented in Fig. 18, indicates that particles located in the "spike" of the cloud have velocities varying from 1700 m/s to 3300 m/s.

Let us examine the case of diverted impact of a paraboloid when the velocity vector is at an angle of 5, 30 and 45 degrees to barrier normal (cases 1-6) to estimate the danger of these cases for the second screen of Whipple shield.

Case 1. Velocity vector of paraboloid is at an angle of 5 degrees to barrier normal (Fig. 19).

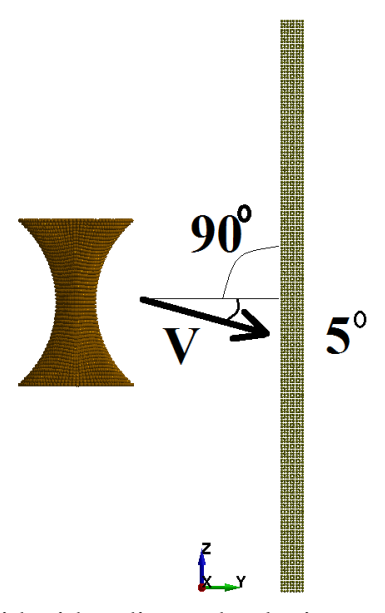


Fig. 19. An impact of paraboloid with a diverted velocity vector at an angle of 5 degrees to barrier normal. Initial condition before calculations t = 0

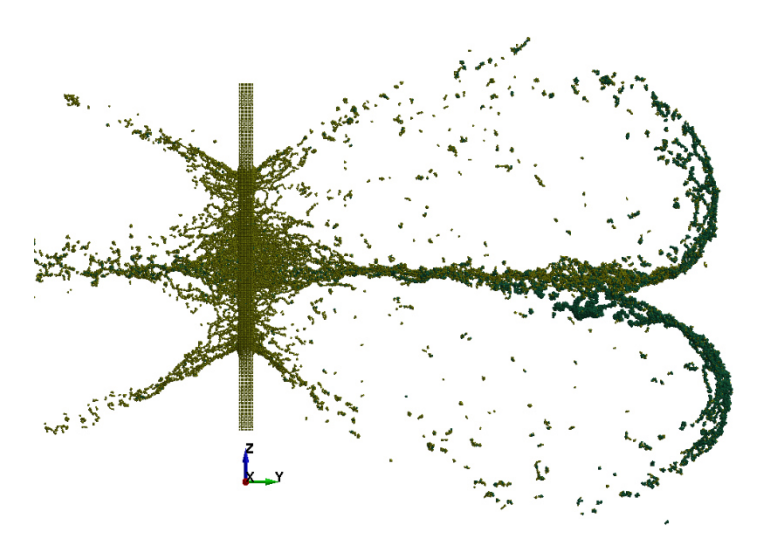


Fig. 20. An impact of paraboloid with a diverted velocity vector at an angle of 5 degrees to barrier normal. Evolution of cloud of debris at $t = 10 \mu s$

Figure 20 indicates that qualitative change did not occur in the shape of the cloud. The debris cloud still consists of 2 semi-clouds, we can no longer observe the evident central "spike", however, we see a concentration of mass in the connection point of two semi-clouds.

Consequently, the second important result of the study: in place of contact of two semi-clouds, which emerged from the impact of a paraboloid against a barrier at a speed of 4190 m/s, a significant portion of mass of the debris cloud is concentrated and hence, diverted impact of a solid paraboloid of rotation is as dangerous for the second screen of Whipple shield (after it has passed the first) as an impact of a sphere of equal mass for the first screen of Whipple shield.

Case 2. The velocity vector of paraboloid is at an angle of 5 degrees to barrier normal, the paraboloid itself is rotated 5 degrees so that an angle between paraboloid's rotation axis and impact axis is 90 degrees (Fig. 21).

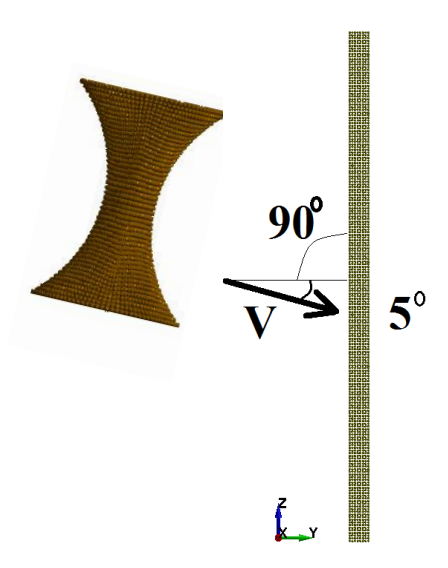


Fig. 21. An impact of paraboloid with a diverted velocity vector at an angle of 5 degrees to barrier normal. Paraboloid is also rotated. Initial condition before calculations, t = 0

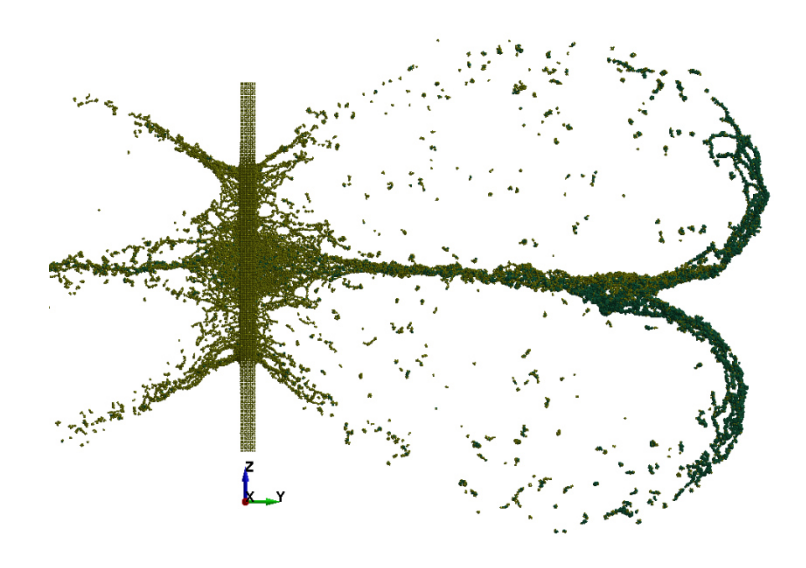


Fig. 22. An impact of paraboloid with a diverted velocity vector at an angle of 5 degrees to barrier normal. Paraboloid is also rotated before impact. Evolution of debris cloud at $t = 10 \mu s$

Conclusions of the second case are identical to the first one. No qualitative changes in the shape of the cloud took place compared to the first case. Consequently, there was no significant mass transfer, as we can see from Fig. 22.

Case 3. Velocity vector of paraboloid is at an angle of 30 degrees to barrier normal (Fig. 23).

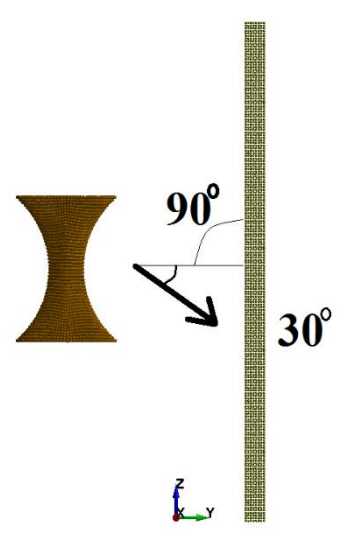


Fig. 23. An impact of paraboloid with a diverted velocity vector at an angle of 30 degrees to barrier normal. Initial condition before calculations t = 0

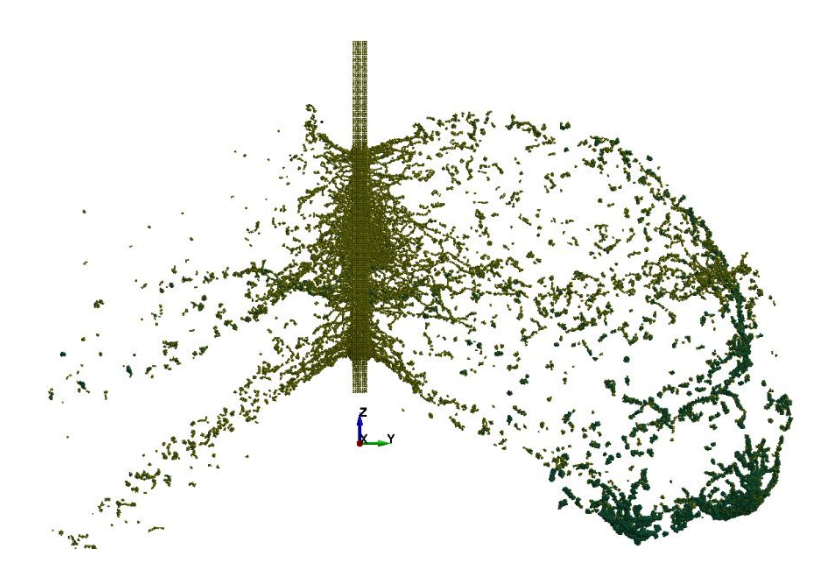


Fig. 24. An impact of paraboloid with a diverted velocity vector at an angle of 30 degrees to barrier normal. Result of numerical simulation at $t = 10 \mu s$.

Observing the result of numerical simulation of the case 3 we can see that the "spike" do not appear along the impact axis (Fig. 24), clouds of fragments are forming with evident deflection from symmetry, in vanguard of clouds we witness particles of the striker (shown in dark green).

Diverted impact of paraboloid at an angle of 30 degrees and beyond is significantly less dangerous for the second screen of Whipple shield because, semi-clouds merge in the process of evolution and considerably divert to the side. Therefore, the second screen will be loaded with sliding impact, which is not dangerous.

Case 4. Velocity vector of paraboloid is at an angle of 30 degrees to barrier normal. Paraboloid is rotated to the same angle (Fig. 25).

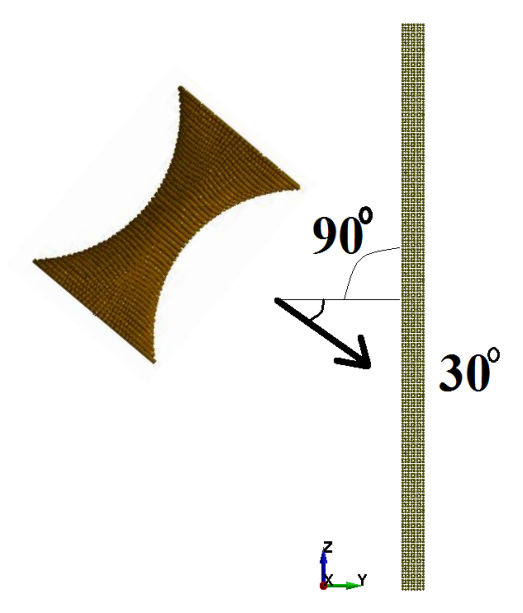


Fig. 25. An impact of paraboloid with a diverted velocity vector at an angle of 30 degrees to barrier normal. Paraboloid is also rotated to the same extent. Initial condition before calculations, t = 0

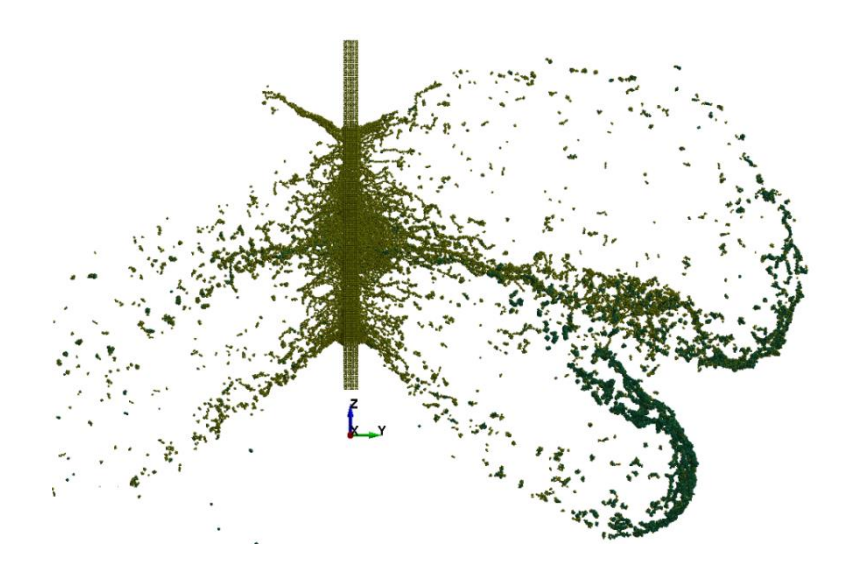


Fig. 26. An impact of paraboloid when both velocity vector and rotation axis are diverted at an angle of 30 degrees to barrier normal. Result of numerical simulation at $t = 10 \mu s$

Figure 26 indicates that two semi-clouds do not merge as a result of such impact however, we can clearly see that there is a significant deviation of both semi-clouds from the axis which is perpendicular to the target's surface.

Case 5. Velocity vector of paraboloid is at an angle of 45 degrees to barrier normal (Figure 27).

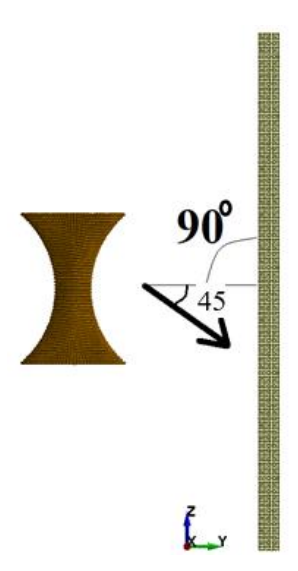


Fig. 27. An impact of paraboloid with a diverted velocity vector at an angle of 45 degrees to barrier normal. Initial condition before calculations t = 0

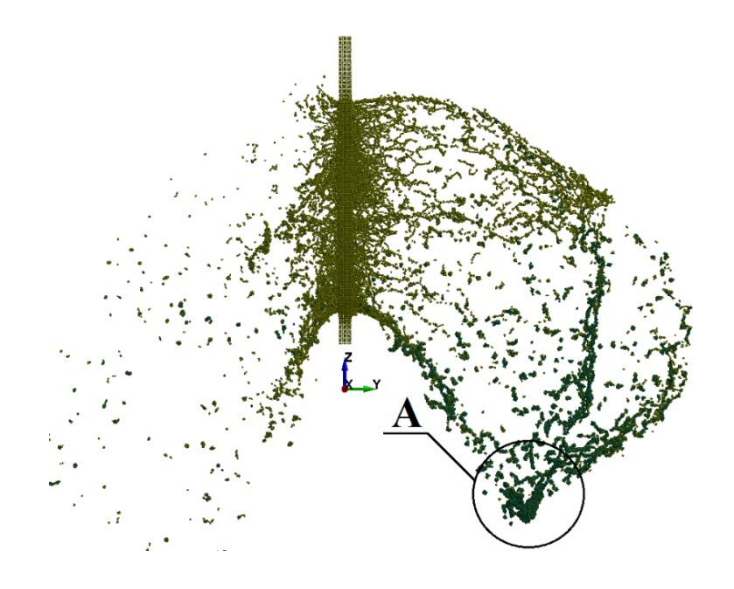


Fig. 28. An impact of paraboloid with a diverted velocity vector at an angle of 45 degrees to barrier normal. Result of numerical simulation at $t = 10 \mu s$

Figure 28 indicates that the case of 45 degree divergence is special. In this case, one can see that particles of the cloud concentrate in vanguard A (Fig. 28), and have a movement direction along the surface of the barrier. Such vanguard can pose a threat for stiffening ribs of a spacecraft and other elements which vanguard can meet along the way.

Case 6. Velocity vector of paraboloid is at an angle of 45 degrees to barrier normal (Fig. 29). Paraboloid is rotated to the same angle.

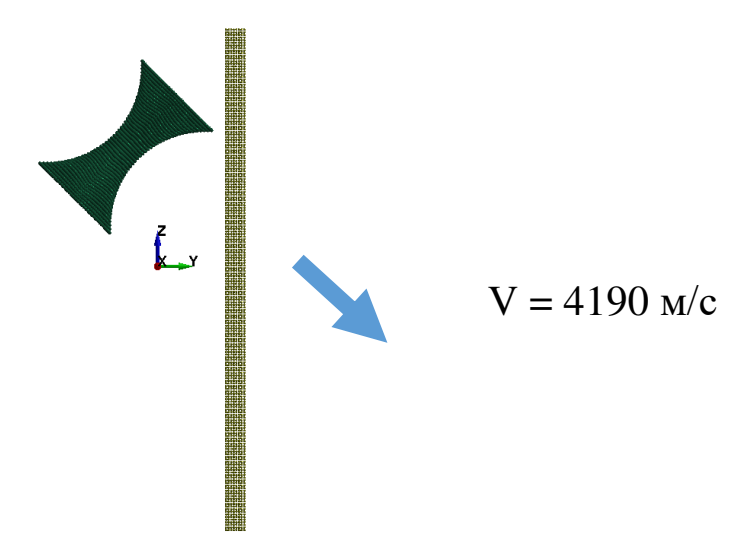


Fig. 29. An impact of paraboloid with a diverted velocity vector at an angle of 45 degrees to barrier normal. Paraboloid is also rotated to the same extent. Initial condition before calculations t = 0

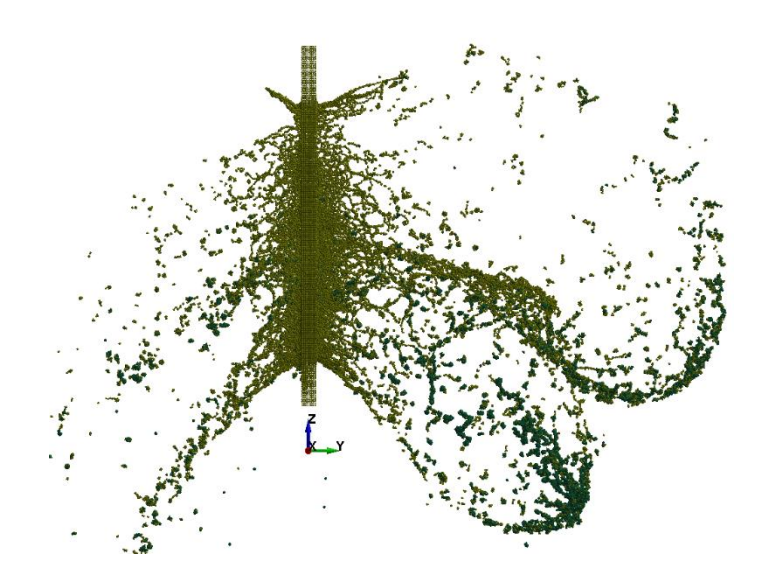


Fig. 30. An impact of paraboloid with a diverted velocity vector at an angle of 45 degrees to barrier normal. Paraboloid is also rotated to the same extent. Results of numerical simulation at $t=10~\mu s$

Thus, in this case one can see that particles do not concentrate in the front of the cloud (Fig. 30), unlike particles in case 5, they have movement direction along the surface of the barrier. And as in case 5 such concentration of fragments is particularly dangerous for stiffeners of a spacecraft and other structural elements.

Results and Discussion

In this article, an impact at high speeds of a solid-paraboloid into a thin aluminum plate was numerically simulated. It was shown in [27] that at velocities of $\sim 240-750$ m/s the nature of aluminum destruction as a result of impact loading is locally-kinetic.

This paper reviews the mechanism of the interaction between the projectile and bumper, the movement and diffusion of the debris cloud, so-called "the effect of mass collapse".

Note that for different collision cases even if all particles of the broken barrier have differently oriented velocity vectors, then they start to gather in reinforced structures and after that they dissociate into smaller ones, in other words, the destruction of the masses begins.

Numerical simulation for high-speed impact of a hyperboloid on an aluminum alloy plate was presented. Central and non-central impacts were considered. It was shown that some types of collisions are very dangerous because significant mass of fragments is concentrated either on the impact axis or along the surface of the barrier.

The case of a normal impact of a paraboloid of rotation into the barrier is very dangerous for the second screen of Whipple shield (relative to the sphere, cube, and other drummers of similar shapes, as was simulated in [22]) because of the particles concentration closer to the axis of impact and their distribution in a rectangle form shown in Fig. 12.

For non-central impact it was shown that particles of the cloud do not concentrate along the impact axis in the front of the cloud (Figs. 28, 30), they have movement direction along the surface of the barrier. This certainly affects the integrity of spacecraft and equipment.

With increasing impact speed, we suppose, a similar process takes place in early stages. That is, after "gathering" of particles into reinforced structures a reverse process takes place – structure crushes, multiple ruptures emerge and clouds of fragments are forming.

References

- 1. Diki C, Uvarov V. *Novyy Soyuz—Appolon» iz kosmicheskogo musora*. Available from: https://kiozk.ru/article/ekspert/novyj-souz-apollon-iz-kosmiceskogo-musora [Accessed 9th June 2023]. (In-Russin)
- 2. Whipple FL. Meteorites and space travel. *The Astronomical Journal*. 1947;52: 131.
- 3. Song Z, Pei X, Yu J, Zhao J, Tan F. Hypervelocity impact tests on a Whipple shield using a flyer plate in the velocity range from 4 km/s to 12 km/s. *Int. J Impact Eng.* 2021;156: 103899.
- 4. Hayhurst CJ, Clegg RA. Cylindrically symmetric SPH simulations of hypervelocity impacts on thin plates. *Int. J. Impact Eng.* 1997;20(1-5): 337–348.
- 5. Christiansen EL, Crews JL, Williamsen JE, Robinson JH, Nolen AM. Enhanced meteoroid and orbital debris shielding. *Int. J. Impact Eng.* 1995;17(1-3): 217–228.
- 6. Hayhurst CJ, Clegg RA. Cylindrically symmetric SPH simulations of hypervelocity impacts on thin plates. *Int. J. Impact Eng.* 1997;20(1–5): 337–348.
- 7. Hayhurst CJ, Livingstone IH, Clegg RA, Fairlie GE. Numerical Simulation of Hypervelocity Impacts on Aluminum and Nextel/Kevlar Whipple Shields. In: *Proc. Hypervelocity Shielding Workshop*, 11 March 1998, Galveston, Texas. 1998. p.TP031.
- 8. Panov DV, Silnikov MV, Mikhaylin AI, Rubzov IS, Nosikov VB, Minenko EY, Murtazin DA. Large-scale shielding structures in low earth orbits. *Acta Astronaut*. 2015;109: 153–161.
- 9. Pierazzo E, Artemieva N, Asphaug E, Baldwin EC, Cazamias J, Coker R, Collins GS, Crawford DA, Davison T, Elbeshausen D, Holsapple KA, Housen KR, Korycansky DG, WÜnnemann K. Validation of numerical codes for impact and explosion cratering: Impacts on strengthless and metal targets. *Meteoritics & Planetary Science*. 2008;43(12): 1917–1938.
- 10. Christiansen EL. Design and performance equations for advanced meteoroid and debris shields. *Int. J. Impact Eng.* 1993;14: 145–156.
- 11. Christiansen EL. International Space Station (ISS) Meteoroid/Orbital Debris Shielding. *Cosmonautics and Rocket Engineering*. 2000;18: 166–180.
- 12. Christiansen EL, Kerr JH. Mesh double-bumper shield: a low-weight alternative for spacecraft meteoroid an orbital debris protection. *Int. J. Impact Eng.* 1993;14: 169–180.
- 13. Christiansen EL. *Meteoroid/Debris Shielding*. NASA. Report number: TP-2003-210788, 2003.

- Etemadi E, Zamani J, Francesconi A, Mousavi MV, Giacomuzzo C. A new set-up to investigate plastic deformation of face centered cubic metals in high strain rate loading. Modern Applied Science. 2014;8(2): 94–106.
- Eiceman GA, Karpas Z. Ion Mobility Spectrometry. 2nd ed. NY: CRC Press; 2005.
- Horz F, Cintala MJ, Bernhar RP, See TH. Multiple-mesh bumpers: a feasibility study, Int. J. Impact Eng. 1995;17: 431–442.
- Cherniaev A, Telichev I. Meso-scale modeling of hypervelocity impact damage in 17. composite laminates. Composites Part B. 2015;74: 95–103.
- Parshikov AN, Medin SA. Smoothed particle hydrodynamics using interparticle contact algorithms. J. Comp. Phys. 2002;180(1): 358-382.
- ANSYS LS-DYNA User's Guide. Release 12.1. 2009.
- Cour-Palais BG, Crews JL. A multi-shock concept for spacecraft shielding. Int. J. Impact 20. Eng. 1990;10: 135–146.
- 21. Brandon EJ, Vozoff M, Kolawa EA, Studor GF, Lyons F, Keller MW, Beiermann B, White SR, Sottos NR, Curry MA, Banks DL, Brocato R, Zhou L, Jung S, Jackson TN, Champaigne K. Structural health management technologies for inflatable/deployable structures: Integrating sensing and self-healing. Acta Astronaut. 2011;68(7-8): 883–903.
- Ke F, Huang J, Wen X, Ma Z, Liu S. Test study on the performance of shielding configuration with stuffed layer under hypervelocity impact. Acta Astronaut. 2016;127: 553-560.
- 23. Silnikov MV, Guk IV, Nechunaev AF, Smirnov NN. Numerical simulation of hypervelocity impact problem for spacecraft shielding elements. Acta Astronaut. 2018;150: 56-62.
- 24. Silnikov MV, Guk IV, Mikhaylin AI, Nechunaev AF, Rumyantsev BV. Numerical simulation of hypervelocity impacts of variously shaped projectiles with thin bumpers. Materials Physics and Mechanics. 2019;42(1): 20–29.
- Liu MB, Liu GR. Smoothed Particle Hydrodynamics (SPH): an Overview and Recent Developments. Arch. Comput. Methods Eng. 2010;17: 25–76.
- Liu MB, Liu GR. Smoothed Particle Hydrodynamics A Meshfree Particle Method. Singapore: World Scientific Publishing; 2003.
- Meshcheryakov YI, Konovalov GV, Zhigacheva NI, Divakov AK, Nechunaev AF. Strain Behavior of Aluminum Alloys Under Dynamic Compression and Tensile. Advanced Structured Materials. 2022;164: 413-453.
- Sagomonyan AY. Pronikaniye. Moscow: Izdatelstvo Moskovskogo universiteta; 2014. 28. (In-Russian)
- Wen K, Chen XW, Lu YG. Research and development on hypervelocity impact protection using Whipple shield: An overview. Defence Technology. 2021;17(6): 1864-1886.

THE AUTHORS

Nechunaev A.F.

e-mail: n.v.naumova@spbu.ru

Naumova N.V.

e-mail: vvkgu@yandex.ru

Dorofeev N.P.

e-mail: nickdorof60@gmail.com

Simulation of the stress-strain state of a rectangular bar using fast trigonometric interpolation in various statements of boundary value problems

Submitted: October 30, 2022

Approved: February 7, 2023

Accepted: May 12, 2023

A.D. Chernyshov ¹, V.V. Goryainov ¹ ^{2 ™}, E.N. Kovaleva ¹

¹ Voronezh State University of Engineering Technology, Voronezh, Russia ² Voronezh State Technical University, Voronezh, Russia ⊠ gorvit77@mail.ru

Abstract. The problem of stresses in a rectangular bar is considered in three statements: 1) with assignment on all boundaries of displacements, 2) stresses and 3) with mixed boundary conditions. The solution is represented by a fast expansion whose coefficients were determined by fast trigonometric interpolation. The solution of the boundary value problem with Dirichlet conditions is the most accurate of the three considered boundary value problems. Compared with this problem, the accuracy of determining the components of the stress tensor and the residual of the Lamé equations in the other two boundary value problems drops by an order of magnitude. The largest residual of the Lamé equilibrium equations is observed in the boundary value problem with given stresses on all sides of the rectangle. Computational experiments showed that the aspect ratio of the rectangle affects the qualitative form of the stress intensity distribution and the location of points with the maximum stress intensity. Among all rectangular sections with different overall dimensions, but the same sectional area, the smallest value of $\tilde{\sigma}_{max}$ is observed in a bar with a square section.

Keywords: displacements; stress tensor components; Lamé equations; fast expansions; fast trigonometric interpolation; boundary value problems; high accuracy

Citation: Chernyshov AD, Goryainov VV, Kovaleva EN. Simulation of the stress-strain state of a rectangular bar using fast trigonometric interpolation in various statements of boundary value problems. *Materials Physics and Mechanics*. 2023;51(4): 160-171. DOI: 10.18149/MPM.5142023_14.

Introduction

A rectangular region is one of the simplest two-dimensional regions for which it is convenient to model the stress-deformed state of a material and consider its properties [1–10]. Approximate solutions for similar object shapes are obtained by various numerical and analytical methods. Thus, in [1], an approximate analytical solution in the form of trigonometric polynomials is constructed by the superposition method from two solutions obtained by the method of initial functions. In [2,9], solutions are presented as series in Papkovich–Fadle eigenfunctions. In [4], the solution is sought as the sum of a trigonometric series and a power function with a root singularity. The superposition method in the form of Fourier series satisfying the differential equation and boundary conditions is used in [5]. Finite difference and finite element methods were used in [3,8], respectively. Unknown displacements in [11] are represented by power series. In [12], the integral Fourier transform with respect to a variable running through an infinite interval was used. For problems of rigid

body mechanics, the nodal integration method for meshfree radial point interpolation is presented in [13]. In the proposed method, radial basis functions supplemented by polynomials are used to construct shape functions that have the delta function property. In [14], a grid method is presented using a special trigonometric basis; the completeness of the trigonometric basis is not discussed. The grid method of collocations and least squares for the residual, applicable in solving multidimensional nonlinear problems of elliptic type, was proposed in [15]. Interpolation methods were used to process the experimental data [16] and to determine the plasticity and creep characteristics of the material [17]. The exact solutions presented in [18] were obtained using group analysis for an elastic model written in Euler variables at finite strains, and in [10], the exact solutions for deflections of a rectangular membrane under the action of a variable load were obtained by the method of fast expansions. The method of fast expansions was developed in [19]. It is based on the fact that the desired solution of the problem is represented as the sum of a special boundary function and a Fourier series. Such a sum is called a fast expansion. Unknown coefficients of fast expansion are found using the operator of fast expansions [20] or fast trigonometric interpolation [21]. The use of classical trigonometric interpolation to determine the coefficients of fast expansion is problematic due to the impossibility of its differentiation in the general case and the large error between interpolation points. Therefore, classical trigonometric interpolation is usually used to solve problems not related to integro-differential equations, for example, to improve the quality of image processing [22] and restore periodic discrete signals of finite duration [23].

In this paper, we present the solution of the problem of stresses in a bar by the method of fast expansions in three statements. They differ from each other in the type of boundary conditions. The coefficients of fast expansions will be determined using fast trigonometric interpolation. In this regard, it is of interest to study the influence of the type of boundary conditions on the accuracy of solving the problem using fast trigonometric interpolation.

Methods

Under conditions of plane deformation, the projections of the displacements vector of the bar material points depend only on the coordinates x, y:

$$U = U(x, y), V = V(x, y), W = 0.$$
 (1)

The stress tensor components will have the following form:

$$\sigma_{xx} = (\lambda + 2\mu) \frac{\partial U}{\partial x} + \lambda \frac{\partial V}{\partial y}, \quad \sigma_{yy} = (\lambda + 2\mu) \frac{\partial V}{\partial y} + \lambda \frac{\partial U}{\partial x},
\tau_{xy} = \mu \left(\frac{\partial U}{\partial y} + \frac{\partial V}{\partial x} \right), \quad \sigma_{zz} = \lambda \left(\frac{\partial U}{\partial x} + \frac{\partial V}{\partial y} \right), \quad \tau_{xz} = \tau_{yz} = 0.$$
(2)

Let us write the Lamé equilibrium equations for displacements taking into account mass forces

$$\left(\lambda + 2\mu\right) \frac{\partial^2 U}{\partial x^2} + \left(\lambda + \mu\right) \frac{\partial^2 V}{\partial x \partial y} + \mu \frac{\partial^2 U}{\partial y^2} + X\left(x, y\right) = 0,\tag{3}$$

$$(\lambda + 2\mu)\frac{\partial^2 V}{\partial y^2} + (\lambda + \mu)\frac{\partial^2 U}{\partial x \partial y} + \mu\frac{\partial^2 V}{\partial x^2} + Y(x, y) = 0.$$
(4)

We add boundary conditions to equations (3), (4). We assume that the elastic bar has a rectangular cross-section $\Omega = (0 \le x \le a, 0 \le y \le b)$. On the sides of the bar, we set three different types of boundary conditions, corresponding to three boundary value problems.

1. Displacements are given on all sides

$$U|_{x=0} = f_1(y), \ U|_{x=a} = f_3(y), \ V|_{x=0} = \varphi_1(y), \ V|_{x=a} = \varphi_3(y).$$
 (5)

Simulation of the stress-strain state of a rectangular bar using fast trigonometric interpolation in various statements of boundary value problems

$$U|_{y=0} = f_2(x), \ U|_{y=0} = f_4(x), \ V|_{y=0} = \varphi_2(x), \ V|_{y=0} = \varphi_4(x). \tag{6}$$

2. Stresses are set on all sides

$$\left(\lambda + 2\mu\right) \frac{\partial U}{\partial x} + \lambda \frac{\partial V}{\partial y} \bigg|_{x=0} = F_1(y), \quad \mu \left(\frac{\partial U}{\partial y} + \frac{\partial V}{\partial x}\right) \bigg|_{x=0} = \Phi_1(y), \tag{7}$$

$$\left(\lambda + 2\mu\right) \frac{\partial U}{\partial x} + \lambda \frac{\partial V}{\partial y}\bigg|_{x=a} = F_2(y), \quad \mu \left(\frac{\partial U}{\partial y} + \frac{\partial V}{\partial x}\right)\bigg|_{y=a} = \Phi_2(y). \tag{8}$$

$$\left(\lambda + 2\mu\right) \frac{\partial V}{\partial y} + \lambda \frac{\partial U}{\partial x}\bigg|_{y=b} = F_3\left(x\right), \quad \mu\left(\frac{\partial U}{\partial y} + \frac{\partial V}{\partial x}\right)\bigg|_{y=b} = \Phi_3\left(x\right), \tag{9}$$

$$\left(\lambda + 2\mu\right) \frac{\partial V}{\partial y} + \lambda \frac{\partial U}{\partial x}\bigg|_{y=0} = F_4(x), \quad \mu \left(\frac{\partial U}{\partial y} + \frac{\partial V}{\partial x}\right)\bigg|_{y=0} = \Phi_4(x). \tag{10}$$

3. Mixed boundary conditions are on the sides x = 0, x = a and y = b. We set the stresses in the form (7), (8) and (9), respectively, and on the side we set the displacements

$$U|_{y=0} = g_1(x), \quad V|_{y=0} = g_2(x).$$
 (11)

The functions included in the boundary conditions (5) - (10) should be selected taking into account the matching conditions. So, for the case of specifying displacements on all boundaries of the rectangle, the matching conditions have the form

$$f_{1}(0) = f_{2}(0) , f_{3}(0) = f_{2}(a) , f_{3}(b) = f_{4}(a) , f_{4}(0) = f_{1}(b),$$

$$\varphi_{1}(0) = \varphi_{2}(0) , \varphi_{3}(0) = \varphi_{2}(a) , \varphi_{3}(b) = \varphi_{4}(a) , \varphi_{4}(0) = \varphi_{1}(b).$$
(12)

In the case of specifying stresses at all boundaries, we write the matching conditions for shear stresses as follows

$$\Phi_4(0) = \Phi_1(0), \ \Phi_3(0) = \Phi_1(b), \ \Phi_3(a) = \Phi_2(b), \ \Phi_4(a) = \Phi_2(0).$$
 (13)

For the mixed boundary conditions specified in the third paragraph, the matching conditions are as follows

$$\Phi_3(0) = \Phi_1(b), \ \Phi_3(a) = \Phi_2(b).$$
 (14)

Compliance with the matching conditions will allow finding a continuous solution to three problems: 1. (3) - (6); 2. (3), (4), (7) - (10); 3. (3), (4), (7) - (9), (11).

As an example of the function from (5) - (11), we set as follows

$$f_1(y) = 0, \ f_2(x) = 0, \ f_3(y) = K \sin 1.2\pi ay, \ f_4(x) = K \sin 1.2\pi bx,$$

 $\phi_1(y) = 0, \ \phi_2(x) = 0, \ \phi_3(x) = -K \sin a \sin y, \ \phi_4(x) = -K \sin x \sin b.$ (15)

$$g_1(x) = g_2(x) = 0.$$

$$F_1(y) = 1.2\pi K(\lambda + 2\mu) y \cos 1.2\pi ay$$
, $\Phi_1(y) = -\mu K \sin y$,

$$F_2(y) = 1.2\pi K (\lambda + 2\mu) y \cos 1.2\pi a y - \lambda K \sin a \cos y,$$

$$\Phi_2(y) = \mu(-K\cos a\sin y + 1.2\pi Ka\cos 1.2ay),\tag{16}$$

$$F_3(y) = -K(\lambda + 2\mu)\sin x \cos b + 1.2\pi\lambda Kb \cos 1.2\pi xb,$$

$$\Phi_3(y) = \mu(-K\cos x\sin b + 1.2\pi Kx\cos 1.2xb),$$

$$F_4(y) = -K(\lambda + 2\mu)\sin x$$
, $\Phi_4(y) = 1.2\pi\mu Kx$,

We write the mass forces in (3), (4) by the expressions

$$X(x,y) = (1.2\pi y)^{2} (\lambda + 2\mu) K \sin 1.2\pi xy + + (\lambda + \mu) K \cos x \cos y + (1.2\pi x)^{2} \mu K \sin 1.2\pi xy, Y(x,y) = -(\lambda + 2\mu) K \sin x \sin y - \mu K \sin x \sin y + + (\lambda + \mu) ((1.2\pi)^{2} xyK \sin 1.2\pi xy - 1.2\pi K \cos 1.2\pi xy).$$
(17)

Dependencies (15) – (17) are chosen so that each of the three boundary value problems (1. (3) – (6); 2. (3), (4), (7) – (10); 3. (3), (4), (7) – (9), (11)) had the exact solution $U(x, y) = K \sin 1.2\pi xy$, $V(x, y) = -K \sin x \sin y$, (18)

where *K* is a constant that controls the amount of displacement.

The exact solution (18) will allow us to study the error in solving three boundary value problems by comparing it with an approximate analytical solution obtained by the fast expansion method. In the comparison, the following will be calculated: the relative error of the stress tensor components (2), the residual of the Lamé equilibrium equations (3), (4) and the residual of the boundary conditions (5) - (11).

Let us show in detail the solution of one of the three boundary value problems, for example, for the case of specifying displacements on all sides of a rectangle. For the other two boundary value problems, we note the distinctive features in the process of the solution.

For the solution, we will use the approximate analytical method of fast sine expansions [1], according to which we represent U = U(x, y) and V = V(x, y) as the sum of the 6th order boundary functions $M_6^U(x; y)$, $M_6^V(x; y)$ and the Fourier series in sines

$$U = M_{6}^{U}(x; y) + \sum_{m=1}^{N_{1}} u_{m}(x) \sin m\pi \frac{y}{b},$$

$$V = M_{6}^{V}(x; y) + \sum_{m=1}^{N_{1}} v_{m}(x) \sin m\pi \frac{y}{b}, \quad x \in [0; a], \quad y \in [0; b].$$
(19)

Here, N_1 – is the number of terms taken into account in the Fourier series. The boundary functions $M_6^U(x;y)$ and $M_6^V(x;y)$ of the sixth order are defined by the equalities

$$M_6^U(x;y) = \sum_{i=1}^8 A_i(x) P_i(y), \ M_6^V(x;y) = \sum_{i=1}^8 B_i(x) P_i(y),$$
 (20)

where $A_i(x)$ is $B_i(x)$, $i=1\div 8$ are the coefficients of boundary functions, $P_i(y)$, $i=1\div 8$ fast polynomials [1].

Fast polynomials $P_i(y)$ and coefficients $A_i(x)$, $B_i(x)$ are defined by the equalities:

$$P_{1}(y) = \left(1 - \frac{y}{b}\right), P_{2}(y) = \frac{y}{b}, P_{3}(y) = \left(\frac{y^{2}}{2} - \frac{y^{3}}{6b} - \frac{by}{3}\right), P_{4}(x) = \left(\frac{y^{3}}{6b} - \frac{by}{6}\right),$$

$$P_{5}(y) = \left(\frac{y^{4}}{24} - \frac{y^{5}}{120b} - \frac{by^{3}}{18} + \frac{b^{3}y}{45}\right), P_{6}(y) = \left(\frac{y^{5}}{120b} - \frac{by^{3}}{36} + \frac{7b^{3}y}{360}\right),$$

$$P_{7}(y) = \left(\frac{y^{6}}{720} - \frac{y^{7}}{5040b} - \frac{by^{5}}{360} + \frac{b^{3}y^{3}}{270} - \frac{2b^{5}y}{945}\right),$$

$$P_{8}(y) = \left(\frac{y^{7}}{5040b} - \frac{by^{5}}{720} + \frac{7b^{3}y^{3}}{2160} - \frac{31b^{5}y}{15120}\right).$$

$$A_{1}(x) = U|_{y=0}, \ A_{2}(x) = U|_{y=a}, \ A_{3}(x) = \frac{\partial^{2}U}{\partial y^{2}}|_{y=0}, \ A_{4}(x) = \frac{\partial^{2}U}{\partial y^{2}}|_{y=a},$$

$$A_{5}(x) = \frac{\partial^{4}U}{\partial y^{4}}|_{y=0}, \ A_{6}(x) = \frac{\partial^{4}U}{\partial y^{4}}|_{y=a}, \ A_{7}(x) = \frac{\partial^{6}U}{\partial y^{6}}|_{y=0}, \ A_{8}(x) = \frac{\partial^{6}U}{\partial y^{6}}|_{y=a},$$

$$B_{1}(x) = V|_{y=0}, \ B_{2}(x) = V|_{y=a}, \ B_{3}(x) = \frac{\partial^{2}V}{\partial y^{2}}|_{y=0}, \ B_{4}(x) = \frac{\partial^{2}V}{\partial y^{2}}|_{y=a},$$

$$B_{5}(x) = \frac{\partial^{4}V}{\partial y^{4}}|_{y=0}, \ B_{6}(x) = \frac{\partial^{4}V}{\partial y^{4}}|_{y=0}, \ B_{7}(x) = \frac{\partial^{6}V}{\partial y^{6}}|_{y=0}, \ B_{8}(x) = \frac{\partial^{6}V}{\partial y^{6}}|_{y=0}.$$

$$(21)$$

To be able to execute expressions (21), it is necessary that U = U(x, y) and V = V(x, y) satisfy the smoothness condition $(U, V) \in C^{(6)}(\Omega)$.

The unknowns in (19) are functions that depend on only one variable x:

$$A_1(x) \div A_8(x), B_1(x) \div B_8(x), u_m(x), v_m(x), m = 1...N_1.$$
 (22)

We represent the functions from (22) by fast expansions in x. Moreover, in these repeated expansions, boundary functions of the same orders are used as in fast expansions (19) in the variable y:

$$A_{i}(x) = M_{6}^{A(i)}(x) + \sum_{n=1}^{N_{2}} a_{n+8}^{(i)} \sin n\pi \frac{x}{a}, \quad B_{i}(x) = M_{6}^{B(i)}(x) + \sum_{n=1}^{N_{2}} b_{n+8}^{(i)} \sin n\pi \frac{x}{a},$$

$$u_{m}(x) = M_{6}^{u(m)}(x) + \sum_{n=1}^{N_{2}} u_{n+8}^{(m)} \sin n\pi \frac{x}{a}, \quad v_{m}(x) = M_{6}^{v(m)}(x) + \sum_{n=1}^{N_{2}} v_{n+8}^{(m)} \sin n\pi \frac{x}{a},$$

$$i = 1...8, \quad m = 1...N_{1}.$$
(23)

In (23), N_2 – denotes the number of terms taken into account in the Fourier series. Boundary functions $M_6^{A(i)}(x)$, $M_6^{B(i)}(x)$, $M_6^{u(m)}(x)$, $M_6^{v(m)}(x)$ are defined by equalities

$$M_{6}^{A(i)}(x) = \sum_{k=1}^{8} a_{k}^{(i)} P_{k}(x), \quad M_{6}^{B(i)}(x) = \sum_{k=1}^{8} b_{k}^{(i)} P_{k}(x),$$

$$M_{6}^{u(m)}(x) = \sum_{k=1}^{8} u_{k}^{(m)} P_{k}(x), \quad M_{6}^{\upsilon(m)}(x) = \sum_{k=1}^{8} \upsilon_{k}^{(m)} P_{k}(x),$$
(24)

where $a_k^{(i)}$, $b_k^{(i)}$, $u_k^{(m)}$ and $v_k^{(m)}$, i = 1...8, $m = 1 \div N_1$ – coefficients of boundary functions of secondary expansions; $P_k(x)$, $k = 1 \div 8$ – fast polynomials [1].

Expressions for coefficients of boundary functions $a_k^{(i)}$, $b_k^{(i)}$, $u_k^{(m)}$, $v_k^{(m)}$ and fast polynomials $P_k(x)$ look like

$$P_{1}(x) = \left(1 - \frac{x}{a}\right), P_{2}(x) = \frac{x}{a}, P_{3}(x) = \left(\frac{x^{2}}{2} - \frac{x^{3}}{6a} - \frac{ax}{3}\right), P_{4}(x) = \left(\frac{x^{3}}{6a} - \frac{ax}{6}\right),$$

$$P_{5}(x) = \left(\frac{x^{4}}{24} - \frac{x^{5}}{120a} - \frac{ax^{3}}{18} + \frac{a^{3}x}{45}\right), P_{6}(x) = \left(\frac{x^{5}}{120a} - \frac{ax^{3}}{36} + \frac{7a^{3}x}{360}\right),$$

$$P_{7}(x) = \left(\frac{x^{6}}{720} - \frac{x^{7}}{5040a} - \frac{ax^{5}}{360} + \frac{a^{3}x^{3}}{270} - \frac{2a^{5}x}{945}\right),$$

$$P_{8}(x) = \left(\frac{x^{7}}{5040a} - \frac{ax^{5}}{720} + \frac{7a^{3}x^{3}}{2160} - \frac{31a^{5}x}{15120}\right),$$

$$(25)$$

$$a_{1}^{(i)} = A_{i}\big|_{x=0}, \quad a_{2}^{(i)} = A_{i}\big|_{x=a}, \quad a_{3}^{(i)} = A_{i}^{"}\big|_{x=0}, \quad a_{4}^{(i)} = A_{i}^{"}\big|_{x=a}, \quad a_{5}^{(i)} = A_{i}^{(4)}\big|_{x=0},$$

$$a_{6}^{(i)} = A_{i}^{(4)}\big|_{x=a}, \quad a_{7}^{(i)} = A_{i}^{(6)}\big|_{x=0}, \quad a_{8}^{(i)} = A_{i}^{(6)}\big|_{x=a}, \quad i = 1..8,$$

$$(26)$$

$$\begin{aligned} b_{1}^{(i)} &= B_{i}\big|_{x=0}, & b_{2}^{(i)} &= B_{i}\big|_{x=a}, & b_{3}^{(i)} &= B_{i}^{\prime\prime}\big|_{x=0}, & b_{4}^{(i)} &= B_{i}^{\prime\prime}\big|_{x=a}, & b_{5}^{(i)} &= B_{i}^{(4)}\big|_{x=0}, \\ b_{6}^{(i)} &= B_{i}^{(4)}\big|_{x=a}, & b_{7}^{(i)} &= B_{i}^{(6)}\big|_{x=0}, & b_{8}^{(i)} &= B_{i}^{(6)}\big|_{x=a}, & i = 1..8, \end{aligned}$$

$$u_{1}^{(m)} = u_{m}\big|_{x=0}, \quad u_{2}^{(m)} = u_{m}\big|_{x=a}, \quad u_{3}^{(m)} = u_{m}^{"}\big|_{x=0}, \quad u_{4}^{(m)} = u_{m}^{"}\big|_{x=a}, \quad u_{5}^{(m)} = u_{m}^{(4)}\big|_{x=0},$$

$$u_{6}^{(m)} = u_{m}^{(4)}\big|_{x=a}, \quad u_{7}^{(m)} = u_{m}^{(6)}\big|_{x=0}, \quad u_{8}^{(m)} = u_{m}^{(6)}\big|_{x=a}, \quad m = 1...N_{1}.$$

$$(28)$$

$$\begin{aligned}
\upsilon_{1}^{(m)} &= \upsilon_{m} \Big|_{x=0}, \quad \upsilon_{2}^{(m)} &= \upsilon_{m} \Big|_{x=a}, \quad \upsilon_{3}^{(m)} &= \upsilon_{m}^{"} \Big|_{x=0}, \quad \upsilon_{4}^{(m)} &= \upsilon_{m}^{"} \Big|_{x=a}, \quad \upsilon_{5}^{(m)} &= \upsilon_{m}^{(4)} \Big|_{x=0}, \\
\upsilon_{6}^{(m)} &= \upsilon_{m}^{(4)} \Big|_{x=a}, \quad \upsilon_{7}^{(m)} &= \upsilon_{m}^{(6)} \Big|_{x=0}, \quad \upsilon_{8}^{(m)} &= \upsilon_{m}^{(6)} \Big|_{x=a}, \quad m = 1...N_{1}.
\end{aligned} \tag{29}$$

Thus, the boundary value problem (3) – (6) is reduced to the definition $2(8+N_1)(8+N_2)$ of unknown coefficients

$$a_k^{(i)}, b_k^{(i)}, u_k^{(m)}, \upsilon_k^{(m)}, i = 1...8, k = 1...8, m = 1...N_1, a_{n+8}^{(i)}, b_{n+8}^{(i)}, u_{n+8}^{(m)}, \upsilon_{n+8}^{(m)}, n = 1...N_2.$$
 (30)

Values of eight coefficients

$$a_1^{(1)}, b_1^{(1)}, a_2^{(1)}, b_2^{(1)}, a_1^{(2)}, b_1^{(2)}, a_2^{(2)}, b_2^{(2)},$$
 (31)

included in (30) are found using the values of the displacement components U = U(x, y) and V = V(x, y) at the corner points of the rectangular region (see formulas (21), (26), (27)). Considering the approval condition (12), the coefficients (31) are determined by the equalities $a_1^{(1)} = b_1^{(1)} = a_2^{(1)} = b_2^{(1)} = a_1^{(2)} = b_1^{(2)} = 0$, $a_2^{(2)} = K \sin 1.2\pi ab$, $b_2^{(2)} = -K \sin a \sin b$.

To find the rest $(2(8+N_1)(8+N_2)-8)$ of the coefficients from (30) we use fast trigonometric interpolation, tested in [3–7]. To do this, we substitute U = U(x, y) and V = V(x, y) from (19) into differential equations (3), (4) and boundary conditions (5), (6). The expressions obtained in this way are not presented in the article because of their cumbersomeness.

From the boundary conditions (5), (6), we obtain linear algebraic equations as follows. We divide the interval [0, b] uniformly by points $y = y_s = sb/(N_1 + 7)$, $s = 0,1,...,N_1 + 7$ into $N_1 + 7$ segments and write down the equations obtained from the boundary conditions (5) by substituting U = U(x, y) and V = V(x, y) from (19) at each internal calculation point $y = y_s$, $s = 1,...,N_1 + 6$. We will have $4(N_1 + 6)$ linear algebraic equations. Similarly, we divide the interval [0, a] uniformly by points $x = x_s = sa/(N_2 + 7)$, $s = 0,1,...,N_2 + 7$ into $N_2 + 7$ segments and write down the equations obtained from the boundary conditions (6) by substituting U = U(x, y) and V = V(x, y) from (19) at each internal calculation point $x = x_s$, $s = 1,...,N_2 + 6$. Thus, we will also have $4(N_2 + 6)$ linear algebraic equations.

From differential equations (3), (4) we write linear algebraic equations as follows. On the area of the rectangle, $x \in [0;a]$, $y \in [0;b]$ we evenly apply a grid at $N_2 + 8$ points $x = x_s = sa/(N_2 + 7)$, $s = 0,1,...,N_2 + 7$ and at $N_1 + 8$ points $y = y_s = sb/(N_1 + 7)$, $s = 0,1,...,N_1 + 7$. To compose a system of linear algebraic equations, only internal points are used, which form a grid of $(N_1 + 6)(N_2 + 6)$ internal points (x_s, y_s) . Then, when substituting U = U(x, y) and V = V(x, y) from (19) into equations (3), (4), we

write at each calculated point (x_s, y_s) . So, we obtain $2(N_1+6)(N_2+6)$ linear algebraic equations. As a result, we arrive at a closed system of $2(N_1+6)(N_2+6)+4(N_1+6)+4(N_2+6)$ linear algebraic equations with respect to the remaining $(2(8+N_1)(8+N_2)-8)$ unknowns from (30). This system of equations is solved in the Maple environment. After that, the found unknowns (30) are substituted into fast expansions (19). Thus, we constructed an approximate analytical solution of the boundary value problem (3) – (6).

The solution of boundary value problems (3), (4), (7) – (10) and (3), (4), (7) – (9), (11) differs from the solution described above only by obtaining linear algebraic equations from the boundary conditions (7) - (10) and (7) - (9), (11). So, when solving a boundary value problem with boundary conditions (7) - (10), coefficients (31) cannot be found in the same way as in a problem with conditions (5), (6). Therefore, to determine them, eight additional calculation points are required (compared to the solution of the above case). Therefore, we divide the interval [0, b] uniformly by points $y = y_s = sb/(N_1 + 8)$, $s = 0, 1, ..., N_1 + 8$ into $N_1 + 8$ segments and write down the equations obtained from the boundary conditions (7), (8) by substituting U = U(x, y) and V = V(x, y) from (19) at each internal calculation point $y = y_s$, $s = 1,..., N_1 + 7$. Thus, we have $4(N_1 + 7)$ linear algebraic equations. Similarly, we divide the interval [0, a] evenly by points $x = x_s = sa/(N_2 + 8)$, $s = 0,1,...,N_2 + 8$ into $N_2 + 8$ segments and write down the equations obtained from the boundary conditions (9), (10) by substituting U = U(x, y) and V = V(x, y) from (19) at each internal calculation point $x = x_s$, $s = 1,..., N_2 + 7$. We will also have $4(N_2 + 7)$ linear algebraic equations. If mixed boundary conditions (7) - (9), (11) are given, then we find the values of four coefficients from (31) $a_1^{(1)}$, $b_1^{(1)}$, $a_2^{(1)}$, $b_2^{(1)}$ using the values of the displacement components U = U(x, y) and V = V(x, y) at the corner points (0,0) and (a,0): $a_1^{(1)} = b_1^{(1)} = a_2^{(1)} = b_2^{(1)} = 0$, which allows the interval [0, a] to be uniformly divided into $N_2 + 7$ segments by points $x = x_s = sa/(N_2 + 7)$, $s = 0,1,...,N_2 + 7$ (as in the case of boundary conditions (6)). Thus, to find the remaining four unknowns from (31) $a_1^{(2)}$, $b_1^{(2)}$, $a_2^{(2)}$, $b_2^{(2)}$, we need to divide the interval [0, b] (as in the case of boundary conditions (7), (8)) evenly into $N_1 + 8$ segments by points $y = y_s = sb/(N_1 + 8), s = 0,1,..,N_1 + 8.$

Results and Discussion

In computational experiments, the number of terms in the Fourier series of the first (19) and second (23) fast expansions is assumed to be the same, i.e. $N_1 = N_2 = N = 3$. As the material of the bar, we choose heavy concrete B30 with the characteristics [24] $E = 32.5 \cdot 10^9 \, \text{Pa}$, v = 0.2. Then the Lamé coefficients will be equal to $\lambda = 9.03 \cdot 10^9 \, \text{Pa}$, $\mu = 1.35 \cdot 10^{10} \, \text{Pa}$, and the size of the section will be taken equal to $K = 10^{-6}$, $a = 1 \, \text{m}$, $b = 1 \, \text{m}$.

The approximate analytical solution (19) is compared with the exact one (18). The relative error of the stress tensor (2), the residual between the Lamé equilibrium equations (3), (4) and boundary conditions (5) – (11) was calculated by the formula $\delta = |\Delta|/f_{\rm max} \cdot 100\%$, where Δ is the absolute error, $f_{\rm max}$ is the maximum value of the object under study.

Let us show the residual δ of the Lamé equilibrium equations (3) and (4) using different boundary conditions in Figs. 1–3.

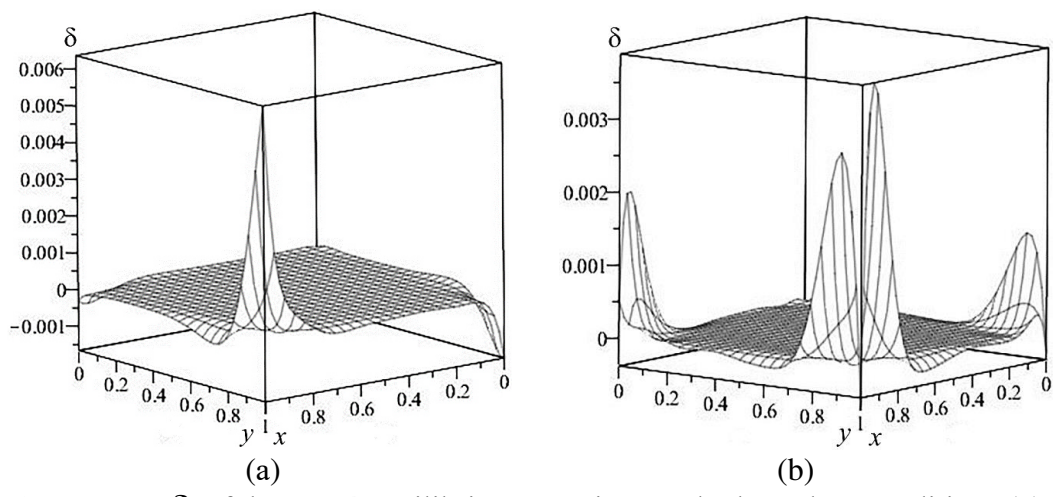


Fig. 1. Residual δ of the Lamé equilibrium equations under boundary conditions (5), (6): (a) (3), (b) (4)

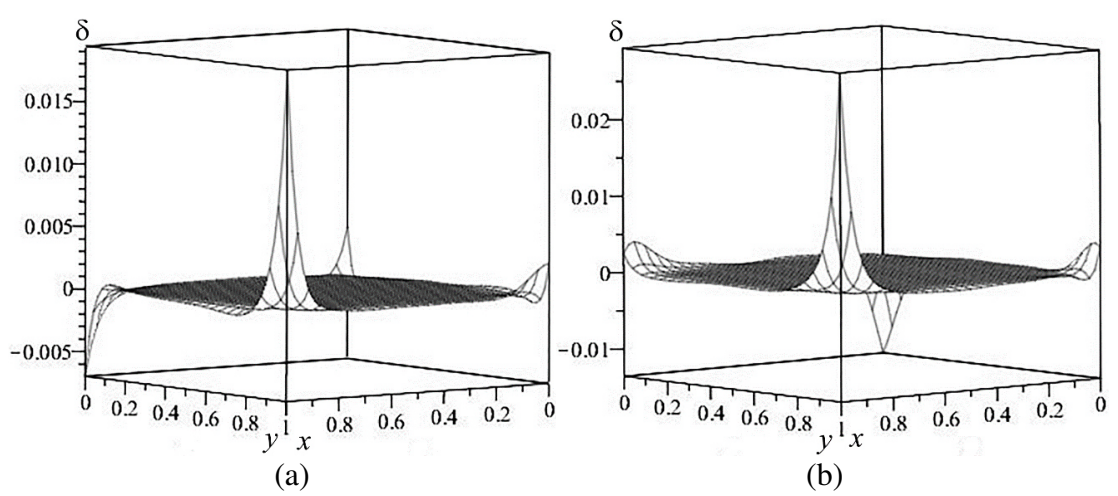


Fig. 2. Residual δ of the Lamé equilibrium equations under boundary conditions (7) – (10): (a) (3), (b) (4)

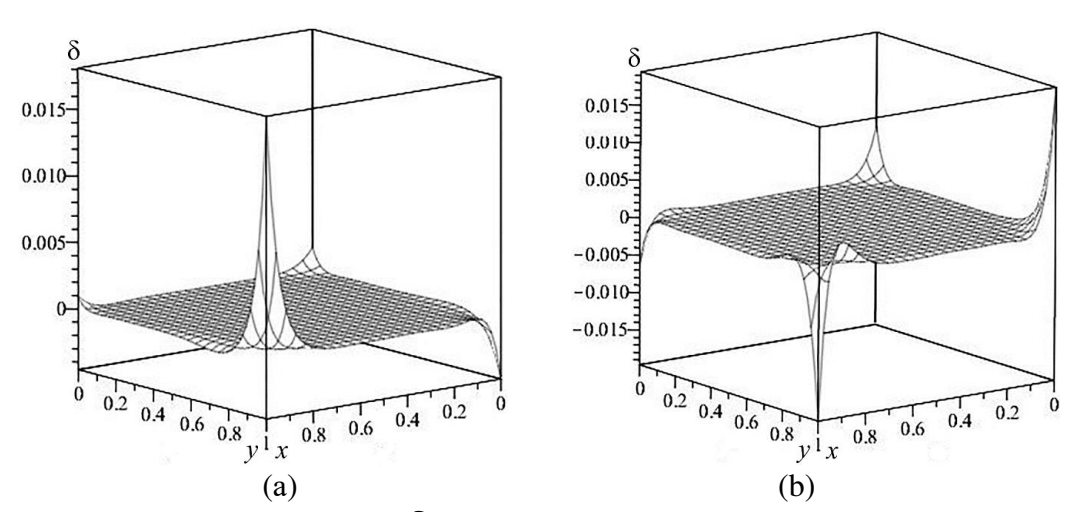


Fig. 3. Residual δ of the Lamé equilibrium equations under boundary conditions (7) – (9), (11): a) (3), b) (4)

It can be seen from the figures that when boundary conditions (7) - (10) and (7) - (9), (11) are specified, the maximum residual δ_{max} of the differential equations will be at the point (1;1). When boundary conditions (5), (6) are specified, the residual δ_{max} of the differential equation (3) is also located at the point (1;1), and δ_{max} of the differential equation (4) is in its neighborhood on the side y=1.

Table 1. Relative error δ_{max} , %

Object unde	or etudy		Used boundary conditions		
Object under study		(5), (6)	(7) - (10)	(7) - (9), (11)	
	σ_{xx}	$4.14 \cdot 10^{-4}$	$9.87 \cdot 10^{-4}$	$1.57 \cdot 10^{-3}$	
Tensor Components	σ_{yy}	$4.18 \cdot 10^{-4}$	$2.19 \cdot 10^{-3}$	$5.39 \cdot 10^{-3}$	
stresses	σ_{zz}	$3.67 \cdot 10^{-4}$	$1.05 \cdot 10^{-3}$	$6.42 \cdot 10^{-4}$	
	τ_{xy}	$3.67 \cdot 10^{-4}$	$1.53 \cdot 10^{-3}$	$6.42 \cdot 10^{-4}$	
Residual DE	(3)	$6.34 \cdot 10^{-3}$	$1.94 \cdot 10^{-2}$	$1.81 \cdot 10^{-2}$	
Residual DE	(4)	$3.82 \cdot 10^{-3}$	$2.93 \cdot 10^{-2}$	$1.96 \cdot 10^{-2}$	
	$U\big _{x=a},U\big _{y=b}$	$2.58 \cdot 10^{-5}$			
	$V _{x=a}$, $V_{y=b}$	$5.59 \cdot 10^{-10}$			
	$U\big _{x=0}$, $V\big _{x=0}$	0			
	$U\big _{{\scriptscriptstyle y=0}},V_{{\scriptscriptstyle y=0}}$	0		0	
	$\sigma_{xx}\Big _{x=a}$		$1.53 \cdot 10^{-3}$	$1.74 \cdot 10^{-3}$	
	$\sigma_{xx}\Big _{x=0}$		$3.28 \cdot 10^{-4}$	$1.80 \cdot 10^{-4}$	
Residual BC	$\left.\tau_{xy}\right _{x=a}$		$1.17 \cdot 10^{-3}$	$7.05 \cdot 10^{-4}$	
	$\left.\tau_{xy}\right _{x=0}$		$1.35 \cdot 10^{-3}$	$1.78 \cdot 10^{-3}$	
	$\sigma_{yy}\Big _{y=b}$		$1.17 \cdot 10^{-3}$	$5.50 \cdot 10^{-3}$	
	$\sigma_{yy}\Big _{y=0}$		$1.38 \cdot 10^{-3}$		
	$\left. \tau_{xy} \right _{y=b}$		$1.29 \cdot 10^{-3}$	$6.91 \cdot 10^{-4}$	
	$\left. \tau_{xy} \right _{y=0}$		$2.50 \cdot 10^{-4}$		

Table 1 lists the values of the maximum relative error δ_{max} of the stress tensor components, residuals of differential equations (DE), and residuals of boundary conditions (BC). It can be seen from the table that when using the boundary conditions of three types (1. (5), (6), 2. (7) – (10), 3. (7) – (9), (11)), the solution to the boundary value problem with the Dirichlet conditions is found most accurately. Compared with this problem, the accuracy of determining the components of the stress tensor and the residual of differential equations in two other boundary value problems drops by an order of magnitude. The residual between boundary conditions (7) – (10) and (7) – (9), (11) is inferior in accuracy to the residual between boundary conditions (5), (6) by more than an order of magnitude. It can also be noted that when using any kind of boundary conditions, the components of the stress tensor σ_{xx} ,

 σ_{yy} , σ_{zz} , τ_{xy} are determined by an order of magnitude more accurately than the residuals of the Lamé equilibrium equations (3), (4).

When studying the properties of the stress field in a bar, it is of interest to locate the point with the highest value of stress intensity $\tilde{\sigma}$ [25]:

$$\widetilde{\sigma} = \sqrt{\frac{\left(\left(\sigma_{xx} - \sigma_{yy}\right)^2 + \left(\sigma_{yy} - \sigma_{zz}\right)^2 + \left(\sigma_{zz} - \sigma_{xx}\right)^2 + 6\left(\tau_{xy}\right)^2\right)}{2}}.$$

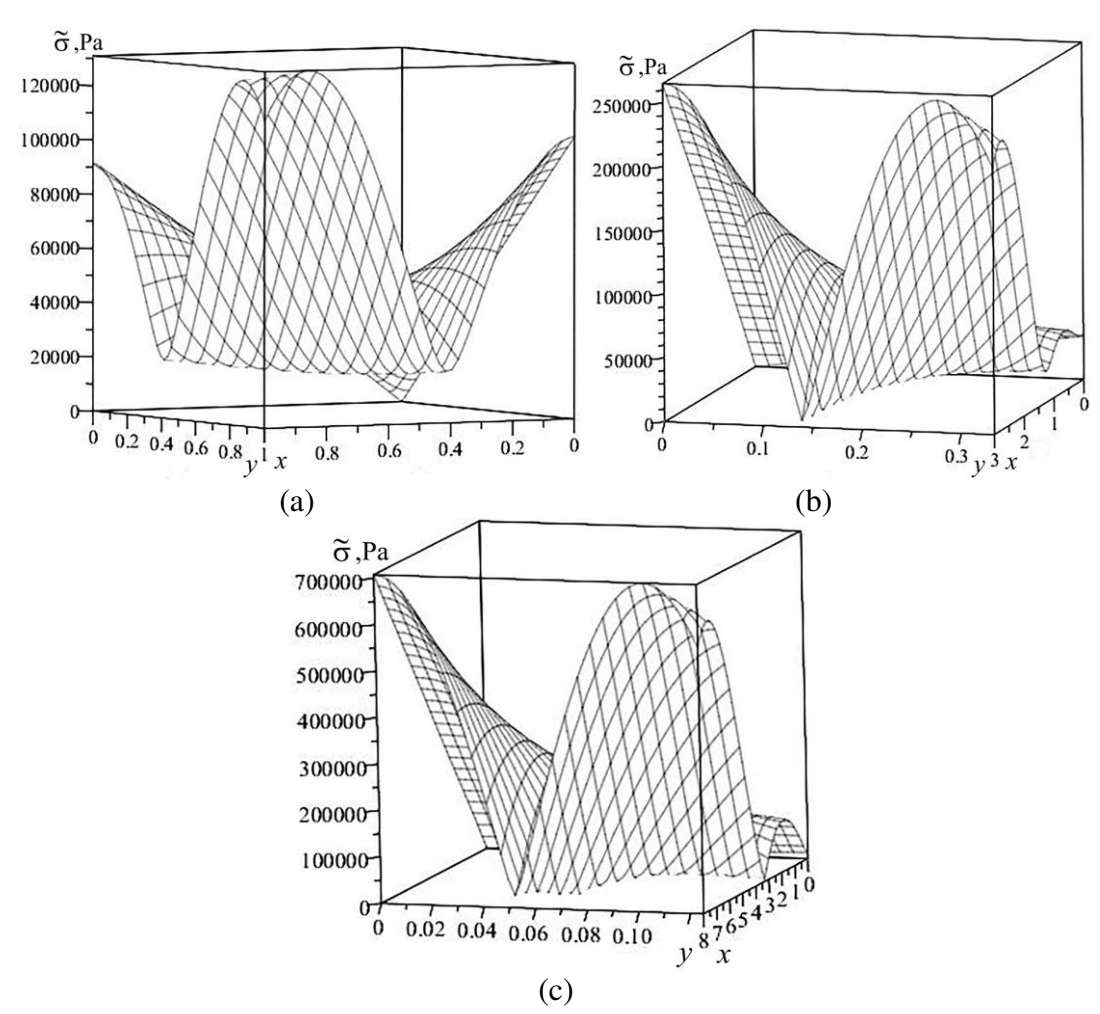


Fig 4. Stress intensity $\tilde{\sigma}$: (a) a = b = 1, (b) a = 3, b = 1/3, (c) a = 8, b = 1/8

Let us carry out calculations for three boundary value problems. The stress intensity profiles $\tilde{\sigma}$ will be the same for all types of boundary conditions. In computational experiments, the aspect ratio of the rectangle was chosen in such a way that the cross-sectional area of the bar remained constant. The stress intensity distribution $\tilde{\sigma}$ is shown in Fig. 4. It illustrates that the location of the point with the maximum stress intensity $\tilde{\sigma}_{\text{max}}$ is affected by the aspect ratio of the rectangle. So, for a square section, the point with the maximum stress intensity $\tilde{\sigma}_{\text{max}}$ is located on the side y=1 near the corner point (a;b) (Fig. 4(a)), and for a rectangular section $\tilde{\sigma}_{\text{max}}$ it is located either at one point or at two points, depending on the aspect ratio a/b. Thus, at $1 < a/b \le 25$ the maximum stress intensity $\tilde{\sigma}_{\text{max}}$ is located at one point (a;0) (Fig. 4(b)), and at a/b > 25 – at two points (Fig. 4(c)) with

coordinates (a;0) and (a;0.8b). The minimum value of $\tilde{\sigma}_{min} = 0$ is at point (0;0) regardless of the aspect ratio of the rectangle. It can also be concluded from Fig. 4 that among all rectangular sections with different overall dimensions (but the same sectional area), the smallest value of $\tilde{\sigma}_{max}$ is observed in a bar with a square section.

Conclusions

In conclusion, we note that the solution of the boundary value problem with the Dirichlet conditions is the most accurate of the three considered boundary value problems. Compared with this problem, the accuracy of determining the components of the stress tensor and the residual of differential equations in two other boundary value problems drops by an order of magnitude. The largest residual in the Lamé equilibrium equations is observed in the boundary value problem with given stresses on all sides of the rectangle.

Computational experiments showed that the aspect ratio of the rectangle affects the qualitative form of the stress intensity distribution $\tilde{\sigma}$ and, as a result, the location of points with the maximum stress intensity $\tilde{\sigma}_{\text{max}}$ and their number. At a/b=1 the point with $\tilde{\sigma}_{\text{max}}$ is located on the side y=1 near the corner point (a;b). For $1 < a/b \le 25$ $\tilde{\sigma}_{\text{max}}$ it is at one point (a;0), and for a/b > 25 it is at two points with coordinates (a;0) and (a;0.8b). The minimum value of $\tilde{\sigma}_{\text{min}}=0$ is at (0;0) regardless of the aspect ratio of the rectangle. Among all rectangular sections with different overall dimensions, but the same sectional area, the smallest value of $\tilde{\sigma}_{\text{max}}$ is observed in a bar with a square section.

References

- 1. Goloskokov DP, Matrosov AV. Approximate analytical approach in analyzing an orthotropic rectangular plate with a crack. *Materials Physics and Mechanics*. 2018;36(1): 137–141.
- 2. Kovalenko MD, Menshova IV, Kerzhaev AP, Shulyakovskaya TD. Some solutions of the theory of elasticity for a rectangle. *Mechanics of Solids*. 2021;56(7): 1232–1242.
- 3. Bogdanov VR, Sulim GT. Plain deformation of elastoplastic material with profile shaped as a compact specimen (dynamic loading). *Mechanics of Solids*. 2013;48(3): 329–336.
- 4. Aleksandrov VM, Bazarenko NA. The contact problem for a rectangle with stress-free side faces. *Journal of Applied Mathematics and Mechanics*. 2007;71(2): 305–317.
- 5. Meleshko VV. Thermal stresses in an elastic rectangle. *Journal of Elasticity*. 2011;105(1-2): 61–92.
- 6. Meleshko VV. Equilibrium of elastic rectangle: Mathieu-Inglis-Pickett solution revisited. *Journal of Elasticity*. 1995;40(3): 207–238.
- 7. Liu K, Li B. A numerical solution of torsional stress wave propagation in layered orthotropic bar of rectangular cross-section. *International Journal of Solids and Structures*. 2001;38(48–49): 8929–8940.
- 8. Zhang ZL, Ødegård J, Søvik OP, Thaulow C. A study on determining true stress curve for anisotropic materials with rectangular tensile bars. *International Journal of Solids and Structures*. 2001;38(26–27): 4489–4505.
- 9. Franco A, Royer-Carfagni G. Contact stresses in adhesive joints due to differential thermal expansion with the adherends. *International Journal of Solids and Structures*. 2016;87: 26–38.
- 10. Chernyshov AD, Goryainov VV, Kuznetsov SF, Nikiforova OYu. Application of fast expansions to obtain exact solutions to a problem on rectangular membrane deflection under

alternating load. *Tomsk State University Journal of Mathematics and Mechanics*. 2021;70: 127–142. (In-Russian)

- 11. Preissner EC, Vinson JR. Application of theorem of minimum potential energy to a complex structure part I: two-dimensional analysis. *International Journal of Solids and Structures*. 2003; 40(5): 1089–1108.
- 12. Sarychev VD, Nevsky SA, Gromov VE. Theoretical analysis of the stress-deformed state of materials with a gradient structure. *Materials Physics and Mechanics*. 2015;22(2): 157–169.
- 13. Liu GR, Zhang GY, Wang YY, Zhong ZH, Li GY, Han X. A nodal integration technique for meshfree radial point interpolation method (NI-RPIM). *International Journal of Solids and Structures*. 2007;44: 3840–3860.
- 14. Smelov VV. Grid version of a nonstandard trigonometric basis and its advantages over a similar polynomial basis. *Numerical Analysis and Applications*. 2014;7: 336–344
- 15. Isaev VI, Shapeev VP. High-accuracy of the collocations and least squares method for the numerical solution of the Navies-Stokes equations. *Computational Mathematics and Mathematical Physics*. 2010;50(10): 1670–1681.
- 16. Zaitseva EV, Shmeleva AG, Kazankov VK. Unstable plastic flow in structural materials: time series for analysis of experimental data. *Materials Physics and Mechanics*. 2022;48(2): 208–216.
- 17. Vasilyev B, Selivanov A. Numerical method of single-crystal turbine blade static strength estimation taking into account plasticity and creep effects. *Materials Physics and Mechanics*. 2019;42(3): 311–322.
- 18. Annin BD, Bondar V.D, Senashov SI. Group Analysis and Exact Solutions of the Dynamic Equations of Plane Strain of an Incompressible Nonlinearly Elastic Body. *Journal of Applied and Industrial Mathematics*. 2020;14(1): 6–8.
- 19. Chernyshov AD. Method of fast expansions for solving nonlinear differential equations. *Computational Mathematics and Mathematical Physics*. 2014;54(1): 11–21.
- 20. Goryainov VV, Popov MI, Chernyshov AD. Solving the stress problem in a sharp wedge-whaped cutting tool using the quick decomposition method and the problem of matching boundary conditions. *Mechanics of Solids*. 2019;54(7): 1083–1097.
- 21. Chernyshov AD, Goryainov VV, Danshin AA. Analysis of the stress field in a wedge using the fast expansions with pointwise determined coefficients. *IOP Conf. Series: Journal of Physics: Conf. Series.* 2018;973: 012002.
- 22. Briand T. Trigonometric Polynomial Interpolation of Images. *Image Processing On Line*, 2019:9: 291–316.
- 23. Porshnev SV, Kusaikin DV. Reconstruction of finite-length periodic discrete-time signals with the use of trigonometric interpolation. *Journal of Instrument Engineering*. 2017;60(6): 504–512.
- 24. SR 63.13330.2018. *Concrete and reinforced concrete structures. General provisions.* Moscow: Standardinform; 2019.
- 25. Pisarenko GS, Mozharovsky NS. *Equations and boundary value problems of plasticity and creep.* Kyiv: Nauk. Dumka; 1981.

THE AUTHORS

Chernyshov A.D.

e-mail: chernyshovad@mail.ru

Kovaleva E.N.

e-mail: kovaleva.lena@gmail.com

Goryainov V.V.

e-mail: gorvit77@mail.ru

Ab initio study of Hydrogen and Lithium behaviors in Cu₂O

Submitted: November 10, 2022

Approved: March 20, 2023

Accepted: April 26, 2023

A. Larabi ¹, M. Mebarki ¹, I. Abdellaoui ¹,

A. Mahmoudi 10 3, S. Merazga 10 1, N. Gabouze 10 1

¹ Centre de Recherche en Technologie des Semi-conducteurs pour l'Energétique (CRTSE), Alger, Algeria

² The Center for the Development of Advanced Technologies, Alger, Algeria

³ Université Abou Bekr Belkaid Tlemcen, Tlemcen, Algeria

☑ Mebarki.Mourad@crtse.dz

Abstract. Nowadays, produced green energy requires efficient storage, the materials to be used must be at unbeatable prices. Lithium and hydrogen are two candidates in several applications in the field of renewable energies. The effect of Hydrogen or Lithium on the electronic, magnetic and optical properties of cuprous oxide Cu_2O has been investigated using the projected augmented wave (PAW) based on the density functional theory (DFT) formalism, within the generalized gradient approximation (GGA). Different concentrations of hydrogen and lithium were taken into consideration. The calculated formation energies indicate that the H-Cu₂O system is stable for all hydrogen concentrations. The density of electronic states calculations show that Cu_2O is p-type and it keeps the same type after hydrogen or lithium incorporation. The correlation of the obtained results gives us more precision on the physical properties of H or Li: Cu_2O .

Keywords: Cu₂O; Hydrogen; Lithium; energy storage; DFT

Acknowledgements. This work was funded under the Algerian General Directorate of Scientific Research and Technological Development (DGRSDT). The authors are grateful to Professor Abdelhamid Layadi, L.E.S.I.M.S., Département de Physique, Université Ferhat Abbas, Setif 1, Algeria, for helpful suggestions.

Citation: A. Larabi, M. Mebarki, I. Abdellaoui, A. Mahmoudi, S. Merazga, N. Gabouze. Ab initio study of Hydrogen and Lithium behaviors in Cu₂O. *Materials Physics and Mechanics*. 2023;51(4): 172-185. DOI: 10.18149/MPM.5142023_15.

Introduction

The evolution of the performance of innovative batteries has played an important role in the energy research community since its beginning. Consequently, it is essential to study excellent materials for applications in advanced batteries of electric vehicles, hybrid electric vehicles and energy storage. The various materials used in lithium battery electrodes are selected for their best performance in cyclability and their high specific capacities. Several studies have been made to come out and test the ability to use cuprous oxides as electrodes in lithium batteries [1–5]. Several candidates, such as cuprous oxide (Cu₂O) with a theoretical capacity of 375 mA h/g, have attracted more interest due to their high abundance, low production cost and nontoxic nature [6–8]. The Cu₂O nanostructures with varied morphology, such as cubic, starshaped crystalline particles [9] and nanowires [10] have a big impact on the enhancement of

nontoxic nature [6–8]. The Cu₂O nanostructures with varied morphology, such as cubic, star-shaped crystalline particles [9] and nanowires [10] have a big impact on the enhancement of the specific capacity and the cycling capability for lithium-ion batteries (LIBs) and Hydrogen storage.

Up to now, several scientific efforts have been focused on the study of the physical properties of Cu₂O and these different applications. The electronic and photocatalytic properties of Cu₂O with different Mn concentrations and configurations have been investigated by the density functional theory (DFT) [11]. The GGA and GGA + U approaches were applied to obtain the Cu₂O band structures and thermoelectric properties [12]. The examination of the halogens doping effects of Cu₂O has been reported in the literature [13]; this was done by using first-principle calculations of the electronic structures and the optical properties. The effect of Li doped Cu₂O has been investigated by Nyborg et al. [14,15]. Yifei et al. demonstrated the feasibility of the successive "conversion-deposition" mechanism for realizing long-cycle-life composite Li anode, thus after insertion of Li ion into Cu₂O and deposited in the form of Li metal at successive low potential [16]. Cu₂O nanowire arrays has been used to provide a new strategy to high performance Li metal battery based on 3d conductive skeleton with lithiophilic [17]. In the other hand, Xue Zhou et al. proposed a new strategy to protect Cu₂O hydrogen-substituted graphdiyne [18]. The hydrogenation strategy is employed, also, to improve sensing performances of Cu₂O [19].

In this work, the first principles calculations were used to study the substitutional hydrogen and lithium effect on the electronic, magnetic and optical properties of Cu₂O. To verify the system stability in presence of hydrogen or lithium, we calculated the formation energies of different proposed concentrations. In addition, the influence of hydrogen and lithium on the physical properties Cu₂O is investigated. We also predict and give an easy, low-cost and scalable strategy to prepare the Cu₂O for energy storage.

Method

We used ab initio total-energy and molecular-dynamics program VASP (Vienna ab initio simulation program) developed at the Fakultät für Physik of the Universität Wien [20,21]. For the exchange and correlation energies treatment, we adopted the generalized gradient approximation (GGA) [22] with projector-augmented wave (PAW) [21,23] pseudo-potentials. Brillouin zone integrals converged with a 450 eV plane-wave cut-off and a $2 \times 2 \times 2$ Monkhorst-Pack k-point mesh, sufficient to insure the energy convergence for the supercell. These calculations showed a discrepancy within 10^{-7} eV. We relaxed the structure with the standard conjugated gradient algorithm. We used the supercell approach to simulate the H or Li doped Cu₂O system. The optimized lattice constant of Cu₂O is a = 4.14 Å which is in good agreement with the experimental value of a = 4.27 Å [24,25] and theoretical values a= 4.18 and 4.20 Å [26,27].

In these calculations, we positioned the H and Li atoms at the cation sites (Cu). We performed the hydrogen and lithium formation energies calculations on $3\times3\times3$ supercell with 162 atoms (Fig. 1), using the calculated lattice constant with the different concentrations in the cell. The supercell size is necessary for a detailed study of many dopant geometric structures. For calculations of the electronic properties of H or Li doped Cu₂O, we suppose that H and Li atoms lead to form a $3\times3\times3$ supercell with chemical composition $Cu_{2(108-x)}H_xO_{54}$ or $Cu_{2(108-x)}Li_xO_{54}$ with different atoms of hydrogen or lithium at the substitutional sites. The calculations were spin-polarized.

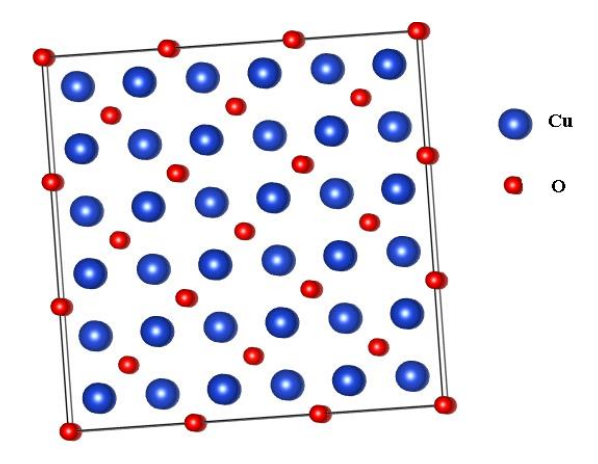


Fig 1. Supercell of $3 \times 3 \times 3$ Cu₂O lattice with 162 atoms

Optical properties can be determined using the complex dielectric function $\varepsilon(\omega)=\varepsilon_1(\omega)+i\varepsilon_2(\omega)$ [28]. The imaginary part of the dielectric function $\varepsilon_2(\omega)$ was calculated from the momentum matrix elements between the occupied and unoccupied wave functions [29]:

$$\alpha(\omega) = \sqrt{2} \left(\frac{\omega}{c} \right) \left[\sqrt{\varepsilon_1^2(\omega) - \varepsilon_2^2(\omega)} - \varepsilon_1(\omega) \right]^{\frac{1}{2}}. \tag{1}$$

Results and discussion

Structures and formation energies. In order to confirm the stability of the system in the presence of hydrogen or lithium, we calculate the formation energies for different concentrations of Hydrogen and Lithium in Cu₂O. The refs. [30–32] give the formation energy for hydrogen in Cu₂O as:

$$E_f = E_{\text{Cu2O} + H} - E_{\text{Cu2O}} - nE_{tot}^H + nE_{tot}^{Cu} + qE_F.$$
 (2)

The formation energy for lithium in the Cu₂O is given by:

$$E_f = E_{\text{Cu2O} + Li} - E_{\text{Cu2O}} - nE_{tot}^{Li} + nE_{tot}^{Cu} + qE_F, \tag{3}$$

where $E_{\text{Cu2O} + H}$ and $E_{\text{Cu2O} + Li}$ are the total energy of the supercell with hydrogen and lithium respectively; E_{Cu2O} is the total energy of the supercell without hydrogen or lithium. The ground state total energies, E_{tot}^H , E_{tot}^{Cu} and E_{tot}^{Li} correspond, respectively, to isolated hydrogen, cuprous and lithium atoms; n denotes the number of H or Li atoms introduced in Cu₂O system. The last term in the formation energy accounts for the fact that H^+ or Li^+ donates an electron and H^- or Li^- accepts an electron. E_F is the Fermi level energy. If the formation energy is negative ($E_f < 0$), the implantation of the hydrogen or lithium atom into the Cu₂O lattice is energetically favorable.

In the Fig. 2(a), we present the variation of the calculated formation energies with the hydrogen concentration. We can see that all calculated formation energies are negative which indicate the stability of Cu₂O in presence of hydrogen. Figure 2(b) shows the formation energy values for different Li concentrations. The formation energies of the first two lithium concentrations are positive. Thus, the system is not stable, which is probably due to the possible formation of Li₂O, this case is reported in the literature [33]. Beyond the two first concentrations, the values of all formation energies become negative and decrease in a linear way with a low slope, this state is more stable and opens the possible feasibility to the experimentation of Li: Cu₂O [34].

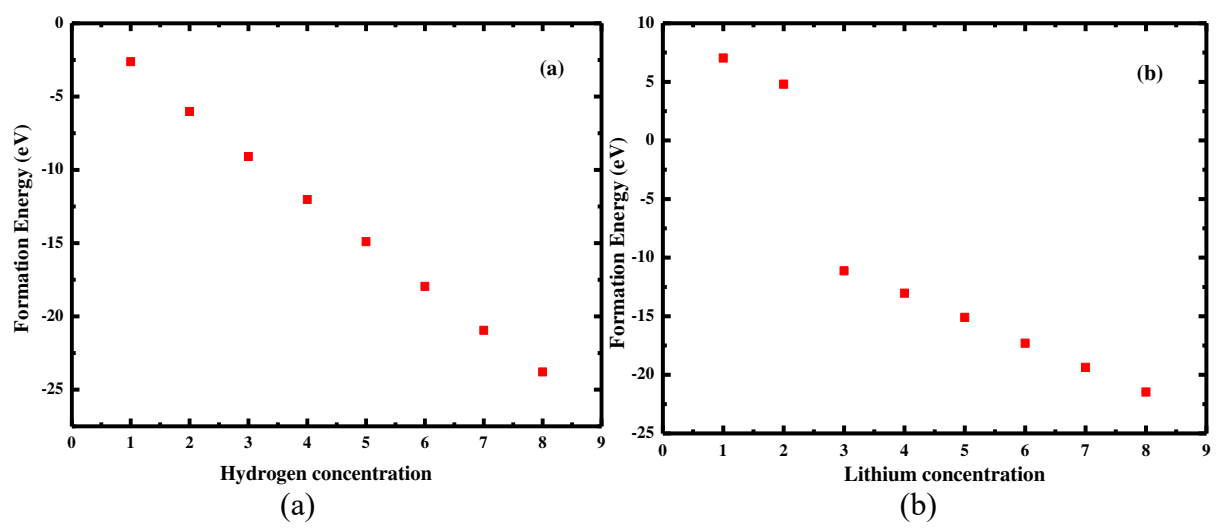


Fig. 2. Formation energy variation with Hydrogen (a) and Lithium(b) concentration

Table 1. System energies, bond lengths (Å), band-gaps and Fermi levels energies in the

undoped, H and Li-doped Cu₂O systems calculated using GGA-PBE

System	Energies	E _g (eV)	E _F (eV)	Cu-Cu	Cu-O	Cu-dopant	O-dopant
Undoped	-739.09	0.55	3.236	2.931	1.794	-	-
1H	-741.67	0.42	2.177	3.037	1.86	2.678	1.198
2H	-741.85	0.32	2.232	3.022	1.865	2.82	1.097
3H	-742.09	0.32	2.299	3.126	1.864	2.697	1.195
4H	-742.26	0.43	2.283	3.003	1.858	2.557	1.078
5H	-742.34	0.43	2.312	3.004	1.873	2.663	1.049
6H	-742.66	0.43	2.302	3.006	1.856	2.521	1.054
7H	-742.8	0.43	2.296	3.009	1.864	2.512	1.046
8H	-742.95	0.43	2.392	3.005	1.848	2.505	1.062
1Li	-726.98	0.66	3.355	2.915	1.785	2.872	1.658
2Li	-727.32	0.66	3.356	2.918	1.787	2.863	1.673
3Li	-742.53	0.42	2.139	3.039	1.857	3.015	1.797
4Li	-742.54	0.52	2.219	3.002	1.861	2.981	1.741
5Li	-742.83	0.52	2.232	3.025	1.86	3.01	1.744
6Li	-743.09	0.52	2.135	2.995	1.848	2.972	1.74
7Li	-743.44	0.52	2.138	3.037	1.863	2.991	1.749
8Li	-743.74	0.52	2.104	3.006	1.86	2.992	1.749

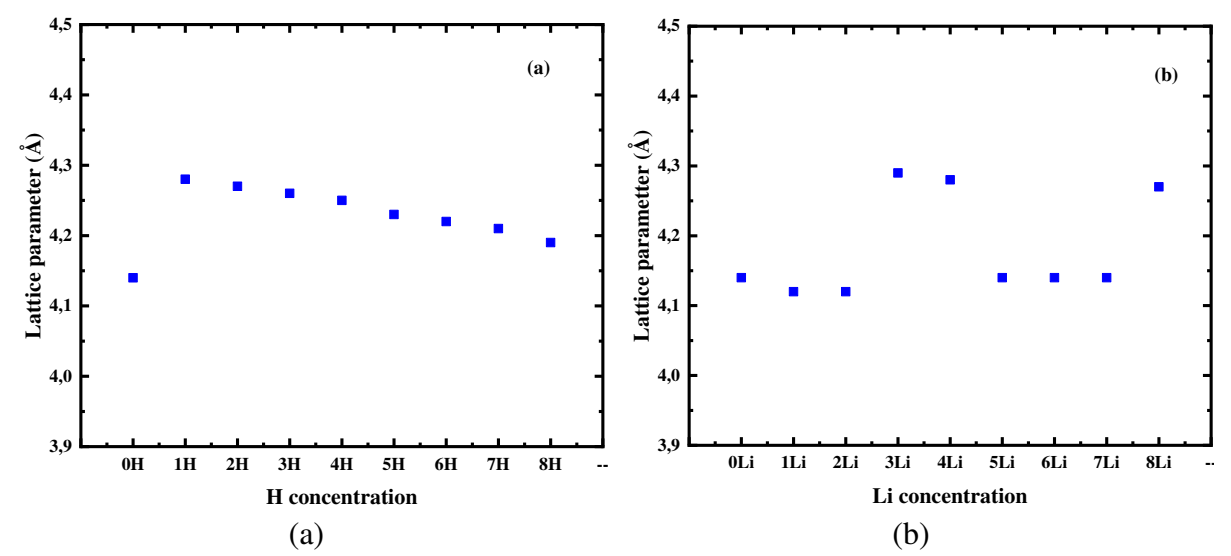


Fig. 3. Lattice parameter variation with Hydrogen (a) and Lithium (b) concentrations

Magnetic and electronic properties. From the densities of states (see Figs. 4 and 5), we note that, for all concentrations (of H or Li), the difference between the majority and minority densities of states near the Fermi energy is equal to zero. This indicates that the presence of substitutional hydrogen or lithium does not generate a magnetic moment order in Cu₂O. The calculated band gap of undoped Cu₂O is about 0.55 eV, which is smaller than the experimental value (2.17 eV) [35] but it agrees well with the previous theoretical value reported in literature (0.6 eV [36,37], 0.64 eV [38] and 0.7 eV [39].

The density of states (DOS) for Cu₂O is calculated in order to understand the electronic structure and nature of the band edge wave functions (see Fig. 6). The projected DOS clearly shows significant *p-d* (O-2*p* and Cu-3*d*) hybridization below Fermi level, with Cu-3*d* bands dominating the valence and the conduction band edge. From this, it is clear that the interaction between metal-metal, which is controlled by the interatomic distances Cu-Cu, defined the band gap energy.

The calculated band gap energies for different concentrations of dopants in Cu₂O are shown in Fig. 7. The decrease in energy values of the Fermi level indicates that the doped system is a degenerate p-type semiconductor, as seen in Table 1. The total and partial DOS of H-1s, Li-2s, O-2p and Cu-3d states are plotted in Figs. 8 and 9(b,c). The dopant contribution to the calculated DOS is at low energy level, no dopants bands in the top VB or in the bottom of CB are observed, where the band edge of doped Cu₂O have the same features as pure system. For H-doping, the sharp peak at -5.5 eV corresponds to the fully symmetric orbital of the hydrogen multicenter bond in Cu₂O [40]. Clearly, it shows strong localized energy bands, which is from O-2p, Cu-4s and H-1s states. The sharp peak at -2 eV shows strong coupling between Cu-3d and H-1s states. Moreover, the states close to the VBM (-2 to 0 eV) are dominated by Cu-3d and O-2p hybrid orbitals. Beyond the CBM, the Cu and H bands are resonant and strongly mix with the host CB states. For Li-doping, the sharp peaks at -6.5 show strong localized energy bands from O-2p states and Li-2s states without the presence of the Li-2s bands near Fermi level and contribution of Cu-4s orbitals considering the H-doping system. The energy bands of the doped system are deeper than that of the undoped system. It can be explained by the strong bonding of substitution atoms with their neighbors compared to Cu atoms. They are further stabilized systems as showing the lower energetic values (see Table 1).

It is known that in the case of doping, the filling effect of the band edge near the Fermi level cannot be ignored. In this context, we analyzed the charge transfer based on Bader's theory. The absolute value of charge transfer of undoped and doped Cu₂O is shown in Fig. 10, which characterizes the ability of atoms to gain and lose electrons. In the case of an undoped system, the cation Cu atom loses electrons and the anion O atom gains electrons. In doped systems, H atoms are considered donors because they undergo negative charge transfer. Therefore, it is slightly changed compared to an undoped system where O atoms receive charges from Cu and H atoms. The charge loss of Cu in the H-doped system is slightly less than that of the undoped system. This shows that the sharing of charge between H+ and O atoms results in the formation of a typical H-O covalent bond, which leads to a decrease in the electronegativity of the O atom and an increase in the strength of the copper-copper covalent bond. This reduces the ionicity of the Cu-O bond and clarifies the peak intensity in DOS. Due to the reduced hybridization between Cu and O atoms, the peak intensity after doping is very weak. In addition, we can see that despite the covalent increase due to the O-H bond, the band gap shrinkage rate is limited to 0.32 eV, with no significant changes in structural distortion and electronic structure.

For Li-doped Cu_2O , we can see that 1Li and 2Li doping increase the band gap. This can be explained by reducing the copper spacing, which increases the Cu-3d band overlap, as listed in Table 1. For the charge transfer from the cation to the anion atom, there is no significant change compared to the undoped system. However, as shown in Table 1, due to the increase in

ion characteristics, 3-8Li doping reduces the band gap less than the H doping case. We can see that there is no important modification in the band gap value in the case of high concentration Li-doping, this result agree with previous work [14]. It can be seen that the band gap changes of the two dopants are the result of the simultaneous filling effects: the Cu-3d band and the orbital-lattice coupling.

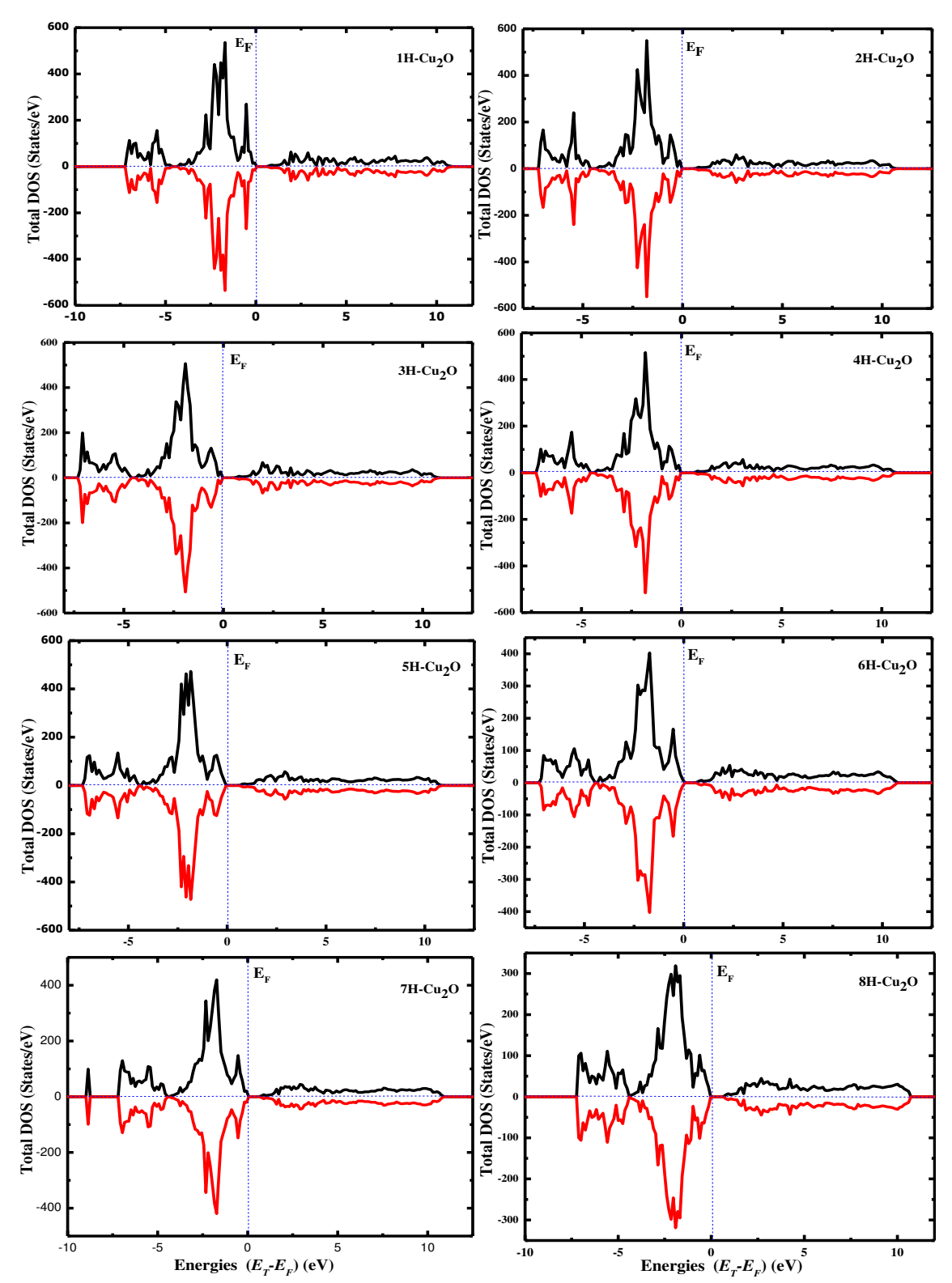


Fig. 4. Calculated density of states of H-Cu₂O for different concentrations of hydrogen. Dashed line is the Fermi level E_F

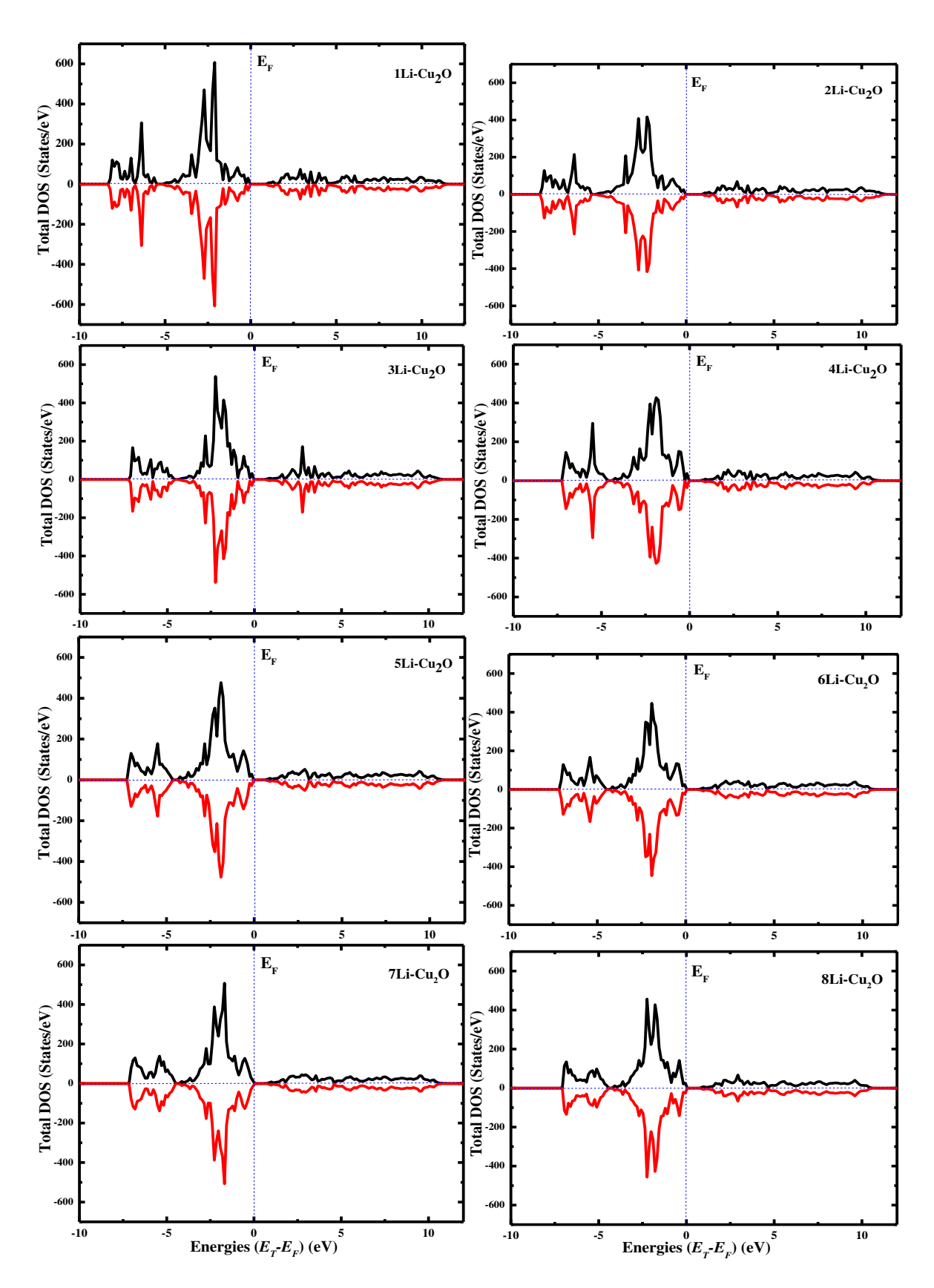


Fig. 5. Calculated density of states of Li-Cu₂O for different concentrations of lithium. Dashed lines is the Fermi level $E_{\rm F}$

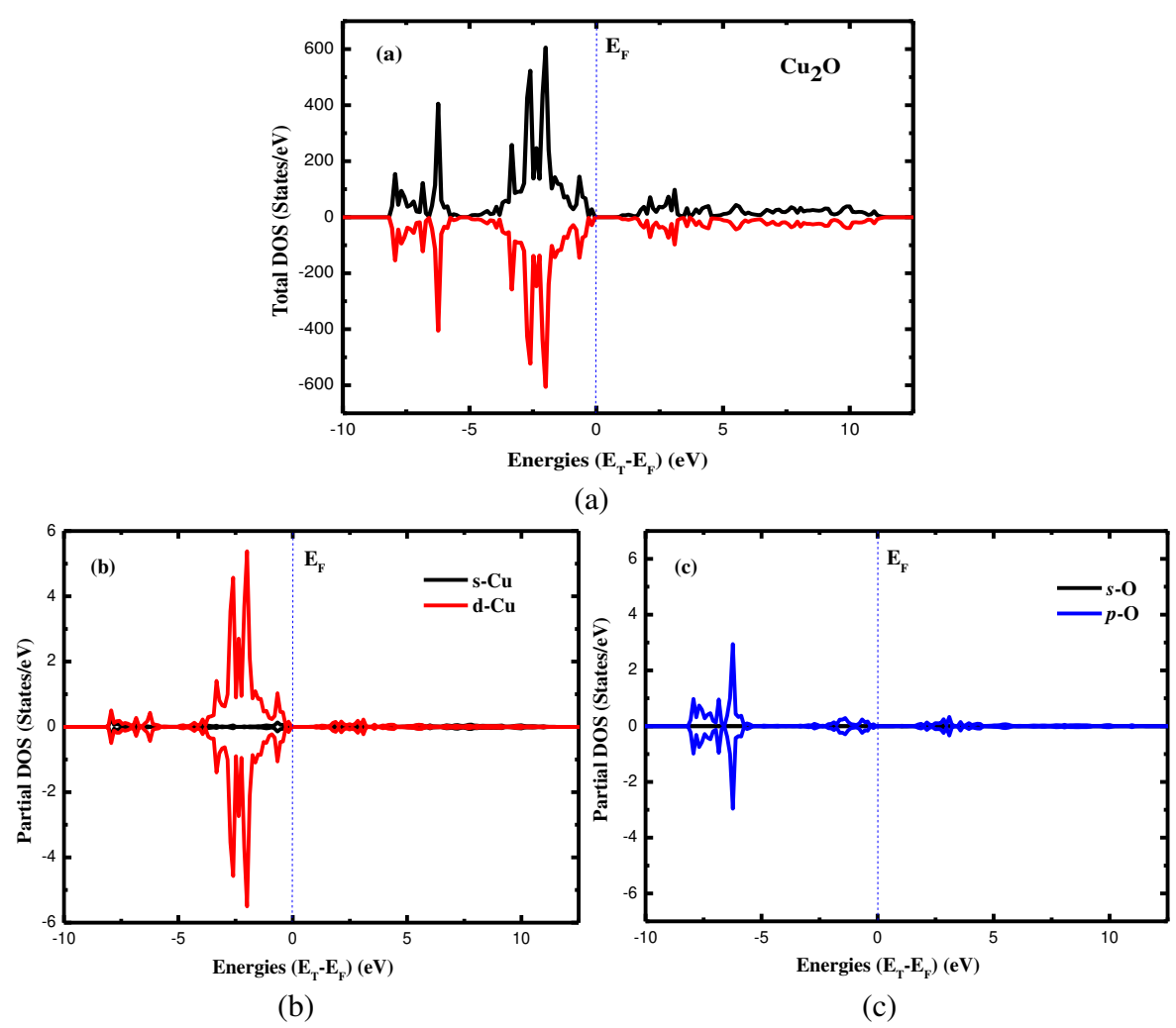


Fig. 6. Calculated density of states of pure Cu₂O: (a) Total DOS; (b) Partial DOS for Cu; (c) Partial DOS for O. Dashed line is the Fermi level E_F

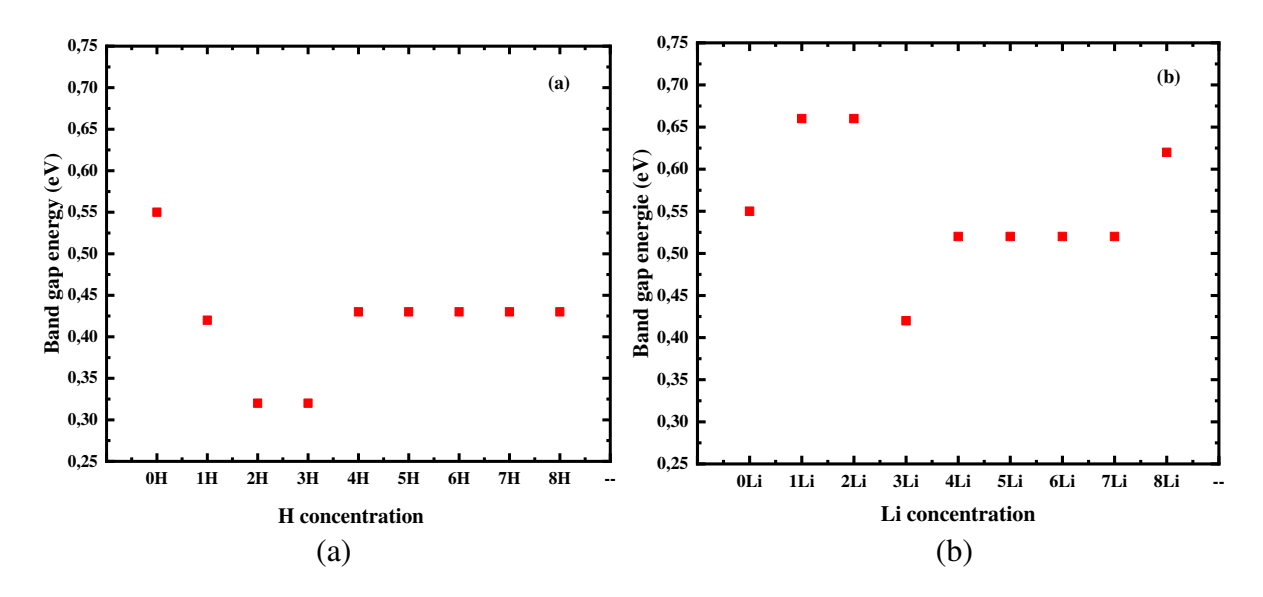


Fig. 7. Calculated bandgap variation with hydrogen (a) and lithium (b) concentrations

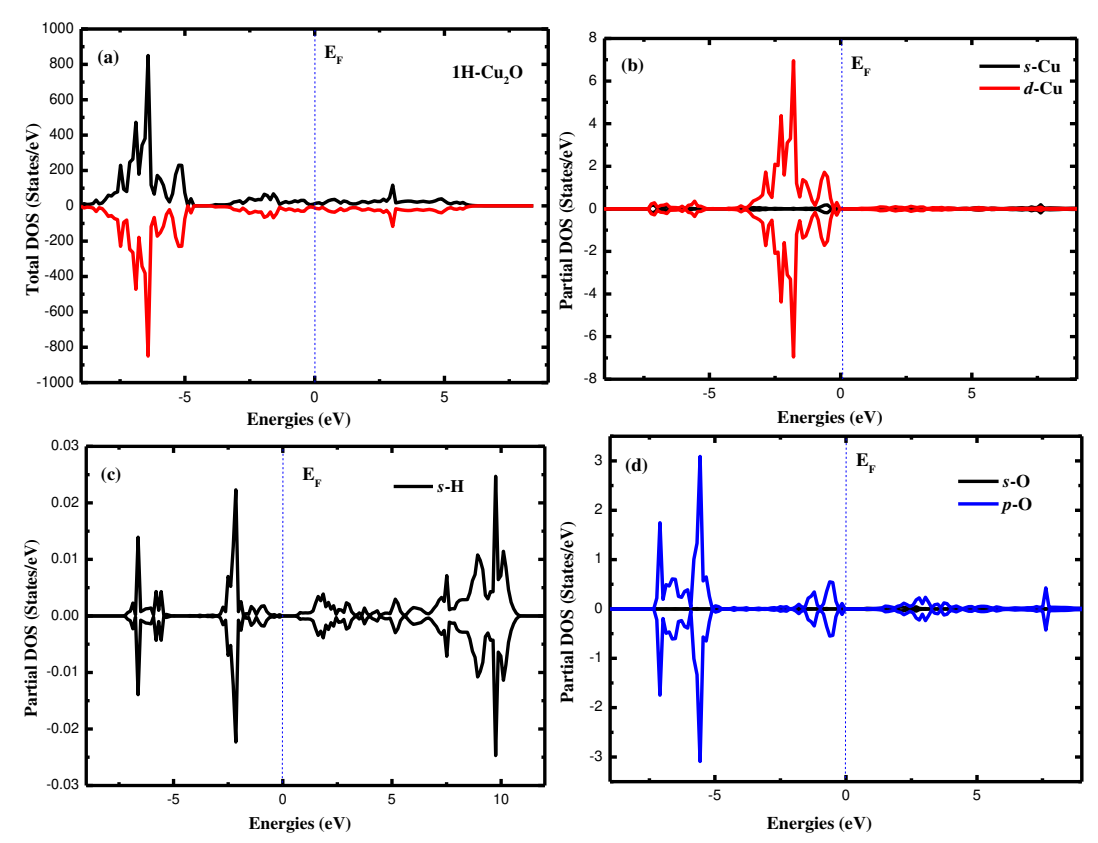


Fig. 8. Calculated density of states of 1H-Cu₂O, (a) Total DOS; (b) Partial DOS for Cu; (c) Partial DOS for H. (d) Partial DOS for O. Dashed line is the Fermi level E_F

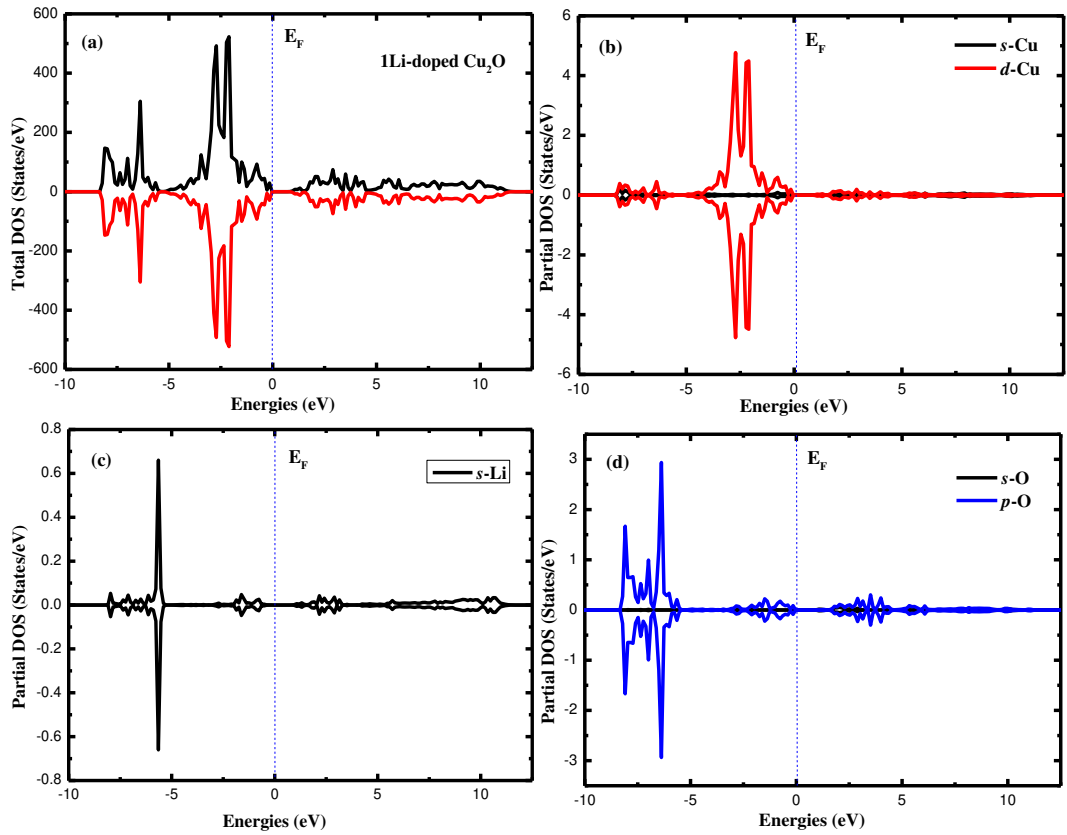
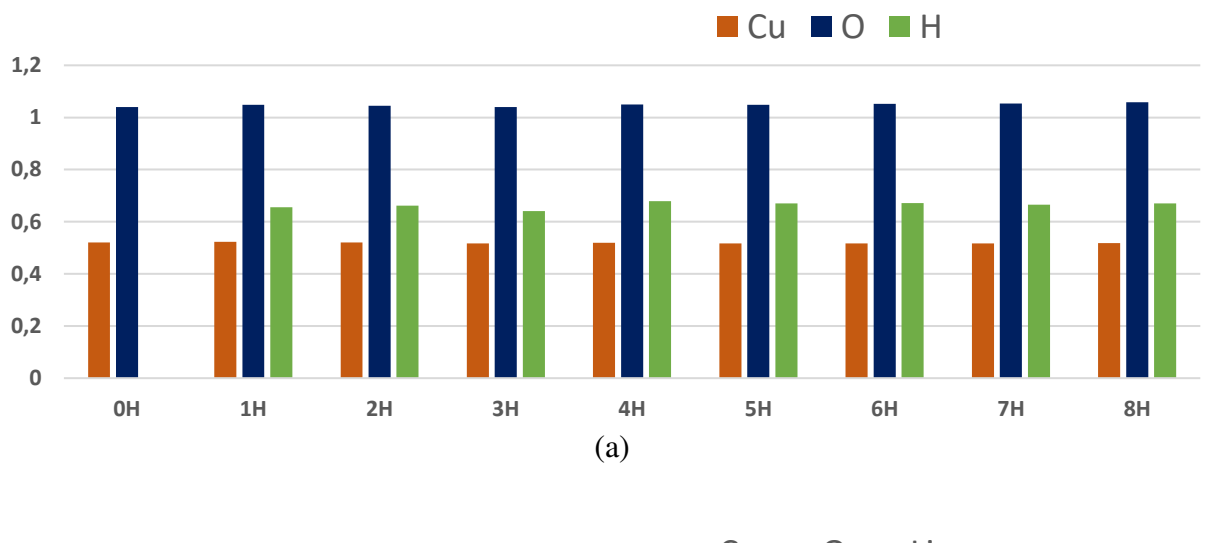


Fig. 9. Calculated density of states of 1Li-Cu₂O, (a) Total DOS; (b) Partial DOS for Cu; (c) Partial DOS for Li. (d) Partial DOS for O. Dashed line is the Fermi level E_F



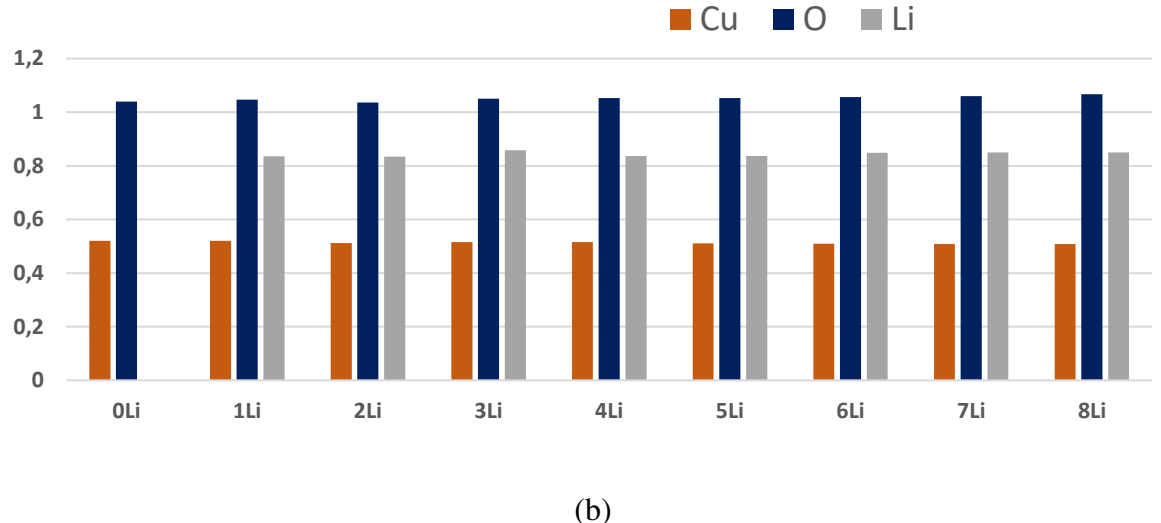


Fig. 10. Average atomic Bader charges (|e|) on undoped (a), H- and Li-doped (b) Cu₂O

Optical properties

The Cuprous oxide Cu₂O is a material with a low absorption coefficient which means more transmitted light and a promising p-type TCO, but its optical transmittance in the visible spectrum is limited by its relatively low band gap (2.17 eV) [35]. In this paper, we aim at increasing this value with different concentration of hydrogen or lithium.

In Fig. 11, we present the absorption coefficients (in order of 10⁵ cm⁻¹) versus the wavelength (nm) of all configurations of H-doped Cu₂O compared to the pure one in the visible light region (400-900 nm) and UV region (250-400 nm). The absorption coefficient of pure Cu₂O can be separated in two regions. The first region, between 250 and 400 nm, where α decreases from 1.815×10⁵ cm⁻¹ to 0.91×10⁵ cm⁻¹ and the second one (400-900 nm) in which the absorbance continues to decrease to 0.09×10⁵, which is in agreement with experimental results [41,42]. The incorporation of hydrogen decreases the absorbance of pure Cu₂O in the two regions. Additionally, the absorbance is significantly decreased in the visible region for low concentration of hydrogen into Cu₂O; while for the high concentration, the absorbance is almost zero in the 400–900 nm region. We remark a small peak at 650 nm when we doped with H, which is largely influenced by decreasing doping levels. The presence of hydrogen atoms increases the transmittance of Cu₂O.

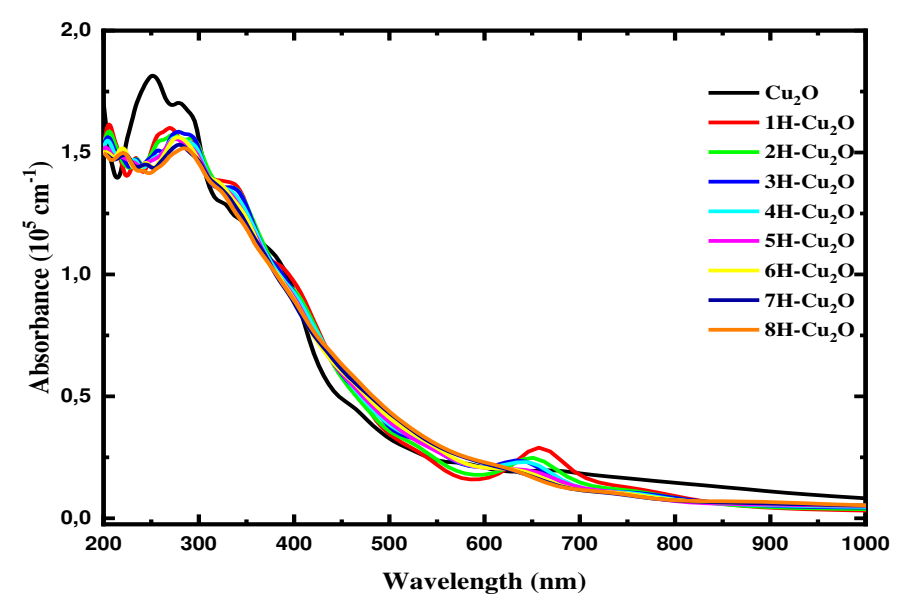


Fig. 11. The variation of the absorption coefficient of 1, 2, 3, 4, 5, 6, 7 and 8 H implanted in Cu_2O compared with pure one

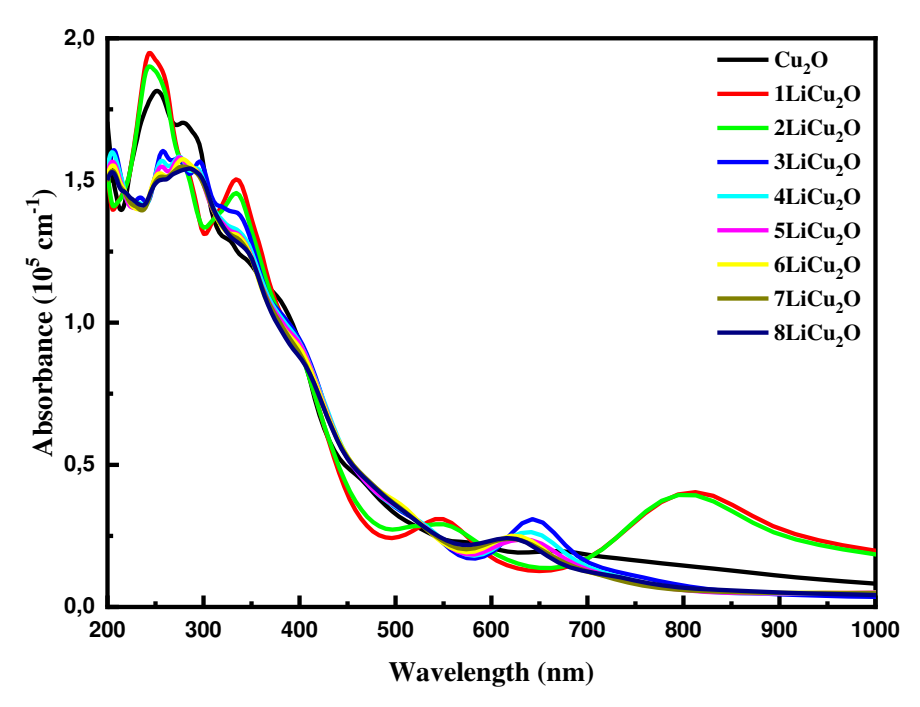


Fig. 12. The variation of the absorption coefficient of 1, 2, 3, 4, 5, 6, 7 and 8 Li inserted in Cu₂O compared with pure one

Figure 12 shows the absorption coefficient versus the wavelength (nm) of all configurations of Li-doped Cu_2O compared to the pure one in the visible and UV region. A small change was observed between different concentrations when the Li atom is inserted in the pure Cu_2O . We remark, in the visible region, the presence of two peaks (at 550 and 800 nm) observed in the low concentration of Lithium (1 and 2 atoms) and one peak (at 650 nm) in the high concentration. One notes that with the incorporation of 1 or 2 atoms of Lithium, the absorbance of pure Cu_2O increases in the 250-300 nm region and decreases in the rest of the UV region. The study of Nyborg & al. found that there is an increase of absorption in the case

of Li doping in Cu₂O [14]. Moreover, in the visible region, the absorbance increases when the concentration of Lithium insertion decreases.

Conclusion

In this study, the electronic, magnetic and optical properties are obtained for Cu₂O with hydrogen and lithium. The physical properties of Cu₂O change depending on the concentrations and the inserted element. The optimized lattice constant of Cu₂O is in good agreement with experimental value. The calculated formation energy of different concentrations of H or Li is negative, indicating the stability of the system. The H atom is tightly bound to the adjacent O ion through the O-H bond. The Cu-Li and O-Li bond lengths are slightly reduced. The presence of replacement hydrogen or lithium will not produce a magnetic moment sequence in Cu₂O. Moreover, according to the Fermi level energies the doping system is a degenerate p-type semiconductor. The metal-metal interaction governs the valence and conduction band edges, where the strength of a covalent bond Cu-Cu increased with doping that decreased the band gap energy. For low lithium doping, the optical properties of Cu₂O are improved in the visible light range. On the other hand, when hydrogen is introduced into the Cu₂O structure, its absorbance in the visible light region will sharply increase. This material (H- or Li-Cu₂O) can open several technical leaflets in terms of solar energy conversion and electricity storage and/or hydrogen production and/or storage and other applications.

References

- 1. Ramanathan S. (Ed.) *Thin Film Metal-Oxides*. NY: Springer; 2010.
- 2. Xu J, Xue D. Five Branching Growth Patterns in the Cubic Crystal System: A Direct Observation of Cuprous Oxide Microcrystals. *Acta Mater.* 2007;55(7): 2397–2406.
- 3. Yuhas BD, Yang P. Nanowire-Based All-Oxide Solar Cells. J. Am. Chem. Soc. 2009;131(10): 3756–3761.
- 4. Kale SN, Ogale SB, Shinde SR, Sahasrabuddhe M, Kulkarni VN, Greene RL, Venkatesan T. Magnetism in cobalt-doped Cu2O thin films without and with Al, V, or Zn codopants. *Appl. Phys. Lett.* 2003;82(13): 2100–21002.
- 5. Miyake M, Chen YC, Braun PV, Wiltzius P. Fabrication of three-dimensional photonic crystals using muitibeam interference lithography and electrodeposition. *Adv. Mater.* 2009;21(29): 3012–3015.
- 6. Han F, Li D, Li WC, Lei C, Sun Q, Lu AH. Nanoengineered Polypyrrole-Coated Fe2O3@C Multifunctional Composites with an Improved Cycle Stability as Lithium-Ion Anodes. *Adv. Funct. Mater.* 2013;23(13): 1692–1700.
- 7. Lou P, Cui Z, Jia Z, Sun J, Tan Y, Guo X. Monodispersed Carbon-Coated Cubic NiP2 Nanoparticles Anchored on Carbon Nanotubes as Ultra-Long-Life Anodes for Reversible Lithium Storage. *ACS Nano*. 2017;11(4): 3705–3715.
- 8. Wang C, Wu L, Wang H, Zuo W, Li Y, Liu J. Fabrication and Shell Optimization of Synergistic TiO2-MoO3 Core—Shell Nanowire Array Anode for High Energy and Power Density Lithium-Ion Batteries. *Adv. Funct. Mater.* 2015;25(23): 3524–3533.
- 9. Inguanta R, Piazza S, Sunseri C, Template electrosynthesis of aligned Cu2O nanowires: Part I. Fabrication and characterization. *Electrochimica Acta*. 2008;53(22): 6504–6512.
- 10. Zhang CQ, Tu JP, Huang XH, Yuan YF, Chen XT, Mao F. Preparation and electrochemical performances of cubic shape Cu2O as anode material for lithium ion batteries. *J. Alloys Compd.* 2007;441(1-2): 52–56.
- 11. Lv Q, Li L, Li Y, Mao J, Chen T, Shao D, Li M, Tan R, Zhao J, Shi S, Wang H, Liu L, Li L. A DFT Study of Electronic Structures and Photocatalytic Properties of Mn–Cu2O. *Russ. J. Phys. Chem. A.* 2020;94: 641–646.

- 12. Maurya V, Joshi K B, Band structure and thermoelectric properties of Cu2O from GGA and GGA+U approaches. *Bull. Mater. Sci.* 2019;42: 261.
- 13. Benaissa M, Si Abdelkader H, Merad G. Electronic and optical properties of halogen (H= F, Cl, Br)-doped Cu2O by hybrid density functional simulations. *Optik.* 2020;207: 164440.
- 14. Nyborg M, Azarov A, Bergum K, Monakhov E. Deposition and characterization of lithium doped direct current magnetron sputtered Cu2O films. *Thin Solid Films*. 2021;722: 138573.
- 15. Nyborg M, Karlsen K, Bergum K and Monakhov E, Dominant acceptors in Li doped, magnetron deposited Cu2O films. *Mater. Res. Express.* 2021;8(12): 125903.
- 16. Cai Y, Qin B, Li C, Si X, Cao J, Zheng X, Qiao L, Qi J. A successive "conversion deposition" mechanism achieved by micro-crystalline Cu2O modified current collector for composite lithium anode. *Journal of Industrial and Engineering Chemistry*. 2023;120: 285–292.
- 17. Zhang N, Zhao T, Wei L, Feng T, Wu F, Chen R. Stable Li/Cu2O composite anodes enabled by a 3D conductive skeleton with lithiophilic nanowire array. *Journal of Power Sources*. 2022;536: 231374.
- 18. Zhou X, Fu B, Li L, Tian Z, Xu X, Wu Z, Yang J. Hydrogen-substituted graphdiyne encapsulated cuprous oxide photocathode for efficient and stable photo electrochemical water reduction. *Nat. Commun.* 2022;13: 5770.
- 19. Chen M, Wang Y, Zhang Y, Yuan Y, Liu J, Liu B, Du Q, Ren Y, Yang H. Hydrogenated Cu2O octahededrons with exposed {111} facets: Enhancing sensing performance and sensing mechanism of 1-coordinated Cu atom as a reactive center. *Sensors and Actuators B: Chemical.* 2020;310: 127827.
- 20. Kresse G, Furthmüller J. Efficient iterative schemes for ab initio total-energy calculations using a plane-wave basis set. *Phys. Rev. B.* 1996;54(16): 11169.
- 21. Kresse G, Joubert D. From ultrasoft pseudopotentials to the projector augmented-wave method. *Phys. Rev. B.* 1996;59(3): 1758.
- 22. Perdew JP, Burke K, Ernzerhof M. Generalized Gradient Approximation Made Simple. *Phys. Rev. Lett.* 1997;77(18): 3865.
- 23. Blochl PE. Projector augmented-wave method. Phys. Rev. B. 1994;50: 17953.
- 24. Hallberg J, Hanson RC. The elastic constants of cuprous oxide. *Phys. Status Solidi B*. 1970;42: 305–310.
- 25. Manghnani MH, Brower WS, Parker HS. Anomalous elastic behavior in Cu2O under pressure. *Phys. Status Solidi A*. 1974;25: 69–76.
- 26. Korzhavyi PA, Johansson B. Literature review on the properties of cuprous oxide Cu2O and the process of copper oxidation. 2011.
- 27. Laskowski R, Blaha P, Schwarz K. Charge Distribution and Chemical Bonding in Cu2O. *Phys. Rev. B.* 2003;67: 075102.
- 28. Zheng C, Tao Y, Cao JZ, Chen RF, Zhao P, Wu XJ, Huang W. The structural, electronic, and optical properties of ladder-type polyheterofluorenes: a theoretical study. *J. Mol. Model.* 2012;18: 4929.
- 29. Reshak AH, Auluck S. Calculated optical properties of 2H-MoS2 intercalated with lithium. *Phys. Rev. B.* 2003;68: 125101.
- 30. Melrose DB, Stoneham RJ. Generalised Kramers-Kronig formula for spatially dispersive media. *J. Phys. A: Math.* 1977;10(1): L17.
- 31. Van de Walle CG, Denteneer PJH, Bar-Yam Y, Pantelides ST. Theory of hydrogen diffusion and reactions in crystalline silicon. *Phys. Rev. B.* 1989;39(15): 10791.
- 32. Neugebauer J, Van de Walle CG. Theory of hydrogen in GaN. In: Nickel NH. (ed.) *Hydrogen in Semiconductors II, Semiconductors and Semimetals*. Boston: Academic Press: 1999. p.479–502.

- 33. Kiran GK, Periyasamy G, Kamath PV. Role of alloying in Cu2O conversion anode for Li-ion batteries. *Theor. Chem. Acc.* 2019;138: 23.
- 34. Luo Z, Fu L, Zhu J, Yang W, Li D, Zhou L. Cu2O as a promising cathode with high specific capacity for thermal battery. *Journal of Power Sources*. 2020;448: 227569.
- 35. Kittel C. Introduction to Solid State Physics. 6th Ed. New York: Wiley; 1986.
- 36. Marksteiner P, Blaha P, Schwarz K. Electronic structure and binding mechanism of Cu2O. *Z. Physik B Condensed Matter*. 1986;64: 119–127.
- 37. Martnez-Ruiz A, Moreno M G, Takeuchi N. First Principles Calculations of the Electronic Properties of Bulk Cu2O, Clean and Doped with Ag, Ni, and Zn. *Solid State. Sci.* 2003;5(2): 291–295.
- 38. Soon A, Todorova M, Delley B, Stampfl C. Oxygen adsorption and stability of surface oxides on Cu(111): A first-principles investigation. *Phys. Rev. B*. 2006;73(16): 165424.
- 39. Islam MM, Diawara B, Maurice V, Marcus P. Bulk and surface properties of Cu2O: A first-principles investigation. *J. Mol. Struc.: THEOCHEM*. 2009;903(1-3): 41–48.
- 40. Janotti A, Van de Walle CG. Hydrogen multicentre bonds. *Nature Mater.* 2007;6(1): 44–47.
- 41. Luo Yu, Liangbin Xiong, and Ying Yu, Cu2O Homojunction Solar Cells: F-Doped N-type Thin Film and Highly Improved Efficiency. *J. Phys. Chem. C.* 2015;119(40): 22803–22811.
- 42. Zhong D. Synergetic effects of Cu2O photocatalyst with titania and enhanced photoactivity under visible irradiation. *Acta Chimica Slovaca*. 2013;6(1): 141–149.

THE AUTHORS

Amina Larabi 🗓

e-mail: Larabi.Amina@crtse.dz

Ibrahim Abdellaoui 🗓

e-mail: abdellaoui.ibrahim@yahoo.fr

Saloua Merazga 🗓

e-mail: Merazga.Saloua@crtse.dz

Mourad Mebarki 🗓

e-mail: Mebarki.Mourad@crtse.dz

Ammaria Mahmoudi 匝

e-mail: amaria_physique@yahoo.fr

Noureddine Gabouze (1)

e-mail: gabouzenoureddine@crtse.dz

МЕХАНИКА И ФИЗИКА МАТЕРИАЛОВ

51 (4) 2023

Учредители: Санкт-Петербургский политехнический университет Петра Великого, Институт проблем Машиноведения Российской академии наук Издание зарегистрировано федеральной службой по надзору в сфере связи, информационных технологий и массовых коммуникаций (РОСКОМНАДЗОР), свидетельство ПИ №ФС77-69287 от 06.04.2017 г.

Редакция журнала

Профессор, д.т.н., академик РАН, А.И. Рудской – главный редактор
Профессор, д.ф.-м.н., член-корр. РАН, А.К. Беляев – главный научный редактор
Профессор, д.ф.-м.н. И.А. Овидько (1961 - 2017) – основатель и почетный редактор
Профессор, д.ф.-м.н. А.Л. Колесникова – ответственный редактор
Профессор, д.ф.-м.н. А.С. Семенов – ответственный редактор
Л.И. Гузилова – выпускающий редактор, корректор

Телефон редакции +7(812)552 77 78, доб. 224

E-mail: mpmjournal@spbstu.ru Компьютерная верстка Л.И. Гузилова

Подписано в печать 29.09.2023 г. Формат 60x84/8. Печать цифровая Усл. печ. л. $\underline{10,0}$. Тираж 100. Заказ_____.

Отпечатано с готового оригинал-макета, предоставленного автором в Издательско-полиграфическом центре Политехнического университета Петра Великого. 195251, Санкт-Петербург, Политехническая ул., 29. Тел.: +7(812)552 77 78, доб. 224.

Study of the microstructure effect of SPD-treated titanium on microhardness and corrosion resistance in physiological environments for implantology purposes E.G. Zemtsova, A.A Petrov, S.O. Kirichenko, N.F. Morozov, V. K. Kudymov, A.Yu. Arbenin, B.N. Semenov, V.M. Smirnov	1-10
Tribological and tensile behaviour of Si ₃ N ₄ reinforced Cu-Sn matrix composites B. Adaveesh, G.V. Prabhushankar, M. Nagaral	11-22
Optimization of wear behaviour of hybrid Al (6061)-Al ₂ O ₃ -B ₄ C composites through hybrid optimization method P.K. Gupta, M.K. Gupta	23-37
The influence of friction stir processing on the microstructure and properties of the AD31T alloy A.E. Medvedev, V.V. Atroshchenko, A.S. Selivanov, A.R. Bogdanov, M.V. Gorbatkov, Y.V. Logachev, V.S. Lobachev, A.R. Sadrislamov	38-49
Study of burnishining effect on the thermal spray coatings A. Agnihotri, S.B.S Kalsi, H. Kansal	50-65
Peculiarities of the two-stage Zn diffusion profile formation from vapor phase into InGaAs/InP heterostructure for avalanche photodiode fabrication S.A. Blokhin, R.V. Levin, V.S. Epoletov, A.G. Kuzmenkov, A.A. Blokhin, M.A. Bobrov, Ya.N. Kovach, N.A. Maleev, E.V. Nikitina, V.V. Andryushkin, A.P. Vasiljev, K.O. Voropaev, V.M. Ustinov	66-75
The effect of ZnO cupping layer on the formation of sol-gel synthesized Ag nanoparticles L.A. Sokura, A.V. Kremleva, A.E. Romanov	76-84
Spin transistor effect in edge channels of silicon nanosandwiches L.E. Klyachkin, N.T. Bagraev, A.M. Malyarenko	85-95
Gas phase large-scale synthesis of Silicon carbide nanowires by industrial electron accelerator S.P. Bardakhanov, D.Y. Trufanov, I.K. Chakin, V.R. Gaponenko	96-106
Laser induced modification of nickel surface for non-enzymatic glucose detection A.S. Kondrateva, D.A. Strekalovskaya, B.V. Babuyk, A. Kuznetsov, L.A. Filatov, P.G. Gabdullin	107-117
Structural and mechanical relaxation on annealing in glass-metal layered composites M.A. Barbotko, O.N. Lyubimova, M.V. Ostanin	118-129
The influence of the altered structure zone characteristics after the material jet treatment on the samples stress state during tensility A.I. Verameichyk, M.V. Neroda, B.G. Holodar	130-141
The effect of mass collapse under hypervelocity impact of solid paraboloid into a thin screen A.F. Nechunaev, N.V. Naumova, N.P. Dorofeev	142-159
Simulation of the stress-deformed state of a rectangular bar using fast trigonometric interpolation in various statements of boundary value problems A.D. Chernyshov, V.V. Goryainov, E.N. Kovaleva	160-171
Ab initio study of Hydrogen and Lithium behaviors in Cu ₂ O	172-185



A. Larabi, M. Mebarki, I. Abdellaoui, A. Mahmoudi, S. Merazga, N. Gabouze